“The Influence of Carrageenan Polysaccharides on Ice Crystal Growth and Recrystallization: Experimental and Computational Insights”

Zur Erlangung des akademischen Grades eines

DOKTORS DER INGENIEURWISSENSCHAFTEN

von der KIT-Fakultät für Chemieingenieurwesen und Verfahrenstechnik des
Karlsruher Instituts für Technologie (KIT)
genehmigte

DISSERTATION

von

M.Sc. Julian Gerhäuser
aus Sinsheim

Tag der mündlichen Prüfung:	02.03.2026
Erstgutachter:	PD Dr. rer. nat. Volker Gaukel
Zweitgutachter:	PD Dr. rer. nat. Mathias J. Krause

Danksagung

In den Jahren von Mai 2019 bis März 2024 habe ich am Institut für Bio- und Lebensmitteltechnik: Lebensmittelverfahrenstechnik des Karlsruher Instituts für Technologie eine intensive Zeit des Wachstums, des Lernens und der wissenschaftlichen Arbeit erlebt. Diese Dissertation ist das Ergebnis dieser spannenden Reise, die ich ohne die Unterstützung vieler Menschen nicht hätte antreten können. Ihnen allen gilt mein herzlicher Dank.

Ich möchte mich bei Frau Prof. Dr.-Ing. Heike P. Karbstein bedanken für die herzliche Aufnahme an ihrem Institut und die damit verbundene Möglichkeit, im Bereich Lebensmittelverfahrenstechnik promovieren zu dürfen. Die Zusammenarbeit mit ihr, besonders in der Anfangsphase des Projektes „Studienstart“, war für mich sehr bereichernd.

Für die hervorragende Betreuung meiner Promotion auf dem Gebiet der eisbindenden Moleküle und der molekulardynamischen Simulation möchte ich mich bei Herrn PD Dr. rer. nat. Volker Gaukel herzlich bedanken. Die gemeinsamen Diskussionen und Besprechungen waren sehr hilfreich, auch wenn diese oft länger als geplant dauerten. Ebenfalls bedanken möchte ich mich für die beruflichen sowie privaten Gespräche am Institut oder in der Bahn. Ich danke für das Vertrauen und die großzügigen Freiheiten, die er mir bei der Umsetzung meiner Arbeit und Ideen eingeräumt hat. Seine Unterstützung war für meine berufliche Weiterentwicklung von unschätzbarem Wert.

Ich möchte mich bei Herrn Dr.-Ing. Marc Wittner für die zusätzliche Betreuung zu Beginn meiner Promotion und die anregenden Diskussionen danken. Herrn PD Dr. Mathias J. Krause danke ich für die fachlichen Diskussionen zum Thema Simulation und für die Übernahme des Korreferates.

Mein herzlicher Dank gilt meinen Kollegen für die großartige Zusammenarbeit, die fachlichen Gespräche und den Zusammenhalt im Team. Ich habe die offene und freundschaftliche Atmosphäre, die das Arbeiten so angenehm gemacht hat, immer sehr geschätzt.

Besonders hervorheben möchte ich Nico, Felix, Eva, Laura und natürlich Désirée. Ich werde die vielen gemeinsamen Kaffeepausen, die lustigen Gespräche und die gegenseitige Unterstützung sehr vermissen. Eure Freundschaft hat mein Berufsleben um ein Vielfaches bereichert.

Mein Dank gilt ebenfalls allen Technikern für ihre stets unermüdliche Unterstützung bei Experimenten und darüber hinaus. Die LVT wäre ohne das Engagement und die Expertise der Techniker nicht denkbar.

Zudem danke ich Klaudia und Renate von Herzen für die vielen Gespräche und die Unterstützung bei allen organisatorischen Belangen.

Ich möchte mich bei dir, Katharina, von ganzem Herzen bedanken für dein Verständnis und deine unermüdliche Unterstützung während dieser herausfordernden Zeit. Dies bedeutet mir unglaublich viel.

Zudem bin ich meinen Eltern zutiefst dankbar für ihren bedingungslosen Glauben an mich. Sie haben mich in jeder Lebenslage unterstützt und ohne sie hätte ich dieses Ziel niemals erreicht.

Summary

While freezing of food and other biological materials is a common and effective preservation method, it poses a high risk of significant damage and quality loss, especially for complex and delicate products. The formation of ice crystals and their growth, particularly through recrystallization processes, is one of the main damaging mechanisms.

A highly effective approach for modulating both ice crystal formation and recrystallization is the addition of specific additives. Ice-binding proteins, which inhibit the growth and recrystallization of ice crystals by adsorbing to their surface, are highly effective, but their application is severely limited due to low availability and resulting high costs. Furthermore, the application of recombinantly produced ice-binding proteins is restricted due to the low consumer acceptance of genetically modified additives in food applications. Consequently, there is a high demand for alternative additives that can be used in foods and produced cost-effectively on a large scale.

Even earlier studies demonstrated the potent ice recrystallization inhibition activity of various carrageenans, polysaccharides isolated from algal cell walls. Carrageenans are made of alternating disaccharide units, each composed of a β-1,3-linked D-galactopyranose and either a α-1,4-linked D-galactopyranose or a 3,6-anhydro-α-D-galactopyranose. The presence of 3,6-anhydro-α-D-galactopyranose units is crucial for the gel-forming properties of the different carrageenan types. Carrageenans are therfore widely used as thickeners and stabilizers in the food industry. In addition, these polysaccharides, with up to two sulfate groups per monosaccharide, exhibit varying functional properties. As exemplified by gel formation, the diverse functional properties of carrageenans arise from their distinct molecular structures. These structures are defined by factors such as the type of the disaccharide units and sulfate content. However, environmental conditions, including salt type and concentration also influence the structural formation and, therefore, gelation of carrageenans.

Beyond its gel-forming properties, κ-carrageenan exhibits a pronounced ice recrystallization inhibition activity, as demonstrated in numerous studies. While smaller ice crystals are formed at the beginning of storage, recrystallization processes during frozen storage are inhibited. The effectiveness of κ-carrageenan is concentration-dependent, reaching a plateau at high concentrations. Moreover, the addition of κ-carrageenan induces a morphology change of the ice crystal shape from spherical to angular and edgy. Gel formation, however, results in a loss of ice

recrystallization inhibition activity of κ-carrageenan. Thus, the type and concentration of ions present are decisive factors, as they can induce gelation.

The exact mechanism behind κ-carrageenan's strong recrystallization inhibition is currently unclear. The similar morphology altering effects observed in both κ-carrageenan and ice-binding proteins indicate a common mechanism of action, likely involving the adsorption of molecules onto the ice crystal surface. However, this hypothesis has not yet been conclusively confirmed, and the specific structural characteristics needed for the recrystallization inhibiting activity also remain unkown. To address this research gap, this work employs targeted experiments, including different types of carrageenans and, for the first time, molecular dynamics simulations. The aim is to gain a deeper understanding of the mechanism underlying the recrystallization inhibiting properties of carrageenans, to identify structural components necessary for their activity, and to facilitate their targeted and optimized application in food products.

Commercial carrageenans can provide a cost-effective solution for controlling recrystallization. However, a major challenge is that their precise composition is often unknown, as manufacturers provide only basic specifications. This makes it difficult to reliably link their functional properties to their specific molecular structures or to exclude the occurrence of mixtures and hybrid carrageenans. Therefore, commercially available κ-, ι-, and λ-carrageenans were characterized using partial enzymatic hydrolysis in combination with HPLC-MS and HPSEC-RI. In addition to variations in associated cations, the characterized carrageenans deviated significantly from the manufacturer's specified type and hybrid carrageenans were identified among the analyzed samples. These structural differences result in alterations in functional properties, as exemplified by their rheological behavior. The strength of the gel network in hybrid carrageenans correlated positively with the proportion of κ-units, while the presence of ν-units inhibited gel formation.

Given the varying gel-forming properties of the carrageenan and hybrid carrageenan samples, it can be inferred that their structural composition is responsible for these differences, and consequently, their recrystallization inhibiting activities may also vary. For this reason, the recrystallization inhibiting properties of the various samples, as well as the influence of different associated cations, were determined. The results confirmed that unlike κ-carrageenan, ι-carrageenan exhibited a lower recrystallization inhibiting activity. In general, a positive correlation was found between the proportion and length of blocks consisting of κ-units and the recrystallization inhibition activtity. In addition, associated cations that had a helix-stabilizing effect led to an improvement in the recrystallization inhibiting properties of κ- and ι-carrageenans.

Considering the importance of sulfate groups for the structural conformation of carrageenans and the decrease in recrystallization inhibition activity with increasing sulfate content from κ- to ι-carrageenan, an investigation of furcellaran seemed promising. Furcellaran, a carrageenan polysaccharide similar to κ-carrageenan but with a lower sulfate content, offered the opportunity to analyze the influence of sulfate groups on recrystallization in greater detail. The results showed a comparable recrystallization inhibiting effect of furcellaran and κ-carrageenan. Therefore, a further reduction in sulfate content did not provide further improvement in recrystallization inhibition. Additionally, it was shown that, in addition to salt addition, an increase in polysaccharide concentration could induce gel formation. This gel formation was accompanied by a reduced recrystallization-inhibiting effect.

Since the mechanism of carrageenan's recrystallization inhibition remained unclear, molecular dynamics simulations were performed to investigate the interaction process at a molevular level and demonstrate the direct interaction with the ice crystal surface. The Gibbs-Thomson effect is widely considered as the primary mechanism for the recrystallization inhibition activity of ice-binding proteins. Using an experimentally and computationally ice-binding protein as an example, the extent to which molecular dynamics simulations could accurately reproduce the Gibbs-Thomson effect was investigated. The analysis of the resulting ice crystal surface structure after binding of the protein showed good agreement between the determined radius of curvature and the theoretical value calculated using the Gibbs-Thomson equation. These results confirm the great potential of molecular dynamics simulations for the detailed investigation of ice-binding molecules and their interaction with the ice crystal surface.

Finally, molecular dynamics simulations were employed to analyze in detail the interaction of κ-carrageenan with various ice surfaces. This approach also enabled the investigation of how the polysaccharide's overall structure and specific functional groups contribute to this interaction. The results indicated a higher affinity of the polysaccharide for the primary and secondary prism planes, whereas the interaction with the basal plane was less pronounced. During the entire simulation time, a slow but steady ice growth was observed, despite the presence of κ-carrageenan at the ice-water interface. This suggests a reversible binding mechanism for κ-carrageenan, similar to antifreeze glycoproteins. Moreover, the ability to interact with the ice surface was independent of the formation of a double helical structure. At the molecular level, hydrogen bonds and the structural adaptation of the κ-carrageenan molecule, especially the oxygens, seem to play a decisive role in the interaction between the polysaccharide and the ice

surface. Despite extending the molecule's length from three to six units to increase the amount of available binding sites, no improvement in binding affinity was observed.

This research significantly contributes to the elucidation of the molecular and structural mechanisms underlying the recrystallization inhibition activity of carrageenans, thereby unlocking new perspectives for their industrial application in foods and other fields. These findings highlight the potential of these natural polysaccharides as a sustainable and effective antifreeze.

Zusammenfassung

Obwohl die tiefgekühlte Lagerung von Lebensmitteln und anderen biologischen Materialien eine etablierte und effektive Konservierungsmethode darstellt, birgt sie insbesondere für komplexe und empfindliche Produkte ein hohes Risiko von Beschädigungen und signifikanten Qualitätsverlusten. Dabei ist die Bildung von Eiskristallen und vorallem deren Wachstum durch Rekristallisationsprozesse einer der Hauptschädigungsmechanismen.

Eine hochwirksame Strategie zur Modulation sowohl der Eiskristallbildung als auch der Rekristallisation ist die Zugabe von speziellen Additiven. Eisbindende Proteine, die durch Adsorption an die Eiskristalloberfläche deren Wachstum und Rekristallisation hemmen, sind zwar hochwirksam, jedoch ist deren Anwendung aufgrund begrenzter Verfügbarkeit und daraus resultierenden hohen Kosten stark eingeschränkt. Zudem ist der Einsatz von rekombinant hergestellten eisbindenden Proteinen durch die geringe Verbraucheraktzeptanz von gentechnischen Zusätzen in Lebensmittelanwendungen limitiert. Aufgrund der genannten Herausforderungen und Einschränkungen besteht ein hoher Bedarf an alternativen Zusatzstoffen, die sowohl in Lebensmitteln eingesetzt, als auch großtechnisch kosteneffizient produziert werden können.

Bereits in früheren Studien zeigten verschiedene Carrageene, aus Algenzellwänden isolierte Polysaccharide, ausgeprägte rekristallisationsinhibierende Eigenschaften. Carrageene bestehen aus alternierenden Disaccharid-Einheiten, die jeweils aus 1,3-glykosidisch verknüpfter β-D-Galactopyranose und entweder 1,4-glykosidisch verknüpfter α-D-Galactopyranose oder 3,6-Anhydro-α-D-Galactopyranose aufgebaut sind. Das Vorhandensein von 3,6-Anhydro-α-D-Galactopyranose-Einheiten ist entscheidend für die Gelbildungseigenschaften der verschiedenen Carragen-Typen. Daher werden Carrageene in der Lebensmittelindustrie häufig als Verdickungsmittel und Stabilisatoren eingesetzt. Darüber hinaus weisen diese Polysaccharide, mit bis zu zwei Sulfatgruppen pro Monosaccharid-Einheit, unterschiedliche funktionellen Eigenschaften auf. Wie sich anhand der Gelbildung zeigt, ergeben sich die vielfältigen funktionellen Eigenschaften von Carrageenen aus ihren unterschiedlichen molekularen Strukturen. Diese Strukturen werden durch Faktoren wie die Art der Disaccharideinheiten und den Sulfatgehalt bestimmt. Allerdings beeinflussen auch Umweltbedingungen, einschließlich der Art und Konzentration von Salzen, die Strukturbildung und somit die Gelierung von Carrageenen.

Über die gelbildenden Eigenschaften hinaus weist κ-Carrageen eine ausgeprägte rekristallisationsinhibierende Aktivität auf, die bereits in einigen Studien nachgewiesen wurde. Einerseits werden zu Beginn der Lagerung kleinere Eiskristalle erhalten, andererseits wird das Wachstum

dieser durch Rekristallisationsprozesse während der gefrorenen Lagerung unterbunden. Die Effektivität von κ-Carrageen ist dabei Konzentrationsabhängig und erreicht ab einer bestimmten Konzentration ein Plateau. Ebenfalls wird durch Zugabe von κ-Carrageen eine Morphologieänderung der Eiskristalle von sphärisch zu eckig und kantig induziert. Im Gegensatz dazu, führt eine Gelbildung zum Verlust der rekristallisationsinhibierenden Eigenschaft von κ-Carrageen. Damit spielt die Art und Konzentration der vorliegenden Ionen ebenfalls eine entscheidende Rolle, da eine Gelbildung dadurch induziert werden kann.

Der genaue Mechanismus, der hinter der starken Hemmung der Rekristallisation durch κ-Carrageen steckt, ist derzeit noch unklar. Die Ähnlichkeit der morpholgieverändernden Eigenschaften, die sowohl bei κ-Carrageen als auch bei eisbindenden Proteinen beobachtet werden, deuten auf einen gemeinsamen Wirkmechanismus hin, der wahrscheinlich auf der Adsorption der Moleküle an die Eiskristalloberfläche beruht. Diese Hypothese konnte jedoch noch nicht eindeutig bestätigt werden, und auch die spezifischen Strukturmerkmale, die für die Aktivität zur Hemmung der Rekristallisation erforderlich sind, bleiben unbekannt. Um diese Forschungslücke zu schließen, wurden in der vorliegenden Arbeit gezielte Experimente mit verschiedenen Caraggeenen und erstmals molekulardynamische Simulationen eingesetzt. Ziel war es, ein tieferes Verständnis des Mechanismus der rekristallisationshemmenden Eigenschaften von Carrageenen zu erlangen, die für ihre Aktivität notwendigen Strukturkomponenten zu identifizieren und ihre gezielte und optimierte Anwendung in Lebensmittelprodukten zu erleichtern.

Kommerziell verfügbare Carrageene könnten grundsätzliche eine kostengünstige Möglichkeit darstellen, die Rekristallisation zu kontrollieren. Eine große Herausforderung besteht jedoch darin, dass ihre genaue Zusammensetzung oft unbekannt ist, da die Hersteller nur grundlegende Spezifikationen angeben. Dies erschwert es, ihre funktionellen Eigenschaften zuverlässig mit ihren spezifischen molekularen Strukturen zu verknüpfen oder das Vorhandensein von Mischungen und Hybrid-Carrageenen auszuschließen. Aus diesem Grund wurden kommerziell erhältliche κ-, ι-, und λ-Carrageene mittels partieller enzymatischer Hydrolyse in Verbindung mit HPLC-MS und HPSEC-RI charakterisiert. Neben Unterschieden in den assoziierten Kationen zeigten die charakterisierten Carrageene erhebliche Abweichungen von dem vom Hersteller angegebenen Carrageen-Typ, zudem wurden unter den analysierten Proben Hybrid-Carrageene nachgewiesen. Diese strukturellen Unterschiede führen zu Veränderungen der funktionellen Eigenschaften, was sich beispielhaft in ihrem rheologischen Verhalten zeigte. Die Stärke des gebildeten Gelnetzwerkes bei Hybrid-Carrageenen korrelierte positiv mit dem Anteil an κ-Einheiten, wohingegen das vorhandensein von ν-Einheiten die Gelbildung inhibierte.

Angesichts der unterschiedlichen gelbildenden Eigenschaften der vorliegenden Carragene und Hybrid-Carrageene lässt sich ableiten, dass ihre strukturelle Zusammensetzung für diese Unterschiede verantwortlich ist und folglich auch ihre rekristallisationsinhibierende Aktivität variieren kann. Aus diesem Grund wurden die rekristallisationsinhibierenden Eigenschaften der verschiedenen Carrageene sowie der Einfluss verschiedener assoziierter Kationen bestimmt. Die Ergebnisse bestätigten, dass reines ι-Carrageen im Gegensatz zu reinem κ-Carrageen eine geringenge rekristallisationsinhibierende Wirkung aufweist. Allgemein zeigte sich ein positiver Zusammenhang zwischen dem Anteil und der Länge von Blöcken bestehend aus κ-Einheiten und der Aktivität zur Hemmung der Rekristallisation. Zudem führten assoziierten Kationen, die eine helixstabilisierende Wirkung besitzen, bei allen Carrageen-Typen zu einer Verbesserung der rekristallisationsinhibierenden Eigenschaften.

Aufgrund der Relevanz der Sulfatgruppen für die Strukturbildung von Carrageenen und der Abnahme der rekristallisationsinhibierenden Wirkung mit steigenden Sulfatgehalt bei ι-Carrageen, schien eine Untersuchung von Furcellaran vielversprechend. Furcellaran gehört ebenfalls zu den Carrageenen und entspricht strukturell κ-Carrageen, weist jedoch einen geringeren Sulfatgehalt auf. Somit bot Furcellaran die Möglichkeit, den Einfluss der Sulfatgruppen auf die Rekristallisation genauer zu analysieren. Die Ergebnisse ergaben eine vergleichbare rekristallisationsinhibierende Wirkung von Furcellaran und κ-Carrageen. Daraus lässt sich schließen, dass eine weitere Reduktion des Sulfatgehaltes keine weitere Verbesserung der Rekristallisationsinhibierung bietet. Zusätzlich wurde gezeigt, dass neben Salzzugabe auch eine Erhöhung der Polysaccharidkonzentration eine Gelbildung induzieren konnte. Diese Gelbildung ging mit einer verminderten rekristallisationsinhibierenden Wirkung einher.

Da der Mechanismus der Rekristallisationshemmung durch Carrageenan unklar blieb, wurden Molekulardynamiksimulationen durchgeführt, um den Interaktionsprozess auf molekularer Ebene zu untersuchen und die direkte Interaktion mit der Eiskristalloberfläche nachzuweisen. Der Gibbs-Thomson Effekt wird weithin als der primäre Mechanismus für die rekristallisationshemmende Aktivität von eisbindenden Proteinen angesehen. Anhand eines experimentell und simulativ bereits charakterisierten eisbindenden Proteins wurde untersucht, inwieweit Molekulardynamiksimulationen den Gibbs-Thomson Effekt genau reproduzieren können. Dabei ergab die Analyse der resultierenden Eiskristalloberflächenstruktur nach der Bindung des Proteins eine gute Übereinstimmung des bestimmten Krümmungsradius mit dem theoretischen

Wert errechnet mittels Gibbs-Thomson Gleichung. Diese Ergebnisse bestätigen das große Potential molekulardynamischer Simulationer zur detaillierten Untersuchung von eisbindenden Molekülen und deren Interaktion mit Eiskristallen.

Abschließend wurde anhand molekulardynamischer Simulationen die detaillierte Interaktion von κ-Carrageen mit verschiedenen Eisoberflächen analysiert. Dieser Ansatz ermöglichte es auch, zu untersuchen, wie die Gesamtstruktur und spezifische funktionelle Gruppen des Polysaccharids zu dieser Interaktion beitragen. Dabei deuten die Ergebnisse auf eine höhere Affinität des Polysaccharids zur primären und sekundären Prismenfläche, wohingegen die Interaktion mit der Basalebene weniger ausgeprägt ist. Während der gesamten Simulationsdauer war ein langsames aber stetiges Eiswachstum zu beobachten, trotz gleichzeitiger Anwesenheit von κ-Carrageen an der Eis-Wasser-Grenzfläche. Dies deutet auf einen reversiblen Bindungsmechanismus hin, wie er bereits für Antigefrierglykoproteine beschrieben wurde. Darüber hinaus erwies sich die Interaktionsfähigkeit von κ-Carrageen mit der Eisoberfläche als unabhängig von der Bildung einer Doppelhelixstruktur. Auf molekularer Ebene scheinen Wasserstoffbrückenbindungen und die strukturelle Anpassung des κ-Carrageenmoleküls and das Eisgitter, insbesondere der Sauerstoffe, eine entscheidende Rolle bei der Interaktion zwischen Polysaccharid und der Eisoberfläche zu spielen. Trotz der Verlängerung der Moleküllänge von drei auf sechs Einheiten, um die Anzahl der verfügbaren Bindungsstellen zu erhöhen, wurde keine Verbesserung der Bindungsaffinität beobachtet.

Die vorliegende Arbeit trägt maßgeblich zur Aufklärung der molekularen und strukturellen Mechanismen bei, die der rekristallisationshemmenden Aktivität von Carrageenen zugrunde liegen. Sie eröffnet damit neue Perspektiven für ihre industrielle Anwendung in Lebensmitteln und anderen Bereichen. Die Ergebnisse unterstreichen das Potenzial dieser natürlichen Polysaccharide als nachhaltiges und wirksames Frostschutzmittel.

Table of Contents

1 General Introduction

1.1 Introduction

The preservation of biologic matter, such as food, commonly involves freezing and subsequent storage at temperatures below -18 °C which has become standard practice. These frigid temperatures tremendously slow down chemical, biochemical, microbial and physical processes. Consequently, food products can be stored for prolonged periods. In addition, seasonal products are made available throughout the year and the quantity of food waste due to spoilage is minimized. Over the past few decades, freezing technology has made its way into private households from industrial applications. Since 2008, approximately 50% of German households utilize a freezer or chest freezer units to store frozen food [1]. This also enables the food industry to offer pre-portioned convenience products for both commercial and domestic consumption. These advancements have resulted in a per-capita consumption of frozen food products in Germany of 49.4 kg in 2023, with continued growth expected [2]. Moreover, an additional 7.9 L ice cream were consumed per person in Germany [3]. The frozen food market (without ice cream) in 2023 was dominated by bakery products, followed by vegetables, frozen meals and potato-based products such as French fries [4]. Consequently, frozen foods have become an important part of today's nutrition.

Besides conventional frozen storage of food products, cryopreservation is considered the gold standard for long term preservation of cells, organs and tissues. The samples are typically stored in liquid nitrogen at -196 °C allowing theoretical preservation periods of thousands of years due to the inhibition of all reactions aside from radiation-induced photophysical processes [5].

While both methods are highly effective, their drawbacks are substantial. In addition to the energy consumption for sample freezing and temperature maintenance, ice crystal formation and structural changes during storage can cause massive damage to the stored materials [5–8]. Changes in ice crystal structure are broadly reffered to as recrystallization, a process significantly accelerated by temperature fluctuations [9,10]. Recrystallization causes ice crystals to grow and rearrange resulting in considerable damage to the product [11,12]. While thawing results in a substantial amount of recrystallization processes, it is unavoidable in the overall preservation procedure.

Furthermore, the freezing process is essential for determining the initial ice crystal size at the beginning of the storage period. Smaller crystals generally cause less damage to the product and are thus preferred. While innovative methods such as high pressure freezing [13,14], ultrasound assisted freezing [15,16] and electric or magnetic field assisted freezing [17–20] were

developed, most industrial processes rely on rapid cooling rates to achieve small ice crystals [21]. Overall, these advanced freezing techniques have achieved a high level of performance [22,23], suggesting limited potential for further substantial improvements [24].

Beyond the freezing process, ice crystal size and recrystallization can be modulated by the addition of certain additives. The most effective of these are ice-binding proteins (IBPs) [25,26]. By directly interacting with the ice crystal surface, these proteins are able to stop further ice growth over a certain temperature range [27]. This phenomenon is referred to as thermal hysteresis (TH). Moreover, IBP are exceptionally potent in ice recrystallization inhibition (IRI) and promote the formation of small ice crystals during freezing [28]. Despite being highly effective, IBP are rarely used in industrial applications due to their low availability and high costs [29]. To address these issues, microorganisms such as yeasts are genetically modified to produce IBPs [30,31]. Nevertheless, there is strong resistance from consumers who are concerned about genetically modified food additives [32,33]. Consequently, alternatives to IBPs are needed.

Carrageenans, linear sulfated polysaccharides from red algal species, appear to be a promising alternative to IBPs. Composed of repeating disaccharide untis, these polymers contain specific galactose variations and may also possess sulfate groups [34–36]. Furthermore, the exact composition of carrageenans is determined by the type of seaweed and the extraction process [37]. However, κ-carrageenan demonstrated the most significant impact on ice recrystallization in various experiments [25,38,39]. Moreover, it is readily available in large quantities as it is used extensively in the food industry as thickener, gelling agent and stabilizer [34,40]. Previous research linked IRI activity of carrageenans to their structural features and sample composition. Some carrageenans are capable of forming thermoreversible gels, a process affected by the presence of certain ions. The findings of Leiter et al. demonstrated that the gel formation of κ-carrageenan negatively impacts its ability to inhibit recrystallization [41]. Additionally, the present ion type and concentration play a role. While the presence of sodium ions reduced the IRI activity of κ-carrageenan [42], very low concentrations of NaCl seemed to improve it [43]. Furthermore, the addition of κ-carrageenan alters the ice crystal morphology from round to rectangular shapes [25]. This change in ice crystal shape is correlated to κ-carrageenan's IRI activity, indicating a binding to the crystal surface similar to IBP. Moreover, the length of the κ-carrageenan polymer influences the IRI activity, with in average smaller molecules being less effective [43]. Comparative studies illustrated that ι-carrageenan appeared to be less effective at inhibiting recrystallization compared to κ-carrageenan [38,44]. The complexity of

the factors influencing IRI activity of κ-carrageenan highlights the necessity of knowing its exact composition. This likely holds true for hybrid carrageenans, as their gelling properties seem to be mainly influenced by the relative abundance of κ- and ν-units within the polymer chain [36], with possible implications for their IRI activity. While the direct interaction of IBPs with the ice surface has been experimentally and computationally validated using molecular dynamics simulations (MD), a simulation technique that predicts the movements of individual atoms, such evidence is currently lacking for carrageenan.

1.1.1 Outline and Structure

This research work aims to deepen the understanding of the interaction mechanism by which these molecules inhibit ice crystal recrystallization, building upon existing findings and assumptions. In order to investigate the fundamental principles of recrystallization inhibition, a multidisciplinary approach was employed, integrating experimental techniques and computational simulations. This thesis will further address the following research questions to deepen the understanding of IRI active carrageenans:

- What are the mechanisms by which carrageenan polysaccharides affect ice recrystallization? → Primarily investigated using MD simulations.
- Does a direct molecular interaction between carrageenan molecules and the ice crystal surface occur? → Examined using MD simulations.
- Which functional groups and structural motifs of the carrageenan molecule facilitate the observed IRI activity? → Studied via experiments and MD simulations.

Chapter 1 establishes the theoretical framework for this thesis, including the principles of freezing biological materials and recrystallization processes, the properties of ice-binding molecules, the structural characteristics of carrageenans and the methodology of MD simulations. Given that direct interaction with the ice crystal surface is a potential mechanism of action for IRI active carrageenans, a detailed explanation of IBPs, the most thoroughly investigated class of ice-binding molecules, and their interaction mechanism is provided. Besides, this thesis can be divided into two parts: experimental and computational. **Chapters 2 – 4** present experimental investigations of various carrageenans, exploring the influence of structural variations on their IRI activity. Given its similarity to κ-carrageenan, furcellaran is also examined for its IRI activity to identify the crucial structural characteristics enabling recrystallization inhibition. To gain a deeper understanding of the precise mechanisms occurring at

the ice crystal surface, MD simulations are employed in **Chapters 5 and 6**. Finally, **Chapter 7** provides a comprehensive discussion and summary of the results presented in **Chapters 3–7**, directly addressing the research questions outlined in the beginning of this section. Furthermore, this chapter explores the potential implications of the findings for practical applications, particularly in areas where the IRI activity of carrageenans is required, and proposes ideas for future research. A graphical representation of the outline of this work is provided in Figure 1.1.

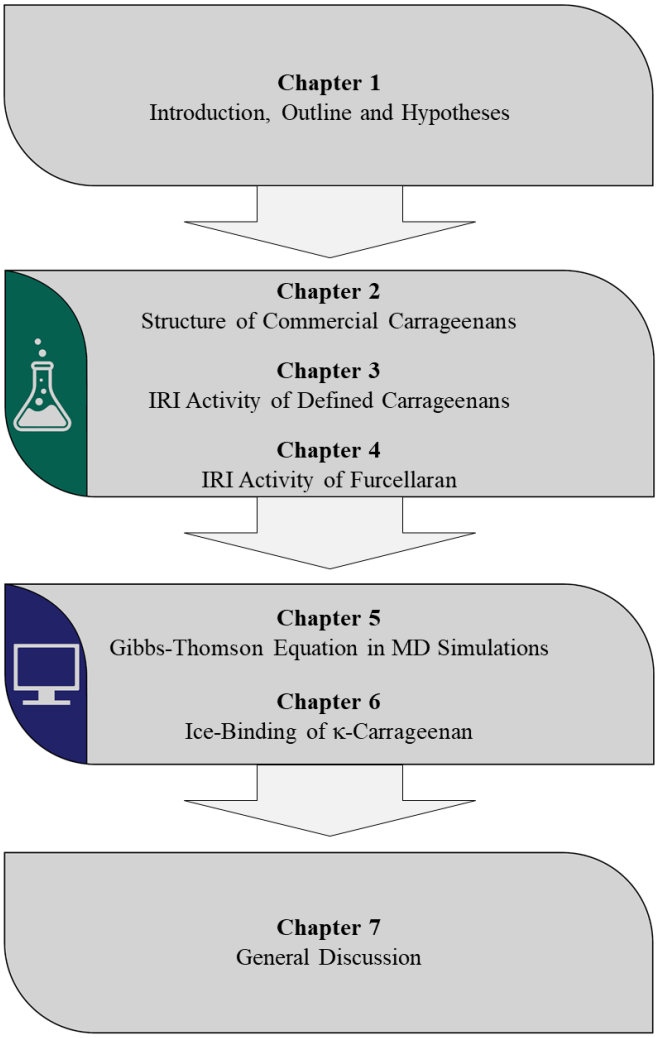

Figure 1.1. *Graphical illustration of the thesis outline.*

In order to identify novel substances capable of inhibit ice growth and recrystallization, a comprehensive understanding the interaction mechanism of polysaccharides, such as κ-carrageenan, is paramount. This knowledge will facilitate the targeted selection of suitable compounds for specific applications and for the rational design of highly effective molecules, serving critical needs in both the food industry and cryopreservation.

1.1.2 Hypotheses

As detailed in **Chapter 1**, different carrageenan polysaccharides demonstrate varying functional properties, with the IRI activity being of particular interest in this thesis. The structure of carrageenan appears to be a major factor influencing its IRI activity. Across different chapters, this research examines various structural characteristics that may impact IRI activity. These include the different structural units, particularly the proportion of κ-units, gelation and aggregation behavior, the amount of sulfate groups, and molecular size.

Carrageenan structure significantly impacts its functional properties, evident in the widely varying gel formation among κ-, ι-, and hybrid types. While structure-function relationships have been presented for various carrageenans in literature, a structural and compositional characterization is frequently lacking. For instance, mixtures or hybrid carrageenans may impact their suitability for specific applications. Consequently, **Chapter 2** provides a comprehensive characterization of commercially available carrageenans, demonstrating how their structural differences affect their functional properties, particularly regarding gel formation. A novel enzymatic approach in combination with two high performance liquid chromatography (HPLC) methods was employed for polysaccharide characterization, and the gel formation was analyzed. Therefore, the following hypotheses were proposed:

H 1: *The structural variations alter the gel formation and the gel strength of hybrid carrageenans. An icrease in the proportion of κ-units is associated with an enhanced gel strength.*

As demonstrated in **Chapter 2**, the structure of carrageenan polysaccharides impacts gel formation. Considering the correlation between gelation and IRI activity, it is anticipated that structural composition may also influence the IRI activity. In addition, the findings of Kiran-Yildirim et al. indicate that κ-carrageenan exhibits a stronger inhibitory effect on the recrystallization of ice crystals compared to ι-carrageenan. Therefore, **Chapter 3** investigates the IRI activity of structurally defined carrageenans. Moreover, the IRI activity of κ-carrageenan is sensitive to low concentration of added ions, indicating that associated cations might also exert an influence. Consequently, different monocationic forms will be analyzed and the following hypotheses will be examined:

H 2: *It is hypothesized that the IRI activity of carrageenan polysaccharides is directly affect by their structural variations, including associated cations.*

H 3: *A higher proportion of κ-units in hybrid carrageenans is expected to enhance their IRI activity,resulting in reduced mean ice crystal sizes after a given storage period.*

In order to gain additional insights into the structural units responsible for the IRI activity of carrageenans, **Chapter 4** investigates a structurally defined furcellaran. Considering that increased sulfate content correlates with decreased IRI activity it is plausible that sulfate groups play a role in IRI activity. Furcellaran, being similar to κ-carrageenan but with fewer sulfate groups, allows for the study of the influence of sulfate groups on the IRI activity of carrageenans. Therefore, the following hypothesis is being investigated:

H 4: *Since a higher sulfate content in carrageenans, as observed in ι-carrageenan, lowers IRI activity, it is hypothesized that furcellaran will exhibit IRI activity and, given its lower sulfate content, may exhibit improved IRI activity.*

Rheological measurements are used in both **Chapter 2** and **Chapter 4** to characterize the gel-forming properties of the respective carrageenans. It is important to note that a universally accepted definition of a gel does not exist. Consequently, the criteria for defining a gel differ in these chapters, with each chapter providing a detailed description of its specific criteria. This implies that the classification of samples as gel-like or gel is interchangeable between the definitions in **Chapter 2** and **Chapter 4**. However, this is irrelevant to the conclusions drawn.

Moreover, **Chapter 5** initiates the simulative investigations. To assess the ability of MD simulations to reproduce the Gibbs-Thomson effect, the binding of an IBP, the subsequent ice growth and the resulting ice surface structure is simulated.

H 5: *The Gibbs-Thomson induced melting point depression of a curved ice surface due to a bound molecule can be accurately modeled by MD simulations.*

Since κ-carrageenan is know to inhibit recrystallization and thereby altering ice crystal shapes, **Chapter 6** uses MD simulations to investigate the molecular interaction of κ-carrageenan with growing ice to uncover the underlying mechanism. In addition, the impact of different ice growth directions, polysaccharide chain lengths and double helix formation is considered.

H 6: *κ-carrageenan can directly interact with the ice crystal surface.*

H 7*: κ-carrageenan, lacking thermal hysteresis, binds to a single ice crystal plane.*

H 8: *The interaction between κ-carrageenan and the ice surface is mediated by hydrogen bond formation and the structural adaption of the molecule to the ice lattice.*

H 9: *The greater number of potential binding sites in longer molecules is proposed to result in stronger ice-binding affinity.*

H 10: *Considering that gel formation eliminates the IRI activity of κ-carrageenan, it is reasonable to hypothesize that even aggregation of individual strands can negatively impact κ-carrageenan's interaction with the ice surface.*

1.2 Impact of Freezing and Frozen Storage on Biological Materials and Food

To improve the quality of frozen food and to effectively preserve biological materials, a comprehensive understanding of the complex processes and the damaging mechanisms that occur during freezing is essential. All living organisms, encompassing plant, animals, fungi, and microorganisms, are fundamentally comprised of cells, which are responsible for their structure and characteristics. This also applies to food products such as meat, fish, vegetables, fruits and milk. Nevertheless, it should be mentioned that recent advancements in cellular agriculture and biotechnology have led to a new category of food products lacking intact cells, such as cultivated meat, plant-based milk alternatives and lab-grown cheese [45].

1.2.1 Ice Crystal Formation and Its Consequences

In general, during the freezing process liquid water within a material is transformed into solid ice crystals. The formation of ice crystals commonly involves a multi-step process encompassing supercooling of the liquid, nucleation of crystals, and the subsequent growth of ice crystals [46,47]. The nucleation and the growth of ice crystals can take place simultaneously. The process of ice crystal formation starts with supercooling of extracellular water, driven by heat transfer. Supercooling represents a metastable state in which a liquid exists below its freezing point without solidification, preceding nucleation and the subsequent growth of ice crystals [46,48].

Ice crystal formation requires the generation of stable nuclei. Unlike most phase transitions occurring at defined pressure-temperature conditions, ice crystal nucleation involves overcoming an activation barrier [49]. Consequently, the phase transition takes place under a variety of pressure-temperature conditions, resulting in a random nucleation process that forms

small and stable nuclei [50]. The driving force of the nucleation is the difference of the chemical potential between the thermodynamically stable ice crystal nucleus and the metastable parent phase [50]. Furthermore, classical nucleation theory relates the frequency J at which nuclei form (nucleation rate) to the energy Δg (Equation 1.1) needed to initiate their formation, often referred to as nucleation work.

$$J = A\, N_0 \exp\left(-\frac{\Delta g}{k_B T}\right) \tag{1.1}$$

Where: $J = nucleation\ rate$

$A = kinetic\ constant$

$N_0 = concentration\ of\ potential\ nucleation\ sites$

$\Delta g = nucleation\ work$

$k_B = Boltzmann\ constant$

$T = absolute\ temerature$

In the first place, nucleation can be categorized as primary or secondary [51]. Primary nucleation involves the spontaneous formation of nuclei directly from the liquid phase itself, while secondary nucleation is initiated by existing crystals or crystal fragments serving as templates [47]. In the second place, primary nucleation can occur through two distinct pathways: homogenous and heterogeneous. During homogenous nucleation, water molecules randomly collide and arrange to hexagonal ice structures of an ice nucleus without the presence of other substances or surfaces. As the necessary alignment of multiple water molecules is very rare, homogenous nucleation occurs only occasionally [52]. With increasing supercooling, more molecules are able to cluster together eventually forming a stable nucleus [53]. For pure water, crystallization occurs approximately at -42 °C [54]. In contrast, heterogeneous nucleation is significantly more prevalent and utilizes foreign particles or surfaces as nucleation sites. This mechanism predominates nucleation in food materials [55]. However, the necessary degree of supercooling to overcome the activation barrier is lower than in homogenous nucleation [56]. Moreover, certain molecules can act as nucleation inhibitors or promoters, depending on their nature [57,58].

However, after the formation of stable nuclei ice crystal growth continues by attachment of water molecules. Concomitantly, other molecules (impurities) diffuse away and are not incorporated into the crystal, while the latent heat of fusion must be dissipated. Under slow freezing conditions, fewer but more stable nuclei form. Due to the gradual heat removal, the limited number of nuclei have plenty of time and available water molecules to grow into large crystals.

Yet, fast freezing conditions increase the likelihood of nuclei formation resulting in numerous small ice crystals [46,53].

In the context of crystallization, the terms melting point and freezing point are often used interchangeably for a pure crystalline substance like water, as they theoretically occur at the same temperature. The melting or freezing point is determined by slowly heating the sample until the last crystal has melted, representing a true equilibrium. Nevertheless, a liquid can undergo supercooling withoud solidifying because the spontaneous formation of a stable crystal nucleus is kinetically hindered. Once the phase change from liquid to solid occurs, latent heat is released and the temperature rises to the equilibrium freezing point or melting point. Accordingly, the freezing point does not indicate when a solution starts to freeze, as the term freezing point might suggest [57].

Given the predominance of water in biological matter, the distribution of water molecules significantly influences the resulting size, shape and distribution of ice crystals. In general, ice crystal formation induces mechanical stress which can disrupt cell membranes and cellular structures, also compromising cohesion of tissues [59].

The location of ice crystal formation, intracellular or extracellular, is an important factor to consider. During slow cooling, ice crystals form exclusively in the extracellular liquid, leading to cellular dehydration and hypertonic conditions intracellularly [60]. These conditions can induce cell shrinkage, membrane instability and protein denaturation resulting in drip loss [61].

Rapid cooling rates lead to significantly smaller ice crystals, including intracellular crystals. Peter Mazur's pioneering work established that the cooling rate and the permeability of the cell membrane to water are crucial determinants of cell viability during freezing [62]. Again the recrystallization occurring during the heating phase is a primary source of cellular injury [63].

Upon significant supercooling, the cell interior can transition into a glassy-state. A glass is considered as amorphous solid with a disordered, liquid-like structure characterized by a very high viscosity in the range of 10^{13} - 10^{14} Pas [64,65]. Vitrification has proven to be highly effective for cryopreservation of mammalian cells [66–68]. Surprisingly, extracellular ice formation and the cooling rate seems to have minimal impact on the survival rate of cells [60]. Instead, the thawing process appears to be considerably more critical, as the intracellular glass

starts crystallizing [63]. The ice crystal formation and the subsequent recrystallization processes causes massive damage. Therefore, inhibition of ice recrystallization is also essential in vitrification and cryopreservation. To enhance the vitrification process by increasing the solute concentration and to minimize recrystallization, cryoprotective agents are employed within and outside the cell [69]. At present, the development of highly effective molecules or molecular combinations remains an ongoing challenge.

Essentially, the characteristics of the materials being frozen substantially influence their preservation after frozen storage [7]. Plant cells are protected by rigid cell walls and individual cells are interconnected by polymers such as pectin and hemicelluloses to form cohesive tissues [70,71]. In contrast, animal cells are considerably smaller ranging from 10 to 30 μm [72] compared to plant cells which measure 10 to 100 μm [73,74]. Given the dense and organized nature of animal tissue, ice crystal formation readily disrupts the tissue's structure. Moreover, animal cells, lacking a robust cell wall, rely entirely on their cell membrane for structure which offers minimal support. Therefore, frozen materials such as foods derived from plants or animals undergo different levels of deterioration of their quality during freezing and frozen storage.

A phase diagram provides a suitable description of the system once it reached equilibrium. Additionally, phase diagrams are used in the food industry to assess changes in the properties of foods during freezing and storage. To simplify this complex diagram, a sequential explanation of its individual components will be provided. For this purpose, the binary system water-sucrose is discussed as it serves as model system for foods in recrystallization experiments.

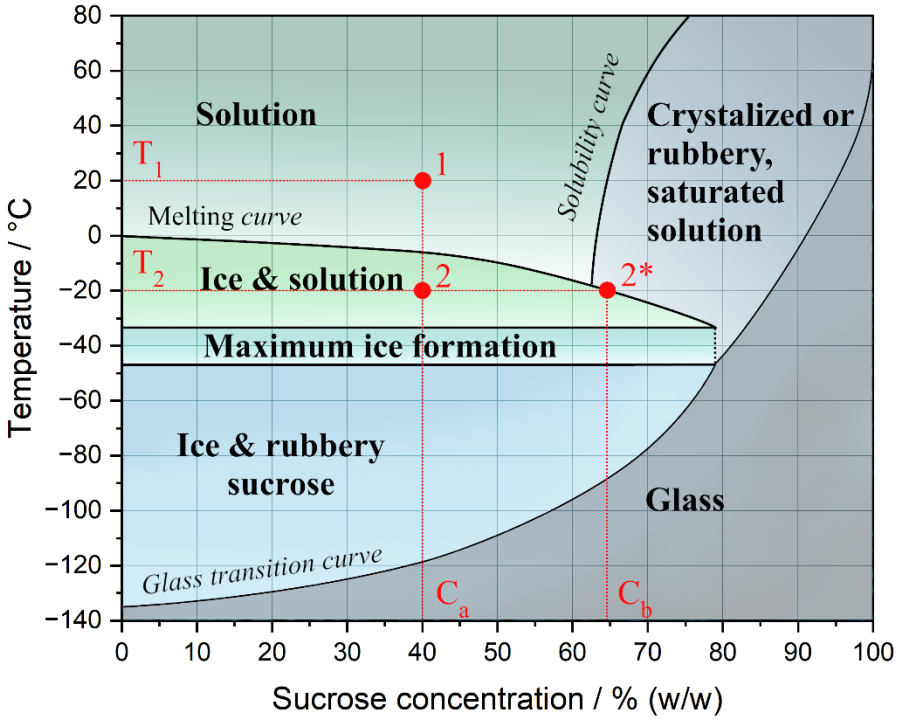

Figure 1.2. *Phase diagram of a sucrose-water system under eliquibrium conditions.*

The phase diagram in Figure 1.2 illustrates the different states of a water-sucrose mixture under equilibrium conditions, depending on the temperature and sucrose concentration present. By representing the actual behavior of the water-sucrose system under realistic conditions, this phase diagram can be considered as extension of the theoretical phase diagram. The freezing, glass transition and solubility curves separate the diagram into distinct regions corresponding to different states. Starting at the freezing point of pure water, the melting curve steadily decreases with increasing solute concentration, in this case sucrose, due to freezing point depression. Generally, the melting point is a key property of food and can be approximated based on its composition. The glass transition curve outlines the conditions under which a system exists as amorphous glass. For solutions with a high water content, these conditions typically occur at low temperatures and gradually shift to higher temperatures with increasing solute concentration [75]. The solubility of a substance depends on its own characteristics and those of the solvent. Sucrose, with its numerous hydroxyl groups is able to interact strongly with water molecules due to the formation of hydrogen bonds resulting in a high solubility as indicated by the solubility curve. At room temperature (20 °C), approximately 67% (w/w) of sucrose can be dissolved in water. Further addition of sucrose at this temperature will lead to the precipitation of sugar crystals. With decreasing temperature, the hydrogen bonding capacity of water and the self-bonding hydrogen populations change, resulting in a reduced solubility [76].

For instance, the phase diagram facilitates straightforward quantification of the solute concentration and ice volume generated upon cooling. A sucrose solution with an initial concentration of C_a = 40% (w/w) is subjected to a temperature decrease from T_1 = 20 °C (condition 1) to T_2 = -20 °C (condition 2). As the solution cools, the growing ice phase excludes the dissolved sucrose molecules, leading to a higher sucrose concentration in the remaining liquid. This process results in a viscosity increase of the residual solution, while its melting point is lowered. Consequently, this high viscosity limits the mobility of sucrose, inhibiting the nucleation and growth of sucrose crystals. Additionally, the complex molecular structure of sucrose kinetically impedes the formation of its crystalline structure. At sufficiently low temperatures, the concentrated sucrose solution can transform into a glassy state [77]. By referring to the melting curve, the sucrose concentration in the residual solution C_b can be determined (condition 2*). Therefore, the remaining unfrozen solution contains nearly 65% (w/w) sucrose at a temperature T_2 of -20 °C.

The lever rule (Equation 1.2) provides a mathematical method to quantitatively analyze the phase diagram of binary mixtures to determine the composition of each phase [78].

$$\varepsilon = \frac{m_{ice}}{m_{liquid}} = \frac{C_b - C_a}{C_a - C_{ice}} \tag{1.2}$$

Where: ε $= ice\ mass\ fraction$

m_{ice} $= mass\ of\ ice$

m_{liquid} $= mass\ of\ the\ residual\ solution$

C_a $= initial\ concentration\ of\ sucrose$

C_b $= concentration\ of\ sucrose\ in\ the\ residual\ solution$

C_{ice} $= concentration\ of\ sucrose\ in\ the\ ice\ phase\ (= 0)$

In this case, the ice mass fraction ε, i.e. the ratio of ice mass m_{ice} to the mass of the unfrozen residual solution m_{liquid}, can be calculated using the respective sucrose concentrations in the initial mixture C_a, in the residual solution C_b and in the ice phase C_{ice}. It is assumed that the sucrose concentration in the ice phase is negligible. Knowing the ice mass fraction ε, the volumetric fraction of the ice phase ϕ in the mixture can be calculated (Equation 1.3).

$$\phi = \frac{V_{ice}}{V_{total}} = \left(1 + \frac{1}{\varepsilon}\,\frac{\rho_{ice}}{\rho_{liquid}}\right)^{-1} \tag{1.3}$$

Where: ϕ $= ice\ volume\ fraction$

V_{ice} $= ice\ volume$

V_{total} $= total\ volume$

ε $= ice\ mass\ fraction$

ρ_{ice} $= density\ of\ ice$

ρ_{liquid} $= density\ of\ the\ residual\ solution$

The ice volume fraction ϕ is the ratio of the volume of the ice phase V_{ice} in regard to the total volume V_{total}. It can be determined by using the ice mass fraction ε and the densities of ice ρ_{ice} and the residual solution ρ_{liquid}.

1.2.2 Recrystallization of Ice Crystals

Recrystallization is a collective term encompassing a variety of processes affecting ice crystals. Consequently, recrystallization occurs mainly during frozen storage and thawing, and is considered the final stage of crystallization [47]. Although the total amount of ice remains unchanged, recrystallization processes lead to a modification of ice crystal size and shape [11,46,47]. The driving force for the recrystallization process is a decrease in free energy of the system, and is additionally influenced by heat and mass transfer phenomena [53]. Recrystallization of ice crystals even occurs at constant temperatures and is a significant concern during extended storage periods above the glass transition temperature typical for frozen food products [9,79]. Recrystallization is typically categorized into three distinct mechanisms: migratory and accretive recrystallization, and isomass rounding [11,47,80–83]. A simplified illustration representing the processes of isomass rounding, accretion and migration can be found in Figure 1.3.

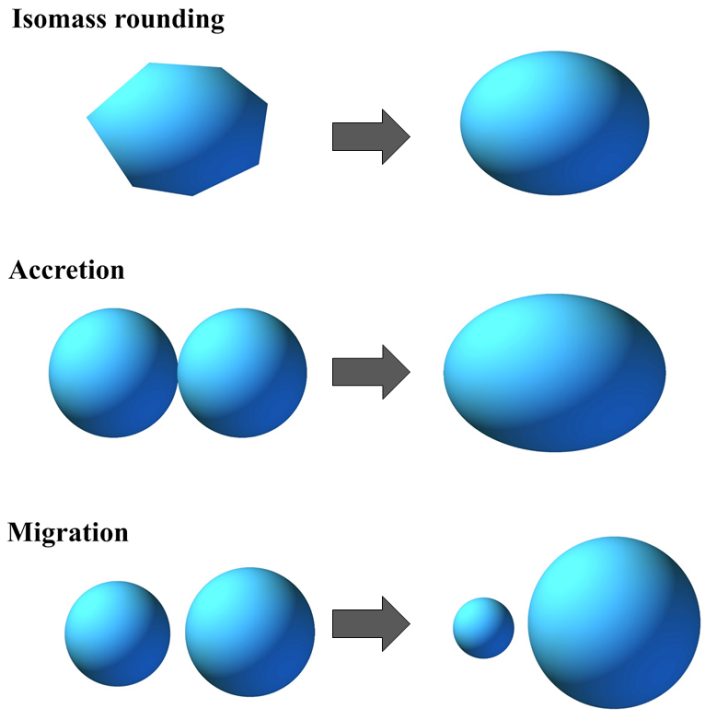

Figure 1.3. *Schematic illustration of the three mechanisms of recrystallization: isomass rounding, accretion and migration.*

Migratory recrystallization, also known as Ostwald ripening, is a fundamental principle in materials science describing the growth of larger particles at the expense of smaller ones within a system. In an ice crystal suspension, the crystal sizes are distributed around an average size due to their statistical formation process. For any given temperature, there is a critical ice crystal size that remains stable, neither melting nor growing. This phenomenon can be explained by the Kelvin equation (Equation 1.4). The relation between the change in vapor pressure and a curved surface was first described by Sir William Thomson, known as Lord Kelvin, in 1871. While the Kelvin equation was initially developed for liquid droplets surrounded by a gas phase, it can be applied to describe crystals in their melt. By replacing vapor pressure with solubility, Equation 1.4 demonstrates that smaller ice crystals are more soluble than larger ones [46,84].

$$ln\frac{p}{p_\infty} = \frac{2\,\sigma\,V_m}{R\,T\,r} \approx ln\frac{c}{c_{sat}} \tag{1.4}$$

Where: p $= actual\ vapor\ pressure$

p_∞ $= saturated\ vapor\ pressure\ of\ a\ flat\ surface$

σ $= surface\ tension$

V_m $= molar\ volume$

R $= universal\ gas\ constant$

T $= temperature$

r $= droplet\ or\ crystal\ radius$

c $= solubility\ of\ the\ solid$

c_{sat} $= solubility\ at\ a\ plane\ surface$

In accordance with the Kelvin equation, ice crystals smaller than this size will fully or partially melt. The liquid water molecules rearrange, causing larger ice crystals to grow further. As Ostwald ripening proceeds, the total volume of ice in the system is constant yet the number of ice crystals decreases while their individual size increases. Over storage time, the critical crystal size for melting or growing becomes larger, eventually resulting in a single, large ice crystal after a very long storage period. While the Kelvin equation relates a particle's size to its vapor pressure at a constant temperature, the Gibbs-Thomson equation (Equation 1.5) links the particle size to its melting temperature at constant pressure. Therefore, both the Kelvin equation and the Gibbs-Thomson equation describe the relationship between the size of a droplet or particle and its thermodynamic property.

$$T_m(r) = T_m^\infty - \frac{2\,\sigma\,V_m}{r\,\Delta S_f} \tag{1.5}$$

Where: $T_m(r) = depressed\ metling\ point$

T_m^∞ $= equilibrium\ melting\ point$

σ $= interfacial\ energy\ \ between\ solid\ and\ liquid\ phase$

V_m $= molar\ volume\ of\ the\ solid$

r $= radius\ of\ the\ solid\ particle$

ΔS_f $= molar\ entropy\ of\ fusion$

Substituting the diameter x for the radius r and replacing the molar entropy of fusion ΔS_f with $\Delta H_f\ (T_m^\infty)^{-1}$ results in the form of the well-know Gibbs-Thomson equation for spherical particles (Equation 1.6).

$$T_m(x) = T_m^{\infty} - \frac{4\,\sigma}{x}\,\frac{T_m^{\infty}}{\Delta H_f}\,\frac{V_m}{1} \tag{1.6}$$

Where: $T_m(x) = depressed\ melting\ point$

$T_m^{\infty} = equilibrium\ melting\ point$

$\sigma = surface\ tension\ between\ water\ and\ ice$

$x = particle\ diameter$

$\Delta H_f = molar\ enthalpy\ of\ fusion$

$V_m = molar\ volume\ of\ ice$

The formation of ice crystals results in a variety of crystal sizes and irregular shapes, rather than uniform structure. Therefore, the overall system tends to minimize its surface energy resulting in the surface diffusion of water molecules to achieve a rounding of ice crystals. During isomass rounding, the mass of ice crystals remains constant, despite the changes in their morphology [46]. Local differences in the melting temperature, which are caused by variations in the radius of curvature on the irregular ice crystal surface, are responsible for the rounding of the crystal shape [79].

Accretive recrystallization is the process by which directly contacting ice crystals merge to form a larger crystal. At the beginning of the recrystallization process, there are numerous small ice crystals packed closely together. This high density of ice crystals favors accretion. Upon contact of two ice crystals, a concave neck with a negative radius of curvature develops at their interface. The curvature induces a change in the vapor pressure ultimately resulting in a driving force that fills the neck. As recrystallization continues, the number of crystals decreases while their individual sizes increase, leading to increased spaces between them. Consequently, accretion becomes less significant in driving the recrystallization process.

A number of factors can in general influence the recrystallization process of ice crystals including their initial size distribution, as already briefly discussed. When the radii of ice crystals are in a similar range, the differences in vapor pressure are minimal, leading to a weaker driving force for the Ostwald-ripening. Consequently, if all ice crystals are exactly the same size, no growth of large ice crystals would occur.

At lower temperature, molecules have less kinetic energy which in turn reduces the reaction rate of chemical and physical processes, including ice recrystallization [39,85]. Moreover, the temperature directly impacts the mobility of water molecules, which is crucial for the rearrangement processes involved in Ostwald-ripening. This mobility is quantified by the diffusion coefficient, described for liquids by the Stokes-Einstein equation (Equation 1.7).

$$D = \frac{k_B\, T}{6\, \pi\, \eta\, r_h} \tag{1.7}$$

Where: $D = diffusion\ coefficient$

$k_B = Boltzmann\ constant$

$T = temperature$

$\eta = dynamic\ viscosity$

$r_h = hydrodynamic\ radius\ of\ the\ diffusing\ particle$

Beyond just the absolute temperature, temperature fluctuations significantly affect recrystallization. Given that ice crystals are susceptible to even small temperature fluctuations, which are unavoidable during storage and distribution of frozen products, recrystallization is promoted leading to a coarsening of the ice crystal structure. Even with a minimal rise in temperature, ice crystals will melt, reducing the overall ice volume. According to Equation 1.4, smaller ice crystals exhibit a higher vapor pressure due to a smaller radius of curvature, and tend to melt first. The subsequent slight and gradual decrease in temperature is typically insufficient for the nucleation of new ice crystals. Consequently, the larger crystals that are already present continue to grow in size. Therefore, fluctuations in temperature result in an increased average ice crystal size and a reduction in the total number of crystals [10,86].

As demonstrated in Figure 1.2, the temperature is a major factor determining the proportion of ice in the system. With a lower ice content, the distance between ice crystals is higher, crystals are more isolated, making the necessary direct contact for merging much less probable. Moreover, when distances are greater, the diffusion time for water molecules to reach larger crystals increases [79,87].

Furthermore, the recrystallization can be affected by adding different substances. These substances lower the melting point due to the number of particles in the solution, known as colligative properties [88]. For instance, sugar is commonly used in ice cream to lower the overall ice content (compare Figure 1.2).

Yet, not all molecules act solely based on their colligative properties. Beyond that, the Stokes-Einstein equation (Equation 1.7) reveals that the dynamic viscosity of the fluid is inversely proportional to the diffusion coefficient. As viscosity increases at a constant temperature, the diffusion coefficient decreases, reducing the mobility of the molecules [89,90]. That's why various hydrocolloids like guar gum, locust bean gum, carrageenan and alginate are commonly employed to achieve a smooth and creamier texture in ice cream [91].

However, there is considerable debate regarding the influence of viscosity on ice recrystallization. More recent studies suggest that there is no link between an increased viscosity and recrystallization [38,92]. The exact mechanism how hydrocolloids alter the recrystallization of ice crystals is still unclear [93]. It is hypothesized that the water-binding properties of hydrocolloids reduce the movement of water molecules [94]. Besides, the formation of a gel network or gel-like structures, sterically hindering the water mobility, is another proposed mechanism [95–97]. The disruption of the water structure at the ice-water interface caused by the presence of hydrocolloids, preventing water molecules to attach to the ice surface, has also been debated [98].

Certain additives, known as ice-binding molecules, can directly interact with the ice crystal surface, dramatically affecting the ice crystal structure and the process of recrystallization. These substances include a variety of different molecules such as specific proteins, salts and both natural and synthetic polymers [99–101]. Certain carrageenan types have been shown to to influence recrystallization processes, independent of their gelling and viscosity-increasing properties. This suggests a direct interaction with ice crystals and a more detailed explanation of proposed mechansims and hypotheses regarding the hydrocolloid carrageenan will be provided in Section 1.4.4.

In order to mathematically quantify ice recrystallization, various approaches have been proposed. One of the most influential models was developed by Lifshitz, Slyozov, and Wagner (LSW) in the early 1960s [84,102]. The LSW theory and its associated equation describe the kinetics of ice crystal growth during prolonged storage at constant temperatures. In this stable environment, the ice crystal growth is mainly driven by Ostwald-ripening. Based on the Kelvin equation (Equation 1.4), the LSW theory is frequently employed in a slightly adjusted form and allows the prediction of the mean ice crystal radius $\bar{r}$ as function of time t, as shown in Equation 1.8.

$$\bar{r}^n = \bar{r}_0^n + \frac{t}{\tau} \tag{1.8}$$

Where: $\bar{r}$ $= mean\ ice\ crystal\ radius\ at\ time\ t$

n $= integer\ constant, ranging\ from\ 2\ to\ 4, determined\ by\ the\ rate\ limiting\ mechanism$

$\bar{r}_0$ $= initial\ mean\ ice\ crystal\ radius$

t $= time$

τ $= constant\ depending\ on\ the\ rate\ limiting\ machanism\ and\ the\ volume\ fraction\ of\ ice$

The initial ice crystal mean diameter $\bar{r}_0$ serves as reference point and both constants n and τ are dependent on the rate-limiting mechanism. In addition τ is affected by the ice volume fraction. As the ice volume increases, τ decreases due to shorter diffusion paths within the given volume. The constant n can only be an integer value from 2 to 4. When n equals 2, the rate-limiting step for ice crystal growth is the attachment of water molecules to a growing or their deattachment from a shrinking crystal [84,103]. In case of Ostwald-ripening, the value of n equals 3, suggesting that the diffusion of solutes from the bulk in a stagnant environment controls the growth process [84,102]. When the grain boundaries of the ice crystals are the active site for diffusion limiting ice growth, the value of n is 4 [104]. However, due to simplifying assumptions made in the LSW theory in order to provide applicable relationships it may not accurately represent all systems. The theory's limitations include the assumption of an infinite medium without constraints. It simplifies particle shape to spheres and considers fixed distances between them, neglecting the effects of accretion and clustering. Therefore, its applicability is limited to systems with a low ice volume [105].

1.2.3 Experimental Approaches to Assess Recrystallization Processes

To evaluate the influence of different factors, such as temperature fluctuations or additives, on ice crystal recrystallization, methods to measure the ice crystal size distribution and its evolution over storage time are required. A major challenge in these methods is to isolate the influence of nucleation from crystal growth. The number of ice crystals, determined by the nucleation process, directly affects the final ice crystal size distribution after storage. Therefore, a reproducible method is essential for understanding and studying recrystallization.

The splat cooling assay, pioneered by Knight, Hallett and DeVries in 1988, continues to be a widely used technique in recrystallization research [106–109]. This technique involves dropping a 10 µL droplet of the sample liquid from the height of 2.6 m onto a polished aluminum plate precooled to -78 °C with dry ice [106]. The sample liquid freezes instantly upon impact, creating a small ice disc with a radius of approximately 5 mm composed of various tiny ice crystals. The ice disc is then transferred to a cold dish and covered with a coverslip to prevent the sample from evaporating. Typically, the sample is kept at temperatures ranging from -5 to -10 °C for a storage period of 10 to 20 h [110,111]. In order to visualize the individual ice crystals, polarized light is used, and the ice disc is periodically photographed to monitor changes in ice crystal size. To obtain accurate results from the splat cooling assay, it is essential to add small amounts of salt to the sample. Adding a neutral salt such as NaCl or phosphate-buffered saline establishes a eutectic phase, ensuring any observed inhibitory effect of

a potential recrystallization inhibitor is attributed to its specific action and not a general solute effect [112].

The sucrose sandwich assay involves the addition of varying amounts of sucrose to the sample to control the volume of the ice fraction formed. The specific amount of sugar used, typically between 20 to 50% (w/w), depends on the storage temperature, the concentration of the test substance, and its efficacy to influence recrystallization [113–115]. Once the sample is prepared, a tiny droplet of 1 to 2 µL is placed on a microscope slide and covered with two coverslips. To prevent evaporation of the sample, the gaps are sealed with silicone. In previous procedures, wax was used as sealant. Subsequently, the prepared microscope slide is rapidly frozen at a low temperature of around -50 °C. The sample is then stored at a fixed temperature between -5 and -15 °C for 1 to 20 h [109,116]. Pictures are taken at regular intervals or at the end of the storage time to determine ice crystal sizes. In contrast to the splat cooling assay, the lower ice content of the sucrose sandwich assay leads to greater distances between the ice crystals. This substantially reduces the impact of accretion on the overall recrystallization process.

The method according to Gaukel is a modified version of the sucrose sandwich assay [117]. It utilizes relatively high sucrose concentrations, typically between 40 and 50% (w/w) and larger sample volumes of 12 to 17 µL. Consequently, a greater number of ice crystals on each prepared slide can be analyzed. Due to the samples thickness, crystal growth is less restricted in the vertical direction. In addition, to minimize the impact of crystal nucleation, samples are flash-frozen in liquid nitrogen. Given that frozen materials are commonly stored for elongated periods, the storage time in this method is extended to more than 100 h to more accurately reflect these conditions.

Both methods, splat cooling and sucrose sandwich assay, share similar limitations. Since each sample must be individually prepared, photographed and observed under the microscope, the experimental effort is substantial. Moreover, the relatively long storage times, while beneficial for precise determination of recrystallization kinetics, significantly prolong the comparisons between different additives or other influencing parameters. Consequently, additional techniques were developed to meet these specific needs. The method developed by Tomczak et al. [118], capable of analyzing multiple samples at once, employs 10 µL glass capillaries. When rapidly frozen at -50 °C, ice crystals develop within the capillary tubes. These can subsequently be stored at the specified temperature and observed under a microscope. In addition, this method allows for archiving the sample set in a frozen state. Furthermore, there are two

alternative methods designed to process a large number of samples. The first method by Gilbert et al. employs a 96-well plate and basic lab equipment, allowing for on-site use [119]. This technique is limited to identify additives with recrystallization inhibition activity and requires 5 days to complete one test. On the other hand, the second technique developed by Graham et al. requires a special designed device and sapphire slides [120]. Although this assay allows for very high throughput and is easy to perform, the initial costs are higher than for other methods.

A major challenge in determining ice crystal sizes and subsequently the recrystallization kinetics remains the image analysis. All of the mentioned techniques generate a large number of images over time, which are used to measure the ice crystal sizes. If the crystals are distinct and show clear edges in the images, computer programs can automate the size measurement. For instance, Olijve and co-workers presented a MATLAB-based analysis tool to process sucrose sandwich assay data for the determination of recrystallization kinetics [121]. However, the appearance of ice crystals in the images can differ substantially between different assays. Therefore, the applicability of automated analysis is limited. The ice crystals formed in the splat cooling assay are characterized by non-uniform shapes and are densely packed. Moreover, the presence of various ice crystals at different focal planes produced in the modified sucrose assay according to Gaukel can cause inaccuracies in automated image analysis. Figure 1.4 illustrates representative images of ice crystals obtained using these methods.

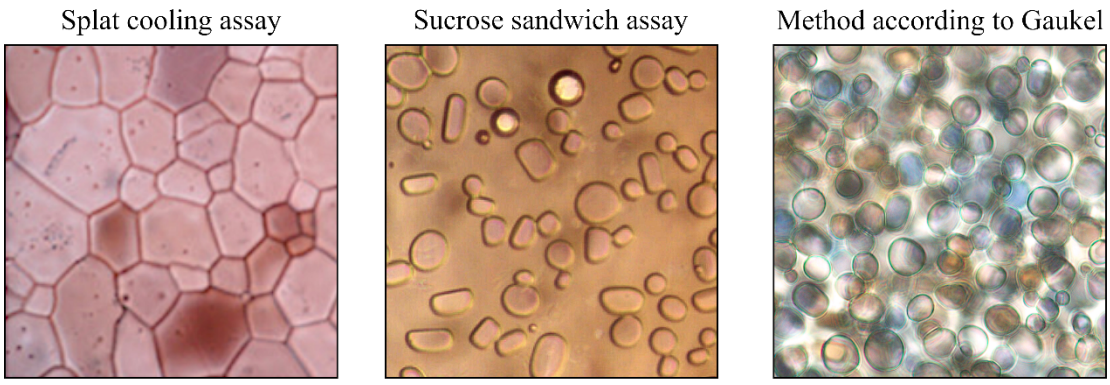

Figure 1.4. *The figure illustrates the characteristic appearances of ice crystals obtained from different methods. The splat cooling assay [122] is depicted on the left, the sucrose sandwich assay [123] in the center, and the modified sucrose sandwich assay according to Gaukel [124] on the right. The ice crystals are colorized for better visualization.*

A further challenge is the often limited comparability of the different methods. Variations in sample preparation and composition coupled with differences in experimental conditions such

as nucleation temperature, cooling rate, and storage temperature, contribute to these inconsistencies [125].

1.3 Ice-Binding Molecules and Their Mechanisms of Action

As previously noted, the growth of ice crystals can be effectively manipulated by the addition of certain substances. The most effective additives not only influence the diffusion of water molecules such as hydrocolloids but directly interact with the ice crystal surface [99,125]. To understand the mechanism limiting ice crystal growth, the Gibbs-Thomson effect and its associated equation are essential. The umbrella term "ice-binding molecules" refers to an extremely diverse and heterogeneous collection of substances encompassing proteins, synthetic polymers, polysaccharides as well as inorganic salts, all of which possess the ability to interact with ice crystals to varying degrees. Subsequent to the adsorption of an ice-binding molecule to the surface of an ice crystal, further ice growth is confined to unoccupied regions of the crystal resulting in the formation of curved ice surfaces [126] (Figure 1.5).

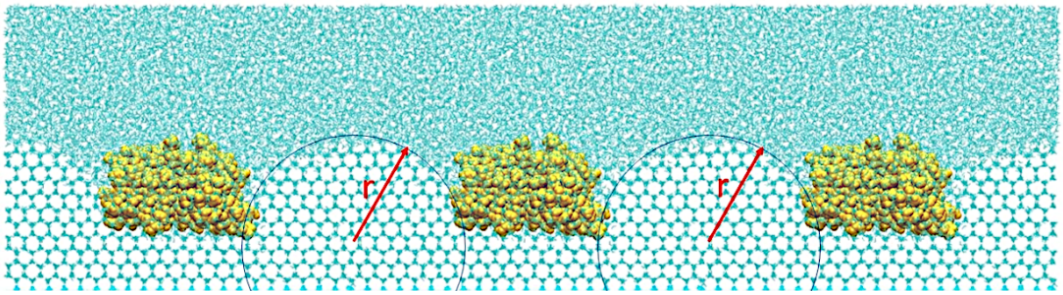

Figure 1.5. *Illustration of the Gibbs-Thomson effect, showcasing the curved ice surface structure induced by spruce budworm ice-binding proteins (yellow) adsorbed onto the ice surface. In addition, the radii of the curvatures are indicated [127].*

In accordance with the Gibbs-Thomson effect, the formation of small curvatures effectively prevents further ice crystal growth due to the substantial reduction in melting temperature [27]. This melting point depression can be calculated by the formerly introduced Gibbs-Thomson equation (Equation 1.6) for specific surface geometries. In 1977, Raymond and DeVries first proposed the adsorption-inhibition theory to explain the ice growth inhibition of ice-binding proteins. This theory proposes an irreversible attachment of the proteins, creating a curved ice surface [128]. It took almost four decades for molecular dynamics simulations to provide evidence supporting the adsorption-inhibition theory and the associated Gibbs-Thomson effect. Thus, the Gibbs-Thomson effect provides the fundamental principle for understanding the action of ice-binding molecules.

The inhibition of ice growth is effective only within a well-defined temperature range. At very low temperatures, the ambient temperature drops below the lowered melting temperature induced by the curved ice surface, leading to resumed ice crystal growth [129]. Furthermore, molecules bound to the ice crystal can hinder the melting process upon temperature increase [130–132]. While this effect is minor, it contributes to the thermal hysteresis. The term thermal hysteresis refers to the overall temperature range, where ice crystal growth is inhibited starting from the melting point. The degree of thermal hysteresis is influenced by both the characteristics of the molecule attached to the ice surface and its abundance [133]. Additionally, the surface density of bound molecules is related to the magnitude of thermal hysteresis [134]. With increasing ice-binding molecule concentration, the thermal hysteresis also increases but in a non-linear relationship [135–137]. Once the available ice surface is saturated with bound molecules, the thermal hysteresis reaches its maximum and additional molecules have no further effect. Moreover, the adsorption rate at which ice-binding molecules bind to the ice crystal surface can influence the thermal hysteresis. This was particularly evident for hyperactive insect IBPs, where extended exposure times resulted in a tremendous improvement of the thermal hysteresis. However, the thermal hysteresis of antifreeze protein (AFP) type III demonstrated no changes regardless of the length of exposure time [138]. Therefore, a wide range of thermal hysteresis activities among different molecules is observed, ranging from 0.1 K of moderately active molecules up to 6 K of hyperactive IBPs proteins [129,139].

The significantly greater thermal hysteresis of hyperactive IBPs can be explained, among other factors, by the binding to multiple ice crystal planes. Ice crystals have various planes resulting in different surface structures. These different ice planes are illustrated in Figure 1.6.

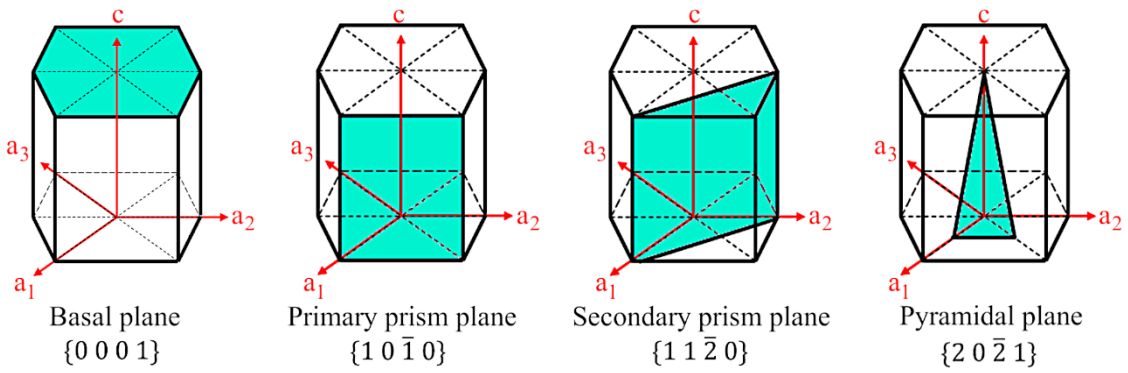

Figure 1.6. *The different crystallographic planes of an ice crystal are depicted, each labeled with its respective Miller-Bravais index according to [127].*

Consequently, the 3-dimensional shape and the arrangement of atoms in ice-binding molecules determine the specific ice planes they can interact with. Molecules capable of binding to more than a single ice crystal plane often exhibit high thermal hysteresis, such as the IBP from *Tenebrio molitor* [129].

The attachment of these molecules to the ice crystal surface has additional significant impacts on ice crystals and their growth. All known ice-binding molecules have been shown to either slow down or completely inhibit the process of Ostwald ripening during recrystallization. However, the exact mechanism for ice recrystallization inhibition (IRI) activity is still unclear [42,140,141]. A prevailing theory suggests that upon binding onto the surface of both large and small ice crystals, identical curved surface structures on both are created [142]. This effectively eliminates the driving force for Ostwald ripening processes. While thermal hysteresis and IRI activity seem to require the attachment of the molecules onto the ice crystal surface, these two properties are not directly linked [143].

As a result of molecules binding to the surface and affecting ice growth, the crystal morphology may change [144]. This process is known as dynamic ice shaping. Depending on the binding plane of the molecule, the crystal shape is altered. When freezing pure water, the resulting ice crystals are flat discs with only the basal planes exhibiting facets. The addition of ice-binding molecules, however, results in various hexagonal and angular ice crystal shapes [44,99,145,146].

In summary, the binding of ice-binding molecules to the surface of ice crystals can induce three distinct effects. They can prevent ice growth entirely within a specified temperature range (thermal hysteresis), inhibit the recrystallization of ice crystals and alter their morphology. While these effects can occur simultaneously, they are not always observed together. For instance, some ice-binding molecules effectively prevent ice recrystallization but show little to no thermal hysteresis activity [147,148]. In consequence, there is no link between thermal hysteresis and IRI activity [149].

1.3.1 Ice-Binding Proteins

Introduction

IBPs are widely considered as the most effective and best-known molecules capable of binding to ice crystals [150]. Arthur DeVries is credited with pioneering the research in the field

of these proteins, having conclusively demonstrated that antifreeze glycoproteins are responsible for the survival of arctic fishes in freezing cold environments by lowering the melting point of their blood and preventing it from freezing [151]. The nomenclature of IBPs is quite inconsistent, typically reflecting the specific function they were discovered to perform. For instance, proteins demonstrating a thermal hysteresis activity are commonly termed antifreeze proteins (AFP) [29], antifreeze glycoproteins (AFGP) [152] or thermal hysteresis proteins (THP) [153]. Given their ability to shape the morphology of ice crystals, these proteins are also known as ice structuring proteins (ISP) [154]. Conversely, proteins promoting ice crystal nucleation are called ice nucleating proteins (INP) [155]. Regardless of their name, all of these proteins share the ability to interact with ice crystals.

Origin and Structure of IBPs

A wide variety of life forms from fishes [156] and frogs [157] to microorganisms [158], fungi, plants [159] and insects [160], have been found to produce IBP. The specific reason for these proteins to perform their function can vary significantly. Thus, IBPs that exhibit significant thermal hysteresis activity are prevalent in fish and insects to prevent the freezing of their body fluids [161,162]. In contrast, plant IBPs demonstrate excellent IRI activity effectively preventing the formation of large ice crystals through recrystallization processes [159]. While plants can withstand small ice crystals, excessive recrystalization must be prevented, as the resulting growth of large crystals causes mechanical damage [163]. Remarkably, certain bacteria such as *Pseudomonas syringae* can actively initiate the formation of ice crystals at warmer temperatures using INPs. To fulfill this purpose, these bacteria have evolved to produce membrane-associated INPs, known as the most effective ice nucleators [150,164,165]. These ice crystals damage the plant tissue, providing an entry point for the bacteria to extract nutrients [166–168]. In addition, ice crystal nucleation helps airborne microorganisms reduce their atmospheric residence time, increasing their chances of reaching a suitable habitat [169]. Furthermore, high altitude clouds contain large amounts of INP-producing bacteria which significantly contribute to cloud glaciation, snow, hail, and cloud formation [170–172]. The membrane-associated nature and large molecular size of these proteins represent a challenge to accurately determine their amino acid sequence and three-dimensional structures. Consequently, there is a lack of high-quality structural information for INPs. Nonetheless, AI tools such as AlphaFold hold promise to address these limitations. The well-studied INP derived from *Pseudomonas syringae* adopts a β-helical conformation in the ice-nucleating region,

characterized by Thr-X-Thr and Ser-X-Leu motifs analogous to the structure observed in insect IBPs [173–175]. However, the assembly into oligomeric complexes is responsible for achieving the high level of ice nucleation activity observed in *P. syringae* INPs [174]. In order to enhance the energy efficiency of artificial snow production, this protein is a key component of the Snomax® product. Moreover, sea ice brine pockets serve as important habitats for numerous organisms. These pockets facilitate the transport of nutrients and the removal of waste products [176,177]. The preservation of brine pockets is vital for various marine microorganisms. Antarctic algae and other psychrophilic microorganisms help maintain this liquid environment by secretion of IBPs, which inhibit ice crystal recrystallization [178,179]. Another biological function of ice-binding proteins has been identified in the marine bacterium *Marinomonas primoryensis*. This phototrophic bacterium forms a calcium-stabilized complex to bind to the ice surface, ensuring a continuous supply of light and oxygen [180]. Given the variety of functions IBPs perform in different organisms, it is not surprising that they have evolved in many divergent molecular structures. Consequently, there is no single ancestral structure from which all IBPs originated [181].

A diverse set of IBPs have been isolated from fishes such as ocean pout, Antarctic notothenioids and winter flounder since their initial discovery fifty years ago [151]. This group includes 8 distinct classes of AFGPs, as well as AFPs of types I to IV [29]. Despite their small molecular weight, these fish proteins exhibit a wide range of structures such as α-helices, polyproline type II helices and globular proteins [99]. In addition, β-solenoids and silk-like solenoids are common molecular structures present in IBPs from insects, bacteria, plants, algae and fungi [125]. Table 1.1 provides examples of the structural diversity of two fish and one insect ice-binding protein.

Table 1.1. *Comparison of three structurally different ice-binding proteins.*

	Type I AFP HPLC6	**Type III AFP QAE1**	***Tm*AFP**
IBP structure	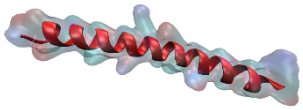	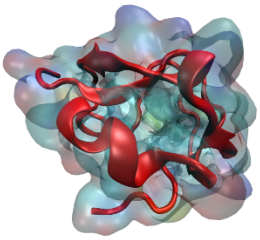	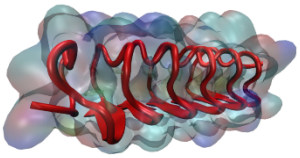
	α-helix	Globular	β-solenoid
Mass	3.3 kDa	7.1 kDa	8.4 kDa
Origin	Winter flounder	European eelpout	*Tenebrio molitor*
Thermal hysteresis	0.6 K	0.6 K	5.8 K

Binding Mechanism

Despite their structural differences, a common feature of IBPs is their planar and rigid ice-binding site (IBS) [182,183]. In contrast to other surfaces of the ice-binding molecule, the IBS is predominantly hydrophobic and contains isolated amino acids capable of forming hydrogen bonds [183]. However, the precise molecular composition of the IBS can vary considerably between different IBPs. The interaction of the helical type I AFP from winter flounder with the ice surface is mediated by Thr-Ala-Asn repeats [184]. Based on the alignment of these residues with the corresponding distances in the ice lattice, it was initially thought that lattice matching and hydrogen bonding are essential for ice-binding [185]. Yet, mutation studies and the analysis of Type II AFP have shown that hydrogen bond formation is not a prerequisite for the interaction with the ice surface [186–188]. Insect IBPs, frequently characterized by a β-solenoid structure, commonly contain a Thr-X-Thr within their IBS [189–191]. This is illustrated in Figure 1.7 using a spruce budworm AFP.

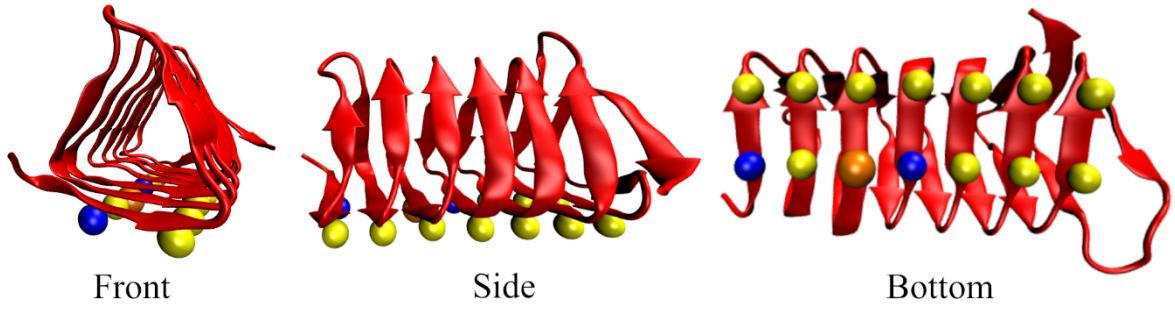

Figure 1.7. *β-solenoid structure of spruce budworm AFP with the protein backbone shown as red cartoon drawing and the IBS amino acids as colored beads. Threonine residues are yellow, blue beads represent valine and isoleucine is colored orange.*

Besides lattice matching, other mechanisms such as the incorporation of methyl moieties into the lattice [182] or the creation of ice-like and clathrate water structures near the IBS have been proposed [175,192]. Contrary to the simple model of a distinct ice-water interface, the ice surface is actually very dynamic and covered by a quasi-liquid layer (QLL) acting as transitional zone between the ordered ice lattice and the disordered bulk water [193]. Consequently, there is a constant exchange of water molecules between these two phases. The QLL is essential to the anchored clathrate water hypothesis, providing a mechanism for the IBP-ice interaction. The specific amino acid sequence of the IBS enables IBPs to organize surrounding water molecules into ice-like, clathrate structures. While hydrophobic residues like the methyl group of threonine repel water molecules, lowering the local density, hydrophilic groups, such as the hydroxyl group of threonine, anchor a water molecule through hydrogen bonding, stabilizing the clathrate structure. By fitting into the QLL, these clathrate structures mediate the attachment of the protein to the ice crystal. Experimental evidence from X-ray crystallography [175,192] and vibrational sum frequency generation spectroscopy [194], along with computational simulations [195,196], verified the ability of IBPs to create ordered water structures. Additionally, terahertz absorption spectroscopy demonstrated that IBPs, including AFP type I and insect AFPs, influence the organization of water molecules within a 2 nm distance [197]. For the *Tenebrio molitor* AFP, the formation of clathrate or ice-like structures in solution is not a prerequisite for binding to the ice surface. Instead, the protein slowly diffuses to the ice surface and rapidly organizes ordered structures within the QLL [198].

Moreover, the size of the IBS substantially affects the antifreeze activity of IBPs. Reducing the IBS area of a springtail AFP by a quarter resulted in a dramatic decrease in its thermal

hysteresis by more than 90%. Conversely, increasing the IBS width by the same amount tripled its thermal hysteresis. Despite this improvement, lengthening of the helix that forms the IBS decreased the antifreeze activity [199].

Reversible vs. Irreversible Binding

The reversibility of IBPs binding to ice crystals remains a topic of debate as different studies provided conflicting results. Microfluidic experiments have demonstrated irreversible binding to the ice surface for both *Tenebrio molitor* AFP and AFP type III [200,201]. Furthermore, the binding mechanism of AFGPs remains a subject of active research. Based on microfluidic experiments, an irreversible binding was suggested [202]. Contrarily, simulations proposed a reversible binding mechanism facilitated by methyl groups of the peptide and the saccharides [203]. The significance of hydroxyl groups in the saccharide component and hydrophobic groups in the peptide portion for the binding process and antifreeze activity has recently been demonstrated [204]. Recent simulations of AFGPs indicate that these molecules can bind to the ice surface in two ways. The protein part engages in reversible binding, whereas the saccharide portion binds irreversibly [205]. Furthermore, Tas and colleagues have developed a new super-resolution microscopy technique to visualize and track fluorescently tagged IBPs on the ice surface in real-time. Using this method, an irreversible binding for AFP type III isoform QAE was confirmed, preventing any further movement of bound molecules [206]. While the QAE isoform demonstrates thermal hysteresis and IRI activity, the T18N mutant lost its thermal hysteresis activity exhibiting only recrystallization inhibition [207]. In contrast, this mutant interacted with the ice surface for extremely short time periods revealing a reversible binding mechanism. Nevertheless, reversible adsorption appears to be sufficient to control recrystallization of ice crystals [206].

1.3.2 Other Ice-Binding Molecules

Despite their extraordinary efficacy to inhibit ice growth and recrystallization, IBPs have several limitations. Physical factors such as temperature, pressure or pH can impact their functionality. Given the currently limited supply and high cost of IBPs, there is a high need for natural or synthetic alternatives [99,125]. So far, several promising substances have been identified that possess IRI activity or induce dynamic ice crystal shaping. These substances include, polyvinyl alcohol [113], a synthetic polymer; κ-carrageenan [25], a polysaccharide from seaweed; xylomannan [208,209], a glycolipid from darkling beetles; zirconium acetate [210], a salt; Safranine O [116], a synthetic dye; and graphene oxide [211], a carbon-based

material. Of all non-protein ice-binding molecules, polyvinyl alcohol is the most potent recrystallization inhibitor and has thus been thoroughly investigated [212]. Since 1955, polyvinyl alcohol has been known to inhibit ice recrystallization with an IRI activity similar to type I antifreeze proteins from winter flounder although polyvinyl alcohol does not demonstrate thermal hysteresis [112]. By hydrogen bond formation with the water molecules in the ice lattice, polyvinyl alcohol is able to attach to the ice crystal surface and effectively hinder ice growth [113,213]. Apart from the enthalpy increase due to hydrogen bond formation, entropic factors caused by the desolvation of methylene groups may also contribute to the binding process [214]. Both computer simulations and scanning transmission electron microscopy images suggest that the polymer molecules align themselves in an elongated and linear conformation upon binding to the ice surface [213]. In contrast, molecular dynamics simulations performed by Bachtiger and colleagues indicate that the specific conformation of polyvinyl alcohol is less important for ice-binding. Instead, the overall surface area available for interaction with the ice crystal appears to be a more significant factor [214]. Furthermore, the activity of polyvinyl alcohol requires a minimum chain length of approximately 10 to 19 repeating monomer units [215]. In general, polyvinyl alcohol's IRI activity is closely related to its degree of polymerization and molecular size, but also to modifications made to the polymer chain such as acetylation [215–217]. Moreover, the flexibility of polymers like polyvinyl alcohol demonstrates that a precise alignment or matching of the molecular structure with the ice lattice structure does not appear to be necessary for ice-binding [217]. Of particular significance in this work is the polysaccharide carrageenan, for which its structural characteristics, gel formation, impact on ice crystal growth, and manufacturing process are thoroughly discussed in Section 1.4.

1.3.3 Applications of Ice-Binding Molecules

While IBM have great potential in diverse areas due to their ability to control ice crystal growth, their widespread use in industrial applications is yet to be realized. Thus far, the only industrial use of AFPs is in the food industry. However, in order to avoid confusion with harmful antifreezes such as ethylene glycol, the term ISP is used in by Unilever [154]. As early as 2003, Unilever introduced ISPs into its commercially available ice cream products in the United States, such as Solero or Popsicle Shots [218]. Following safety assessments, the European Union granted approval for ISPs in food applications as novel food in 2008 [219]. The specific AFP originally from ocean pout is recombinant produced in *Saccharomyces cerevisiae* and serves multiple roles in ice cream. The size and uniformity of the ice crystal size

distribution determine the texture and mouthfeel of the ice cream. Smaller crystals result in a smooth and creamy texture. ISP addition enables substantial reduction in ice crystal size during the manufacturing process, while subsequent ice growth due to recrystallization is minimized [220]. Moreover, the ice cream exhibits enhanced thermal stability, and new possibilities for formulation optimization open up. By incorporating ISP, the amount of sugar and fat can be reduced, while a creamy consistency is maintained. In addition, high-water-content ingredients such as fruit juices or purees can be incorporated in a greater extent without compromising the ice cream's creamy texture.

Furthermore, substantial quality improvements have been demonstrated for various frozen foods following IBM addition. When applied to frozen meat and fish, the integrity of the tissue is preserved, leading to reduced drip loss upon thawing and maintained textural properties [221–223]. IBMs may find additional application in dough formulations. During freezing and frozen storage, dough is susceptible to dehydration, gluten network destruction, and loss of yeast activity. This leads to a dense, compact, and low-volume loaf after thawing. Using IBMs, these issues can be mitigated [224,225]. The given examples illustrate a subset of potential applications of IBM in the food industry. Generally, IBMs offer the possibility of preserving products which are currently difficult to freeze without significant damage.

Besides, IBMs may also enable significant advancements in agriculture. By means of genetic modifications, plants can be engineered to enhance their freeze resistance or tolerance, expanding their geographic regions of growth. The feasibility of generating cold resistant plants has been proven for *Arabidopsis thaliana* [226,227]. Animals can also undergo genetic engineered. A prime example is the modification of salmon to produce type I AFP [228]. This was the first genetically modified animal approved by the U.S. Food and Drug Administration as safe for human consumption.

While the application of IBM for the cryopreservation of cells, tissues and organs might appear straightforward, their effectiveness can vary tremendously. Despite the use of vitrification protocols to prevent ice crystal formation, the thawing phase will result in ice formation and recrystallization processes, causing substantial damage. In this regard, AFPs demonstrated substantial protective effects following vitrification in different biologic samples, including sperm [229], oocytes [230] and embryos [231]. Furthermore, the preservation of donated blood for extended periods necessitates cryopreservation at extremely low temperatures. The use of recrystallization-inhibiting glycosides has been shown to boost post-thaw viability and reduce the amount of glycerol that needs to be removed prior to transfusion [232]. By

using polyvinyl alcohol and hydroxyethyl starch, glycerol can be replaced entirely [233]. Additionally, AFPs enhance red blood cell survival during freezing [234]. Even when stored at temperatures close to 0 °C, AFPs can improve the survival rate and extend the storage duration of rat heart [235], bovine embryos [236] or neurons [237]. The burst-like growth of ice crystals and the sharp ice crystal forms induced by the binding of fish AFPs to ice crystals can cause damage to cells and tissues. This property, however, offers potential for application in cancer treatment by cryosurgery [238].

Ice and frost formation can be problematic in various applications, including transportation [239] and energy infrastructure [240,241]. To mitigate these issues, surface coatings incorporating AFPs are being developed. For instance, glass surfaces coated with AFP-linked polymers exhibited reduced ice formation [242]. Experiments conducted on aluminum surfaces showed similar results [243].

By polyvinyl alcohol addition to cement mixtures, frost damage to the resulting concrete structures is minimized, while the concrete's overall performance was not negatively affected [244].

1.4 Carrageenans – Sulphated Polysaccharides Derived from Seaweed

Carrageenans are linear polysaccharides derived from red algae (*Rhodophyceae*), commonly used in various applications due to their functional properties of thickening and gel formation [34,245]. Hydrogels, such as those formed by carrageenans, are elastic, three-dimensional structures capable of retaining water within a network of hydrophilic polymers. The type of cross-links between these polymers, ranging from strong covalent bonds to weaker, temporary interactions, significantly influence the gel's properties [246–248]. In addition, the chemical characteristics of the polymer used, determines the gelation mechanism. In terms of carrageenan, these biopolymers are widely employed in the food industry to adjust the texture of sauces and creams or to stabilize beverages [249]. Beyond food, carrageenans are used in personal care products such as toothpaste and nasal sprays, in the pharmaceutical industry as excipient in pills and recently even in eco-friendly packaging material [250–252].

1.4.1 Chemical Structure of Carrageenans

In general, carrageenans are made up of repeating units of β-1,3-linked D-galactopyranose (G-unit) and α-1,4-linked D-galactopyranose (D-unit). The exact structural composition of

carrageenan is characterized by a repeating pattern of disaccharide units and their classification into distinct types primarily depends on the specific arrangement of these disaccharides and the presence of sulfate groups. Among the different types of carrageenan, designated by Greek letters, κ-, ι- and λ-carrageenan are the most commercially important [253,254]. Additionally, carrageenans can be subdivided into two main forms based on the presence of anhydrogalactose (DA-unit). For instance, λ-carrageenan without an anhydrogalactose unit is considered as precursor form. Under alkaline conditions, these precursors can be transformed into the basic forms. Thus, μ- and ν-carrageenan are the precursors to κ- and ι-carrageenan, respectively. Furthermore, a letter- and number-based classification system for carrageenans, proposed by Knutsen et al., is commonly found in scientific literature [255]. The initial letter specifies the type of monosaccharide, while the subsequent numbers and letters denote any present sulfate groups. Accordingly, the repeating disaccharide of κ-carrageenan is composed of a galactose sulfated at position O-4 (G4S-unit), and a DA-unit. Similar to κ-carrageenan, ι-carrageenan consists of a G4S- and a DA2S-unit, while λ-carrageenan is composed of a G2S- and D2S6S-unit.The structures of the disaccharide units are shown in Figure 1.8.

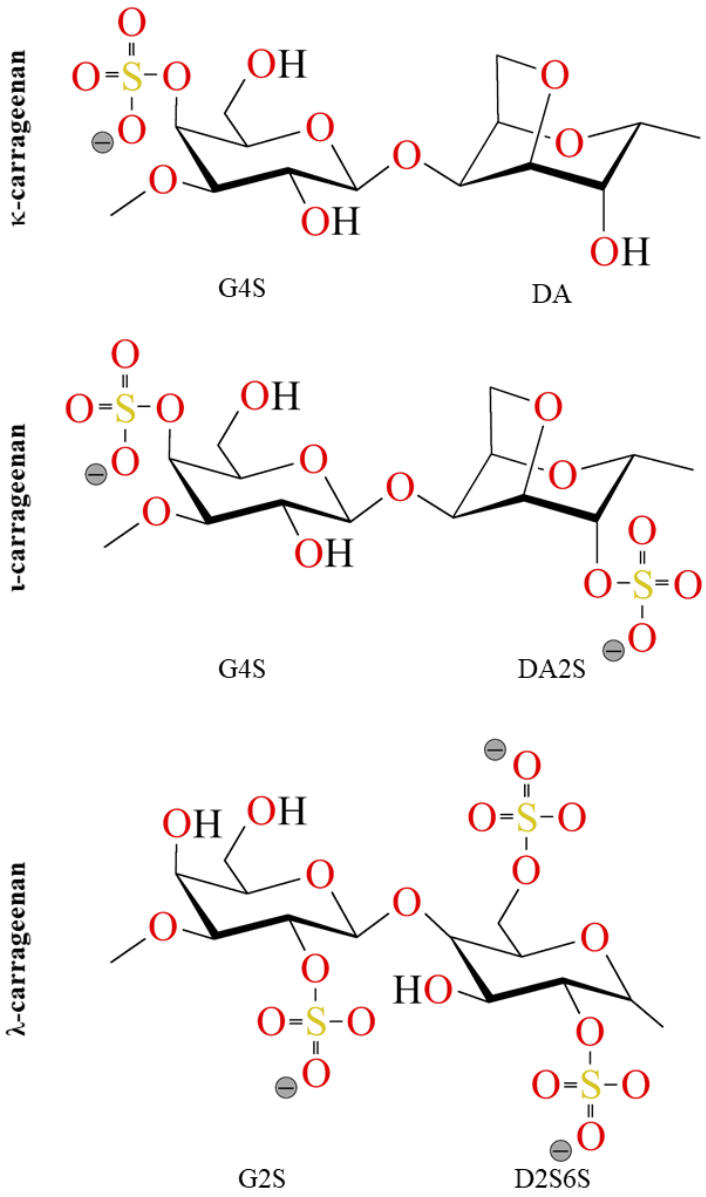

Figure 1.8. *Idealized representation of the disaccharide building blocks for κ-, ι-, and λ-carrageenan. Oxygen and sulfur atoms are highlighted in red and yellow, respectively. The negative charge on each disaccharide unit gradually increases from κ- to λ-carrageenan.*

Accordingly to Figure 1.8, the sulfate content of carrageenans progressively increases from κ- to λ-carrageenan. Commercial available κ-carrageenan typically contains around 22% (w/w), whereas ι-carrageenan has a significantly higher sulfate content of 32% (w/w). λ-carrageenan exhibits the highest sulfate content among these three carrageenans, with about 38% (w/w) [34,250]. Carrageenans used in the food industry typically range from 400 to 600 kDa in molecular weight, with a minimum of 200 kDa [249].

Besides mixtures of non-covalently linked carrageenans, hybrid carrageenans with varying disaccharide units distributed in blocks, alternating sequences or randomly within the polymer chain can occur [36,256]. Furcellaran, a hybrid carrageenan, is primarily composed of κ disaccharide units. Additionally, it includes a smaller amount of β disaccharide units, compromising a galactose without any sulfate groups (G-unit) and an anhydrogalactose (DA-unit) [257]. Replacing some of the G4S-units with G-units reduces furcellaran's sulfate content to 16-18 % (w/w), in comparison to κ-carrageenan. Moreover, the average of the molecular weight of furcellaran is typically around 500 kDa, although there are instances of samples with smaller average molecular sizes [257,258].

1.4.2 Gel Formation Mechanism

Although all carrageenans can be used to alter the viscosity of liquids, the ability to form gels is a specific property of carrageenans that include a DA-unit. The adoption of helical conformation, facilitated by the presence of anhydrogalactose, is a prerequisite for gel formation [250]. Therefore, κ- and ι-carrageenan, both containing anhydrogalactose units, are capable of gel formation. Despite extensive research, the exact gel formation mechanisms and the structure of κ- and ι-carrageenan in solution are still subject to debate. Two main models, the widely accepted domain model according to Morris [259] and the Smidsrød-Grasdalen model [260], have been proposed to describe the gelation process. Both models are illustrated in Figure 1.9. At elevated temperatures, both models assume that carrageenan adopts a random coil structure. In this state, the molecules are highly flexible and no intermolecular hydrogen bonds exist. However, the models differ in the molecular structure adopted during the cooling process. Morris et al. propose that individual carrageenan strands form double helices which can be linked to create structures known as domains. Cation-mediated aggregation of different domains results in the formation of a stable gel structure [259]. In contrast, Smidsrød-Grasdalen assume that cooling induces the formation of simple helices starting from the random coil structure. By adding cations, the electrostatic repulsion is minimized and the helices can aggregate to form a stable gel network [260].

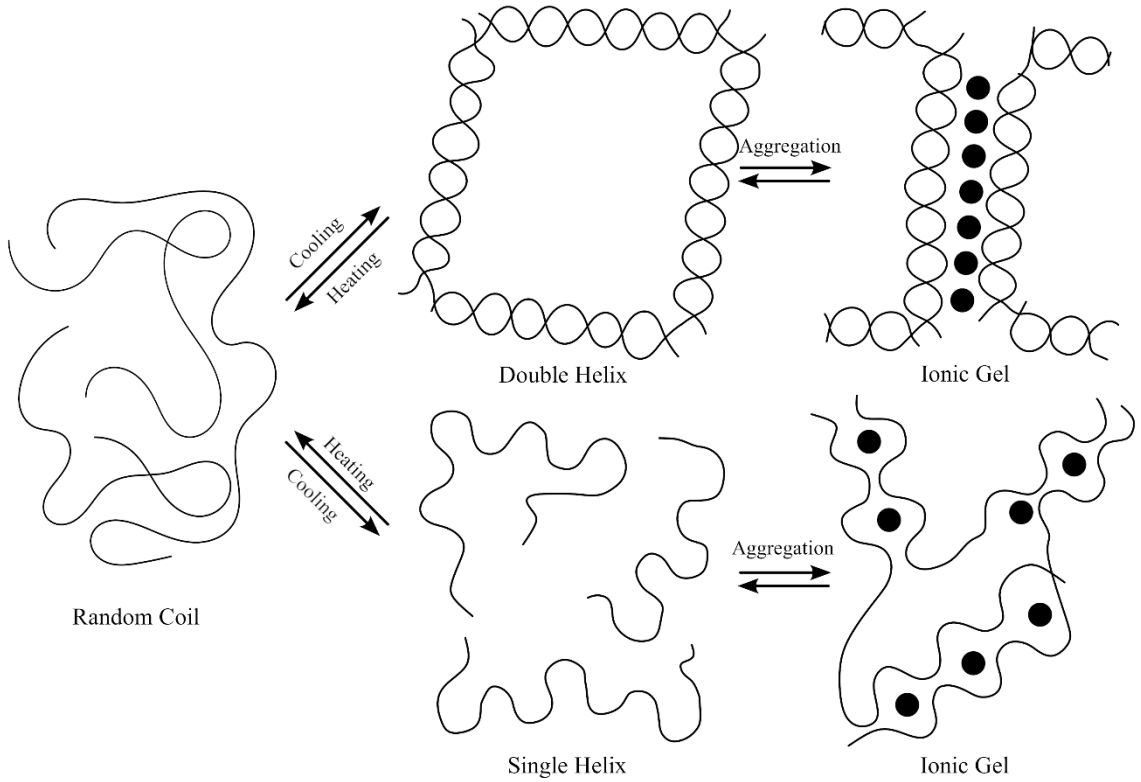

Figure 1.9. *Illustration of the models according to Morris [259] and Smidsrød-Grasdalen [260] for carrageenan gelation, both starting from a random coil structure. Morris et al. propose that cooling results in the formation of double helices (upper panel), which aggregate forming a gel network upon cation (black dots) addition. The Smidsrød-Grasdalen model (lower panel) assumes the formation of single helices upon cooling followed by cation-mediated aggregation.*

Both models agree that the gelation process is triggered by cations. Additionally, multiple studies provided evidence that the formation of a gel depends on the aggregation of helices [261–264]. Furthermore, the role of anions in the aggregation process of carrageenans is complex. While anions play a less direct role in carrageenan conformation, they can influence the aggregation by interacting with either the carrageenan molecules or the cations themselves. Direct interactions of thiocyanate and iodide with the carrageenan helix have been observed, but the precise mechanism is still unclear [265–267]. In general, the rheological properties of carrageenan gels can be modified by various different influencing factors, such as the type and concentration of ions present [268,269]. κ-carrageenan gels formed with potassium ions are rigid while those formed with calcium are of a brittle nature [270–272]. Moreover, the carrageenan type and concentration of the polymer directly correlates with the mechanical properties of the resulting gels. Pure κ-carrageenan gels are strong, while pure ι-carrageenan forms weaker gels. In consequence, the gel strength can be adjusted by altering the proportion

of κ- to ι-carrageenan with synergistic effects under specific conditions [273–276]. In addition, gels composed of κ-carrageenan are stronger and more elastic with increasing molecular weight of the polymers [277]. Besides, process parameters during gel formation, such as the cooling rate and the gelation time, affect the final properties of the gel [278,279].

1.4.3 Commercial Manufacturing of Carrageenans

Cost-effective and large-scale production of carrageenans typically involve simplified extraction methods that directly process washed seaweed material. A straightforward method to obtain carrageenan-rich seaweed material uses a potassium hydroxide solution to process the raw seaweed at 70 to 80 °C. This converts the carrageenan precursors into κ-, ι- or λ-carrageenan and removes low-molecular-weight substances. The processed seaweed is washed again, dried and ground into a powder [280]. However, refined or semi-refined carrageenan extracts are commonly employed in the food industry, labeled as E407 (refined) or E407a (semi-refined), and in scientific research. Similarly, an alkaline extraction process at temperatures exceeding 110 °C is used to release carrageenan from the plant cell wall and to convert the precursor molecules. The specific cations present the final carrageenan extract are determined by composition of the alkaline solution. Subsequently, any insoluble solids are removed by filtration steps and the remaining liquid is concentrated to achieve a 3 % carrageenan solution. This filtration step is only applied to refined-grade carrageenan extracts. To separate the carrageenan polymers from the solution, isopropyl alcohol is added to precipitate the carrageenan. After drying, the solid carrageenan extract is milled and mixed into the final product. An alternative process, referred to as gel pressing method, can be used for the extraction of κ-carrageenan. Instead of the precipitation with alcohol, κ-carrageenan is transformed into a gel by the addition of a potassium chloride solution. The resulting gel is then pressed to remove excess liquid, dried and further processed. A schematic representation of both methods is provided in Figure 1.10.

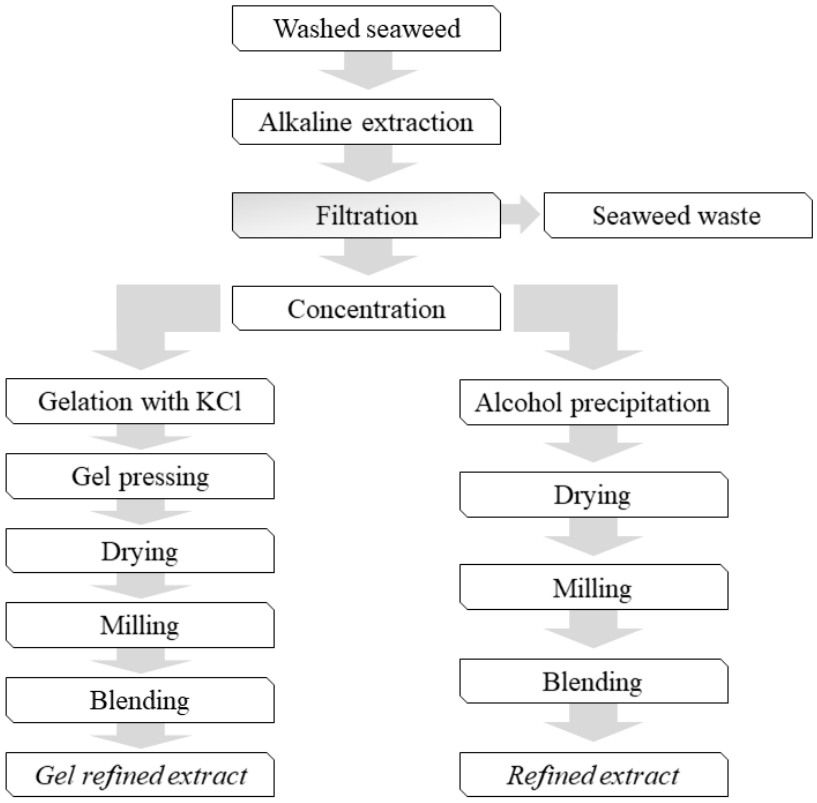

Figure 1.10. *A schematic representation of the production process for refined carrageenan. The traditional method, using alcohol precipitation, is illustrated on the right. The left side depicts the gel pressing method, commonly employed for the extraction of κ-carrageenan.*

1.4.4 Impact of Carrageenan on Ice Crystal Growth

With regard to ice crystal growth, both κ- and ι-carrageenan have been shown to inhibit ice crystal recrystallization [38,44]. However, κ-carrageenan is more potent in preventing ice crystal growth and has been studied in greater detail. Upon the addition of κ-carrageenan, the formation of smaller ice crystals is promoted and their growth is significantly slowed down over time. Additionally, the IRI activity of κ-carrageenan increases as its concentration is increased, even at relatively low levels [25,38]. Through extensive research, Leiter and colleagues have made substantial advancements in understanding κ-carrageenan's role in preventing the recrystallization of ice crystals. Reducing the molecular weight using acid hydrolysis decreased the IRI activity of κ-carrageenan which may be attributed to the lower number in available binding sites [43]. Heat processing, such as pasteurization, is a common process in the food industry to extend shelf life by eliminating microorganisms and deactivating enzymes [281]. Leiter et al. demonstrated that κ-carrageenan is able to withstand these heat

treatments without any loss in IRI activity [42]. The IRI activity is also unaffected by changes in pH, but is substantially influenced by the type and amount of ions present [42]. This is significant for food and cryopreservation applications, as salts are almost always present in foods, buffer solutions or the surrounding medium. Moreover, the formation of a gel or gel-like character due to aggregation of multiple κ-carrageenan molecules, triggered by the addition of specific ions, negatively impacts the IRI activity. Unlike gelatin, which did not impact ice recrystallization even when a gel was formed, it may be inferred that the presence of a gel network does not necessarily reduce recrystallization processes [90]. It is hypothesized that the aggregation process limits the number of molecules able to interact with the ice crystal surface [41]. As discussed in section 1.2.2, an increased viscosity caused by hydrocolloids does not necessarily mean better recrystallization inhibition [25,85,94]. Budiaman and Fennema have shown that the type of hydrocolloid, rather than viscosity, impacts the rate of the recrystallization process [282]. For the three commercially used carrageenans, κ-, ι-, and λ-carrageenan, no relationship between the viscosity of their solutions and their IRI activity has been found. Therefore, this implies an ice-binding mechanism of κ-carrageenan to ice crystals. In addition, the altered ice crystal shape, from round to angular and elongated, in sucrose solutions containing κ- or ι-carrageenan provides further evidence [42,44]. Dynamic ice crystal shaping is typically associated with IBPs and attributed to the interaction of the molecule directly with the ice crystal surface.

1.5 Molecular Dynamics Simulations

1.5.1 Introduction

This section explores the principles and applications of MD simulations. Unlike Monte Carlo simulations, which rely on stochastic sampling for exploring configurational space, MD simulations offer a deterministic approach to understand molecular systems. MD simulation uses the laws of classical mechanics to describe the physical movements of a many-body system, such as atoms and molecules, over time [283]. The ability to precisely observe atomic-scale phenomena has made this simulation method essential in diverse fields such as biochemistry, drug discovery, nanotechnology, material science, and chemical engineering. Consequently, the number of publications employing or discussing this simulation method demonstrated a consistent increase up to 2020. Figure 1.11 shows the number of MD publications for every fourth year starting from 1970.

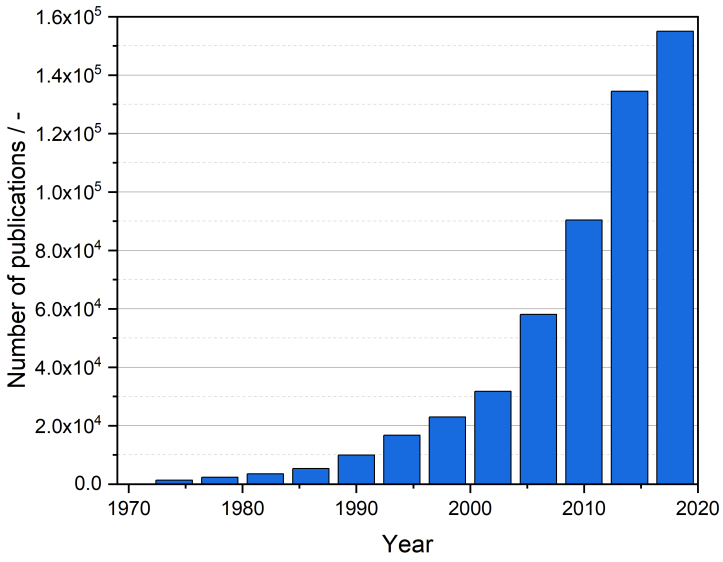

Figure 1.11. *Trend of publications related to MD simulations since 1970. The height of each bar corresponds to the total number of publications for a given year, as measured by Google Scholar search results.*

Experimental research often requires substantial cost and time investments. In general, simulations provide a favorable alternative to explore various scenarios and identify potential outcomes without conducting physical experiments. These advantages of MD simulations have become even more apparent during the COVID-19 pandemic. The rapid emergence and spread of SARS-CoV-2 necessitated accelerated drug development. However, the limited understanding of this new virus's interactions with the human body made it experimentally difficult to identify its exact target. In addition, obtaining real-world biologic samples and virus structures can be costly and risky. Moreover, clinical trials are time-consuming taking years to achieve approval of new drugs. Computational methods, in particular MD simulations, allowed *in silico* screening of drug-molecule interactions to identify potential lead structures and to understand the mechanism of action of SARS-CoV-2. Consequently, targeted experiments could be conducted to investigate the most promising compounds, increasing the chance of a positive outcome while saving time and money. [284–290]

As early as the late 1950s, both Monte Carlo and MD simulations were developed once electronic computing machines had been established to handle complex computing challenges. The demand for advanced computational capabilities during World War II, in particular the Manhattan Project and the breaking of the Enigma code substantially accelerated the development of these devices. In 1957, the first simple application of MD simulations was performed by Alder and Wainwright to investigate the interaction between hard spheres [291]. The field of molecular simulations made substantial progress in the 70s with the first Monte Carlo simulation of water by Barker and Watts [292]. At the end of this decade, McCammon

and colleagues made a significant contribution by conducting the first simulation of a protein, bovine pancreatic trypsin inhibitor, a small protein composed of 58 residues [293]. This research was conducted under the guidance of Martin Karplus, who played a pivotal role in advancing the field of MD simulations. In recognition of his contributions, he was honored with the 2013 Nobel Prize in Chemistry together with Michael Levitt and Arieh Warshel for the development of multi-scale modeling techniques.

1.5.2 Fundamental Concepts – Force, Potential Energy and Force Fields

By employing MD simulations, the intricate dynamics of individual atoms can be examined, facilitating the observation of microscopic mechanisms of energy and mass transfer. According to classical mechanics, a system of N particles can be fully characterized by specifying the location $r_1(t)$ to $r_N(t)$ and velocity $v_1(t)$ to $v_N(t)$ of each particle at any given time t. Internal and external forces acting on these particles induce their motion, which can be mathematically quantified using Newton's second law (Equation 1.9). The force $\vec{F}_i$ acting on an atom results from the potential energy U and can be calculated by taking the negative gradient of the potential energy field at that atom's location.

$$\vec{F}_i = m_i \, \overrightarrow{a_i} = m_i \, \frac{d\overrightarrow{v_i}}{dt} = m_i \, \frac{d^2\overrightarrow{r_i}}{dt^2} = -\vec{\nabla} U(\overrightarrow{r_i}) \tag{1.9}$$

Where: $\vec{F}_i$ $= force\ acting\ on\ each\ individual\ particle$

m_i $= mass\ of\ each\ individual\ particle$

$\overrightarrow{a_i}$ $= acceleration\ of\ each\ individual\ particle$

$\frac{d\vec{v}_i}{dt}$ $= derivative\ of\ velocity\ with\ respect\ to\ time$

$\frac{d^2\vec{r}}{dt^2}$ $= second\ derivative\ of\ the\ position\ with\ respect\ to\ time$

$-\vec{\nabla} U(\vec{r}_i) = negative\ gradient\ of\ the\ potential\ energy\ of\ atom\ i\ with\ respect\ to\ its\ position\ r$

Therefore, the accuracy of MD simulations directly depend on the precision of the potential energy calculations. The potential energy is modelled using a force field, which is a set of empirical functions approximating the energy associated with different types of atomic interactions. Typically, force fields include terms describing bonded and non-bonded interactions. Non-bonded interactions encompass van der Waals forces (E_{vdW}), arising from fluctuations in electron density, electrostatic forces between charged particles ($E_{electrostatic}$) and hydrogen bond formation between a hydrogen atom and a specific electronegative atom ($E_{H\ bond}$). Additionally, there are equations to model the energy of covalently bonded atoms. These bonded interactions include a term describing the energy associated with changing the bond length

($E_{stretching}$), another term to account for the energy required to bend a bond angle ($E_{bending}$), and a term representing the energy related to the rotation around a single bond ($E_{torsion}$). Figure 1.12 provides a visual representation of the bonded interactions.

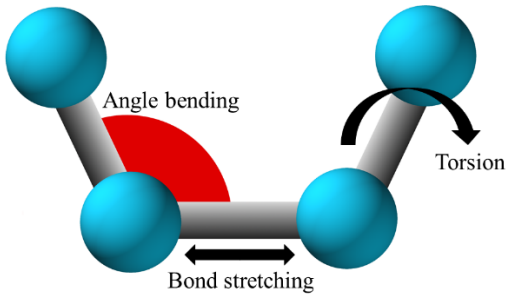

Figure 1.12. *Illustration of the bonded interactions in a force field, which account for energy changes associated with bond angle deviations, changes in bond lengths, and rotations around single bonds.*

Accordingly, the total energy (E_{tot}) of a system, described by the force field, is obtained by adding up the contributions from all individual terms (Equation 1.10). Additional terms may be introduced to Equation 1.10 to improve the accuracy of certain force fields, depending on the material properties they aim to represent, for example polarizable terms to reflect charge redistribution.

$$E_{tot} = E_{stretching} + E_{bending} + E_{torsion} + E_{vdW} + E_{electrostatic} + E_{H\ bond} \tag{1.10}$$

Where: $E_{stretching}$ $= Energy\ associated\ with\ changing\ bond\ lenghts$

$E_{bending}$ $= Energy\ associated\ with\ bond\ angles$

$E_{torsion}$ $= Energy\ associated\ with\ rotation\ around\ a\ bond$

E_{vdW} $= Energy\ arising\ from\ van\ der\ Waals\ interactions$

$E_{electrostatic}$ $= Energy\ arising\ due\ to\ electrostatic\ forces$

$E_{H\ bond}$ $= Energy\ arising\ due\ to\ the\ formation\ of\ hydrogen\ bonds$

The Lennard-Jones 12-6 potential (Equation 1.11) is a popular interatomic potential that describes the interaction energy between pairs of uncharged particles as a function of their separation distance r. For instance, it is commonly employed for the calculation of non-bonded interactions. Even though the Lennard-Jones 12-6 potential only considers the interaction of two particles and is therefore computationally efficient, it reproduces the properties of a wide range of materials, from simple substances to complex fluids remarkably well [294,295]. In Equation 1.11, the mathematically expression of the Lennard-Jones 12-6 potential is provided.

$$\phi_{LJ} = 4\varepsilon_0 \left[\left(\frac{\sigma}{r}\right)^{12} - \left(\frac{\sigma}{r}\right)^{6} \right] \tag{1.11}$$

Where: ϕ_{LJ} $= Lennard - Jones\ potential$

ε_0 $= energy\ minimum\ of\ the\ potential\ function$

σ $= interatomic\ distance\ at\ which\ the\ potential\ equals\ 0$

r $= interatomic\ distance$

Fundamentally, the general Lennard-Jones potential is a combination of two terms accounting for the attractive and repulsive forces of intermolecular interactions. Intermolecular attraction, such as van der Waals forces, arises when atoms or particles come within a sufficiently close distance to each other. With decreasing distance, those attractive forces increase. At a particular distance, commonly referred to as equilibrium distance, the attractive and repulsive forces are balanced, corresponding to a state of minimum potential energy. As the distance between the atoms or particles decreases further, the repulsive forces become increasingly dominant. Repulsive forces arise due to the Pauli Exclusion Principle preventing overlapping of electron orbitals. In addition, at extremely short distances, repulsion between atomic nuclei contributes to this force. The total potential energy equals 0 at a distance of σ. At extremely short distances, the repulsive forces rapidly increase to infinity. This relationship between distance and potential energy is graphically illustrated in Figure 1.13. To achieve a more accurate description of material properties in specific simulation scenarios, the Morse [296] and the Buckingham [297] potentials, can be employed. However, these potentials, incorporating exponential terms, require more computational resources compared to the Lennard-Jones potential.

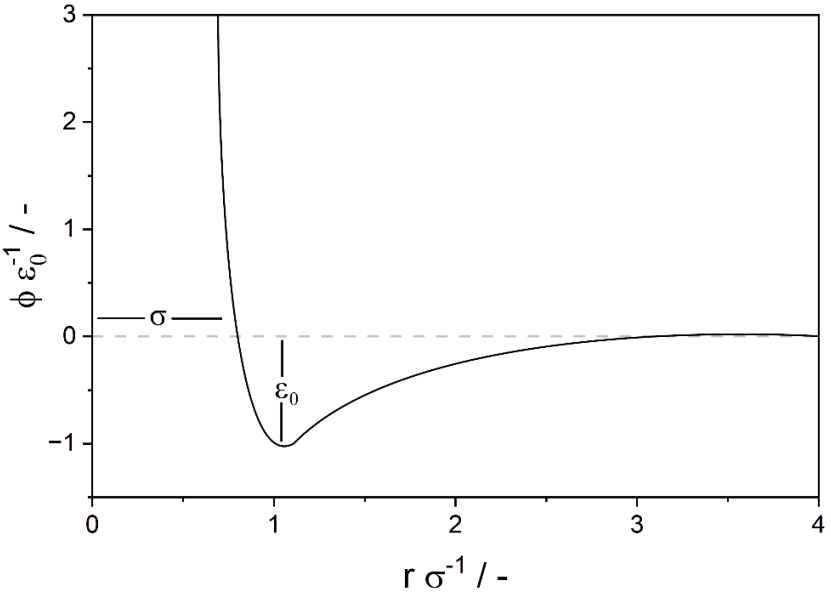

Figure 1.13. *Illustration of the dimensionless Lenard-Jones potential.*

Besides the mathematical form of the potential energy functions for non-bonded, bonded, electrostatic, and other interactions, force fields require parametrization to define the strength and range of the atomic interactions. The precise determination of these parameters is crucial for the reliability and accuracy of the force field. Since metals, ions or molecules have unique properties distinct parametrization strategies are required. In consequence, there are specialized force fields for different materials and applications. Generally, force field parametrization can be done using either information obtained from the atomistic level [298,299], such as quantum mechanical calculations or spectroscopic measurements, or from macroscopic properties e.g. hardness or compressibility. Experimental data, compromising enthalpies of vaporization and sublimation, vibrational frequencies, and dipole moments, can be integrated into the parameterization process to improve the accuracy of the force field. In addition, hybrid approaches utilizing both atomistic and macroscopic data are also commonly employed [300]. Recently, machine learning has emerged as promising technique to bridge the gap between computationally expensive quantum mechanics simulations and the efficiency of classical force fields [301]. Typical force field parameter sets include masses, charges, Lennard-Jones parameters, equilibrium bond lengths, angles, and dihedral angles. Moreover, force fields employ a cut-off radius to limit the range of non-bonded interactions. While a larger cut-off radius improves accuracy, it also increases the computational costs. Consequently, a trade-off between accuracy and efficiency must be carefully considered. By employing neighbor lists to identify pairs of atoms closer than the cut-off distance, computational costs can be substantially reduced. However, long-range interactions, such as electrostatic forces, extend beyond the cut-off radius. To accurately model these long-range effects, specialized techniques like Ewald summation [302,303] or Particle Mesh Ewald [304] are employed.

1.5.3 Water Models in MD Simulations

Water is an essential molecule for life and chemical or biological processes, acting as exceptionally effective solvent. This ability is thought to result from its distinct molecular characteristics, including mobility, hydrogen bonding structures, strong permanent dipole moment, self-ionization, and high dielectric constant [305]. Given that water constitutes a large fraction of the molecules in a MD simulation, it is extremely important to accurately model its properties without incurring high computational costs. Consequently, specialized force fields for water molecules have been designed and their fundamental structure is illustrated in Figure 1.14. Simple 3-point force fields, such as SPC [306] or TIP3P [307], are based on the tetrahedral structure of water and offer reasonable accuracy, while requiring minimal computational

resources. Yet, not all bulk properties, such as the melting point, density or enthalphy of vaporization, can be reproduced accurately. Among the 4-point water models, the TIP4P model gained significant recognition. By placing the negative charge of the oxygen atom on a separate dummy atom, this model achieves improved structural properties [307]. Despite the availability of more accurate and complex models, these simple force fields are still popular in many simulations. The TIP5P model, a 5-point representation of water, incorporates two dummy atoms to represent the lone pairs of electrons on the oxygen atom [308]. This geometry enables precise predictions of water density across wide pressure and temperature conditions. Polarizable force fields employ an oscillating atom, resulting in a correct vaporization enthalpy, density, static dielectric constant, and self-diffusion constant [309]. Fundamentally, the selection of an appropriate water model should be adapted to the specific requirements of the system under investigation. For instance, when simulating a system involving ice growth, it is crucial to employ a water model that accurately describes the liquid-solid phase transition.

In order to simulate systems containing water and other molecules like proteins, carbohydrates, or lipids, water force fields are combined with other force fields for those additional components. However, not all force fields are compatible with each other, which can lead to compatibility issues.

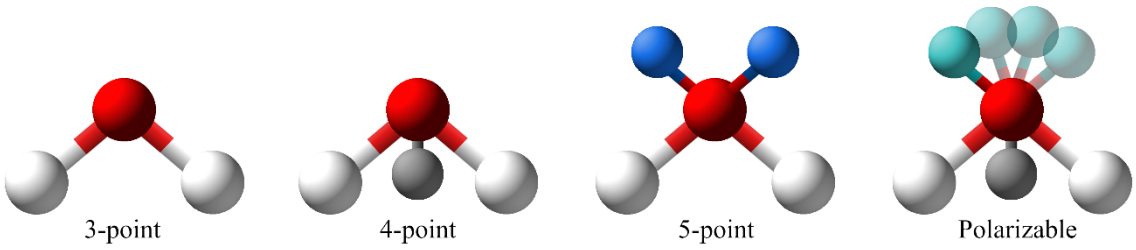

Figure 1.14. *Illustration of various geometries of water models, encompassing simple 3-point and complex polarizable models. Oxygen atoms are depicted as red spheres, while hydrogen atoms are shown as white spheres. The 4-point and polarizable models introduce a grey dummy atom. The 5-point model incorporates two additional blue dummy atoms, representing the lone electron pairs of the oxygen atom, while the oscillator of the polarizable model is shown as cyan sphere.*

1.5.4 Numerical Integration Methods

In order to determine the trajectories of individual atoms, Newton's equation of motion (Equation 1.9) needs to be numerically solved at discrete time intervals. This enables the calculation of velocities and positions of individual atoms at each subsequent time step $t + \Delta t$. Similar to solving the Navier-Stokes equations in computational fluid dynamics, finding an exact analytical solution is not possible and numerical methods are necessary to obtain an approximation. The accuracy of the solution directly depends on the length of the integration time step

Δt, which must be sufficiently small to capture the fastest motions, particularly hydrogen bond vibrations. Therefore, time steps on the femtoseconds scale are employed. Depending on the system simulated, total simulations times of nano- or even milliseconds are required leading to a vast number of integration time steps needed. This immense computational demand has only become manageable with recent advancements in computing power.

The Verlet integration scheme, dating back to the 1960s, is a simple yet effective method for solving Newton's equations of motion [310]. Its numerical stability and efficiency made it a staple in MD simulations [311]. The time-reversibility of the Verlet integrator ensures that simulations can be run forward and backward in time, retracing the systems trajectory to its original state. Additionally, it conserves the total energy of the system well, making it suitable for long-term simulations where energy drifts are of concern. Due to the Verlet integrator's straightforward implementation, it offers a good balance between accuracy and computational costs. While Equation 1.12 is used to compute the new positions, the velocity calculation is omitted.

$$r(t + \Delta t) = 2r(t) + r(t - \Delta t) + a(t)\Delta t^2 \tag{1.12}$$

Where: $r(t + \Delta t) = position\ at\ the\ next\ time\ step$
$r(t) = position\ at\ the\ current\ time\ step$
$r(t - \Delta t) = poition\ at\ the\ previous\ time\ step$
$a(t) = acceleration\ at\ the\ current\ time\ step$

Even though the trajectory can be determined without the calculation of the velocity, it is essential for evaluating the kinetic energy and ensuring that the total energy of the system is conserved. Consequently, the velocity Verlet integration incorporates additional equations for the velocity calculation, which substantially increases the accuracy for long-term simulations [312]. Just as the standard Verlet integrator, the velocity Verlet integration scheme is time-reversible. Moreover, it is likely the most widely employed integration method for MD simulations. At first the half-time step velocity is calculated according to Equation 1.13.

$$v\left(t + \frac{1}{2}\Delta t\right) = v(t) + \frac{1}{2}a(t)\Delta t^2 \tag{1.13}$$

Where: $v\left(t + \frac{1}{2}\Delta t\right) = half\ time\ step\ velocity$
$v(t) = velocity\ at\ the\ current\ time\ step$
$a(t) = acceleration\ at\ the\ current\ time\ step$

This intermediate velocity is used to compute the new position as described in Equation 1.14.

$$r(t + \Delta t) = r(t) + v\left(t + \frac{1}{2}\Delta t\right)\Delta t \tag{1.14}$$

Where: $r(t + \Delta t)$ $= position\ at\ the\ next\ time\ step$

$r(t)$ $= position\ at\ the\ current\ time\ step$

$v\left(t + \frac{1}{2}\Delta t\right) = half\ time\ step\ velocity$

Subsequently, the new position is used to calculate the force and acceleration $a(t + \Delta t)$. Finally, the velocity is updated to its corresponding value at the next time step $t + \Delta t$ as given in Equation 1.15.

$$v(t + \Delta t) = v\left(t + \frac{1}{2}\Delta t\right) + \frac{1}{2}a(t + \Delta t)\Delta t \tag{1.15}$$

Where: $v(t + \Delta t)$ $= velocity\ at\ the\ next\ time\ step$

$v\left(t + \frac{1}{2}\Delta t\right) = half\ time\ step\ velocity$

$a(t + \Delta t)$ $= acceleration\ at\ the\ next\ time\ step$

Another method is the leapfrog integration, which is also a variation of the Verlet integrator. The velocity Verlet and leapfrog integrators both involve a time-stepping approach where positions and velocities are calculated at alternating time intervals. Despite both methods exhibit same levels of accuracy and time-reversibility, velocity Verlet is often favoured due to its slightly better energy conservation. Nevertheless, it is a common integration method in many simulation packages.

While the mentioned integration methods are sufficient for a lot of simulations, specific scenarios can necessitate alternative approaches. These alternative integrators, such as higher-order Runge-Kutta methods, offer higher accuracy and are employed in non-conservative systems. For instance, Beeman's integration algorithm offers higher accuracy and better energy conservation especially in systems with rapidly changing forces [313].

1.5.5 Constraint Algorithms

In order to preserve specific molecular geometries, MD simulations often utilize constraint algorithms. These algorithms generally enforce fixed distances between two atoms, thereby maintaining constant bond lengths, angles and torsional angles. Additionally, constraints can be employed to restrict these parameters to a range of certain configurations. The use of constraints offers three main advantages. Accurately modeling the fastest molecular motions in unconstrained simulations demands very small time steps Δt. Imposing constaints on these

motions leads to a significant increase in the permissible Δt, enhancing computational efficiency. Therefore, hydrogen bonds lengths are commonly constrained. Moreover, biomolecules with a rigid structure, such as proteins and nucleic acids, can be constrained to keep their structure intact throughout the simulation. Two popular constraint algorithms are SHAKE and LINCS. Initially designed to maintain fixed bond lengths, the SHAKE algorithm iteratively corrects atomic positions. Subsequently, this method was extended to handle any holonomic constraints, including bond angles or overall molecular rigidity [314]. In contrast, the non-iterative LINCS method solves a matrix equation to determine the corrected atomic positions. Consequently, LINCS offers enhanced stability, making it suitable for large systems, and provides a speedup of up to four times compared to SHAKE [315]. However, the use of constraints is limited to systems where they do not interfere with the dynamics of the simulated molecules.

1.5.6 Periodic Boundary Conditions to Mimic Bulk Behavior

Experimentally observable quantities, such as melting point or density, are properties of the material itself independent of the exact size or shape of the sample, as long as the sample is sufficiently large. Macroscopic samples in real-world experiments contain enormous numbers of particles making surface effects negligible and fluctuations of global quantities statistically insignificant. However, MD simulations use finite systems with a much smaller number of particles to limit computational costs to a manageable level. Therefore, periodic boundary conditions (PBC) are applied to mitigate the impact of finite simulation box sizes and surface effects, which can introduce false atomic forces resulting in non-physical system behavior [316]. By infinitely replicating the simulation cell in all spatial directions, the bulk behavior of liquids and solids can be accurately modelled. A simplified two-dimensional visualization of the concept of PBCs is provided in Figure 1.15. The primary simulation box, located at the center (highlighted in blue), is sourrounded by identical, periodically replicated images. Within the simulation, this replication occurs not only two-dimensionally as depicted in Figure 1.15, but in all three dimensions. Whenever an atom leaves the primary simulation box through one side, the corresponding atom from the adjacent periodic image enters the primary simulation box from the opposite side. This dynamic equilibrium ensures that the total number of atoms within the primary simulation box is conserved and the simulation is explicitly performed for the atoms in this box.

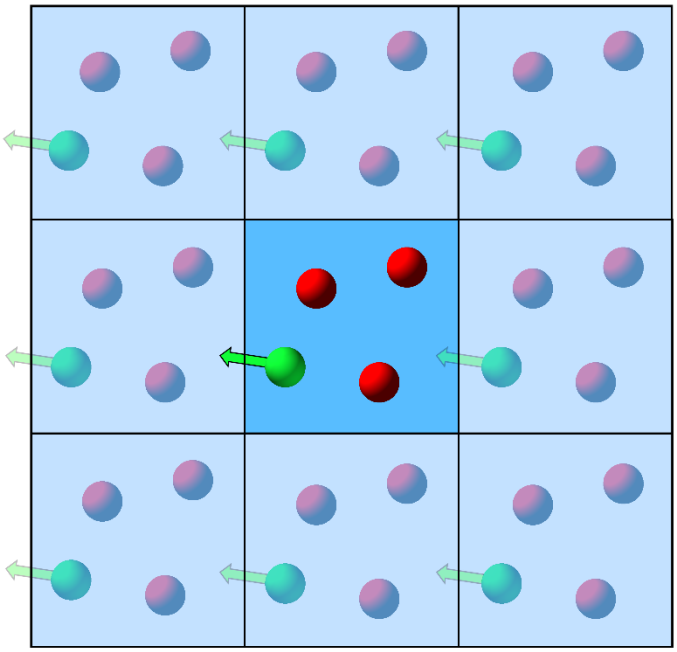

Figure 1.15. *2D representation of periodic boundary conditions. The primary simulation box, located at the center contains 4 atoms. As the green atom exits this simulation cell on the left side, it re-enters the primary simulation box on the right side, due to the mirror images of the simulation box.*

While PBCs are a powerful tool, they can pose challenges, especially when dealing with long-range forces such as electrostatic interactions. This necessitates the introduction of specialized methods for the calculation of these interactions, such as the previously mentioned Ewald summation.

1.5.7 Simulation Setup and Workflow

Overall, the workflow of a MD simulation can be broken down into three fundamental steps, as depicted in Figure 1.16. Initially, an appropriate molecular model has to be selected or prepared. In the second step, the system's energy is minimized and it is equilibrated to ensure realistic initial conditions including pressure and temperature, for the subsequent simulation. Once the system reaches a stable state, a production run is performed to generate molecular trajectories and colletc the data of interest for subsequently analyzed.

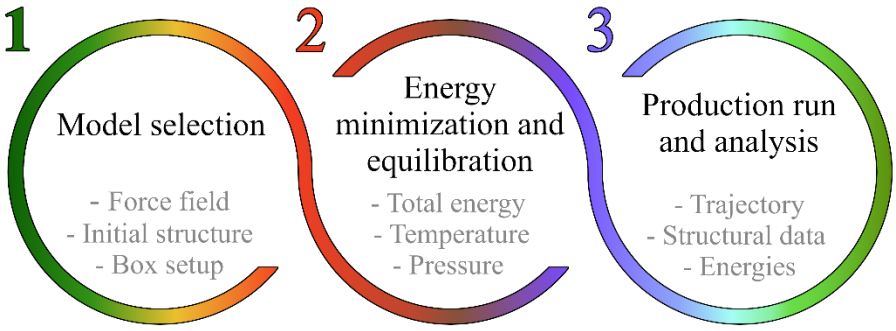

Figure 1.16. *Typical MD simulation workflow consists of model selection, energy minimization and equilibration, and production run with corresponding analysis.*

Model Selection

The model selection is the foundation of MD simulations, as the accuracy of the simulation heavily depends on the quality of the model. Following the selection of the molecule as subject of investigation, the appropriate structural data must be obtained. Experimental data, such as crystal structures from the Protein Data Bank, provide a solid starting point. In addition, PubChem serves as repository for chemicals and offers also structural data. However, experimental data may not be available for novel or complex molecules. Therefore, computational tools like Avogadro [317] or PyMOL [318] can be used to generate, modify, and add missing atoms to the molecule of interest, including hydrogens. Given that classical MD simulations do not inherently account for pH, protonation states of the individual groups within the molecule must be manually adjusted. Furthermore, the chosen force field must be compatible with the specific atoms of the molecules being studied to accurately describe the system. It is imperative that this force field must be consistent with the force field for describing the water molecules. Subsequently, the simulation setup is completed by defining the box size, solvent, ions and other relevant parameters. This box building process can be facilitated by software tools such as CHARMM GUI [319].

Energy Minimization and Equilibration

In the second step, the system is finalized for the following production simulation. Energy minimization removes any steric clashes or energetically unfavorable interactions between atoms optimizing the system's total energy. Different minimization algorithms are available for this purpose. A simple and widely employed method for energy minimization is the steepest descent algorithm [320]. While relying on gradients of the potential energy landscape, this method is effective for initial optimization, but may experience difficulties converging near

the energy minimum. To address this limitation of the steepest decent method, the conjugate gradient algorithm was introduced [321,322]. This method additionally incorporates information from previous iterations to improve convergence, especially near the minimum with low gradients. Different thermodynamic conditions are represented in MD simulations by the use of specific ensembles, which are microscopic states sharing similar macroscopic properties. The choice of ensemble is determined by the specific property of interest. The most common used ensembles are Microcanonical, Canonical, and Isothermal-Isobaric. The Microcanonical ensemble (NVE) is characterized by a constant particle number, volume and total energy, making it suitable to study fundamental dynamics [323]. However, controlling temperature and pressure is difficult, limiting its applicability to open, real-world systems. In contrast, the canonical ensemble (NVT) maintains a constant temperature by coupling the system to an external heat bath. A heat bath is an algorithm or mathematically construct interacting with the system's particles to regulate temperature through controlled energy addition or removal. Additionally, both particle number and volume are fixed. The NVT ensemble is commonly employed to investigate isolated systems, including material properties, protein folding and drug discovery. To simulate real-world conditions, the isothermal-isobaric ensemble (NpT) is utilized. While the particle number, temperature and pressure remain constant, the simulation box is allowed to contract or expand, resulting in a fluctuating volume. For systems where the exchange of particles is needed, such as in adsorption or electrochemical processes, the grand canonical ensemble (μVT) is employed. This ensemble ensures constant chemical potential, temperature and volume [283,324].

Different ensembles require specialized control methods. Thermostats are used to maintain a constant temperature, while barostats are employed to control the pressure of a simulation. The choice of thermostat depends on the characteristics of the system being simulated. Given the various available methods, three commonly used thermostats will be outlined. The Nose-Hoover thermostat is considered the most effective method for temperature regulation in MD simulations. It couples the system with a heat bath, which is treated as an addition degree of freedom. This approach enables the correct sampling of the NVT ensemble, granting that the system's properties align with the specified temperature. Additionally, the velocity rescale thermostat is a popular alternative. By calculating the system's kinetic energy and actual temperature from the velocity of all particles, a scaling factor is determined to adjust the velocities to match the set temperature. Refined methods of this thermostat have been optimized for accuracy and numerical stability, ensuring the correct sampling of the system [325]. The

Langevin thermostat uses a frictional force to slow down particles in combination with a random force inducing thermal motion. While this method is easy to implement, it is not suited for systems strongly interacting with a heat bath. In terms of pressure regulation, the Parrinello-Rahman barostat is predominantly applied method for maintaining a constant pressure in MD simulations. This is achieved by introducing an additional degree of freedom to the system allowing the box size to deform in response to pressure changes. Furthermore, this method offers high precision and can be employed in anisotropic systems where the pressure varies depending on the direction [326,327]. In contrast, the computationally efficient Berendsen barostat adjusts the box volume by rescaling the positions of the particles [328]. The Martyna-Tuckerman-Tobias-Klein barostat is a more complex technique modifying both volume and box size. However, this flexibility leads to higher computational costs [329].

Production Run and Analysis

Once the system's energy has been minimized and the correct ensemble has been sampled, a production run can be performed to generate data for analysis. An important aspect is the simulation length, with longer simulations typically providing more reliable results. To maintain numerical stability and accuracy, the time step Δt must be relatively small, resulting in a lot of iterations. For a 250 ns simulation consisting of 25000 particles and a Δt of 2 fs, a total of 125 million iterations are required. A workstation configured with 128 GB of RAM, 16 processing threads, and an NVIDIA consumer-grade graphics card will need approximately 5 days to execute such a simulation. The overall simulation time depends also on other parameters. For instance, the frequency at which atomic positions and velocities are saved impacts the simulation duration substantially.

MD simulations generate extensive datasets. In order to obtain valuable insights from these datasets, several analytical approaches are utilized. A fundamental analysis method involves a visual inspection of the system's trajectory over time. This qualitative assessment can help to quickly identify potential issues, artifacts or unusual behavior. Numerous visualization tools are available with Visual Molecular Dynamics (VMD) [330] and PyMOL [331]. These tools have evolved in recent years, offering diverse functionalities such as calculating densities, identifying and analyzing hydrogen bonds, and determining Root Mean Square Deviations (RMSD). Hydrogen bond analysis identifies and tracks their formation and breakage between specific atoms or groups, typically based on geometric criteria, in order to investigate molecular stability or interactions. Moreover, RMSD asses a molecule's structural stability

and the extent of its conformational changes over the simulation time. This technique quantifies the average deviation of a group of atoms from a reference structure, which is often its starting structure. A stable system shows consistently low RMSD values, while large deviations suggest significant conformational shifts. To identify a molecule's flexible and rigid regions, Root Mean Square Fluctuation (RMSF) is used. It measures how much individual atoms or residues fluctuate around their mean position during the simulation. Highly mobile and flexible regions will exhibit high RMSF values, whereas stable, well-ordered regions will show low RMSF values. Dedicated analysis software like MDAnalysis [332] or PLUMED [333] offer a wide range of pre-built functions and analysis tools, thereby eliminating the need for users to develop custom scripts. However, many simulation packages, such as GROMACS [334] or NAMD [335], also incorporate a variety of built-in analysis functionalities capable of performing thorough investigations of MD simulations.

2 Commercially Available Carrageenans Show Broad Variation in Their Structure, Composition, and Functionality

This chapter was published as: Hale, J.; Gerhäuser, J.; Gaukel, V.; Wefers, D. (2024): Commercially available carrageenans show broad variation in their structure, composition, and functionality. In: European Food Research and Technology, 250, 2989–3003. doi:10.1007/s00217-024-04605-w

2.1 Abstract

Carrageenans are polysaccharides from red algae which are widely used as food additives and in other applications. Their structure is often described by different disaccharide repeating units, although it was already demonstrated that reality is more complex. In many studies, commercial carrageenans were used to establish structure function relationships, but a structural and compositional analysis was rarely conducted. Therefore, the aim of our study was to systematically and comprehensively characterize a broad collection of commercial carrageenans with different specifications from different manufacturers. For a more detailed characterization, an analytical approach based on partial enzymatic hydrolysis in combination with HPLC–MS and HPSEC-RI was developed and applied. Furthermore, rheology was used to gain detailed insights into the functionality of selected samples. Our results demonstrate that significant structural variation can be observed for commercial carrageenans. The samples contained different cations and the carrageenan type specified by the manufacturer did not always represent the structure of the corresponding polysaccharides. This was especially true for λ-carrageenans: Of the six commercial samples analyzed, none contained structural elements from the λ-type. Instead, the corresponding carrageenans contained κ-, ι- and ν-units. The application of the developed enzymatic-chromatographic approach showed that different hybrid carrageenans are present. In addition, the rheological analysis of the commercial carrageenan samples showed clear differences in the gelling properties upon calcium addition which could influence their behavior in different applications. Our results demonstrate that before an investigation of structure–function relationships, commercial carrageenan samples should be analyzed for their structure and composition. We also showed that the enzymatic-chromatographic approach described in this study is well suited for this purpose.

2.2 Introduction

Carrageenans are polysaccharides extracted from red algae which are commonly used as food additives, e.g. as thickening, stabilizing or gelling agent [34]. They are linear polysaccharides and often described by using repeating disaccharide units. These units are composed of a 1,3-linked β-D-galactopyranose (G-unit) and a 1,4-linked α-d-galactopyranose (D-unit) or 3,6-anhydro-α-D-galactopyranose (DA-unit). The individual monosaccharide units can be substituted with sulfate groups [35,280]. The substitution position depends on the type of carrageenan and is usually annotated by adding the position and "S" to the monosaccharide descriptor (e.g. G4S for a 1,3-linked galactose unit which is sulfated at position C4) [255].

Carrageenans are commonly classified into different types based on the disaccharide repeating units. These types are abbreviated using Greek letters, with κ-, ι- and λ-carrageenan being the most commercially important carrageenans [35,253,254,280]. The κ-carrageenan repeating unit is composed of a G4S- and a DA-unit, while the ι-carrageenan repeating unit contains a G4S-unit and a DA2S-unit. In contrast, λ-carrageenan is composed of two galactose units (G2S and D2S,6S) [34,255]. Carrageenans with a D-unit instead of a DA-unit are commonly referred to as natural precursors. For example, μ-carrageenan (G4S, D6S) is the precursor of κ-carrageenan, while ν-carrageenan is the precursor of ι-carrageenan. The sulfated D-units of precursor carrageenans can be converted into DA-units by the use of enzymes or under alkaline conditions. The latter usually occur during the extraction of carrageenans from red seaweed [35]. Due to the use of different bases, different cations can be associated with the carrageenans. The most abundant cations are potassium, sodium and calcium ions [336]. The cations are an important factor for the aggregation of carrageenan helices during gel formation [261]. Thus, they are important for the functional properties but possibly also for the physiological properties.

The usually applied classification of carrageenans assumes that only the disaccharide unit characteristic of one type of carrageenan is present in the polymer. However, some carrageenans contain different disaccharide repeating units within one polymer chain and are also known as hybrid carrageenans or kappa-2 carrageenans [36,253,254]. Hybrid/kappa-2 carrageenans gained relevance for selected applications and several types have been described and structurally characterized in the literature, such as κ/ι- [37,337], ν/ι- [338] and μ/κ-hybrid carrageenans [256]. In addition, mixtures of different carrageenan types may occur, in which the individual polymers are not covalently attached to each other [36].

The physicochemical properties of carrageenans are closely linked to their chemical structure. For example, carrageenans without 3,6-anhydrogalactose units, such as λ-carrageenan, lack gel-

forming properties. On the other hand, κ- and ι-carrageenans containing DA-units are able to form gels [34,35]. In addition to the rheological properties [276,277,339], other physiological and technological effects of carrageenans have been investigated in many studies, such as the ice recrystallization inhibition activity [25,41–44], inflammatory effects in the gut [340–345] as well as anti-viral effects [346–348]. However, the structure and composition of the carrageenans used in these studies were either not characterized or only roughly characterized. In many cases, researchers rely on the specifications from the manufacturers or literature data. However, using well-characterized samples is crucial which has also been pointed out by the European Food Safety Authority [349]. The aim of our study was to comprehensively and systematically characterize different commercial carrageenans in detail to document possible structural and compositional differences, to point out influences on functionality and in general to raise awareness for this issue. Furthermore, an enzymatic-chromatographic approach was developed for a detailed structural characterization of the carrageenan samples.

2.3 Experimental

2.3.1 Carrageenans

Carrageenan samples were obtained from a variety of manufacturers, including samples from both the food industry (Eurogum (Denmark), CP Kelco (USA), Tate & Lyle (United Kingdom)) and chemical suppliers [Merck (Germany), Alfa Aesar (USA), Biosynth (Switzerland), Dextra Laboratories (United Kingdom)]. A total of 16 samples was included into the initial characterization, before selected samples were further characterized by partial enzymatic hydrolysis and rheology. The individual samples were named by using a descriptor for the carrageenan type (KC for κ-carrageenan, IC for ι-carrageenans, LC for λ-carrageenans and C for unspecified carrageenans) and consecutive numbers which correspond to different manufacturers. According to the manufacturer's specifications, 3 κ-carrageenans (KC1-3), 5 ι-carrageenans (IC1-5), 6 λ-carrageenans (LC1-6), and 2 unspecified carrageenans (C1 & C2) were present.

2.3.2 Other Materials

Deuterium oxide (≥ 99.9% D) was purchased from Deutero (Germany), dimethyl sulfoxide (≥ 99.5%) from Carl Roth (Germany), and 35% (v/v) hydrogen peroxide from J.T. Baker (USA). Sodium dihydrogen phosphate dihydrate, Isopropyl β-D-1-thiogalactopyranoside (ultrapure), ammonium formate (≥ 99%) and acetonitrile (MS-grade) were obtained from VWR

International (Germany). Disodium hydrogen phosphate (≥ 99%) was purchased from Honeywell (USA), and ampicillin from AppliChem (Germany). Neocarrabiose-4-sulfat sodium salt (≥ 95%) and Neocarratetraose-4,4-disulfate disodium salt (≥ 95%) were purchased from Biosynth (Switzerland). Other chemicals were obtained from Merck (Germany). For all experiments, chemical solvents with suitable purity and Milli-Q water were used.

2.3.3 NMR Spectroscopy

NMR experiments were conducted by using a Bruker Avance Neo 400 MHz spectrometer, which was equipped with a temperature-controlled 5 mm-probe head. The spectra were recorded at a temperature of 65 °C and a standard ^{1}H pulse program from Bruker ('zg90') was used. The relaxation delay (d_1) was set to 25 s, the acquisition time was 2 s, and a total of 16 (or 32) scans were performed. For the analysis, carrageenan solutions with a concentration of 5 mg/mL were prepared in deuterium oxide and treated in a water bath at 70 °C until complete dissolution of the sample. As an internal reference, 0.5 µL of dimethyl sulfoxide was added (2.696 ppm, according to van de Velde et al. [350]). The signals of the anomeric protons of the D/DA-unit can be used to identify the different types of carrageenan [350].

2.3.4 Molecular Weight

The weight average molecular weight (M_W) of the carrageenans was determined by using a Hitachi system (Merck, Germany) with a refractive index detector (L-7490, Hitachi, Merck, Germany) and a multi angle laser light scattering (MALLS) detector (SLD7100, PSS Polymer Standards Service, Germany). The system was equipped with a TSKgel G6000PW$_{XL}$ column (Tosoh Bioscience, Japan) and the column temperature was set at 60 °C. 0.1 M lithium chloride was used as the eluent to prevent aggregation of the carrageenans, as recommended by Lecacheux et al. [351], with an isocratic flow rate of 0.5 mL/min. The M_W of the samples was determined using a refractive index increment of 0.115 g/mL [351]. For the analysis, carrageenan solutions with a concentration of 2 mg/mL were used. The sample solutions were prepared in 0.1 M lithium chloride (eluent) and treated in a water bath at 60 °C until the polysaccharides were completely dissolved.

2.3.5 Inductively Coupled Plasma Atomic Emission Spectrometry (ICP-OES)

For the ICP-OES analysis of associated cations as well as sulfur, 10 mg of carrageenan were dissolved in 10 mL of 1% (v/v) nitric acid. The solutions were analyzed on a Varian 715-ES (Agilent Technologies, USA) or an iCAP 7000 instrument (Thermo Fisher Scientific, USA).

The instrument was calibrated with standard solutions of sodium, potassium, calcium and sulfur, covering a concentration range of 0.25—50 mg/L. Based on the sulfur content, the sulfate content of the carrageenans was calculated.

2.3.6 Sulfate Analysis

To release the sulfate groups, the polysaccharide was subjected to acid hydrolysis. For this purpose, 25 mg of the carrageenan sample were mixed with 2.25 mL of 2.3 M trifluoroacetic acid and 0.25 mL of 35% (v/v) hydrogen peroxide. Hydrolysis was carried out for 16 h at 100 °C. Subsequently, the samples were cooled to room temperature (20 °C) and then centrifuged for 10 min at 220 × g. After centrifugation, 250 µL of the supernatant was dried by evaporation. The dried residue was dissolved in 3.25 mL of water and treated in a water bath at 70 °C for 15 min [352]. Sulfate analysis was carried out on a Dionex ICS-6000 system (Thermo Fisher Scientific, USA) equipped with a conductivity detector and a Dionex AERS 500e suppressor (4 mm, Thermo Fisher Scientific, USA) to suppress the conductivity of the eluent. 30 mM sodium hydroxide solution was used as the eluent with an isocratic flow rate of 0.38 mL/min. Separation of inorganic ions was carried out on a Dionex IonPac AS10 column (250 × 4 mm, particle size 8.5 µm, Thermo Fisher Scientific, USA) and the column temperature was set at 30 °C.

2.3.7 Production of Recombinant Enzymes

Two carrageenases from *Zobellia galactanivorans* (ZGAL_236 (κ-carrageenase) and ZGAL_4265 (ι-carrageenase), according to Ficko-Blean et al. [353]) were cloned and heterologously expressed in this study. Genes were amplified from genomic DNA (DSM 12802, Deutsche Sammlung von Mikroorganismen und Zellkulturen (DSMZ), Germany) by PCR using the Phusion High-Fidelity PCR Kit (Thermo Fisher Scientific, USA). The primers used are listed in Table A1.1. Specific overhangs were added to the genes, PCR products were purified by using the MicroElute Cycle-Pure Kit (Omega Bio-Tek, USA), and cloned into the pLIC-SGC1 vector (plasmid #39187, Addgene, USA) by ligation-independent cloning [354]. The vector was previously linearized by BseRI and the gene vector constructs were transformed into *E. coli* NovaBlue. The sequence of the plasmids containing the gene of interest was verified by Sanger sequencing (Eurofins, Germany).

For protein expression, *E. coli* (BL21) cells (Thermo Fisher Scientific, USA) were transformed with the plasmids and selected on an agar plate containing 100 µg ampicillin/mL. A single colony was used to inoculate 5 mL of LB medium (100 µg ampicillin/mL). The cells were

grown over night at 37 °C with constant shaking (225 rpm). The suspension was transferred into 400 mL of LB medium (100 µg ampicillin /mL) and grown another 4 h (37 °C, 225 rpm). Overexpression was induced by adding 80 µL of 500 mM isopropyl β-D-1-thiogalactopyranoside solution. The culture was incubated over night at 20 °C with constant shaking (225 rpm). Subsequently, cells were removed by centrifugation (4.000 × g) and the cell pellet was resuspended in lysis buffer (50 mM sodium phosphate, 300 mM sodium chloride, pH 8.0). Bacterial cells were lysed by sonication (pulse 3 × 20 s, amplitude 50%, pause 59,9 s) using a Sonifier W-250 D (Branson Ultrasonics, USA) and the lysate was centrifuged at 4 °C and 14.000 × g for 30 min. The supernatant was then used for immobilized metal affinity chromatography to purify the overexpressed proteins.

For protein purification, 4 mL of a Ni–NTA resin (Thermo Fisher Scientific, USA) were used, pre-equilibrated with wash buffer (2 mM sodium phosphate, 12 mM sodium chloride, 10 mM imidazole, pH 8.0). The supernatant was added to the Ni–NTA-resin and incubated at 4 °C for 30 min. After incubation the resin was washed twice with 4 mL of wash buffer. The proteins were eluted by adding 5 mL of elution buffer (50 mM sodium phosphate, 300 mM sodium chloride, 250 mM imidazole, pH 8.0).

2.3.8 Partial Enzymatic Hydrolysis

1% (w/v) carrageenan suspensions were prepared and treated in a water bath at 60 °C until the polysaccharides were completely dissolved. For partial enzymatic hydrolysis, 250 µL of the carrageenan solution were mixed with 200 µL of water and 50 µL of enzyme solution. The samples were incubated for 24 h at 37 °C with constant agitation. After incubation, the enzymes were inactivated at 95 °C for 10 min. For comparison, carrageenan solutions without the addition of enzyme (250 µL of 1% (w/v) carrageenan solution, 250 µL of water) and enzyme solutions without the addition of polysaccharide (50 µL of enzyme solution, 450 µL of water) were prepared.

2.3.9 HPLC–MS

The analysis of enzymatically released oligosaccharides was carried out on a LCMS-2020 system (Shimadzu, Japan) equipped with an ACQUITY UPLC BEH amide column (2.1 mm × 150 mm, particle size 1.7 µm, Waters, USA). 20/80 (v/v) acetonitrile/water (A) and 80/20 (v/v) acetonitrile/water (B) were used as eluents. Both eluents contained 10 mM ammonium formate and 0.2% formic acid and the following gradient program was applied: 5 min at 100% B, in 26 min linear to 20% B, in 1 min back to 100% B and finally 8 min at 100% B. The analysis

was carried out at a flow rate of 0.4 mL/min and a column temperature of 35 °C was used. MS detection with electrospray ionization was carried out in negative full scan mode (m/z 250–1000). For sample preparation, 50 µL of the hydrolysate were mixed with 150 µL acetonitrile to precipitate undigested high molecular weight material and to adjust the solvent composition. The samples were centrifuged for 4 min at 16.100 × g and the supernatant was used for HPLC–MS analysis.

2.3.10 HPSEC-RI

For HPSEC analysis, 100 µL of the hydrolysate were mixed with 150 µL of 0.1 M lithium chloride solution (eluent). The analysis was carried out on a Hitachi system (Merck, Germany) equipped with a TSKgel G6000PW$_{XL}$ column (Tosoh Bioscience, Japan). 0.1 M lithium chloride was used as the eluent with an isocratic flow rate of 0.5 mL/min. The analysis was performed at a temperature of 60 °C and a refractive index detector (L-7490, Hitachi, Merck, Germany) was used for detection.

2.3.11 Rheology

To assess the rheological characteristics of the seven commercial carrageenan samples a Physica MCR 301 (Anton Paar GmbH, Austria) rheometer was used. The rheological measurements were conducted in pure polysaccharide solutions in Milli-Q water and upon addition of $CaCl_2$ (Carl Roth GmbH & Co. KG, Germany) to characterize the gelling behavior. Calcium chloride was chosen due to the typical use of carrageenan in dairy products, which are rich in calcium ions. Each carrageenan sample was weighed to obtain a suspension with a polysaccharide concentration of 5 mg/mL. The polysaccharides were completely dissolved by heating to a temperature of 60 °C. For the samples containing 0.1 M $CaCl_2$, the salt and carrageenan were weighed simultaneously and were dissolved subsequently. All samples were maintained at 60 °C until transferred onto the measurement geometry of the rheometer. The measurement geometries were preheated to 60 °C. Once the sample was loaded, the temperature was lowered to 25 °C within 7 min. To allow for sample relaxation or gelation, the temperature was kept constant for 5 min prior to initiating the frequency sweep. The frequency sweep to determine the storage modulus G’ and the loss modulus G’’ took 25 min. To prevent water evaporation during all measurements, the sample was overlaid with a low viscosity paraffin oil (Carl Roth GmbH & Co. KG, Germany). More details on this method can be found in [339]. Due to the absence of gelation of the samples without added salt, the measurements were carried out using a double gap geometry (DG26.7-SN97573, Anton Paar GmbH, Austria), which is suited for less viscous

samples. The amplitude γ was set to 10% during the frequency sweep between 0.1 and 10 Hz to ensure that the strain applied remained within the linear viscoelastic region. In case of the gel-forming samples containing $CaCl_2$, a plate-plate geometry (PP25-SN19091, Anton Paar GmbH, Austria) with a diameter of 25 mm and a constant gap width of 1 mm was used. The amplitude γ during the frequency sweep had to be set to 2% to remain the strain within the linear viscoelastic region. It should be noted that gel formation can potentially lead to an inaccurate measurement due to volume changes during gelation [355]. Therefore, the normal force was carefully monitored during the cooling process and the measurement. No significant deviation was detected indicating that gelation did not impact the accuracy of the measurement. Triplicate measurements were conducted for each sample and the corresponding standard deviation was calculated. The graphs of the storage and loss moduli for each sample are provided in the supplementary materials.

2.4 Results and Discussion

To study the structural and functional heterogeneity of commercial carrageenans, 16 samples were purchased from different suppliers. The carrageenans were classified into different types (see Section "Carrageenans") and intended for use as laboratory chemicals or food additives. All samples were analyzed for their structural composition by using NMR spectroscopy, HPSEC-RI/MALLS, ICP-OES, and ion chromatography. Based on the results, selected carrageenans were subjected to further analysis by partial enzymatic hydrolysis and rheology.

2.4.1 Compositional Analysis

The results of the NMR spectroscopic analyses of the structural units are shown in Table 2.1. The characteristic signals of the D-/DA-units were assigned according to van de Velde et al. [350] and signal integrals were used to calculate the portions of the individual structural elements. Only κ-units were detected in all κ-carrageenan samples, whereas the NMR spectrum of IC1, IC2, IC4, and IC5 solely contained signals which resulted from ι-units (exemplary spectra are shown in Fig. A1.1). However, IC3 contained 73% ι-units and 27% κ-units suggesting the presence of a carrageenan mixture or a hybrid carrageenan. Notably, none of the λ-carrageenans contained signals of λ-units. LC1, LC3, LC4, and LC5 were composed of comparable portions of κ- (42–47%), ι- (31–37%) and ν-units (21–30%), whereas LC2 contained 72% κ-units and 28% ι-units. The two unspecified carrageenans C1 and C2 also contained κ- and ι-units (C2) or κ-, ι-, and ν-units (C1). Therefore, our results show that the analyzed commercial λ-carrageenans as well as the unspecified carrageenans are structurally heterogeneous polysaccharides.

The results also demonstrate that it should not be assumed that commercial λ-carrageenans actually contain λ-units. Furthermore, the samples KC2, IC4, and C2 contained a signal at 5.40 ppm, whereas IC3 contained a signal at 5.22 ppm. The corresponding signals could not be assigned to any carrageenan unit. By comparison with different standard compounds, these signals were assigned to sucrose (5.40 ppm) and glucose (5.22 ppm). These sugars were most likely added to standardize the viscosity of the individual carrageenans. Therefore, the presence of mono- and dimeric sugars must also be taken into account when commercial carrageenans are used to study physiological effects. The results of the molecular weight analyses by HPSEC-RI/MALLS are shown in Table A1.2. The M_W and the polydispersity index of the samples as well as the chromatograms obtained for the samples (Fig. A1.2) demonstrated that all carrageenans had a rather high molecular weight and a rather narrow molecular weight distribution. Both parameters were in a range typical for carrageenans [351,356–358].

Table 2.1. *Carrageenan composition of the commercial samples used in this study as determined by ^{1}H NMR spectroscopy.*

Sample	**Structural unit (portion, mol%)**	**Sample**	**Structural unit (portion, mol%)**
KC1	κ	LC1	κ (47), ι (31), ν (22)
KC2	κ	LC2	κ (72), ι (28)
KC3	κ	LC3	κ (42), ι (37), ν (21)
IC1	ι	LC4	κ (42), ι (33), ν (24)
IC2	ι	LC5	κ (44), ι (33), ν (23)
IC3	κ (27),ι (73)	LC6	κ (59), ι (41)
IC4	ι	C1	κ (37), ι (33) , ν (30)
IC5	ι	C2	κ (59), ι (41)

The contents of potassium, calcium, and sodium cations (determined by ICP-OES) are shown in Table 2.2. As expected, the three κ-carrageenan samples mainly contained potassium ions besides smaller amounts of sodium and calcium ions. The ι-carrageenan samples were more heterogeneous, although potassium was the predominant cation in all five ι-carrageenan samples. In addition, IC1, IC3, and IC4 showed significant amounts of calcium, whereas for samples IC2 and IC5 significant amounts of sodium were detected. The observations made for κ- and ι-carrageenan are in good agreement with the literature [336]. The λ-carrageenans and the unspecified samples showed even more variation. Notably, the carrageenans LC3, LC5, and LC6 as well as C1 mainly contained sodium ions. Potassium was observed as the predominant

cation in LC2 and C2, whereas sample LC1 showed high amounts of calcium. Furthermore, a 1:1 mixture of potassium and sodium was detected for sample LC4. The results demonstrate that commercial carrageenans show significant heterogeneity with regards to the associated cations. The contents of the three cations in combination with the sulfate contents also suggest that a slight excess of salt is present in all carrageenans. This is most likely caused by the inclusion of some of the salt present during the manufacturing (inclusion during precipitation or gel pressing). Because the cation type in the carrageenans is largely dependent on the conditions during extraction, it can be concluded that significantly different methods were used during the production of the analyzed samples. The results also demonstrate that the cation type must be taken into account when the functional properties of carrageenans are being analyzed because it may influence aggregation [261].

Table 2.2. *Contents of K^+, Na^+, and Ca^{2+} (determined by ICP-OES) of the carrageenans used in this study.*

Sample	K^+, g/100 g	Na^+, g/100 g	Ca^{2+}, g/100 g
KC1	6.84	0.10	0.82
KC2	7.44	0.08	0.64
KC3	6.81	0.37	0.30
IC1	4.45	0.07	4.00
IC2	4.26	3.15	1.34
IC3	5.71	0.09	2.65
IC4	3.84	1.37	2.96
IC5	5.43	4.46	0.04
LC1	0.98	0.25	5.48
LC2	5.73	0.30	2.33
LC3	1.77	6.12	0.29
LC4	5.36	5.79	0.13
LC5	2.46	6.25	0.26
LC6	1.72	6.59	0.16
C1	1.69	5.58	0.37
C2	4.18	2.39	0.11

The sulfate contents of the carrageenans are shown in Table 2.3. Generally, comparable sulfate contents were obtained by using the two methods, but some differences were observed between

the carrageenan types. For the κ-carrageenan and unspecified carrageenan samples, the sulfate contents calculated from ICP-OES were slightly lower than from the IC analysis, whereas no trend was observed for ι-carrageenans. In contrast, the sulfate contents determined by ICP-OES were in some cases higher than the ones determined by IC in case of the λ-carrageenan samples. Nevertheless, both methods are suitable to obtain information on the degree of sulfation. As expected, the ι-carrageenan samples contained higher sulfate contents than the κ-carrageenan samples which is caused by the presence of a second sulfate group at the DA-unit. However, IC3 and IC4 showed a clearly lower sulfation degree. This can be explained by the presence of κ-units (IC3) as well as the presence of glucose and sucrose (IC3 and IC4). Furthermore, the presence of sucrose also explains the sulfate content of C2 which was lower than expected for a carrageenan with 41% ι-units. Although the obtained values for κ- and ι-carrageenans were slightly lower than in the literature [352], the results confirm the carrageenan type determined by NMR spectroscopy. The sulfate contents obtained for the LC samples were all below the theoretical value for λ-carrageenan (calculated from the mass fraction of sulfate in a carrageenan with strictly repeating G2S-units and D2S,6S-units). This is in good agreement with the absence of λ-units in the NMR spectra. For LC2 and LC6, the sulfate contents were in good agreement with the contents which were expected based on the NMR spectroscopically determined carrageenan composition. The samples LC1, LC3, LC4, LC5, and C1 showed higher degrees of sulfation which is in good agreement with the occurrence of ν-units (trisulfated repeating unit) in these carrageenans. Therefore, the determination of the sulfate content is in some cases suited to confirm the carrageenan types and the purity of the carrageenans. However, it cannot provide unambiguous information on the structural composition of carrageenans without further analyses. This is for example illustrated by the mean sulfate content of the ι-carrageenans (IC1-5) and the λ-carrageenans (LC1-6) which is very similar between the two groups.

Table 2.3. *Sulfate content of the commercial carrageenans used in this study.*

Sample	Sulfate content, % (w/w)	
	IC	**ICP-OES**
KC1	19.4 ± 0.3	18.1
KC2	17.1 ± 0.1	16.2
KC3	17.8 ± 0.1	16.4
IC1	29.6 ± 0.3	28.2
IC2	29.3 ± 0.4	28.8
IC3	22.7 ± 0.3	21.7
IC4	23.3 ± 0.9	24.7
IC5	29.5 ± 0.3	30.1
LC1	29.3 ± 0.7	29.4
LC2	22.6 ± 0.1	21.9
LC3	26.9 ± 0.4	29.7
LC4	31.3 ± 0.4	35.1
LC5	27.7 ± 0.4	32.5
LC6	24.0 ± 0.3	26.7
C1	29.6 ± 0.1	28.9
C2	17.9 ± 0.4	17.4

2.4.2 Detailed Characterization of Selected Carrageenans

The compositional analysis of the carrageenans showed significant heterogeneity with regards to the structural elements and cations present. However, the methods used cannot differentiate between mixtures of individual carrageenans and hybrid carrageenans. Therefore, an enzymatic chromatographic approach was developed to gain further insights into the structural composition and five potential hybrid carrageenans were selected for a more detailed characterization: IC3, LC1, LC2, C1, C2. These samples were selected because they showed varying ratios of κ- and ι-units (LC2: 72:28, C2: 59:41, IC3: 27:73) and contained ν-units as well as different portions of κ- and ι-units (LC1 & C1). To gain insights into their functionality, the rheological properties of the selected carrageenans were also analyzed and compared to KC1 and IC1.

Characterization after Partial Enzymatic Hydrolysis

To obtain more detailed information about the presence of carrageenan mixtures or hybrid carrageenans, an analytical approach based on partial enzymatic hydrolysis followed by chromatographic analysis was developed. To selectively cleave κ- and ι-units, a κ-carrageenase and a ι-carrageenase from *Zobellia galactanivorans [353]* were heterologously expressed in *E. coli*. The activity as well as the specificity of the two enzymes were tested by hydrolyzing a 0.5% solution of KC1 and IC1 at 37 °C for 24 h. To gain insights into the extent of carrageenan hydrolysis, the hydrolysates were analyzed by HPSEC-RI (Fig. 2.1). This approach allows for the reliable detection of general hydrolytic activity as well as the detection of high molecular weight blocks which are resistant to hydrolysis by the individual enzymes. To analyze the oligosaccharides liberated by κ- or ι-carrageenase, the hydrolysates were also analyzed by HPLC–MS (Fig. 3.1). A HILIC column was selected for chromatographic separation of the carrageenan oligosaccharides and MS detection was carried out after electrospray ionization in negative mode. By using this setup, dimeric repeating units as well as oligosaccharides with a higher molecular weight could be detected.

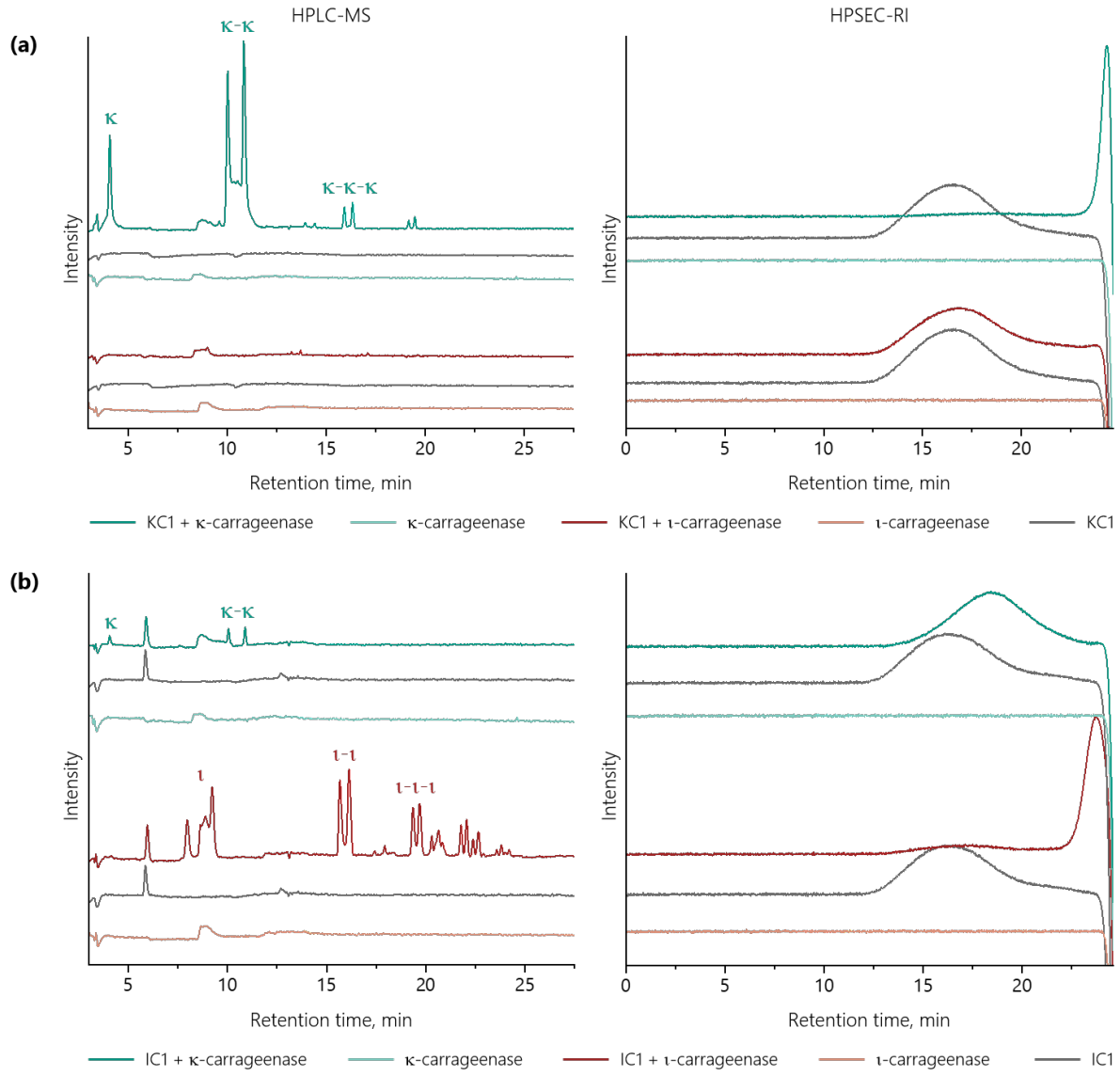

Figure 2.1. *HPLC–MS and HPSEC-RI chromatograms of KC1 (a) and IC1 (b) after partial enzymatic hydrolysis with κ- and ι-carrageenase. The chromatograms of the untreated carrageenans and the enzyme solutions are shown for comparison. The letters κ and ι are used as descriptors for the corresponding disaccharide repeating unit.*

The HPSEC-RI chromatograms clearly demonstrated that the κ-carrageenase completely hydrolyzed KC1, because the high molecular weight peak disappeared and later eluting low molecular weight compounds were formed. In contrast, a peak shift was observed after the incubation of IC1 with κ-carrageenase. This is most likely the result of small portions of κ structural elements within IC1 which cannot be detected by NMR spectroscopy but are hydrolyzed by the enzyme and lead to a molecular weight reduction. The HPSEC results are also supported by the HPLC–MS oligosaccharide analysis. The HPLC–MS chromatogram of the hydrolysate obtained from the incubation of KC1 with κ-carrageenase contained several peaks which were in part present as double peaks (result of mutarotation of the reducing oligosaccharides). The two

early eluting peaks were identified as κ-carrabiose and κ-carratetraose by using standard compounds. The identification of all other oligosaccharides was carried out by analyzing the mass spectra of the corresponding peaks (see Figs. A1.3 and A1.4). However, especially the spectra of larger oligosaccharides were characterized by multiple signals (double / triple charge quasi-molecular and fragment ions) and significant source fragmentation (cleavage of sulfate). Therefore, only the later eluting small double peak at 16 min was identified as κ-carrahexaose, whereas the other peak could not be assigned to a specific structure. In the κ-carrageenase hydrolysate of IC1, trace amounts of κ-carrabiose and κ-carratetraose were present. This confirms the occurrence of small amounts of κ-units in IC1 as well as the specificity of the κ-carrageenase. ι-carrageenase completely degraded IC1 to low molecular weight products, while no change was observed for KC1. In the HPLC–MS chromatogram obtained from the hydrolysis of IC1 with ι-carrageenase, three peaks could be assigned to ι-carrabiose, ι-carratetraose, and ι-carrahexaose. The mass spectra of the other later eluting peaks contained to many fragments which prevented an unambiguous assignment. However, the two methodological approaches demonstrated the specificity of the enzymes and allowed for the detection of κ and ι structural elements and longer κ- and ι-blocks. Thus, the analytical approach is well suited to analyze potential hybrid carrageenans.

The chromatograms obtained from the enzymatic hydrolysis of IC3 (NMR: 27% κ-units, 73% ι-units) confirm that a high portion of ι-carrageenan structural elements were present (Fig. 2.2a). This can be seen from the detection of ι-carrageenan oligosaccharides by HPLC–MS and the detection of high portions of low molecular weight compounds by HPSEC-RI after ι-carrageenase hydrolysis. However, the HPSEC-RI chromatograms revealed that IC3 is not completely digested and small portions of polymeric compounds with varying molecular weight are present. κ-carrageenase also released significant amounts of κ-carrageenan-derived oligosaccharides and low molecular weight compounds. Furthermore, the κ-carrageenase digestion resulted in a slight shift of the IC3 peak to higher retention times in the HPSEC-RI chromatogram. The underlying, relatively minor reduction in molecular weight suggested that consecutive κ-units are present in rather small blocks. The broad molecular weight distribution after ι-carrageenase hydrolysis could be caused by some long κ-chains, small alternating blocks of κ- and ι-units or some longer carrageenan chains with alternating κ- and ι-units. Nevertheless, the combination of the results indicated that IC3 is largely composed of a ι/κ hybrid carrageenan which mainly contains long blocks of consecutive ι-units and comparably small blocks of consecutive κ-units.

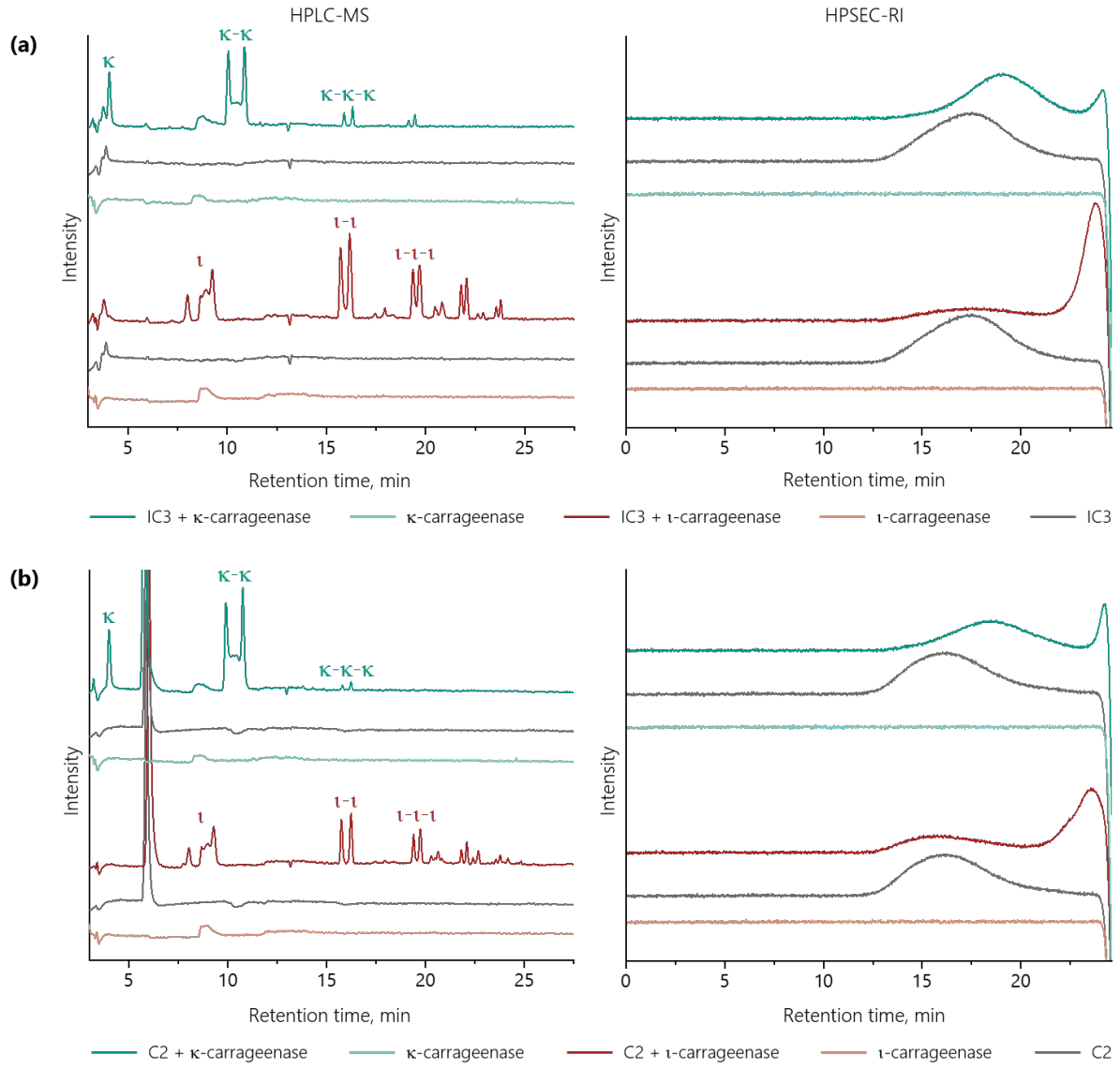

Figure 2.2. *Chromatograms from HPLC–MS and HPSEC-RI analysis of IC3 (a) and C2 (b) after partial enzymatic hydrolysis with κ- and ι-carrageenase. The chromatograms of the untreated carrageenans and the enzyme solutions are shown for comparison. The letters κ and ι are used as descriptors for the corresponding disaccharide repeating unit.*

Comparable elution profiles were obtained for sample C2 (NMR: 59% κ-units, 41% ι-units, Fig. 2.2b). However, the intensities of the peaks corresponding to oligomeric ι-units, low molecular weight products after ι-carrageenase digestion, and polymeric compounds after κ-carrageenase digestion were lower than for IC3. In contrast, higher intensities were observed for the peaks corresponding to oligo- and polymeric products derived from κ-units. This is most likely a result of the higher portion of κ-units in C2 compared to IC3. Therefore, the results from the enzymatic hydrolysis showed that C2 is largely composed of a κ/ι hybrid carrageenan with rather long blocks of ι-units and comparably short blocks of κ-units.

For sample LC2 (NMR: 72% of κ-units, 28% of ι-units), significant amounts of κ-oligosaccharides and a clear molecular weight reduction were detected after incubation with κ-carrageenase (Fig. 2.3). In contrast, ι-carrageenase did not have a significant impact on the HPSEC-RI chromatogram (only traces of low molecular weight compounds) and only small amounts of ι-carrageenan oligosaccharides were liberated. This indicates that LC2 is composed of long blocks of κ-units, whereas a major part of the ι-units is most likely present in smaller sections or as single residues. This is also supported by additional oligosaccharides present in the chromatogram of the κ-carrageenase hydrolysate (eluting between 17.9 and 22.3 min) which could be derived from κ-oligosaccharides with single ι-units (mass spectra are shown in Fig. A1.5). Although the presence of small portions of isolated κ or ι chains cannot be completely excluded, LC2 is mainly composed of a κ-/ι-hybrid carrageenan with long blocks of consecutive κ-units and small sections with ι-units.

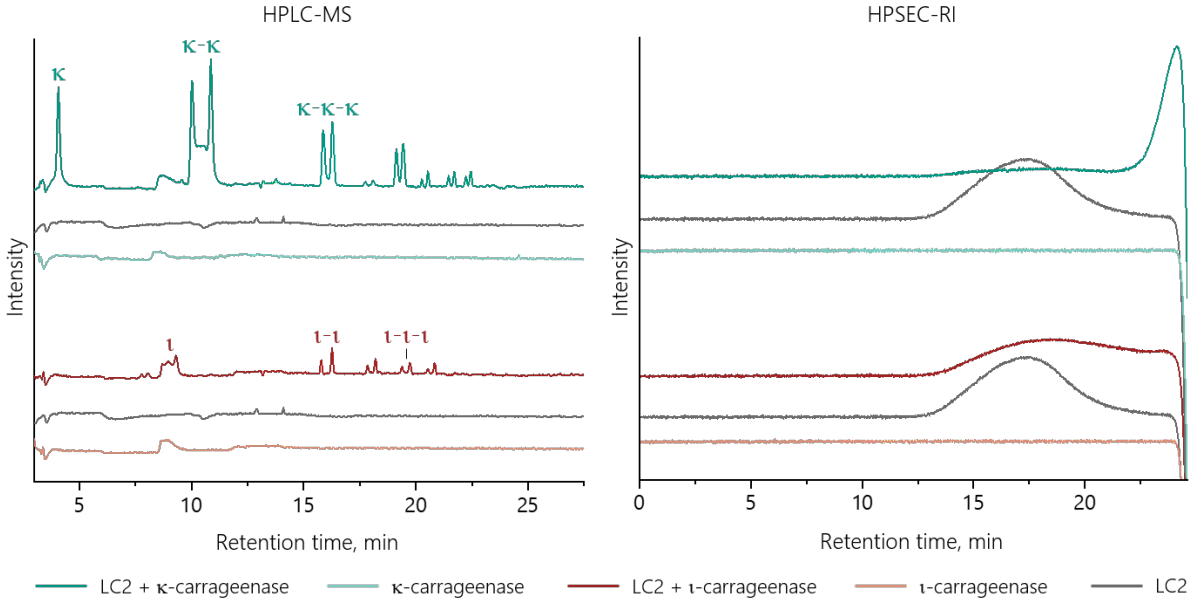

Figure 2.3. *Chromatograms from HPLC–MS and HPSEC-RI analysis of LC2 after partial enzymatic hydrolysis with κ- and ι-carrageenase. The chromatograms of the untreated carrageenans and the enzyme solutions are shown for comparison. The letters κ and ι are used as descriptors for the corresponding disaccharide repeating unit.*

The carrageenan samples LC1 (NMR: 47% κ-units, 31% ι-units, 22% ν-units) and C1 (NMR: 37% κ-units, 33% ι-units, 30% ν-units) showed comparable HPLC–MS and HPSEC–RI elution profiles (Fig. 3.4): Only κ-oligosaccharides were released and only κ-carrageenase resulted in a formation of low molecular weight compounds, while ι-carrageenase only resulted in a slight change of the HPSEC–RI elution profile. The variation in the intensity of oligosaccharides and low molecular weight compounds after κ-carrageenase digestion can be well explained by the higher portion of κ-units in LC1. The undigested residue after κ-carrageenase hydrolysis may

result from some complex carrageenan chains, which contain small blocks of κ-units and/or longer blocks of ι-, and ν-units. However, the results suggested that LC1 and C1 are hybrid carrageenans with long blocks of κ-units, which are intercepted by short blocks of ι- and ν-units. This observation is also supported by the presence of an additional oligosaccharide in the κ-carrageenase hydrolysate (eluting at 17.9 min, for mass spectra see Fig. A1.6 and A1.7).

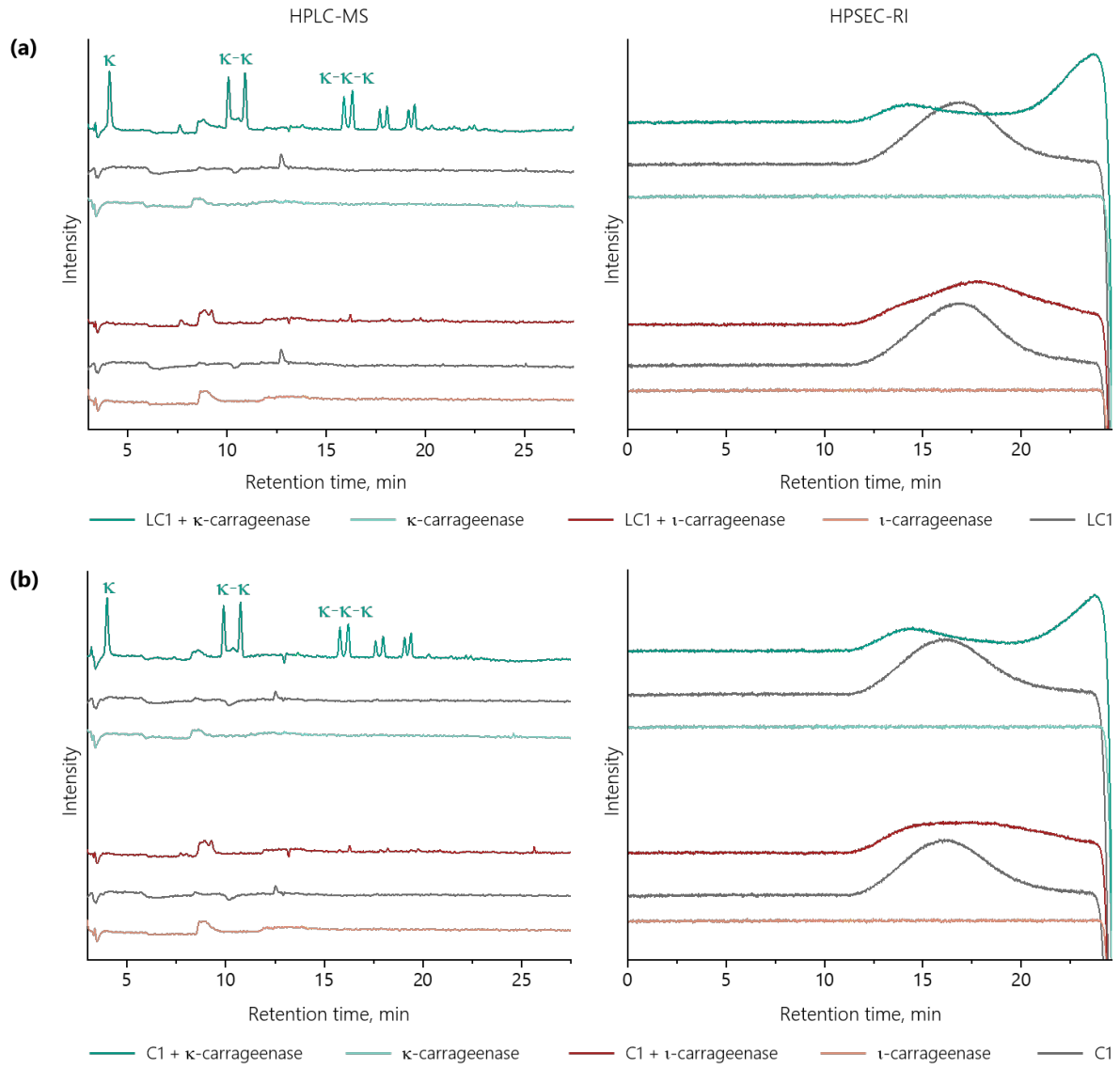

Figure 2.4. *Chromatograms from HPLC–MS and HPSEC-RI analysis of LC1 (a) and C1 (b) after partial enzymatic hydrolysis with κ- and ι-carrageenase. The chromatograms of the untreated carrageenans and the enzyme solutions are shown for comparison. The letters κ and ι are used as descriptors for the corresponding disaccharide repeating unit.*

Altogether, the chromatographic analysis after hydrolysis with selective carrageenases confirmed the structural heterogeneity of commercial carrageenans and revealed differences and similarities between the investigated samples. The results demonstrate that the developed approach can be used to obtain detailed information on the structural composition of carrageenans

and is thus well-suited to complement existing methods. To gain further insights into potential variations in the functional properties of the individual polysaccharides, the rheological properties of the five carrageenans were analyzed and compared to KC1 and IC1.

2.4.4 Rheological Characterization

The rheological characterization aims to establish a connection between the structural composition of the commercial carrageenan samples and their functional properties. Given that gel formation is the most relevant functional property for industrial applications, this aspect was investigated. Unfortunately, the definition of a gel is not uniform across different scientific fields. As a result, there is no universally accepted gel definition. According to Guenet [359], a gel must fulfill two key characteristics: It must consist of a continuous network of connected fibers or other structures and the formation or melting of a thermoreversible gel must occur through a first-order transition. Picout and Ross-Murphy proposed another definition of a gel focusing on the rheological properties [360,361]. Following their definition, a substance can be stated as a gel if the storage modulus G' is consistently greater than the loss modulus G''. Furthermore, both moduli G' and G'' exhibit near-parallel behavior across a broad range of frequencies. The storage modulus G' defines the elastic properties of the material. It reflects the mechanical energy stored inside the sample during deformation. In contrast, the loss modulus G'' characterizes the viscous behavior of the material and represents the energy dissipated during flow under shear stress. For characterizing elastic materials, the loss factor tan δ is a commonly used parameter. It is defined as the ratio of the loss modulus G'' to the storage modulus G' (Eq. 2.1).

Equation 2.1. Definition of the loss factor tan δ.

$$tan\delta = \frac{Loss\ modulus\ G''}{Storage\ modulus\ G'} \tag{2.1}$$

Where: $tan\delta = Loss\ factor$
$G' = Storage\ modulus$
$G'' = Loss\ modulus$

Due to the well-known ability of κ- and ι-carrageenan to form gels when specific ions such as calcium ions are present, a simplified gel definition is used in this study. When the storage modulus G' is clearly greater than the loss modulus G'' over the respective frequency range, a gel is considered to be present.

To characterize the rheological behavior of carrageenan in water, the seven selected commercial carrageenans (KC1, IC1, IC3, C1, C2, LC1, LC2) were first subjected to rheological measurements without $CaCl_2$ addition. Following sample preparation, it was evident that no gelation occurred, and that the samples remained highly fluid. Consistent with this observation, the measured storage moduli G' were correspondingly low remaining below 1 Pa (Fig. A1.8). The lack of data points at higher frequencies, particularly for sample LC2 and IC3, can be attributed to the inability to measure such an excessively low storage modulus. All values of the loss modulus G'' exhibit a linear increase with increasing frequency, consistently falling in a range of 0.01 to 1 Pa. In addition, all G'' values exceed their corresponding values of the storage modulus. Consequently, the loss factors tan δ for all samples exceeded 1 in all cases (Fig. 2.5). Therefore, it can be concluded that gel formation in the absence of salt does not take place, the different samples show predominant viscous behavior, and the rheological properties of the various solutions exhibit no significant differences despite their varying structural composition. These observations are valid for the applied test conditions. However, gelation might occur at lower temperatures or higher carrageenan concentrations.

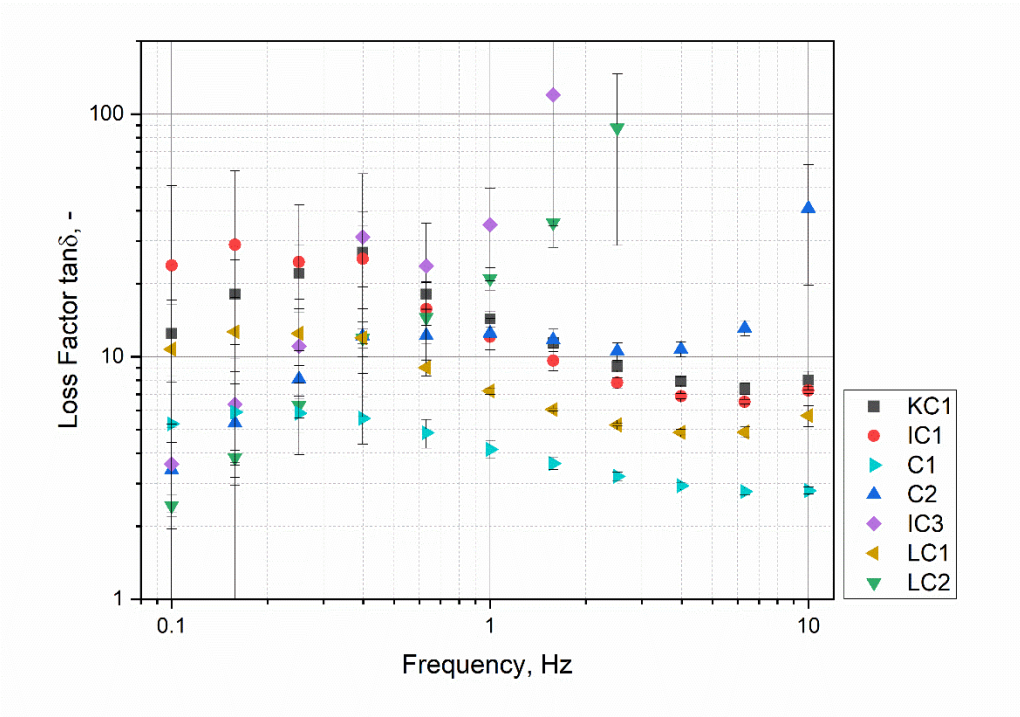

Figure 2.5. *Loss factors tan δ of the selected commercial carrageenans measured in water. The frequency sweep ranged from 0.1 to 10 Hz with a strain amplitude γ of 2%.*

The addition of $CaCl_2$ to a final concentration of 0.1 M alters the rheological properties of the carrageenan solutions. This is evident in the results of the rheological measurements shown in

Fig. 2.6. The storage modulus G' showed a tremendous increase for all samples and remained at a constant level, except for samples C1 and LC1 (Fig. 2.6c). The pure κ-carrageenan (KC1) exhibited the highest storage modulus and maintained a constant value above 100 Pa, while samples C1 and LC1 retained values of G' below 1 Pa over the frequency range of 0.1 to 10 Hz. Even with the addition of $CaCl_2$, those samples remained highly fluid, which made it difficult to obtain precise measurements with the plate-plate measurement geometry. Therefore, the data of samples C1 and LC1 exhibit high standard deviations and occasionally, measurements with a storage modulus of 0 Pa were observed. The values of the storage modulus G' for the remaining samples IC1, IC3 and C2 were approximately around 10 Pa.

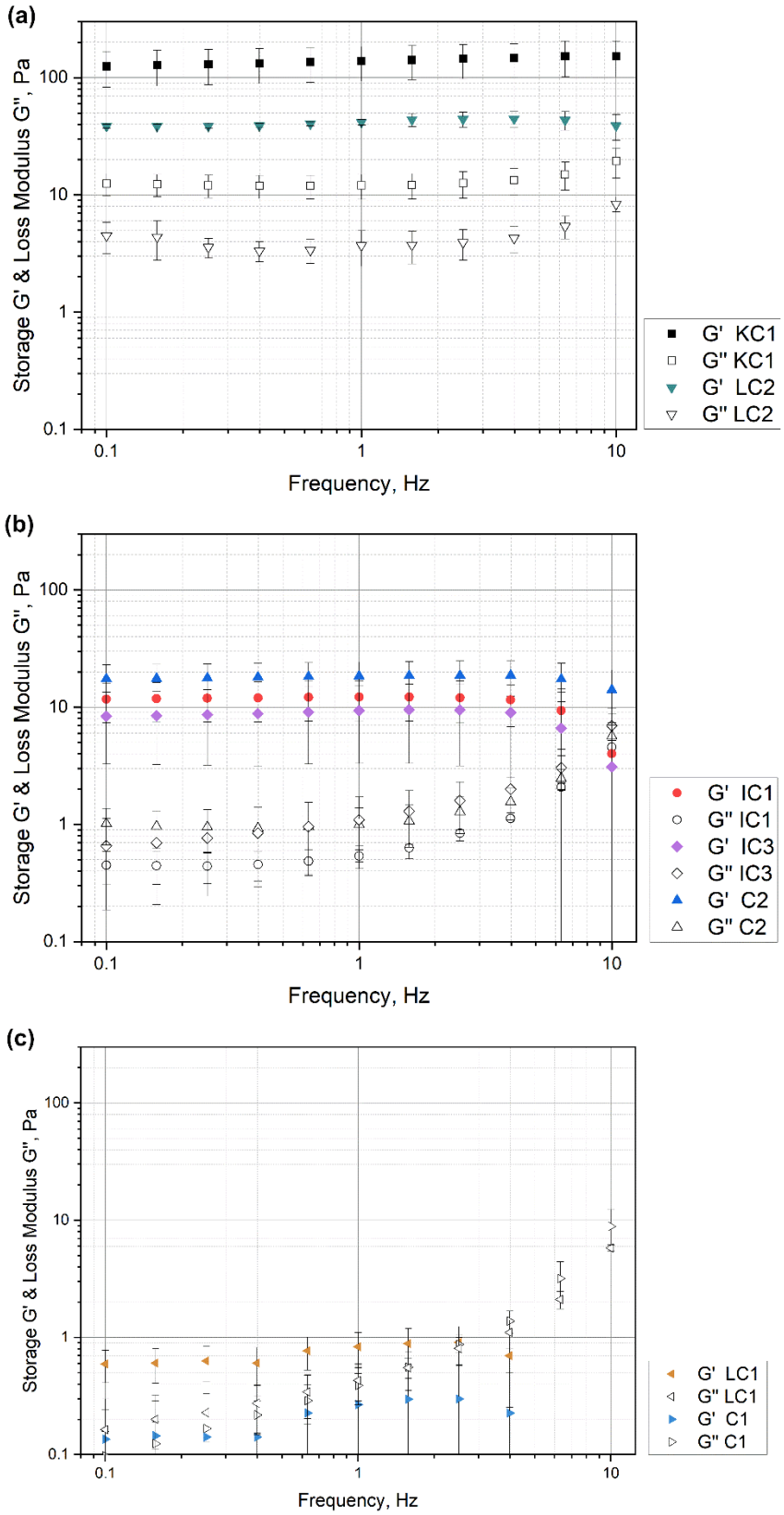

Figure 2.6. *Storage and loss moduli G' and G'' of the seven commercial carrageenan samples in 0.1 M CaCl2 solution measured at a frequency range between 0.1 and 10 Hz and an amplitude γ of 2%. Graph (a) displays the results for the samples KC1 and LC2, graph (b) presents the finding for samples IC1, IC3 and C2, and graph (c) shows the data for samples LC1 and C1.*

In addition to the storage modulus G′, Fig. 2.6 also illustrates the values of the corresponding loss modulus G″. Samples KC1 and LC2 exhibited a constant loss modulus between 1 and 10 Pa over the measured frequency range from 0.1 to 10 Hz. Furthermore, the values for samples IC1, IC3 and C2 were slightly lower than those of KC1 and LC2. The loss modulus exhibited a constant behavior up to a frequency of 1 Hz. Beyond this frequency, the values of the loss modulus G'' experienced a serious increase for all three samples. The samples LC1 and C1 showed even lower loss modulus values, starting around 0.2 Pa, which then increased tremendously during the measurement. In comparison to the storage modulus G', the loss modulus values were generally lower, except for samples LC1 and C1.

Consequently, the loss factor tan δ for KC1, LC2, IC1, IC3 and C2 were generally below 1. This observation holds true only up to a frequency of 1 Hz for IC1, IC3 and C2 (Fig. A1.10). Due to the inaccurate measurements of the storage modulus for sample C1, it was not feasible to derive reliable loss factors for this sample. Therefore, C1 is not shown in Fig. A1.10.

Based on these findings, the samples KC1, LC2, IC1, IC3 and C2 formed gels in presence of 0.1 M $CaCl_2$. Unlike the other samples, LC1 and C1 retained their liquid state and did not form gels. Both samples contained ν-units and $CaCl_2$ addition only had a minor influence on their rheological properties. These results indicate that the presence of ν-units in κ/ι hybrid carrageenans, and thus the partial substitution of 3,6-anhydrogalactose with disulfated galactose, has a negative effect on gelation and the development of a gel-like character upon $CaCl_2$ addition. This is in good agreement with data on ι/ν hybrid carrageenans and the observation that D-units do not adopt a helical conformation which is crucial for gel formation [280,359]. Van de Velde demonstrated that ι-carrageenan loses its ability to form gels when the content of ν-units exceeds 20 mol% [336]. This observation seems to apply also to κ/ι/ν hybrid carrageenans, as a ν-units content of 22 mol% was already sufficient to prevent gel formation. Due to the absence of samples with lower content of ν-units, it remains unclear whether κ/ι hybrid carrageenans exhibit even greater sensitivity to the presence of ν-units than ι-carrageenan.

In addition, more information upon the rheological behavior of the formed gel can be drawn from Fig. 2.6. The magnitude of the storage modulus G' serves as indicator for the strength of the gel network. Sample KC1 containing pure κ-carrageenan exhibited the highest storage modulus values and consequently formed the most stable gel. The proportion of κ-units appears to influence the magnitude of the storage modulus G'. With increasing content of structural components of the κ-type of carrageenan (IC3 < C2 < LC2 < KC1), the storage modulus increased

(Fig. 2.7). This finding aligns with the data reported by Bui et al. [274], where the storage modulus of mixed κ-ι-carrageenan gels is mainly dependent on the portion of κ-carrageenan. Our data demonstrate that commercial hybrid carrageenans exhibit a similar behavior.

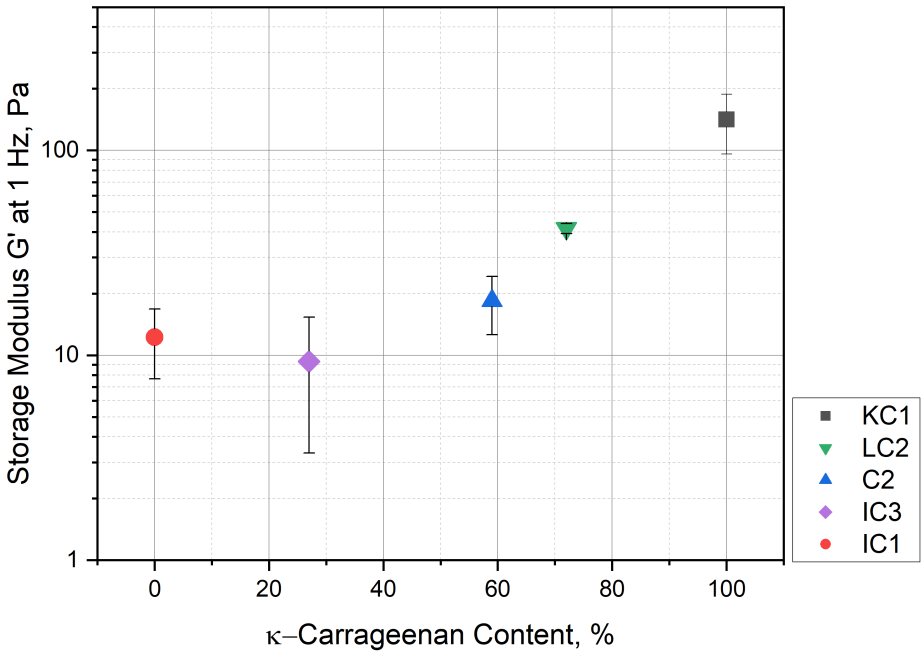

Figure 2.7. *Relationship between the storage modulus G' measured at a frequency of 1 Hz and the κ-carrageen content.*

Visual examination of the samples confirmed that KC1 produced the most stable gel upon $CaCl_2$ addition. None of the other samples formed a cohesive and self-supporting gel. Additionally, the combined plot of the storage modulus G' and loss modulus G'' in Fig. 2.6 allows an estimation of the gel point. The point where the storage modulus G' and the loss modulus G'' intersect defines the gel point and marks the transition of the sample's behavior from solid-like to liquid-like. The gel structure can no longer withstand the energy input from the measurement at this critical frequency resulting in the rupture of the gel. This intersection of G' and G'' for samples KC1 and LC2 did not fall within the measurement range of 0.1 to 10 Hz. This further confirms the formation of stable gels in these samples. Furthermore, the gel points for the samples IC1, IC3 and C2 in Fig. 2.6b were clustered around a frequency of 10 Hz. While the gel points of IC1 and IC3 were indistinguishable, sample C2, with a slightly higher content of κ-units of 59%, exhibited a gel point slightly above 10 Hz. The absence of gel formation in the samples LC1 and C1 eliminates the possibility of a gel point for these samples. Therefore, the gel point's position also supports the correlation between the κ-unit content and the gel properties.

Altogether, the results from the rheological characterization clearly demonstrate that the selected commercial carrageenans not only show heterogeneity in their structural, but also their functional properties. All analyzed hybrid carrageenans showed gelling behavior, except for samples LC1 and C1, which both contain ν-units. Therefore, the gel forming capability of hybrid carrageenans depended on the portion of κ- and the presence of ν-units.

2.5 Conclusion

Our results demonstrate that commercially available carrageenans show significant variation with regard to the structure of the polysaccharides as well as with regard to the cations in the carrageenan samples. Furthermore, the carrageenan type specified by the manufacturers is not always in agreement with the actual molecular structure. Furthermore, our results suggested that the investigated λ-carrageenans, as well as one ι-carrageenan and two unspecified carrageenans, were actually hybrid carrageenans with κ-, ι-, and (in part) ν-units. Therefore, a detailed structural characterization is essential when carrageenans are purchased to investigate structure function relationships. Otherwise, the properties cannot be related to specific structural elements and false conclusion might be drawn about the physiological and technological effects of carrageenans. This was further supported by the rheological characterization. In absence of calcium ions, no gelation was observed. In contrast, the addition of $CaCl_2$ at a final concentration of 0.1 M induced gel formation in all samples, except of samples LC1 and C1. The formed gels displayed considerable variations in their characteristics. It was shown that the proportion of κ-units in the hybrid carrageenans corresponds to the value of the storage modulus G' and the location of the gel point, suggesting that the content of κ-units is a key factor for gel formation. Moreover, the presence of ν-units seems to hinder gelation of κ/ι hybrid carrageenans upon $CaCl_2$ addition. The findings of this study emphasize that future studies should focus on an analysis of the properties of well-defined carrageenans. The samples characterized in this study as well as the characterization of carrageenans after partial enzymatic hydrolysis are well suited for this purpose.

3 Ice Recrystallization Inhibition Activity of Chemically Defined Carrageenans

This chapter was published as: Hale, J.; Furch, A.; Gerhäuser, J.; Gaukel, V.; Wefers, D. (2024): Ice Recrystallization Inhibition Activity of Chemically Defined Carrageenans In: Food Hydrocolloids, Volume 157, ISSN 0268-005X. doi:10.1016/j.foodhyd.2024.110423

3.1 Abstract

Carrageenans are sulfated galactans from algae which are commonly used as thickeners, gelling agents, or stabilizers. It has been demonstrated that they also have significant ice recrystallization inhibition (IRI) activity. Previous studies mainly focused on κ-carrageenan, but recent studies suggested that other carrageenans such as ι-carrageenans or carrageenans with multiple structural elements also have this functionality. Therefore, the aim of our study was to analyze and compare the IRI activity of carrageenans with defined chemical structures and associated cations. For this purpose, κ- and ι-carrageenans as well as several hybrid carrageenans showing broad heterogeneity with regards to the molecular structure and the cations present were investigated. The selected commercial samples were subsequently converted into their potassium, calcium and (in part) sodium forms. Chemical characterization of the modified carrageenans demonstrated that the molecular structure was unaltered by the applied procedures and that the carrageenans were successfully converted into the different cation forms. The analysis of the IRI activity demonstrated that both molecular structure and associated cations had an influence on carrageenan functionality. The κ-carrageenan and hybrid carrageenans with consecutive κ-units showed a high IRI activity, whereas ι-carrageenan was less active. For κ-carrageenan, the potassium form showed a clearly higher activity than the calcium form, whereas the calcium form was more active for hybrid carrageenans and ι-carrageenans. Our results significantly expand the knowledge on the relationship between the molecular composition and the IRI activity of carrageenans. Furthermore, they can be used to optimize carrageenan production to obtain an enhanced IRI activity.

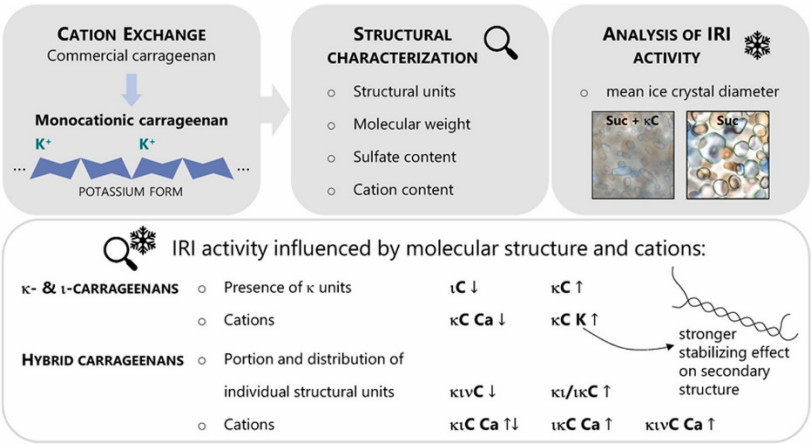

Figure 3.1. *Graphical abstract.*

3.2 Introduction

Carrageenans are sulfated galactans which are extracted from red algae [34]. These polysaccharides consist of alternating 1,3-linked β-D-galactopyranose units (G-unit) and 1,4-linked α-D-galactopyranose units (D-unit). The D-unit may also be present as 3,6-anhydro-α-D-galactopyranose, which is then referred to as DA-unit. Both the G-unit as well as the D/DA-unit can be sulfated at different positions [35,280]. Depending on the structural composition of the polysaccharide, the sulfate content usually varies between 22 and 38% (w/w) [34].

To describe the chemical structure of carrageenans, Knutsen, Myslabodski, Larsen, and Usov [255] proposed a nomenclature including the descriptor for the monosaccharide unit and the position of the sulfate group in combination with the letter S. According to this nomenclature, a 1,3-linked β-D-galactopyranose that is sulfated at position *O*-4 is for example named 'G4S' [255]. Moreover, the structures of carrageenans are often described by using repeating disaccharide motifs (consisting of one G-unit and one D-/DA-unit). Depending on the disaccharide unit present, carrageenans are categorized into different types, which are abbreviated with Greek letters. The commercially most important types are κ-carrageenan (G4S-DA), ι-carrageenan (G4S-DA2S), and λ-carrageenan (G2S-D2S,6S) [35,280]. Carrageenans containing a D-unit instead of a DA-unit (e. g. λ-carrageenan, ν-carrageenan, μ-carrageenan) are often referred to as natural precursors. The conversion into the DA-unit typically occurs under alkaline conditions or by the use of enzymes. For example, ν-carrageenan (G4S-D2S,6S) can be converted into ι-carrageenan (G4S-DA2S) [35].

Categorizing carrageenans into different types can be challenging because one sample can contain more than one type of disaccharide unit. When multiple units are present within one polymer chain, the corresponding carrageenans are referred to as hybrid carrageenans. However, it is also possible that mixtures are present, which contain multiple non-covalently linked carrageenans [36]. Accordingly, carrageenans show highly heterogeneous chemical structures that determine the physicochemical properties of the polysaccharides.

It has been demonstrated that different carrageenans have a significant ice recrystallization inhibition (IRI) activity. While κ-carrageenan showed a strong IRI activity in all studies, the results for ι-carrageenan were somewhat ambiguous [25,38,41–44,362]. However, commercial carrageenans were used in previous studies and a structural characterization has not been conducted in all cases. An analysis of IRI activity of carrageenans characterized by NMR spectroscopy suggested that ι-carrageenan exhibited a lower IRI activity than κ-carrageenan. Furthermore, carrageenans with different structural units (κ, ι and, in part, ν) showed different levels

of IRI activity [38]. However, NMR spectroscopy cannot distinguish between carrageenan mixtures and hybrid carrageenans. In a previous study, we demonstrated that commercial carrageenans show considerable structural heterogeneity and that carrageenan types specified by the manufacturer do not necessarily reflect the actual structural composition [363]. Several samples specified as λ-carrageenans were actually κ-ι or κ-ι-ν hybrid carrageenans. Our investigation also revealed that commercial carrageenans contain different types of cations. Different types of monovalent and divalent cations are known to influence aggregation of carrageenan chains in solution which may also impact the interaction with the ice crystal surface [42,245,261,263,363,364] already demonstrated that the addition of different salts influences the IRI activity of κ-carrageenan. Therefore, it is highly likely that cations which are already present in carrageenans influence carrageenan functionality as well. However, this aspect has not been investigated yet.

Altogether, the IRI activity of carrageenans is well established but its dependence on the molecular structure and the cations present in carrageenans is poorly understood. Therefore, the aim of our study was to produce chemically defined carrageenans and investigate them for their IRI activity. For this purpose, we used commercial carrageenans which were previously characterized in detail and converted them into their monocationic forms.

3.3 Experimental

3.3.1 Materials

The carrageenans used in this study were obtained from various manufacturers, including food and chemical suppliers (Eurogum (Denmark), CP Kelco (USA), Tate & Lyle (United Kingdom), Merck (Germany), Alfa Aesar (USA), Biosynth (Switzerland), and Dextra Laboratories (United Kingdom)). From a total of 16 samples, seven carrageenans were selected for the preparation of monocationic forms and an analysis of IRI activity. The chemical structure of the selected carrageenans was investigated in detail in a previous study [363]. Calcium chloride dihydrate (≥99%), sodium hydroxide (≥99%), dimethyl sulfoxide (≥99.5%), and sucrose (≥99.5%) were purchased from Carl Roth (Germany). Hydrochloric acid (37%) and isopropanol were obtained from VWR International (Germany). Deuterium oxide (≥99.9% D) was obtained from Deutero (Germany). All other chemicals were purchased from Merck (Germany). If necessary, Milli-Q water was used for the experiments.

3.3.2 Cation Exchange and Chemical Modification

The monocationic carrageenans were prepared as described by Polowsky and Janaswamy [365]. Briefly, 400 mg of carrageenan were dissolved in 150 mL of 800 mM sodium chloride, 800 mM potassium chloride, or 100 mM calcium chloride. The solution was treated in a water bath at a temperature of 80 °C for 2 h. The polysaccharide was then precipitated with two volumes of cold isopropanol (0 °C). The precipitate was washed with 80% and 100% isopropanol, and dried at a temperature of 50 °C.

To convert ν-units into ι-units, 250 mg of carrageenan were mixed with 125 mL of a 1 M sodium hydroxide solution. The sample was treated in a water bath at a temperature of 80 °C for 35 min [366,367]. The solution was then cooled to room temperature in an ice bath and neutralized with 1 M hydrochloric acid. After neutralization, the volume of the solution was reduced to 100 mL by rotary evaporation. To remove excess salt, the sample solution was dialyzed for 20 h against Milli-Q water (dialysis solution was changed twice). Finally, the sample was freeze-dried. By using sodium hydroxide for the structural modification, the sodium form of the modified carrageenan was obtained. In order to prepare other monocationic forms of the modified carrageenan, the sample was subjected to the cation exchange process described above.

3.3.3 NMR Spectroscopy

NMR experiments were carried out on an Avance Neo 400 MHz spectrometer (Bruker, Germany) equipped with a temperature-controlled 5 mm probe head. The spectra were recorded at a temperature of 65 °C. A standard ^{1}H pulse program (‘zg90’) from Bruker was used with a relaxation delay (d_1) of 25 s and an acquisition time of 2 s. The number of scans was either 16 or 32. For sample preparation, 5 mg of carrageenan were mixed with 1 mL of deuterium oxide and treated in a water bath at 70 °C until the polysaccharide was completely dissolved. Dimethyl sulfoxide (0.5 µL) was used as an internal reference (2.696 ppm according to Van de Velde, Pereira, and Rollema [350]). The structural units of the different carrageenan types can be identified by the signals of the anomeric protons of the D-/DA-unit [350].

3.3.4 HPSEC-RI/MALLS

An HPSEC-RI/MALLS system was used to determine the weight average molecular weight (M_W) of the carrageenans. The system was equipped with a refractive index detector (L-7490, Hitachi, Merck, Germany) and a multi angle laser light scattering (MALLS) detector

(SLD7100, PSS Polymer Standards Service, Germany). The polymers were separated on a TSKgel G6000PW$_{XL}$ column (Tosoh Bioscience, Japan) at 60 °C. As described by Lecacheux, Panaras, Brigand, and Martin [351], 0.1 M lithium chloride was used as the eluent to suppress aggregation of the carrageenans. The analysis was conducted at an isocratic flow rate of 0.5 mL/min. To calculate the M_W of the carrageenans, a refractive index increment of 0.115 g/mL was used [351]. For sample preparation, 2 mg of carrageenan were mixed with 1 mL of 0.1 M lithium chloride and treated in a water bath at a temperature of 60 °C until complete dissolution of the sample.

3.3.5 ICP-OES

For the analysis of associated cations and sulfur, a Varian 715-ES (Agilent Technologies, USA) or an iCAP 7000 instrument (Thermo Fisher Scientific, USA) was used. The external calibration covered a range from 0.25 to 50 mg/L and was prepared using standard solutions of potassium, sodium, calcium and sulfur. For ICP-OES analysis, carrageenan solutions with a concentration of 1 mg/mL were used. The solutions were prepared in 1% (v/v) nitric acid and had a total volume of 10 mL.

3.3.6 Ice Recrystallization Inhibition Activity

The IRI activity of the carrageenan samples was determined in a 49% (w/w) sucrose solution to which 1 mg/mL carrageenan was added. For sample preparation, sucrose, carrageenan and Milli-Q water were weighed and mixed. The solution was treated in a water bath at a temperature of 60 °C until complete dissolution of the samples (1–2 h). As a control, 49% (w/w) sucrose solution without the addition of carrageenan was used. 10 µL of the sample solution were placed on a microscopic slide between two cover slips that had been previously glued to the slide at a distance of 8–10 mm. The sample was covered with a third cover slip and the edges were then sealed with silicone to prevent the solution from evaporating. After drying of the silicone, the microscopic slides were rapidly frozen in liquid nitrogen to ensure that the sample solution reached a glassy state. The samples were stored for 72 h in three small cooling chambers at a temperature of −12.0 °C ± 0.1 °C. The temperature of the cooling chambers was controlled by an external cryostat (FP50, Julabo, Germany). The three cooling chambers were placed inside a glove box, which maintained a temperature of −12.0 °C ± 1.0 °C. Over storage time, the temperatures of the cooling chambers and the glove box were recorded by thermocouples.

Microscopic images of each sample were taken with a polarizing microscope (BX41, Olympus, Japan) equipped with a camera (Mikrocam II 5 MP HIS, Bresser, Germany). To determine the

mean ice crystal diameter of a sample, the area of at least 200 ice crystals per microscopic slide was manually analyzed using either ImagePro 9.3 (Media Cybernetics, USA) or ImageJ (National Institutes of Health (NIH), USA) software. The equivalent diameter of each ice crystal was determined by calculating the diameter of a circle with the same area. Based on the equivalent diameters of the individual crystals, the mean ice crystal equivalent diameter of the sample was calculated. Four microscopic slides were prepared for each carrageenan and the mean ice crystal diameter was derived from the mean equivalent diameters of the four slides.

3.4 Results and Discussion

3.4.1 Production of Chemically Defined, Monocationic Carrageenans

Based on the detailed structural and compositional characterization of commercial carrageenans [363], 7 samples were selected for the production of chemically defined carrageenans. These samples were selected because they show a high structural diversity and are thus well-suited for an evaluation of structure-function relationships. The selected carrageenans included a κ- and ι-carrageenan (previously KC1 and IC1, subsequently referred to as κC and ιC) and five carrageenans with different structural units. In our previous study, NMR spectroscopy and partial enzymatic hydrolysis suggested that two carrageenans (IC3 and C2) were ι/κ and κ/ι hybrid carrageenans which are mainly composed of consecutive blocks of ι- and κ-units. These samples will be referred to as ικC (IC3) and κιC1 (C2). In contrast, the κ-/ι-carrageenan κιC2 (previously LC2) contains long blocks of κ-units and only single ι-units or very small sections thereof. The carrageenans LC1 and C1 were hybrid carrageenans with long blocks of κ-units and small blocks of ι- and ν-units. Therefore, these samples will be referred to as κινC1 and κινC2. In our previous study, we also demonstrated that the commercial carrageenans show significant variation of the associated cations (potassium, calcium, and sodium) [363]. As described above, this may significantly influence IRI activity, thus, monocationic carrageenans were produced. The focus was on potassium and calcium because these cations are most common in carrageenans due to the manufacturing process. However, the κ- and ι-carrageenan samples κC and ιC as well as two hybrid carrageenans (κινC1 and κιC2) were also converted to their sodium form and analyzed for their IRI activity. In addition, κινC1 was also subjected to alkaline treatment to convert ν-units to ι-units (sodium and potassium form). By comparing the IRI activity before and after conversion, the influence of ν-units can be evaluated. The structural composition of all carrageenans was fully characterized to exclude significant changes which could affect the IRI activity.

3.4.2 Characterization of the Chemically Defined, Monocationic Carrageenans

Structural Composition

To evaluate if the molecular structure of the carrageenans was modified, ^{1}H NMR spectroscopy was applied (Table 3.1).

Table 3.1. *Structural composition of the carrageenans used in this study before and after cation exchange and alkaline modification (κινC1m). The characteristic signals of the D-/DA-units were assigned according to Van de Velde et al. [350] and signal integrals were used to calculate the portions of the individual structural elements. NMR spectra are shown in Fig. A2.1.*

Sample	Structural unit (portion, %)	Sample	Structural unit (portion, %)
κC	κ	κιC2	κ (72), ι (28)
κC K	κ	κιC2 K	κ (67), ι (33)
κC Na	κ	κιC2 Na	κ (68), ι (32)
κC Ca	κ	κιC2 Ca	κ (67), ι (33)
ιC	ι	κινC1	κ (47), ι (31), ν (22)
ιC K	ι	κινC1 K	κ (51), ι (29), ν (20)
ιC Na	ι	κινC1 Na	κ (47), ι (32), ν (21)
ιC Ca	ι	κινC1 Ca	κ (46), ι (30), ν (23)
ικC	κ (27), ι (73)	κινC1 m K	κ (53), ι (47)
ικC K	κ (27), ι (73)	κινC1 m Na	κ (52), ι (48)
ικC Ca	κ (25), ι (75)	κινC2	κ (37), ι (33), ν (30)
κιC1	κ (59), ι (41)	κινC2 K	κ (37), ι (34), ν (29)
κιC1 K	κ (42), ι (58)	κινC2 Ca	κ (38), ι (32), ν (30)
κιC1 Ca	κ (40), ι (60)	-	-

For all carrageenan samples except κιC1, the same structural elements were detected in similar portions before and after modification. Minor variations could be derived from inaccuracies during the integration of the diagnostic NMR signals. Therefore, the cation exchange does not lead to a structural modification. However, the potassium and calcium forms of κιC1 showed 42%/40% κ-units and 58%/60% ι-units and thus a clearly different structural composition than the unmodified carrageenan (59% κ-units and 41% ι-units). This variation is caused by the presence of sucrose (added for standardization by the manufacturer) in the unmodified carrageenan: The sucrose-derived signal at 5.40 ppm interferes with the integration of the signal derived from the DA-unit of the ι-units at 5.28 ppm. Sucrose is removed during the precipitation

step of the cation-exchange, thus, the results obtained for the monocationic carrageenans better reflect the structural composition of κιC1. For the modified versions of κινC1 (κινC1m), ν-units were not detected which confirms the successful modification.

Molecular Weight

To investigate if the carrageenans were partially hydrolyzed during the treatment with strong salt solutions or NaOH, the molecular weight was analyzed by HPSEC-RI/MALLS (Table 3.2).

Table 3.2. *Molecular weight (determined by HPSEC-RI/MALLS) of the carrageenans used in this study before and after cation exchange and alkaline modification (κινC1m). Chromatograms of the individual carrageenans are shown in Fig. A2.2.*

Sample	**M_W, kDa**	**Sample**	**M_W, kDa**
κC	1013 ± 35	κιC2	641 ± 8
κC K	919 ± 8	κιC2 K	639 ± 15
κC Na	901 ± 42	κιC2 Na	613 ± 0
κC Ca	644 ± 14	κιC2 Ca	491 ± 12
ιC	999 ± 16	κινC1	923 ± 8
ιC K	924 ± 15	κινC1 K	860 ± 4
ιC Na	925 ± 91	κινC1 Na	831 ± 5
ιC Ca	838 ± 6	κινC1 Ca	868 ± 37
ικC	523 ± 61	κινC1 m K	540 ± 27
ικC K	519 ± 2	κινC1 m Na	686 ± 2
ικC Ca	514 ± 0	κινC2	1158 ± 21
κιC1	886 ± 30	κινC2 K	1068 ± 55
κιC1 K	890 ± 0	κινC2 Ca	1163 ± 14
κιC1 Ca	825 ± 16	-	-

Most of the monocationic carrageenans showed a similar molecular weight than the unmodified samples, except for the calcium forms of κC, ιC, and κιC2. However, because the molecular weights of other calcium forms were unaltered, these changes could be derived from a selective precipitation due to the different ionic environment. Because the molecular weights were still high (491–838 kDa), an influence on the IRI activity is highly unlikely: Leiter, Mailänder, et al. [43] showed that a reduction of the molecular weight of κ-carrageenan from 1420 kDa to 262 kDa did not result in a decreased IRI activity. Altogether, the results from the HPSEC analysis demonstrated that the conditions during cation exchange do not lead to significant changes

in the molecular weight of carrageenans. The alkaline conditions which were applied to remove ν-units from κινC1 led to a decreased molecular weight from 923 kDa to 540 kDa. This may be the result of degradation due to base peeling or due to some hydrolysis during the short dialysis step in the purification. However, the molecular weight is still in an acceptable range, thus, the modified samples are suitable to evaluate the influence of ν-units on IRI activity.

Sulfate Content and Associated Cations

The sulfate content as well as the type and content of cations were analyzed by ICP-OES (Table 3.3).

Table 3.3. *Contents of K+, Ca2+, Na+, and sulfate (determined by ICP-OES) of the carrageenans used in this study before and after cation exchange and alkaline modification (κινC1m). +++ = > 1 %, ++ = 0.5–1 %, + = 0.1–0.5 %, - = ≤ 0.1 %. The individual contents can be found in Table A2.2.*

Sample	K^+	Na^+	Ca^{2+}	Sulfate, % (w/w)
κC	+++	-	++	18.1
κC K	+++	-	-	16.3
κC Na	+	+++	-	20.0
κC Ca	++	-	+++	20.4
ιC	+++	-	+++	28.2
ιC K	+++	-	-	27.5
ιC Na	+	+++	-	30.2
ιC Ca	+	-	+++	26.4
ικC	+++	-	+++	21.7
ικC K	+++	-	-	26.9
ικC Ca	+	-	+++	26.0
κιC1	+++	+++	+	17.4
κιC1 K	+++	-	-	24.3
κιC1 Ca	+	-	+++	24.3
κιC2	+++	+	+++	21.9
κιC2 K	+++	-	-	18.9
κιC2 Na	+	+++	-	23.1
κιC2 Ca	++	-	+++	21.8
κινC1	++	+	+++	29.4
κινC1 K	+++	-	-	29.5
κινC1 Na	-	+++	-	30.3
κινC1 Ca	+	+	+++	27.8
κινC1 m K	+++	-	-	22.9
κινC1 m Na	-	+++	+	25.2
κινC2	+++	+++	+	28.9
κινC2 K	+++	-	-	29.2
κινC2 Ca	+	+	+++	29.9

The results confirm that the cations in the carrageenans were successfully exchanged. The potassium and sodium forms of the carrageenans almost exclusively contain this cation and only trace amounts of the respective other cations. For the calcium forms of carrageenans containing a comparably high portion of κ-units, small amounts of potassium can be detected in addition to calcium. This is most likely caused by the strong affinity of κ-units to this cation. Nevertheless, the corresponding carrageenans are clearly dominated by the presence of calcium. The sulfate contents (calculated from the sulfur contents) of the cation-exchanged carrageenans were slightly different from the unmodified carrageenans. For ικC and κιC1, a clearly higher sulfate content was observed after cation-exchange. This can be explained by the presence of sucrose and glucose in the unmodified samples. These low molecular weight compounds are added for the standardization of the carrageenans and are removed by the precipitation step during the cation exchange. For all other samples, the sulfate content was comparable or in some cases even lower than in the unmodified samples. The partially lower contents can be explained by small amounts of salt in the samples. This is also supported by a comparison of the sulfate contents from ICP-OES and the theoretical sulfate content (calculation based on the structure). However, small amounts of salt are not expected to influence the determination of the IRI activity significantly: The salt excess in the monocationic carrageenans would lead to a salt concentration of about 0.2–2.4 mM in a 1 mg/mL carrageenan solution. Leiter et al. [41] demonstrated that low concentrations of salt (0.3 mM KCl) do not significantly influence IRI activity, whereas high concentrations (30 mM KCl or 100 mM NaCl) lead to a significant increase in ice crystal diameter. Given that the salt concentration of the samples used in this study is notably lower than 30 mM, it can be assumed that the effect on IRI activity is minimal. The sodium and potassium forms of sample κνC1m contained almost exclusively the corresponding cation and showed a clearly lower sulfate content than the unmodified sample. A lower sulfate content was expected for this sample because the aim of the alkaline modification was the removal of the sulfate group at position *O*-6 of the 1,4-linked α-galactose units (part of ν-units) and the resulting formation of a 3,6-anhydrogalactose unit. Therefore, ICP-OES results also confirm the successful structural modification of κνC1.

Altogether, the selected carrageenans were successfully converted into monocationic carrageenans without an unwanted modification of the molecular structure. Therefore, they are ideal for an investigation of the relationship between structural composition and IRI activity.

3.4.3 Ice Recrystallization Inhibition Activity of Chemically Defined Carrageenans

Ice Crystal Morphology of Selected Samples

The IRI activity in the model system (see section 3.3.6) was analyzed by comparing the ice crystal morphology and mean ice crystal diameters after 4 h and 72 h in a carrageenan solution to a carrageenan-free control solution. For an initial evaluation of the effect of different cations on the IRI activity, exemplary pictures of the ice crystals obtained after 72 h in solutions prepared with the potassium, calcium, and sodium forms of κC, ιC, κινC1, and κιC2 were visually assessed (Fig. 3.2).

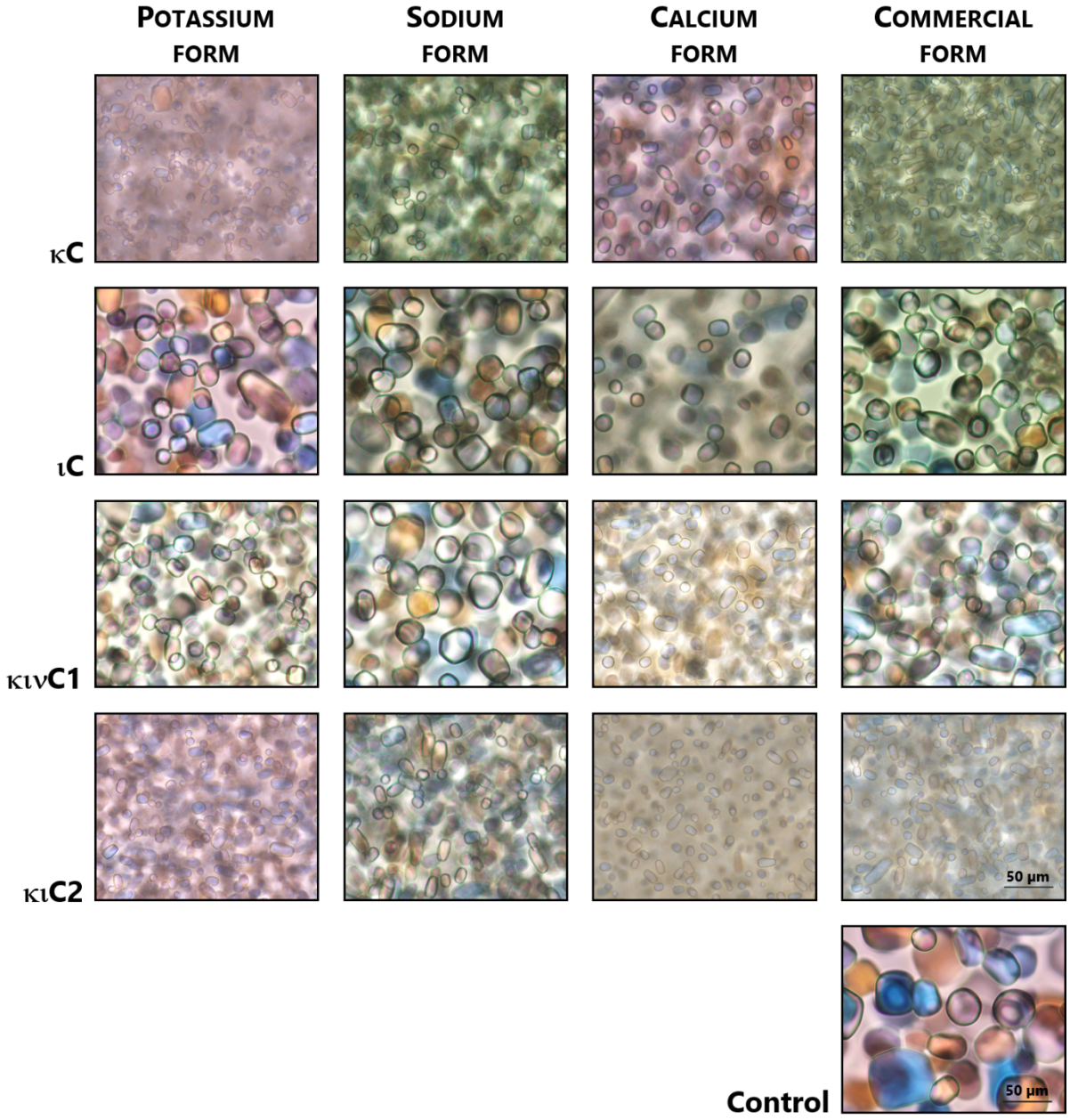

Figure 3.2. *Ice crystals grown in a 49% (w/w) sucrose solution with and without the addition of carrageenans κC, ιC, κινC1, and κιC2 in their potassium, sodium, calcium, and commercial form after storage for 72 h at −12 °C.*

The comparison of the ice crystal images to a sucrose solution without carrageenans clearly demonstrated that all carrageenans exhibited some IRI activity. However, clear variations in the ice crystal size and morphology were observed. As it would be expected for κ-carrageenan, κC led to comparably small ice crystals with the characteristic rectangular ice crystal shape. This was observed for all ionic forms, but it was most evident for the potassium form which is also the predominant form of commercial κ-carrageenans [363]. Although the sodium and calcium form showed a comparable morphology, the corresponding samples contained clearly larger ice crystals. The ice crystal images obtained for κιC2 suggest a comparably high IRI activity for all forms. In addition, a rectangular ice crystal morphology was observed, which was most noticeable for the calcium form. Therefore, this carrageenan has at least a comparable although not identical functionality than κ-carrageenan despite its clearly different molecular composition. The samples ιC and κινC1 showed rather circular ice crystals as well as a rather low IRI activity for all cation forms. Although the ice crystals obtained from the calcium form were smaller, they were still visibly larger than the ones obtained from κC and κιC2. A comparison of the monocationic carrageenans and the unmodified carrageenans showed that the cation-exchange is suitable to enhance the IRI activity of carrageenans: The ice crystal images indicated smaller ice crystals for the individual most active monocationic forms than for the unmodified carrageenans.

To assess the IRI activity in a more quantitative way, mean ice crystal diameters were determined for the monocationic carrageenans.

IRI Activity of κC and ιC

The mean ice crystal diameters of the monocationic forms of κC and ιC are shown in Fig. 3.3.

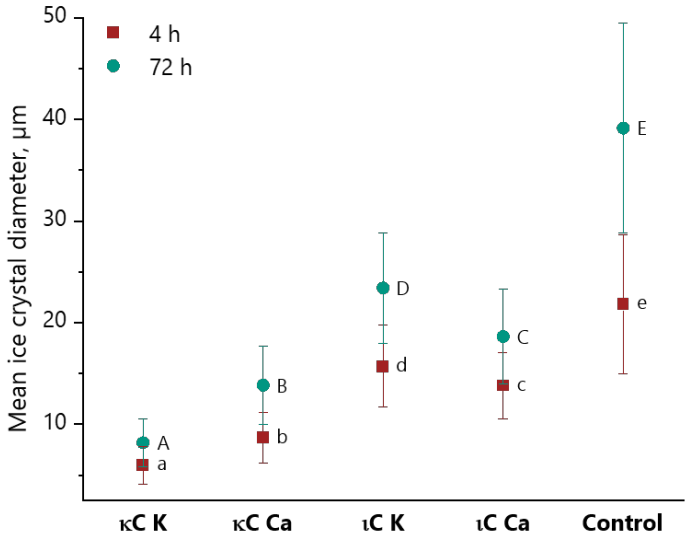

Figure 3.3. *Mean ice crystal diameter (n = 4) after 4 h and 72 h at −12 °C of a 49% sucrose solution with 1 mg/mL of the potassium and calcium forms of the κ-carrageenan κC and the ι-carrageenan ιC. The control sample refers to a sucrose solution without carrageenan addition. The statistical analysis was conducted by using one-way analysis of variance (ANOVA) with post-hoc Tukey test (α = 0.05). In case of heterogeneity of variances, Welch ANOVA was applied.*

The results clearly underline the observations made from the ice crystal images. The potassium form of κ-carrageenan κC showed the lowest mean ice crystal diameter after 72 h of storage, while the diameters observed for the potassium form of ιC were clearly higher. Exchanging potassium for calcium had a positive effect on the IRI activity of ιC, whereas larger ice crystals were observed for the calcium form of κC. However, κC still showed a significantly higher IRI activity than ιC. These results suggest that the stabilization of the helical conformation of carrageenans as well as κ structural elements are important for the IRI activity of carrageenans: Monovalent ions (especially potassium) were described to stabilize helices of κ-carrageenans [245,368], whereas calcium ions stabilize the helices of ι-carrageenans [369]. In the literature, varying IRI activities were observed for different carrageenan types: In a previous study, we found a lower IRI activity for ι-carrageenan compared to κ-carrageenan [38], while Kamińska-Dwórznicka et al. [362] described a comparable activity of the two carrageenan types. However, the structure of the carrageenans used in the second study was not analyzed. As we also demonstrated in a previous study, the structural composition of commercial carrageenans shows considerable variation depending on the source [363]. For example, ικC was declared as ι-carrageenan, although it also contains 27 % of κ structural elements. Furthermore, Kamińska-Dwórznicka et al. analyzed the IRI activity in a model food (sorbet) and not a defined model system which could also explain the different results (cations from the matrix may influence IRI activity) [362].

IRI Activity of Hybrid Carrageenans

The mean ice crystal diameters of the potassium and calcium forms of the hybrid carrageenans are shown in Fig. 3.4, comparisons of the two cation forms of all samples is shown in Fig. A2.3.

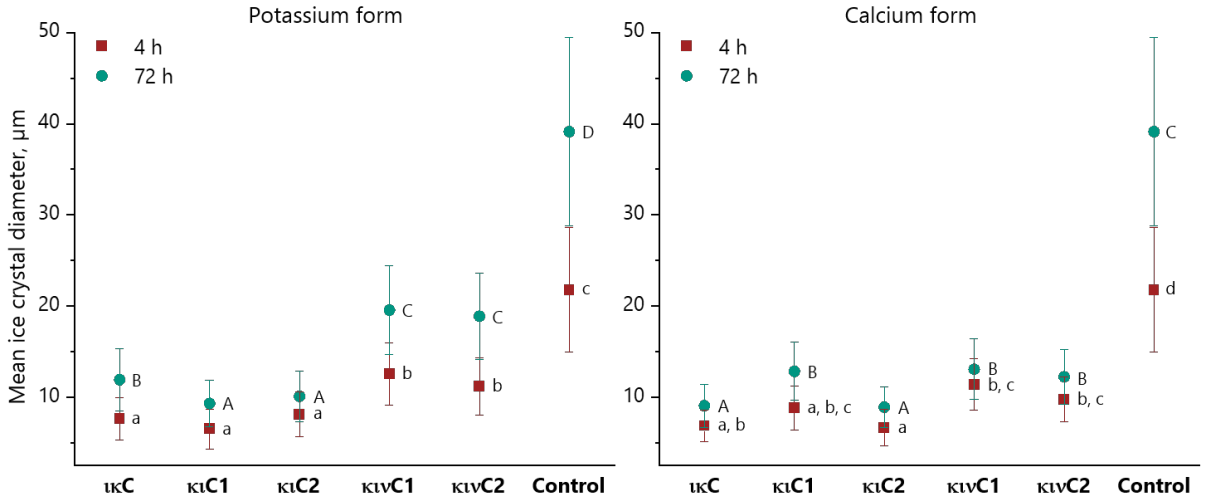

Figure 3.4. *Mean ice crystal diameter (n = 4) after 4 h and 72 h at −12 °C of a 49% sucrose solution with 1 mg/mL of the potassium and calcium forms of the hybrid carrageenans used in this study. The control sample refers to a sucrose solution without carrageenan addition. The statistical analysis was conducted by using one-way analysis of variance (ANOVA) with post-hoc Tukey test (α = 0.05). In case of heterogeneity of variances, Welch ANOVA was applied.*

The results suggested that the IRI activity of the potassium forms is associated with the portion of structural elements of the κ-type. κιC2 and κιC1 (67% and 42% κ-units) showed low ice crystal diameters which were not significantly different from κC (Fig. A2.3). ικC yielded a significantly different mean ice crystal diameter than κιC1 and κιC2 after 72 h, which could be derived from the comparably low portion of κ-units (27%). The ν-unit containing carrageenans κινC1 and κινC2 showed a significantly lower IRI activity which suggests a negative effect of structural elements with a higher degree of sulfation. However, the IRI activity of the carrageenans κιC2, κιC1, and ικC showed that a certain portion of ι structural elements does not significantly impede IRI activity.

The conversion into the calcium forms clearly improved the properties of κιC2 and ικC which showed the highest IRI activity among the calcium forms (8.92 ± 2.26 µm and 9.07 ± 2.36 µm after 72 h). Notably, the mean ice crystal diameters were lower than for the calcium form of κC (13.84 ± 3.81 µm after 72 h) and comparable to the potassium form of κC (8.19 ± 2.35 µm after 72 h). κινC1 and κινC2 also showed a higher IRI activity in the calcium forms although it was still comparably low. Notably, κιC1 showed a slightly although statistically significant lower IRI activity than ικC which has a comparable structure (consecutive blocks of κ- and ι-units)

but a higher portion of ι-units. Nevertheless, the results demonstrate that the IRI activity of hybrid carrageenans is improved by exchanging the associated cation from potassium to calcium. In a previous study, carrageenans with more than one structural unit also showed a considerable IRI activity [38]. However, the samples used were inhomogeneous with regards to their associated cations. Thus, it was not possible to attribute the IRI activity to a specific structural feature. In contrast, the results from this study clearly demonstrate the influence of the associated cations as well as the structural composition of the carrageenans.

Influence of ν-Units on IRI Activity

To investigate the influence of the ν-units on IRI-activity, the potassium form of κινC1m (obtained after alkali-modification) was analyzed. Fig. 3.5 shows the ice crystal morphology and the mean ice crystal diameters after 4 h and 72 h.

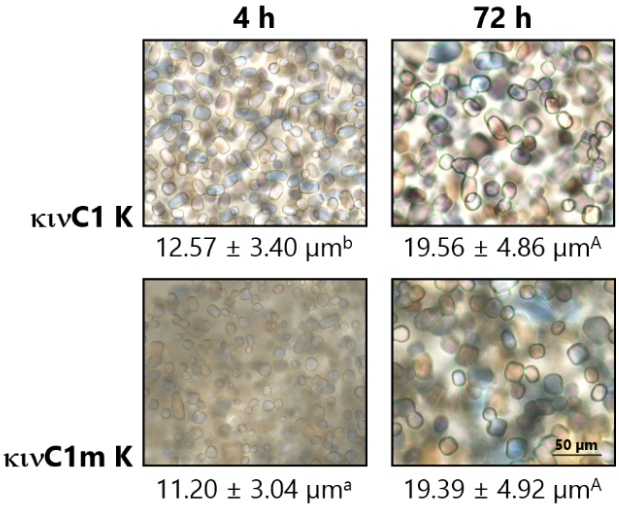

Figure 3.5. *Ice crystals grown in a 49% (w/w) sucrose solution with the potassium form of κινC1 before and after alkaline modification after storage for 4 h and 72 h at −12 °C and their mean ice crystal diameters (n = 4).*

Both the mean ice crystal diameter as well as ice crystal morphology were not significantly different between κινC1 and κινC1m. These results suggest that the presence of ν-units does not influence the IRI activity of this carrageenan. Because the IRI activity of κιC2 was clearly higher, the varying functionality must be derived from the structural composition. Based on the IRI activity of the other carrageenans, the distribution of κ-units or the length of blocks with κ structural elements may be an important factor: κιC2 was excessively degraded with κ-carrageenase while κινC1 was hydrolyzed to a lower extent. This is most likely the result of a higher portion of consecutive κ-units.

3.5 Conclusion

In the present study, we used well-characterized carrageenans and successfully converted them into their monocationic forms. The samples which contained only potassium, calcium, and, in part, sodium as associated cations were subsequently investigated for their IRI activity in a model system. Our results clearly demonstrated that both the molecular structure as well as the associated cations clearly influence IRI activity. The κ-carrageenan κC showed the overall highest IRI activity, but only in its potassium form. In contrast, the calcium form of the ι-carrageenan ιC was more active than its potassium form. Therefore, a higher IRI activity was observed for cations which lead to a strong helix stabilization for the individual carrageenans [368,369]. These results suggest that helix formation or a rigid conformation is important for an interaction with the ice crystal surface. Generally, IRI activity was higher for κC than for ιC, independent from the cation form. Therefore, κ structural elements seem to have a positive influence on functionality. Carrageenans with both κ and ι structural units also showed significant IRI activity. A high IRI activity was observed for the potassium forms of carrageenans with a high portion of consecutive κ-units. However, conversion into the calcium form in part even improved the properties of these carrageenans. Our results also suggested that not only the portion of the individual structural elements are important but also the abundance and length of the corresponding blocks. The results of this study lay the basis for a targeted extraction of carrageenans to optimally exploit their functionality. Future work could focus on the application of structurally defined carrageenans in different food products.

4 Furcellaran: Impact of Concentration, Rheological Properties, and Structure on Ice Recrystallization Inhibition Activity

Reprinted (adapted) with permission from: Gerhäuser, J.; Hale, J.; Wefers, D.; Gaukel, V. (2024): Furcellaran: Impact of Concentration, Rheological Properties, and Structure on Ice Recrystallization Inhibition Activity In: Biomacromolecules, 25, 7, 4535–4544. doi:10.1021/acs.biomac.4c00541.

4.1 Abstract

Recrystallization is considered the main damaging mechanism during the frozen storage of biologic materials. In this study, furcellaran, a polysaccharide related to κ-carrageenan, was studied for its concentration-dependent effect on ice crystal growth and recrystallization. The structure and sulfate content of the utilized furcellaran was analyzed by ^{1}H nuclear magnetic resonance spectroscopy, ion chromatography, and high-performance size-exclusion chromatography. Additionally, the rheological properties of furcellaran solutions were investigated. Our findings demonstrate that furcellaran inhibits ice growth as effectively as κ-carrageenan. Furthermore, the rheological properties change with increasing furcellaran concentration, resulting in a gel-like consistency at 5 g/L, which coincides with decreased recrystallization inhibition activity and larger crystals. This suggests that gel formation or a gel-like consistency has to be avoided for optimal recrystallization inhibition activity.

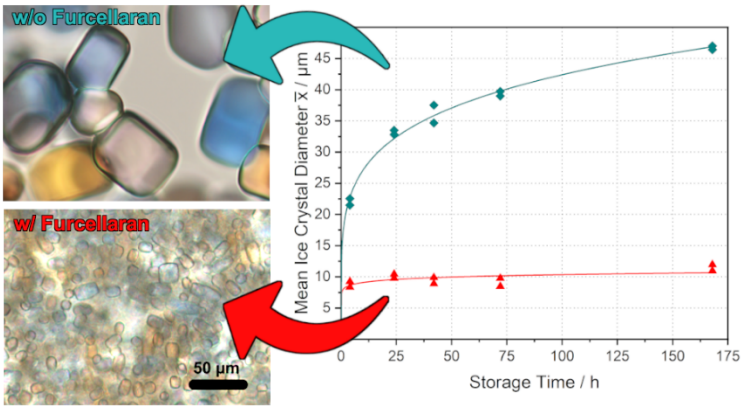

Figure 4.1. *Graphical abstract.*

4.2 Introduction

While effective for preserving food and other biological substances such as cells, [370] freezing and subsequent storage at low temperatures can also have negative effects. Though ice crystal formation can damage structural components, [371,372] recrystallization during storage is the primary factor determining the final ice crystal size distribution at the end of storage [373] and is therefore considered the main damaging mechanism. [374,375] Ice recrystallization occurs throughout the entire freezing and thawing process and frozen storage. Ice recrystallization leads to the coarsening of the ice crystal structure within the product, where larger crystals grow at the expense of smaller ones while maintaining a constant overall ice fraction. [376] Ice recrystallization is considered a major damaging mechanism in the context of frozen storage. [5,8] To minimize those negative effects, additives can be used. The potential influence of viscosity on ice crystal recrystallization has been a topic of research in the context of the addition of hydrocolloids, especially in the field of ice cream production within the food industry. [81] The modulation of the viscosity improves ice cream stability with respect to melting and seems to slow down the rearrangement of water molecules during recrystallization. [90,377,378] However, a recent publication by Kiran-Yildirim et al. investigating hydrocolloids derived from algae did not show a correlation between viscosity and ice recrystallization. [38] In addition, Li et al. reported that the reduced recrystallization due to nanocellulose addition is not linked to the viscosity modulation. [92] Consequently, the increase in viscosity does not necessarily lead to a reduction of recrystallization. Ice-binding proteins (IBP) or antifreeze proteins (AFP) are widely acknowledged as the most prominent and efficacious biological ice recrystallization inhibitors. [99] By binding and interacting with the ice crystal surface, they can inhibit recrystallization. [128,200,379] Beyond IBP, various polymers are effective recrystallization inhibitors and therefore able to interact with ice crystals such as poly(vinyl alcohol) (PVA). In general, the efficacy of ice-binding molecules, such as ice-binding proteins and other polymers, results from their interaction with the ice crystal surface. The adsorption inhibition model developed by Raymond and Devries serves as underlying principle for the antifreeze properties of those molecules. [128] Over the past few decades, the question of reversible versus irreversible binding of ice-binding molecules to the ice crystal surface has been a recurring topic of debate. While a lot of publications suggest irreversible binding of IBPs to the ice crystal surface, [126,128,200] conflicting results, especially regarding glycosylated ice-binding proteins, have emerged. [202,380] Recently, a computational study suggested the possibility of both irreversible and reversible binding of glycosylated ice-binding proteins. Carbohydrate-mediated interactions with the ice crystal surface led to irreversible binding, while protein-ice interactions

resulted in reversible binding. [205] A recent publication by Tas et al. suggests that reversible binding is sufficient for the inhibition of recrystallization. [206]

However, IBPs also have disadvantages. Due to their complex purification and production process, they are very expensive and currently only available in limited quantities. [381] Consequently, there is a need for alternative ice recrystallization inhibition (IRI) active molecules, which are effective, affordable, and readily available.

A promising alternative is polysaccharides and other polymers derived from red algae such as carrageenan. They can be easily extracted and are abundantly available, primarily due to their widespread use as thickening agents in various food products. [382,383] Carrageenan is generally composed of alternating units of β-D-galactopyranose (G-unit) and α-D-galactopyranose (D-unit), with the D-unit sometimes occurring as 3,6-anhydro-α-D-galactopyranose (DA-unit). [35,350] The monosaccharide units are sulfated to a varying extent, with sulfate contents of up to 40%. [384,385] Depending on the sulfation pattern and monosaccharide composition, carrageenans can be divided into different types, which are distinguished by Greek letters. [35,350] In case of κ-carrageenan, the β-D-galactopyranose (G-unit) is sulfated at the position *O*-4, resulting in a single negative charge on the disaccharide unit and a sulfate content of approximately 25–30%. [386] Upon cooling, it exhibits thermoreversible gelation via helix formation and aggregation, with the gel properties being related to the ions present. [387,388] In addition, IRI activity and ice crystal shaping have been demonstrated for κ-carrageenan. [25,38] It has already been shown that the IRI activity depends on molecular size [43] and decreases upon gel formation. [41] This may be due to the immobilization of the molecules within the gel network, limiting the availability of molecules for interaction with the ice crystal surface. Based on these findings, it is likely that κ-carrageenan exhibits ice-binding properties.

Compared with IBP, the ice-binding mechanism of linear polymers remains less extensively investigated. Unlike the ice-binding site of IBP, no ordered water structure, which may mediate ice binding, has been observed yet. For PVA [214,389] and a modified glycerol, [390] the importance of hydrogen bonds in the interaction with ice has been demonstrated. Potential interaction sites for the formation of hydrogen bonds between κ-carrageenan and water or ice molecules are the sulfate groups and the numerous hydroxyl groups of the two different saccharide units.

Furthermore, ι-carrageenan consists of the same disaccharides as κ-carrageenan but has an additional sulfate ester group at the DA-unit. While it also reduces recrystallization, it is less ef-

fective than κ-carrageenan and seems to have a negative effect on IRI activity. [38,44] Presuming the validity of this correlation, carrageenan polysaccharides with an even lower sulfate content than κ-carrageenan may be more active in inhibiting recrystallization. To elucidate this hypothesis, furcellaran, a carrageenan-like polysaccharide with a lower degree of sulfation, could be used.

Furcellaran is structurally similar to κ-carrageenan and is composed of β-D-galactose (G-unit) and 3,6-anhydro-α-D-galactose (DA-unit), differing only in the degree of sulfation. Approximately one-third of the G-units in furcellaran are substituted with a sulfate group, resulting in a sulfate content of 16–18%. [258,391] Disaccharide units that have no substitution with sulfate correspond to the structural unit characteristic of β-carrageenan. [350]

Another factor influencing the interaction of ice-binding polymers with the ice crystal appears to be the flexibility of the polymer. Bachtiger et al. demonstrated that PVA can bind to ice regardless of its conformation by adapting to the ice surface structure. [214] In comparison to κ-carrageenan, the lower sulfate content of furcellaran may potentially lead to an enhanced flexibility and, therefore, a better adaption to the ice surface. In the case of ι-carrageenan, the higher sulfate content might restrict its flexibility, thereby hindering its ability to adapt to the ice crystal surface. This may contribute to its lower IRI activity.

In addition, the ability of κ-carrageenan to inhibit ice recrystallization decreased with gel formation. It was suggested that the polymers are immobilized within the gel network, which prevents their interaction with the ice crystals. [41] Similarly, the aggregation of polymers should be considered in this context. Aggregate formation without gelation may limit ice binding by reducing the number of available molecules and limiting their flexibility. For this reason, the gelation behavior of furcellaran depends on the concentration at which it is investigated.

In summary, this study aims to investigate the ability of furcellaran to modulate the recrystallization of ice crystals, encompassing the influence of the sulfate groups and the potential role of gel formation in recrystallization inhibition. Furthermore, the structure of the polysaccharide is analyzed to ensure that the material used is authentic, high-molecular-weight furcellaran.

4.3 Materials and Methods

4.3.1 Structural Analysis and Sulfate Content

^{1}H NMR Spectroscopy

5 mg of the furcellaran sample was mixed with 1 mL of deuterium oxide (Deutero, Germany) and treated in a water bath at 70 °C until the sample was completely dissolved. 0.5 µL of dimethyl sulfoxide (DMSO) (Carl Roth, Germany) was added as an internal reference (2.696 ppm, according to van de Velde et al.). [350] NMR experiments were carried out on a Bruker AVANCE Neo 400 MHz spectrometer equipped with a temperature-controlled 5 mm-probe head. A standard ^{1}H pulse program from Bruker ("zg90") was used, and the spectra were recorded at 65 °C. The relaxation delay d_1 was 25 s, the acquisition time was 2 s, and the number of scans was 16. The type of carrageenan can be identified by the signals of the anomeric protons of the D- or DA-unit. The chemical shift of the α-anomeric protons is determined relative to the signal of DMSO at 2.696 ppm and compared with literature data. [350]

Sulfate Content

25 mg of the sample was hydrolyzed with 2.25 mL of 2.3 M trifluoroacetic acid (Merck, Germany) and 0.25 mL of 35% (v/v) hydrogen peroxide (J. T. Baker, USA). Hydrolysis was carried out in a closed screw-cap tube for 16 h at 100 °C. After cooling, the solution was centrifuged for 10 min at 220 g, and 0.25 mL of the supernatant was then evaporated to dryness. The dried sample was dissolved in 3.25 mL of Milli-Q water for 15 min at 70 °C in a water bath. [352]

For ion chromatographic analysis, a Dionex ICS-6000 system (Thermo Fisher Scientific, Germany) equipped with a Dionex IonPac AS10 column (8.5 µm, 250×4 mm, Thermo Fisher Scientific, Germany) at 30 °C and a conductivity detector was used. 30 mM sodium hydroxide (Merck, Germany) was used as the eluent with an isocratic flow rate of 0.38 mL/min. The conductivity of the eluent was suppressed using a Dionex AERS 500e suppressor (4 mm, Thermo Fisher Scientific, Germany). Quantitation was carried out using an external calibration.

Molecular Weight

2 mg of the sample was mixed with 1 mL of 0.1 M lithium chloride (Merck, Germany) and treated in a water bath at 60 °C until the sample was completely dissolved. The analysis was performed by using a TSKgel G6000PW$_{XL}$ column (Tosoh Bioscience, Japan). In order to suppress the aggregation of the polysaccharides, the analysis was carried out at a temperature of 60 °C and by using 0.1 M lithium chloride (Merck, Germany) as eluent [351] with a flow rate

of 0.5 mL/min. The M_W of the sample was determined using a MALLS detector with a refractive index increment of 0.115 mL/g, as described by Lecacheux et al. [351]

4.3.2 Recrystallization Experiments and Image Analysis

Sample Preparation

To investigate the impact of furcellaran on the recrystallization of ice crystals, a sucrose (Carl Roth, Germany) solution with a total solids content of 49% (w/w), functioning as a model solution for frozen food systems, was used. Different concentrations of furcellaran (Biosynth Ltd., United Kingdom) were used, ranging from 0.05 to 5 g/L. For comparison, a 49% (w/w) sucrose solution without furcellaran addition is used. The appropriate amounts of furcellaran and sucrose were weighed, and then the mixtures were diluted with Milli-Q water to achieve the desired volume, resulting in a total solid content of 49% (w/w) in each sample. To completely dissolve the solids, the prepared solutions were heated to 60 °C. After cooling to room temperature, 15 µL of the sample solution was pipetted onto a previously prepared microscope slide. The increase in viscosity of furcellaran solutions is apparent when the furcellaran concentration in the sample is raised. For this reason, the highest furcellaran concentration applied was 5 g/L. The prepared microscope slides consist of a microscope slide with two coverslips glued on top of it with a gap of around 8 mm in between the coverslips. The sample was placed between the coverslips, and on top, a third coverslip was sealed with silicone (Henkel AG & Co. KGaA, Pattex Express, Germany) to ensure airtightness. In total, two of those microscope slides were prepared from each sample solution and quickly cooled in liquid nitrogen to reach the glassy state, allowing for a uniform crystallization. The frozen samples were stored in a small cooling chamber that was maintained at -12 ± 0.1 °C by an external cryostat (Julabo GmbH, FP50, Germany). The cooling chamber was housed inside a glovebox, which maintained a constant temperature of -12 ± 1 °C. The temperature profile throughout the storage period was monitored and recorded using thermocouples (Ahlborn Mess- and Regelungstechnik GmbH, Almemo, Germany). Under these conditions, an ice volume fraction of about 22% is present. [392]

Analysis

At 4, 24, 48, 72, and 168 h storage, images of the ice crystals in each sample were taken using a camera (Bresser GmbH, Mikrocam II 5MP HIS, Germany) mounted on a polarizing microscope (Olympus, BX41, Japan). Camera and microscope are located inside the glovebox. In total, 300 ice crystals were analyzed per microscope slide, and the area of each ice crystal was determined using the ImagePro 9.3 (Media Cybernetics, USA) software. The area equivalent diameter of each ice crystal was calculated by determining the diameter of a circle with the

same area as that of the ice crystal. Subsequently, the mean equivalent diameter $\bar{x}$ was calculated as the average of all equivalent diameters, resulting in two mean equivalent diameters $\bar{x}$ per furcellaran concentration. The experimental data were fitted to the Lifshitz–Slyozov and Wagner (LSW) theory (Eq 4.1) [25,84,102] using Origin 2023 software (OriginLab Corporation, USA). The constants K and n in the LSW equation were adjusted to the experimental data by using regression analysis.

Eq 4.1: Lifshitz–Slyozov and Wagner theory.

$$r^n = r_0 + \frac{t}{\tau} \tag{4.1}$$

Where: r = *Ice crystal radius*
r_0 = *Initial ice crystal radius*
n = *First fitting parameter*
t = *Time*
τ = *Second fitting parameter*

The initial ice crystal radius r_0 was assumed to be 0 µm as the samples were in the glassy state at the beginning of the storage period. The variable t denotes the specific time instant at time t. The rate-limiting mechanism is reflected in the LSW theory via the constants n and τ. In addition, the constant τ depends on the ice fraction and decreases with increasing ice fraction. Eq 4.1 is transformed as follows in order to replace the radius r by the mean diameter $\bar{x}$:

Eq 4.2: Transformed LSW theory.

$$\bar{x} = K \times t^{1/n} \tag{4.2}$$

Where: $\bar{x}$ = *Mean diameter*
K = *Rate constant of ice crystal growth*
t = *Time*
n = *Fitting parameter*

With the constant *K* being the rate constant of ice crystal growth:

Eq 4.3: Definition of the rate constant K.

$$K = 2 \times \tau^{-1/n} \tag{4.3}$$

Where: K = *Rate constant of ice crystal growth*
n = *First fitting parameter*
τ = *Second fitting parameter*

4.3.3 Rheological Characterization

Since gel formation can affect recrystallization, the rheological properties of furcellaran solutions with different concentrations were investigated. The measurements were performed with a Physica MCR 301 (Anton Paar GmbH, Austria) rheometer at a temperature of −12 °C to determine the rheological properties under temperature conditions similar to those present in the recrystallization experiments. To avoid ice crystal formation, which would interfere with the rheological measurement, a higher sucrose concentration of 60% (w/w) as in the experiments was used. Rheological measurements were performed according to the method established by Leiter et al. [41] using a plate–plate geometry with a plate diameter of 50 mm and a gap distance of 0.3 mm. The measurements were performed over a frequency range of 0.1 to 10 Hz with an amplitude γ of 15%, ensuring that the applied strain always remained within the linear viscoelastic region, which was previously verified by amplitude sweeps. Four different furcellaran concentrations ranging from 0.05 to 5 g/L were analyzed. To prepare the solutions, sucrose and furcellaran were weighed and dissolved in Milli-Q water at 60 °C until the solids were completely dissolved. The hot sample was then applied to the plate that has been preheated to 60 °C. A low-viscosity paraffin oil (Carl Roth GmbH & Co. KG, Germany) was applied to the exposed sample to prevent the evaporation of water. [339] The temperature was then lowered to 25 °C within 7 min and held for additional 5 min. The final cooling step to the measurement temperature of −12 °C was carried out with a cooling rate of 0.04 °C/s and lasted for approximately 16 min. The sample was again equilibrated for 5 min prior to the measurement. This method is based on the publication of Leiter et al. [41] and aims to facilitate comparability of results. Three samples are taken of each prepared solution and measured, and the standard deviation of the data is calculated.

4.4 Results and Discussion

4.4.1 Structural Analysis of Furcellaran

As a first step, the structure of furcellaran used in this work was analyzed. The ^{1}H NMR spectrum of furcellaran (Figure 4.2) showed a signal in the anomeric region with a chemical shift of 5.09 ppm. According to van de Velde et al., [350] this signal can be assigned to the DA-unit present in κ-carrageenan and furcellaran. However, furcellaran should also contain structural units of the β-type, which yield a signal at 5.074 ppm. [350] However, only one broad signal at 5.09 ppm was detected. Most likely, the signal of the β-type (5.07 ppm) overlaps that of the κ-type (5.09 ppm). Nevertheless, the results from NMR spectroscopy demonstrate the presence

of typical DA-units and the absence of other carrageenan types. To gain further insights into the structural composition, the sulfate content was determined by ion chromatography.

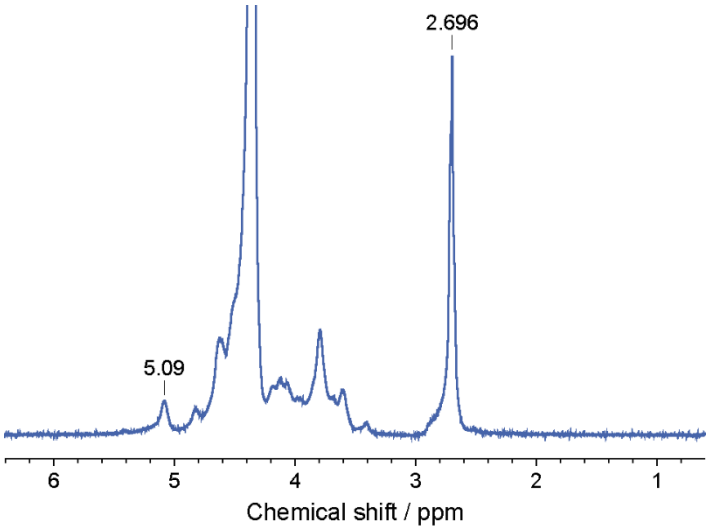

Figure 4.2. *^{1}H NMR spectrum of furcellaran at 65 °C in deuterium oxide. The signal at 2.696 ppm corresponds to dimethyl sulfoxide, which was added as an internal reference. The signal at 5.09 ppm corresponds to the α-anomeric proton of the DA-unit present in furcellaran and κ-carrageenan.*

The sulfate content of the furcellaran sample was 14.1 ± 0.5% (w/w), which is significantly lower than the sulfate content typically found in commercial κ-carrageenan (25–30%). [386] Since the disaccharide unit characteristic of the β-type (present in furcellaran) differs from the κ-type by the absence of the sulfate group at position O-4 of the G-unit, [350] the lower sulfate content of the analyzed furcellaran is consistent with the expected structure. Furthermore, the sulfate content of the sample is comparable to that described in the literature for furcellaran obtained from *Furcellaria lumbricalis* [16–18% (w/w)]. [258] The presence of β-type repeating units was also confirmed by the detection of characteristic oligosaccharides after κ-carrageenase digestion (data not shown). The M_W of the sample, as determined by HPSEC-MALLS, was 407 ± 18 kDa, and low-molecular-weight compounds were not detected. The observed molecular weight is also consistent with literature data, which reported about 500 kDa for furcellaran. [393] In conclusion, the results of the structural characterization demonstrate that the furcellaran sample used in this study has the anticipated chemical structure.

4.4.2 Recrystallization

Visual Inspection and Ice Crystal Shape

Prior to this study, furcellaran was not known to exhibit recrystallization inhibiting activity. The visual inspection of the ice crystal images of different furcellaran solutions shown in Figure

4.3 clearly demonstrates an effect of furcellaran addition on ice crystal growth and recrystallization. Considering the substantial amount of data, only representative images of the individual furcellaran concentrations will be shown.

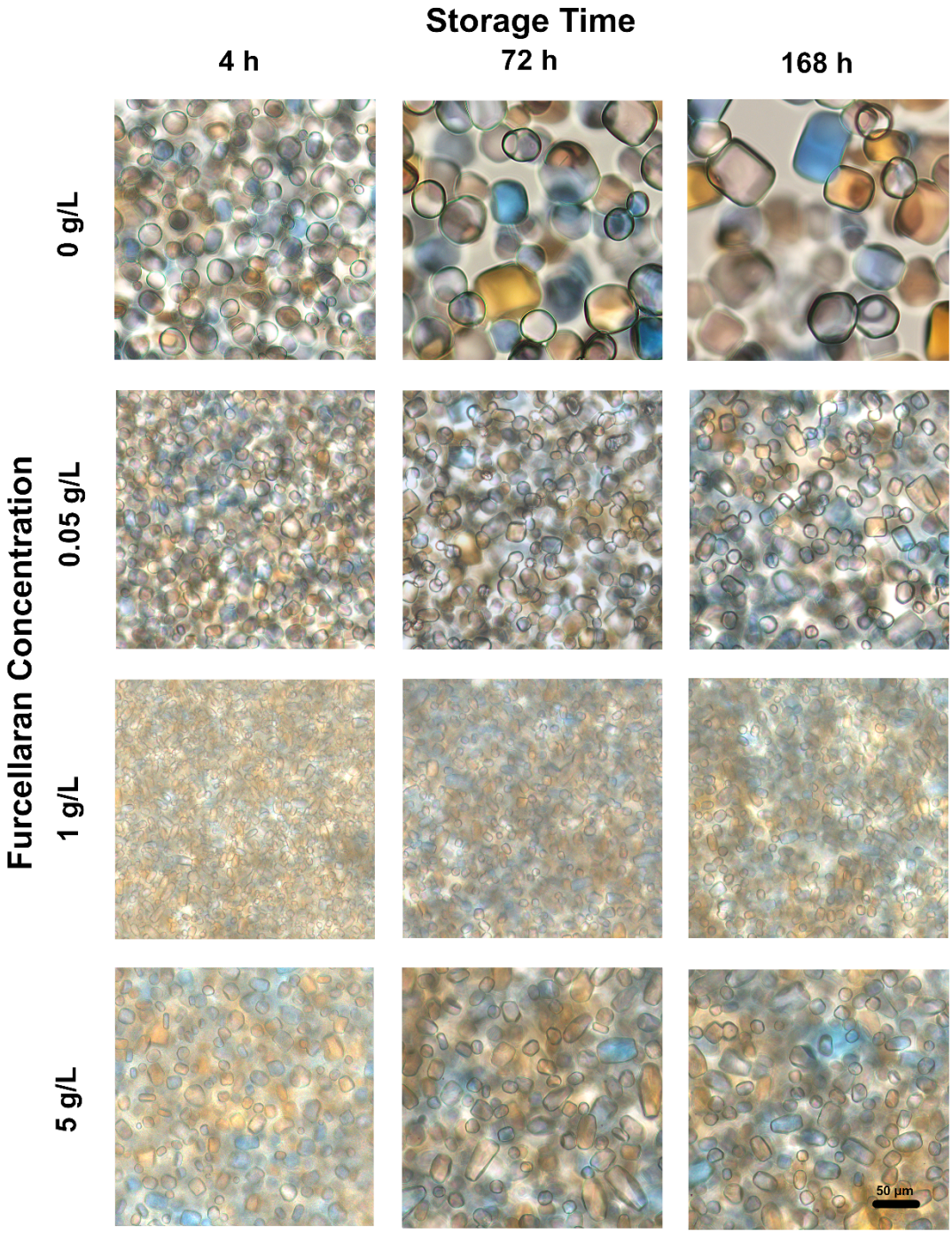

Figure 4.3. *Images of four different furcellaran concentrations including the control sample (0, 0.05, 1, and 5 g/L) at three different storage times (4, 72, and 168 h).*

In the control sample, the process of recrystallization was clearly observed. Over the storage period, the size of the ice crystals increased steadily. The addition of furcellaran, regardless of

concentration, results in the formation of visibly smaller ice crystals, in comparison to the control sample without furcellaran. This is notable already at the onset of storage. Even at the lowest furcellaran concentration of 0.05 g/L, a decrease in the crystal sizes compared to the control can be observed, while at a concentration of 1 g/L, the crystals are even smaller. However, this trend does not continue for higher furcellaran concentrations. A furcellaran concentration of 5 g/L promoted larger ice crystal sizes compared to 1 g/L, yet the sample remained substantially smaller than the control. Upon visual inspection, the addition of furcellaran may cause slight changes in the morphology of ice crystals toward more angular and elongated ice crystals, but a clear statement cannot be made based on this. Although the sphericity values were obtained by image analysis, the deviations preclude a definitive conclusion regarding the ice crystal shape. If furcellaran has an effect on the ice crystal shape, it is clearly less pronounced than the effect of ice-binding proteins from fish on the morphology of ice crystals. [25] To conclusively determine the effect of furcellaran on ice crystal morphology, future studies should investigate the effect on individual ice crystals and at a lower overall ice volume fraction. A low ice volume fraction allows ice crystals to grow freely and minimizes possible crystal–crystal interactions, which may influence their shape. This has already been performed successfully to show the change of ice crystal shape in κ- and ι-carrageenan solutions. [44]

A detailed examination of the images of the furcellaran solutions with the highest concentration of 5 g/L reveals that very large ice crystals form repeatedly, as can be seen in Figure 4.4. This was not observed to such an extent in all other samples.

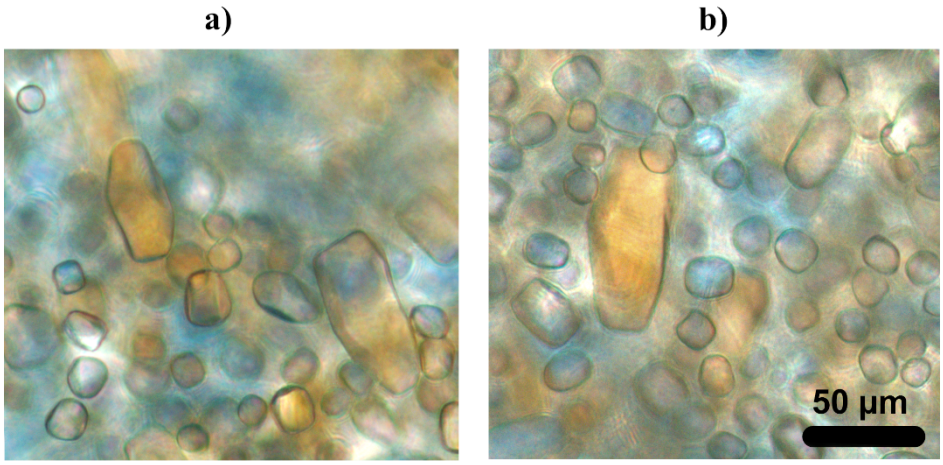

Figure 4.4. *Images (a,b) show two different samples at a furcellaran concentration of 5 g/L after a storage period of 72 h at −12 °C. Both samples exhibit large ice crystals, which are not observed at lower furcellaran concentrations.*

Cumulative Ice Crystal Size Distributions

To gain additional information from the image analyses, the cumulative distributions of Q_0 are examined. In Figure 4.5, the distributions of ice crystal diameters of individual samples at 0.05, 1, and 5 g/L furcellaran after a storage period of 168 h are compared. Although the mean ice crystal diameter $\bar{x}$ after 168 h of storage of the samples with 0.05 and 5 g/L furcellaran is comparable, the width of the distributions is different. The distribution for a furcellaran concentration of 5 g/L demonstrates a wider spread, especially in the upper range of ice crystal sizes.

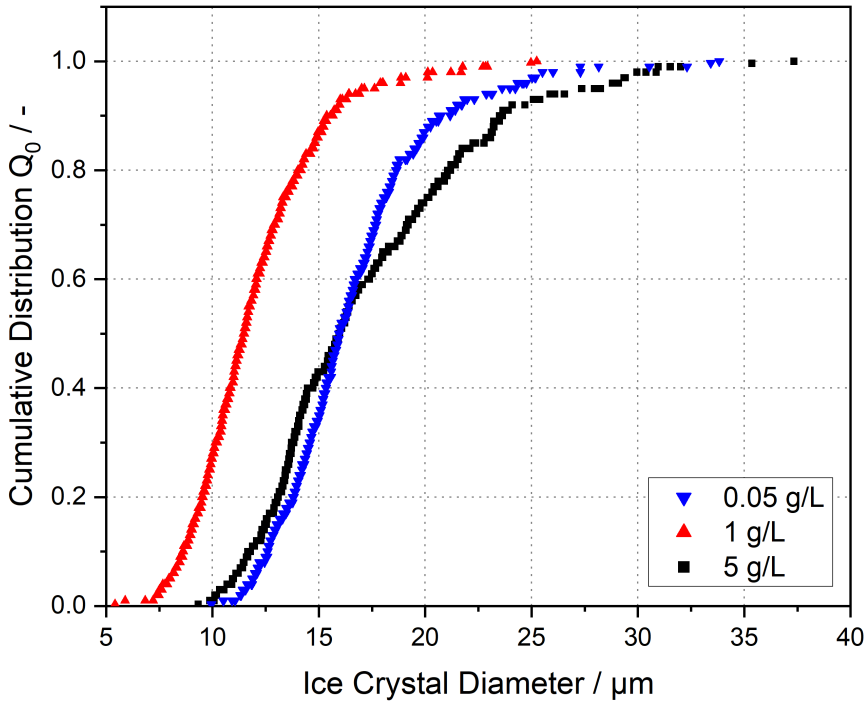

Figure 4.5. *Cumulative distribution Q_0 of ice crystal sizes after a storage period of 168 h. The samples containing 0.05 and 1 g/L of furcellaran (triangles) show a narrower distribution compared to the sample with 5 g/L furcellaran (squares), which exhibits a shift toward larger diameters.*

To further quantify the spread of the different distributions, we used the span value. The span is calculated according to Eq 4.4.

Eq 4.4: Definition of the span.

$$Span = \frac{Q_0(90) - Q_0(10)}{Q_0(50)} \tag{4.4}$$

Where: $Q_0(90) = 90\%\ quartile$
$Q_0(50) = 50\%\ quartile$
$Q_0(10) = 10\%\ quartile$

with the 90% [$Q_0(90)$], 50% [$Q_0(50)$], and 10% quartile [$Q_0(10)$] of the ice crystal sizes of a single sample. The calculation of the span normalizes the distribution width to $Q_0(50)$, meaning that the absolute value of $Q_0(50)$ affects the size of the span for the same distribution width [$Q_0(90) - Q_0(10)$]. To improve the assessment of differences in the span values, the standard deviations of the distributions are calculated in addition (Table 4.1). All required quartiles were calculated independently for each of the two samples. The span values for both samples with the same concentration are highly similar. For 1 g/L, the span is greater than that of 0.05 g/L. This is likely due to the smaller $Q_0(50)$ value of the sample containing 1 g/L furcellaran. The analysis of the standard deviations reveals similar values for samples with identical concentration. The samples with 1 g/L furcellaran, which displays the most pronounced effect on ice crystal sizes, also show the lowest standard deviations. In comparison, the samples containing 5 g/L furcellaran exhibit the highest standard deviations. In addition to the visual observation in Figure 4.6, the span confirms that the distribution of ice crystals is widest at a furcellaran concentration of 5 g/L, which is also in agreement with the standard deviations of the individual ice crystal size distributions. The exact cause of the formation of individual, extremely large ice crystals at high furcellaran concentrations remains unclear. A potential contributing factor may be the rheological properties of the solutions, which will be discussed in a subsequent section.

Table 4.1. *Span values and standard deviation of the two samples with furcellaran concentrations of 0.05, 1, and 5 g/L measured after a storage time of 168 h.*

Furcellaran concentration (g/L)	$Q_0(10)$	$Q_0(50)$	$Q_0(90)$	**Span**	**Standard deviation (µm)**
		Sample 1			
0.05	14.37	18.07	23.68	0.52	4.2
1	8.63	11.48	15.61	0.61	3.1
5	11.78	15.98	23.54	0.74	5.1
		Sample 2			
0.05	12.61	15.96	20.79	0.51	3.7
1	8.16	10.52	14.54	0.61	2.6
5	12.06	15.60	23.79	0.75	4.9

Recrystallization Kinetic

To gain more information about the crystal sizes and growth kinetics, the mean diameters are analyzed over the storage period (Figure 4.6). The mean diameter $\bar{x}$ is plotted as a function of storage time and fitted using Eq 4.2 to allow for better discrimination between different furcellaran concentrations.

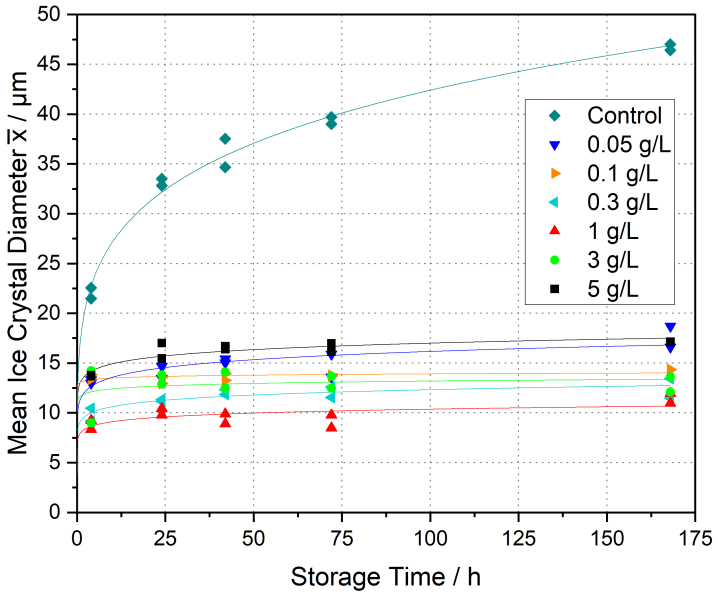

Figure 4.6. *Mean ice crystal diameters of furcellaran samples at different concentrations over a total storage period of 168 h at a constant storage temperature of −12 °C. All furcellaran samples reduce the recrystallization kinetic.*

The analysis of the mean diameters confirms previous observations. In the absence of furcellaran, the mean ice crystal diameter of the control sample is slightly larger than 20 µm at 4 h after the start of the experiment. The crystals grow rapidly during the initial phase of the storage. After a 24 h period, the mean diameter has already reached 33 µm and continues to increase until it attains a mean diameter of about 48 µm after a storage period of 168 h. In comparison, the addition of only 0.05 g/L furcellaran reduces the crystal sizes to a mean diameter of around 13 µm after 4 h of storage. Although the ice crystals continue to grow during the storage period, the growth is much less pronounced, and the recrystallization kinetics is reduced, resulting in a mean diameter of around 18 µm after 168 h. With a further increase in furcellaran concentration up to 1 g/L, ice crystal sizes reach a range of 8 to 9 µm at 4 h and remain the same size for up to 72 h of storage. A slight increase in the mean ice crystal diameter to 12 µm can be observed after 168 h of storage. However, the observed trend of declining mean ice crystal size decreasing with increasing furcellaran concentration did not continue for concentrations exceeding 1 g/L, at least for the concentrations studied. At a furcellaran concentration of 3 g/L, the mean

crystal diameters start to increase again, and at a concentration of 5 g/L, the ice crystal sizes are comparable to crystal sizes at 0.05 g/L. This increase in mean diameter at 3 and 5 g/L furcellaran concentrations may be attributed to changes in the rheological properties of the solutions. These properties are discussed in a subsequent section of this paper.

Influence of Sulfate Groups on Recrystallization

To further investigate the impact of the sulfate group in algae-derived polysaccharides on the recrystallization-inhibiting properties, existing data from the literature can be consulted. Therefore, the data from Leiter et al. on the recrystallization-inhibiting properties of κ-carrageenan are used for comparison [41,43]. This data was obtained using the identical experimental setup and methodology (Table 4.2). As previously mentioned, κ-carrageenan is sulfated at position *O*4 of every G-unit, which leads to sulfate contents of 25–30% (furcellaran: 16–18%).

Table 4.2. *Comparison of mean ice crystal diameters in furcellaran and κ-carrageenan solutions with concentrations of 1 g/L κ-carrageenan, 49% (w/w) sucrose at a temperature of −12 °C.*

	Leiter et al. 2017 κ-carrageenan	**Leiter et al. 2018 κ-carrageenan**	**Furcellaran sample 1**	**Furcellaran sample 2**
Storage time (h)	*Mean diameter (µm)*	*Mean diameter (µm)*	*Mean diameter (µm)*	*Mean diameter (µm)*
42	-	-	8.9	9.9
48	9.7 ± 0.95	10.2 ± 0.8	-	-
72	-	-	9.8	8.5
96	10.4 ± 0.63	11.1 ± 0.84	-	-

In addition, data on ι-carrageenan is included, [38,44] which has sulfate contents of around 33% due to the additional sulfation of the DA-unit. [352] This data was collected with the same method but under different experimental conditions. Therefore, a direct comparison to the results of furcellaran is not feasible. Both publications by Kiran-Yildirim et al. [38,44] clearly demonstrate that ι-carrageenan impacts the recrystallization of ice crystals less than κ-carrageenan. In 49% (w/w) sucrose solution at a storage temperature of −8 °C, the mean ice crystal diameter for 1 g/L ι-carrageenan was around 16.7 µm after 5 h of storage. The crystals grew to 31.1 µm after 99 h of storage. Contrary, the mean ice crystal diameters for 1 g/L κ-carrageenan under the same conditions only grew from 8 to 10.8 µm. [44]

While the measurement times for furcellaran and κ-carrageenan are not exactly the same, a qualitative comparison of the mean diameters is still possible. In the publications of Leiter et

al., three samples were analyzed, and the standard deviations were calculated. In the case of furcellaran from this study, only two samples were measured, and the mean diameter of both samples are presented in Table 5.2. When stored for 42 and 48 h, respectively, the mean ice crystal diameters of furcellaran and κ-carrageenan at concentrations of 1 g/L were both around 9 to 10 µm. The mean diameters remained relatively constant with further storage. After 96 h, the mean diameter of ice crystals in κ-carrageenan solution was between 10 and 11 µm. Due to the standard deviations and variability in the measurement data, no clear statement can be made whether furcellaran affects ice crystal growth more strongly than κ-carrageenan.

Based on these findings and the investigations of Kiran-Yildirim et al., it can be concluded that a decrease in the sulfate content of carrageenan polysaccharides does not automatically lead to increased IRI activity. While the sulfate content decreases from ι-carrageenan to κ-carrageenan to furcellaran, the IRI activity does not increase in a similar extent.

Nevertheless, this does not imply that the sulfate groups are devoid of any influence on the IRI activity. Current investigations on the ice growth inhibition of polymers such as PVA suggest that the high flexibility of the molecule eliminates the requirement for lattice matching for ice binding. [214] The introduction of an additional sulfate group to ι-carrageenan might reduce its flexibility and alter the 3-dimensional structure, making it more difficult for ι-carrageenan to interact with the ice surface. Furcellaran, on the other hand, might be more flexible due to the lower amount of sulfate groups. It is plausible that a certain degree of flexibility in these linear polymers is necessary to effectively interact with the ice surface. Since no differences in IRI activity between furcellaran and κ-carrageenan are discernible, the flexibility of κ-carrageenan may already be adequate. To gain further insights into the interaction mechanism and to support these hypotheses, molecular dynamics simulations may be employed. These simulations can provide detailed information at the molecular level.

4.4.3 Rheological Characterization

The potential formation of a gel or gel-like character of furcellaran solutions due to aggregation at elevated concentrations of 3 and 5 g/L may account for their reduced effect on ice crystal growth. To determine whether the increase in ice crystal size at furcellaran concentrations of 3 and 5 g/L is caused by changes in the gelling properties, they were measured. Therefore, the storage modulus and the loss modulus were measured by using a rheometer in an oscillatory mode. To enable comparability of the rheological measurements with the recrystallization experiments, these measurements were performed at the same temperature conditions of −12 °C.

Due to the formation of ice crystals during the recrystallization experiments, the furcellaran concentration in the liquid phase is increased, which is not considered in the rheological measurements. However, the increasing sucrose concentration within the residual unfrozen solution was considered. When the initial sucrose concentration at a temperature of −12 °C is 49% (w/w), the sucrose concentration in the unfrozen phase is 60% (w/w) with an ice content of about 22%. [392] Therefore, the actual furcellaran concentration at −12 °C at an initial concentration of 1 g/L is approximately 1.29 g/L. [41] At initial furcellaran concentrations of 3 and 5 g/L, the actual furcellaran concentrations are calculated to be 3.86 and 6.44 g/L, respectively.

It is unambiguously noticeable in the handling of furcellaran solutions that the viscosity increases with increasing furcellaran concentrations, especially at concentrations of 3 g/L or higher. However, this increase in viscosity does not automatically imply the formation of a gel network. Therefore, the storage modulus G' and the loss modulus G'' of the solutions must be determined. The storage modulus G' is a quantitative measure of the elastic behavior of a material and describes the amount of energy stored in a material when it is deformed and may be interpreted as gel strength. Contrarily, the loss modulus G'' describes the energy which dissipates as heat during a shear cycle. It represents the viscous behavior of a material. Unfortunately, there is no universally accepted definition of a gel, and different sources define gel in different ways. One definition according to Picout and Ross-Murphy [361] states that the storage and loss modulus G' and G'' are constant over a wide frequency range (10^{-3}–10^{2} Hz), and the loss factor is less than 1. The loss factor tan δ is the ratio of the loss modulus G'' to the storage modulus G' (Eq 4.5).

Eq 5.5: Definition of the loss factor $\tan\ \delta$.

$$\tan\ \delta = \frac{G''}{G'} \tag{5.5}$$

Where: $\tan\ \delta = Loss\ factor$
$G' = Storage\ modulus$
$G'' = Loss\ modulus$

Figure 4.7 presents the results of the rheological measurements for various furcellaran concentrations.

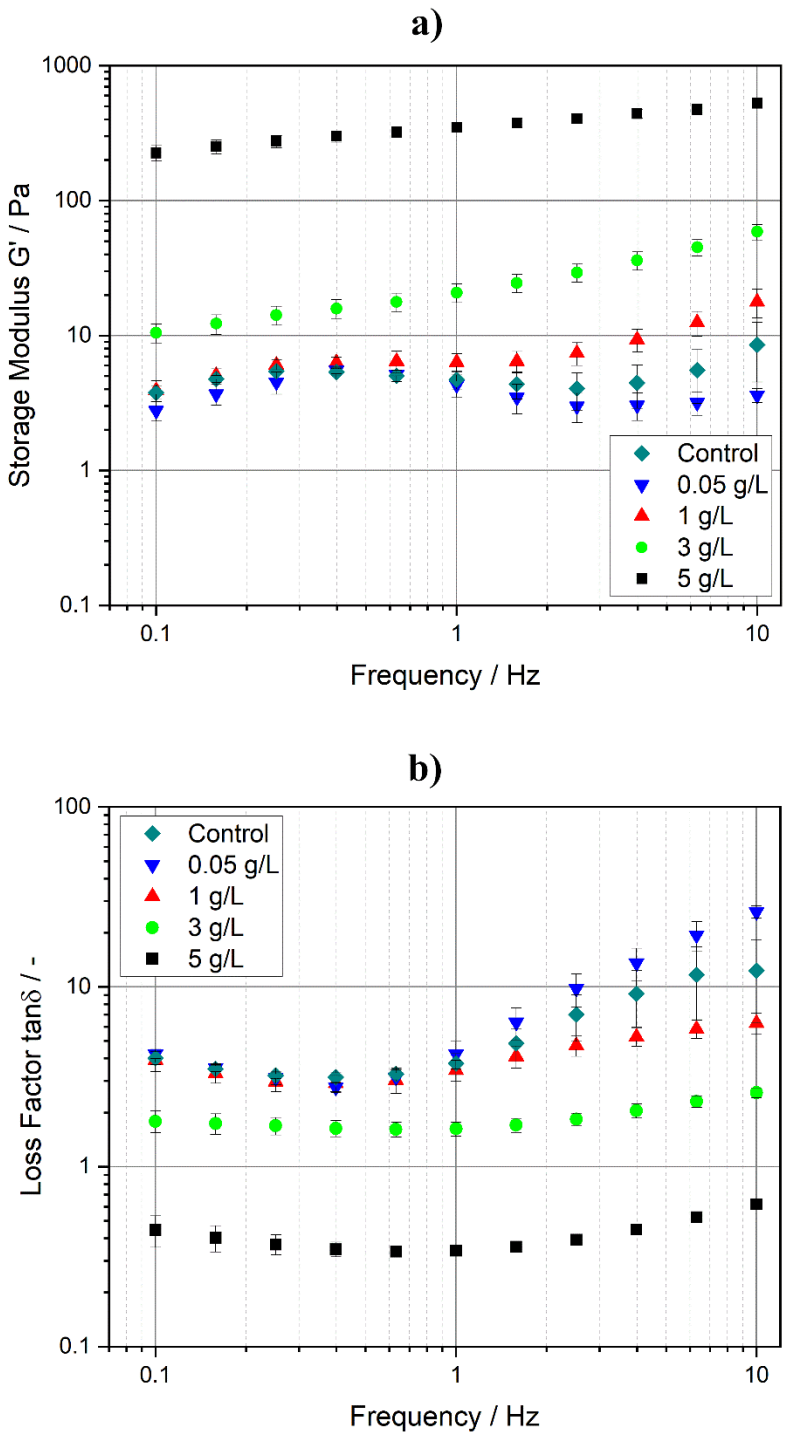

Figure 4.7. *Storage modulus G' (a) and loss factor tan δ (b) of different furcellaran solutions at −12 °C and a sucrose concentration of 60% (w/w).*

Across all furcellaran solutions studied, the storage modulus G' increases with increasing frequency (Figure 4.7a). The storage moduli G' of furcellaran solutions up to 1 g/L are all within a range of 1 to 11 Pa. At higher concentrations, the storage modulus G' of furcellaran solutions

increases significantly. At 3 g/L, the storage modulus is shifted to higher values between 10 and 100 Pa. This is even more pronounced at a concentration of 5 g/L. At this concentration, the storage modulus G' has values in the range of 200 to 600 Pa. The storage modulus G' and the loss factor show comparable trends but in a reversed order. At furcellaran concentrations up to 1 g/L, the loss factors are in a similar range between 3 and 11. Only at higher concentrations, for example, at 3 g/L, the loss factor decreases visibly and ranges between 1 and 2. In the sample containing 5 g/L, the loss factor is significantly smaller than 1 over the whole frequency range of 0.1 to 10 Hz. The furcellaran data can be directly compared to the data for κ-carrageenan obtained by Leiter et al. [41] They investigated the effect of different ions at a constant κ-carrageenan concentration of 1 g/L on the IRI activity and the rheological properties. The addition of certain ions, such as calcium and potassium, substantially increased the storage modulus G' to values above 200 Pa within the frequency range of 0.1 to 10 Hz. In addition, the loss factor decreased to values below 1, leading to a gel-like character, which resulted in a complete loss of the IRI activity. Furcellaran solutions at 5 g/L exhibit similar rheological properties. Despite a frequency-dependent storage modulus G', precluding the classification of the sample as gel at a furcellaran concentration of 5 g/L, a gel-like character can be attributed to this sample according to the definition of Picout and Ross-Murphy. [360,361] During the recrystallization experiments, the initial furcellaran concentration undergoes concentration due to ice crystal formation. Therefore, it may be possible that a gel forms at 5 g/L. The rheologically analyzed sample containing 3 g/L furcellaran is close to having a gel-like character, and the concentration may lead to the development of a gel-like character in this system. Consequently, the observed reduction in IRI activity at elevated furcellaran concentrations can be attributed to a gel-like character of the solution. Our findings indicate that the recrystallization inhibiting activity of carrageenan polysaccharides, such as furcellaran and κ-carrageenan, is modulated by the rheological properties through the addition of specific ions and the polysaccharide concentration.

This observed behavior fails to explain the formation of individual, large ice crystals, as described previously in Figure 4.4. A similar effect has been described for κ-carrageenan solutions in combination with various added salts. [41]The formation of large ice crystals was observed across multiple samples, irrespective of whether a gel-like character is present or not. Therefore, the development of a gel or a gel-like character is inadequate to explain this observation. Local aggregation of furcellaran molecules without building a connected network may be a potential explanation leading to a local reduction of available molecules for ice crystal interaction. However, the rheological measurability of such aggregates remains uncertain. The use of labeled carrageenan or furcellaran molecules could yield valuable information in future investigations

to fully understand the interaction of such polysaccharides with ice crystals. In addition, the effects of carrageenan-based polysaccharides as cryoprotective agents on the cryopreservation of cells remain largely unknown. Unraveling the influence of cryoprotective agent on phase transition behavior within these systems demands a diverse approach that combines various experimental and simulative techniques. [394]

4.5 Conclusion

The furcellaran studied in this work showed the expected structural units, a sulfate content of 14.1 ± 0.5% (w/w), and an average molecular weight of 407 ± 18 kDa. Furcellaran was shown to inhibit ice crystal growth and recrystallization effectively with the greatest effect at a concentration of 1 g/L. The effectiveness of recrystallization inhibition is comparable to that of κ-carrageenan. This finding suggests that the sulfate content does not directly correlate with the interaction of furcellaran and other carrageenan polysaccharides or a more effective IRI activity. This further indicates that the sulfate group is not directly involved in the interaction with the ice crystal surface. For ι-carrageenan, with its higher degree of sulfation, the differences in sulfation position, flexibility, and gel formation compared to those of κ-carrageenan and furcellaran might explain the different IRI activity. At furcellaran concentrations of 3 and 5 g/L, the effect on ice recrystallization is reduced. Rheological characterization in the respective concentration range reveals that the loss factor tan δ decreases reaching values close to or below 1. A similar behavior has already been shown for κ-carrageenan in the presence of certain ions at constant polymer concentration. These findings suggest that formation of gel-like properties through ion addition and high polysaccharide concentration can negatively affect the ability of carrageenan polymers to inhibit recrystallization. Therefore, in applications where ice recrystallization inhibition is important, gel formation and the formation of a gel-like character should be avoided. To further understand the behavior and interaction mechanism of polymers and polysaccharides, molecular dynamics simulations could be used to investigate the flexibility and hydrogen bonding between the polymer and the ice surface or surrounding water molecules.

5 Detailed Analysis of the Ice Surface after Binding of an Insect Antiffreeze Protein and Correlation with the Gibbs–Thomson Equation

5.1 Abstract

Antifreeze proteins (AFPs) are able to influence the ice crystal growth and the recrystallization process due to the Gibbs–Thomson effect. The binding of the AFP leads to the formation of a curved ice surface and it is generally assumed that there is a critical radius between the proteins on the ice surface that determines the maximal thermal hysteresis. Up to now, this critical radius has not yet been proven beyond doubt or only in poor agreement with the Gibbs–Thomson equation. Using molecular dynamics (MD) simulations, the resulting three-dimensional surface structure is analyzed and the location of the critical radius is identified. Our results demonstrate that the correct analysis of the geometry of the ice surface is extremely important and cannot be guessed upfront a simulation. In contrary to earlier expectations from the literature, we could show that the critical radius is not located directly between the adsorbed proteins. In addition, we showed that the minimum temperature at which the system does not freeze is in very good agreement with the value calculated with the Gibbs–Thomson equation at the critical radius, as long as dynamic system conditions are taken into account. This proves on the one hand that the Gibbs–Thomson effect is the basis of thermal hysteresis and that MD simulations are suitable for the prediction of the melting point depression.

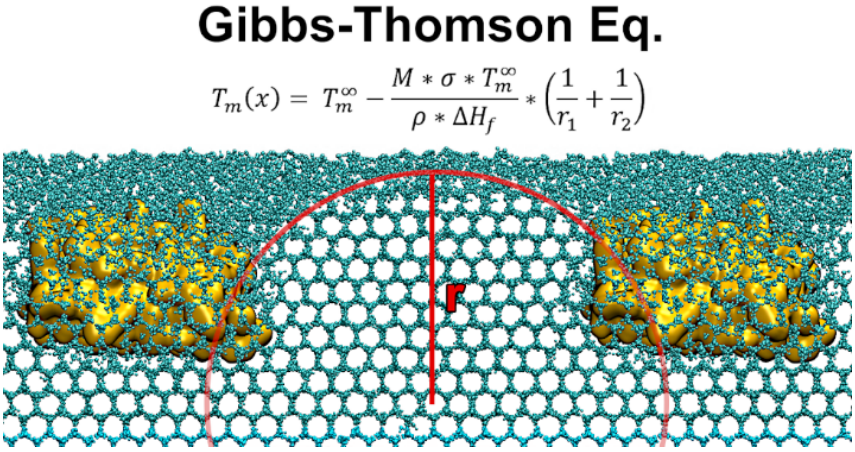

Figure 5.1. *Graphical abstract.*

5.2 Introduction

Several microorganisms, animals, and plants inhabiting cold climates produce specialized proteins called antifreeze proteins (AFPs) or ice-binding proteins (IBPs). These proteins protect body fluids from cold damage. [101,159,395,396] Under subzero temperature conditions, ice crystals can form in body fluids like cytoplasm, blood, or hemolymph and in the apoplast of plants. [159] This leads to serious damage within the surrounding tissue. In addition to physical damage, the formation of intracellular ice results in an increase in osmotic pressure due to the removal of liquid water and concentration of the remaining solutes, [397] which causes plasmolysis and disruption of the cell integrity. For this reason, AFPs are of special interest in industrial and medical applications, for example, as food additives in frozen meat, fish, or ice cream or as a cryoprotective agent during frozen storage of cells, tissues, and organs. [150]

AFPs bind to specific planes of ice crystals and thus inhibit further ice growth during cooling to a certain extent. The resulting gap between the equilibrium melting temperature and the temperature of sudden ice growth is called thermal hysteresis (TH). [26,128] Many authors term the temperature of sudden ice growth the “freezing point”, which is physically not correct, as ice crystals are already present when their growth is stopped by AFPs. Moreover, bound AFPs are able to increase the equilibrium melting temperature of the ice crystal but to a smaller extent compared to TH. [398]

Different characteristics of AFPs influence their ability to stop ice crystal growth and thereby the extent of TH. One critical property is the ice plane bound by the AFP (Figure A3.1). Two types of AFPs can be distinguished, moderately active and hyperactive AFPs. Hyperactive AFPs are able to bind to the basal plane or to the basal plane in combination with other planes [399,400] and are found in insects and some microorganisms. [99] Their activity is up to 10-folds higher than that of moderately active AFPs, which are typically found in fish. [143] Moderately active AFPs bind preferably to planes parallel to the c-axis. [128] For example, winter flounder AFPs bind to the pyramidal plane. [401] In addition to being able to influence the freezing and melting behavior of an ice crystal, AFPs affect ice recrystallization. During the process of ice recrystallization, the total mass of ice crystals is constant, while the number of crystals decrease and the mean ice crystal sizes increase [11,12] by thermodynamic reasons. The addition of AFPs reduces recrystallization effects even when they are added in low concentrations. [25,28]

In general, it is postulated that, due to their ability to interact with the ice crystal surface, the presence of AFPs leads to a pinned surface with a characteristic curvature [402] (Figure 5.2).

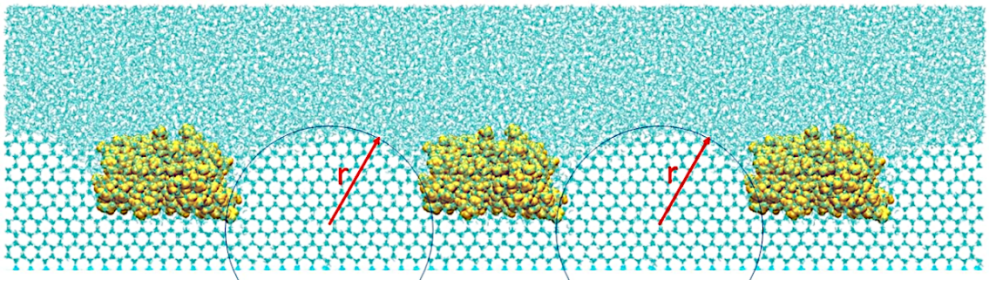

Figure 5.2. *Curved ice surface between three AFPs (yellow). Ice can grow between the proteins and forms a curved surface. The radius r of the curvature influences the vapor pressure of the solid phase, which leads to a limitation of ice growth, although the temperature decreases.*

Both effects, TH and ice recrystallization inhibition, involve the Gibbs–Thomson effect (Eq 5.1), which describes the change in the melting temperature due to a curved surface at constant pressure. A decisive parameter here is the radius r or the diameter $x = 2r$ of the curvature.

Eq 5.1: Gibbs–Thomson equation for a spherical particle.

$$\Delta T_m = T_m^{\infty} - T_m(x) = \frac{4\ \sigma_{sl}\ T_m^{\infty}}{x\ \Delta H_f\ \rho_s} \tag{5.1}$$

Where: ΔT_m $= thermal\ hysteresis$
T_m^{∞} $= bulk\ melting\ temperature$
$T_m(x)$ $= depressed\ melting\ point$
σ_{sl} $= ice - water\ surface\ tension$
x $= diameter$
ΔH_f $= enthalpy\ of\ fusion$
ρ_s $= density\ of\ the\ solid$

For the calculation of TH ΔT_m, which is the difference between the bulk melting temperature T_m^{∞} and the melting temperature of the ice crystal $T_m(x)$ with a diameter of size x, the surface tension σ_{sl} between the solid and liquid phase, the bulk enthalpy of fusion ΔH_f, and the density of the solid ρ_s is needed. The factor of 4, often referred to as the geometry factor, originates from the Young–Laplace equation (Eq 5.2), which describes the pressure difference Δp across a curved interface.

Eq 5.2: Young–Laplace equation.

$$\Delta p = -\sigma\left(\frac{1}{r_1}+\frac{1}{r_2}\right) \tag{5.2}$$

Where: $\Delta p = pressure\ difference$
$\sigma = surface\ tension$
$r_1 = radius\ 1$
$r_2 = radius\ 2$

If a spherical particle or surface is assumed, both principal radii r_1 and r_2 are of the same length and can be combined to $2/r$ or $4/x$. This results in a geometrical factor of 4 as seen in Eq 5.1. In the case of a cylindrical shape, one of the radii becomes infinite and therefore only the radius perpendicular to the height of the cylinder has an influence. This results in $1/r$ or $2/x$ and leads to a geometric factor of 2 for a cylindrical shape in Eq 5.1. It is obvious that the value of $T_m(x)$ depends not only on the radius but also on the given geometry. Unfortunately, less attention is paid to the latter in the literature.

To prove the assumption that the Gibbs–Thomson effect leads to TH of AFPs, many attempts have been discussed in the literature. As it is impossible by direct observation to prove the existence of the curvature on an AFP-studded ice crystal surface, to measure the curvatures or the surface allocation of the bound molecules, most studies are based on simulation results from molecular dynamics (MD) studies.

Experimentally, the binding plane or multiple binding planes can be identified with fluorescence-labeled AFPs, [403,404] and the TH activity can be determined by differential scanning calorimetry, sonocrystallization, or other methods. [136,405,406] In addition, the ice recrystallization inhibition can be quantified by several assays and optical methods. [25] An attempt to determine the surface distribution of bound AFP molecules experimentally in an indirect way was described by Drori et al. [134] Fluorescence-labeled *Tenebrio molitor* AFPs (*Tm*AFPs) bind to a single ice crystal in a specialized microfluidic system. Due to the intensity of the emitted light, the number of bound molecules can be determined. From these investigations, they calculated an average distance of 7 nm for a measured TH value of 0.73 K.

In contrast to experimental methods, MD simulations can deliver information about the details on a molecular level. During the last decade, MD simulations gained a lot of importance in the field of antifreeze and ice-binding molecules. It is shown that the simulation results support the theory of a curved ice surface and the applicability of the Gibbs–Thomson effect. [126,407,408] A point that one has to keep in mind for MD simulations of AFPs is that the simulations provide

only information about the interaction of the AFP with one specific ice plane. Nevertheless, crystal growth is a three-dimensional process and AFPs have different affinities for the different planes, which makes a direct comparison of TH between the experiment and simulation unfeasible. Furthermore, it is necessary to run the simulation long enough to allow rare events to happen. These in turn can lead to overgrowth of the protein if the ice crystal surface has developed a distinctive curvature. The time period of the experiment is of course much longer than that of the simulation.

A good example is provided by Naullage et al. [409] They compared the experimental findings of Drori et al. with a MD simulation of *Tm*AFPs with a distance of 7.4 nm between the centers of mass of the molecules resulting in a TH of 9 K after 100 ns of simulation time. [409] According to the large difference of TH of the experimental results, they argued that the experimental distance is determined by averaging the statistical distribution of antifreeze molecules and that it is likely that there are also larger open spaces in between, which lower the extent of TH in the experiment. In addition, the observation time in the experiment is much longer than that in the simulation, allowing for rare formation of ice bridges. Based on this and additional simulations, they suggest "that the longest distances in the distribution control the thermal hysteresis" (Naullage et al. 2018, page 1716). This seems reasonable, because the ice radius between two bound AFPs may increase with a greater distance between the bound molecules and because of this, $T_m(x)$ rises. We go along with this argumentation and want to add that the three-dimensional aspects of ice growth and the dynamic equilibrium on the surface must be taken into account too, especially when it comes to the critical radius and the linkage of this radius to the Gibbs–Thomson equation.

There are publications that analyze and address these aspects but do not combine them into a complex overall picture. Kuiper et al. simulated the binding of spruce budworm (sbw) AFPs to a growing ice crystal and found that the binding of the protein to the ice surface is facilitated by ordered water molecules. [126] Moreover, this ordering seems responsible for the ice plane specificity. In addition, they calculate the radius according to the Gibbs–Thomson equation with the cylindrical geometry factor and create an overlay of the curvature and the circular segment obtained. Unfortunately, it is not clear from their publication why the cylindrical geometry factor is used and why the overlay is created at the location between the sbwAFPs, since no complete analysis of the three-dimensional ice surface structure is shown.

Also, Midya et al. [410] calculated the expected length of the radius according to the Gibbs–Thomson equation and compared it with their simulations at different temperatures. However,

it is not clear what geometry factor is used and where and how they measured the radius. Furthermore, the expected and calculated radii differ by at least 1.8 nm from each other. Additionally, there are several other publications that show a curved ice surface but do not link the radius of curvature with the Gibbs–Thomson equation. [407,408,411]

An interesting difference between the simulations of Kuiper et al. and Midya et al. is the overall structure of the ice surface. While Midya et al. visualize a spherical or ellipsoidal curvature with the center at the intersection of the diagonals, Kuiper et al. assumes a cylindrical surface. As shown above, the geometrical factor used in the Gibbs–Thomson equation is critical for the calculation of TH. As many different radii of curvature can be formed during the process of ice growth, from our point of view, the critical location where ice starts to overgrow the AFP needs first to be identified. Second, the surface geometry at this point needs to be evaluated to identify the correct Gibbs–Thomson equation for the calculation of TH. This illustrates the importance of knowing the structure of the ice surface and where different radii can be located.

Another important aspect is the dynamic behavior of the ice surface close to the equilibrium. Water molecules are able to join or desorb the ice lattice, which leads to a fluctuation of the surface curvature and thus its radius, making a static evaluation unfavorable. [126]

To accomplish these aspects in this study, radii in all directions inside the simulation box will be analyzed (Figure 5.4A) to identify the critical radius, which is decisive for the overgrowing ice front. Due to the rectangular arrangement of the AFPs in the simulation (Figure A3.2B), we expect a spherical elevation in the center similar to Midya et al. to arise. As stated by Naullage et al., the longest distance should yield the critical radius, which is the diagonal direction between two AFPs in our simulation setup. [409] To our knowledge, this is the first time that the diagonal is explicitly taken into consideration and that radii in all directions within the system are observed to identify the critical radius. Moreover, the temperature T_{min} at which the system remains unfrozen is determined by simulating different temperatures. The ice surface in the system at T_{min} is then analyzed in the static and dynamic way and $T_m(x)$ is calculated with the Gibbs–Thomson equation. This should yield the observed T_{min}, verifying that MD simulations can predict accurately the melting point depression in accordance with the Gibbs–Thomson equation for a given geometry.

5.3 Experimental Section

5.3.1 Software and Simulation Parameters

The MD simulations done with GROMACS [412] version 2019.3 are visualized and analyzed using the Visual Molecular Dynamics [330] (VMD) viewer. In order to achieve realistic properties of ice and the freezing process, the TIP4P/Ice water model [413] in combination with the OPLS-AA/L [414] force field is used. The OPLS-AA force field is a versatile and widely used force field and the L version is improved for peptides. [415] The water model is based on the four-site TIP4P model but the parameters are adapted to yield a better phase transition behavior. With a melting point of 269.8 ± 0.1 K [416] compared to 229 K of TIP4P [417] it is appropriate for the simulated system. In addition, the surface tension values of the ice–water interface can be discriminated for the individual ice planes. These parameters, specific for the TIP4P/Ice model, will be required for the correct application of the Gibbs–Thomson equation. Therefore, the surface tension for the secondary prism plane is used, since this is the growing ice plane in the simulated system. To control the pressure inside the simulation box during the production run to 1 bar, an anisotropic Parrinello–Rahman barostat with a coupling constant of 2 fs is applied. After energy minimization, the temperature is set to the desired value using a V-rescale thermostat in the canonical ensemble. Subsequently, the pressure in the isobaric–isothermal ensemble is controlled with a Berendsen barostat. All bonds including hydrogen atoms are constraints with the LINCS [315] algorithm enabling an integration time step of 2 fs during the production run.

Furthermore, periodic boundary conditions (PBC) are used during the simulation to eliminate boundary effects and to create a defined geometry of regularly distributed AFP molecules. Therefore, the unit cell, which is the simulated system, is duplicated in all three dimensions and placed around the simulation box (Figure A3.2). In Figure A3.2A, the principle of PBC is exemplarily shown in two dimensions for the yellow molecule. Due to the periodic boundary the yellow atom, which leaves the simulation box at the right side, re-enters from the left.

5.3.2 Simulation System

The simulation box with a size of 9.95 nm × 9.98 nm × 7.35 nm in the *x*-, *y*-, and *z*-direction contains 93,560 atoms in total, whereof 1760 water molecules are restrained as a single ice layer (Figure 5.3A). Since it is highly unlikely that water will start crystallizing under the simulation conditions, this ice layer functions as a seed crystal to promote ice crystal growth. To

ensure binding of the insect AFP, the ice layer is able to grow freely in the direction of the secondary prism plane. The AFP is oriented with its ice-binding site toward the ice front and can move freely during the simulation. A slab of 919 restraint water molecules prevents the growth of ice to the lower direction, which has to be avoided since three-dimensional PBC are applied. The simulated sbwAFP (Figure 5.3B) (RCSB: 1M8N) is a hyperactive insect AFP, which is able to bind to the secondary prism plane and the basal plane. [404,418] Kuiper et al. already demonstrated that this specific AFP is able to bind to the secondary prism plane of a growing ice crystal in an MD simulation. [126]

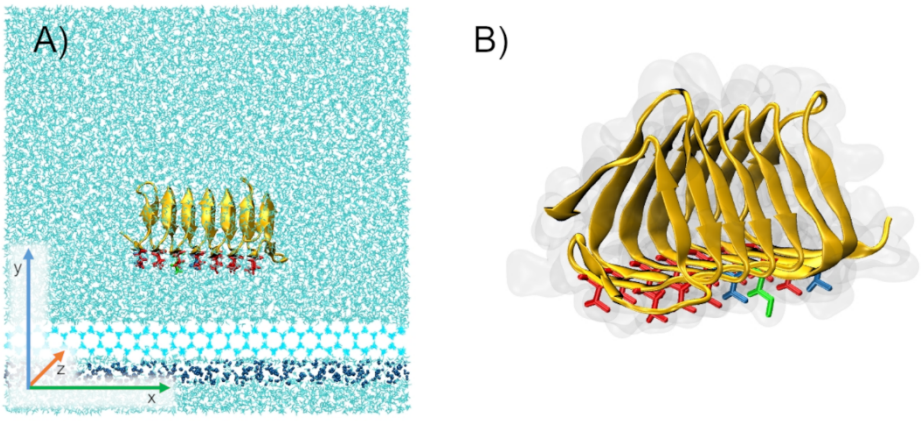

Figure 5.3. *(A) Starting configuration of the system. The sbwAFP is placed in the center, and the ice-binding site is oriented toward the fixed ice layer (light blue). In addition, a fixed layer of water molecules (blue dots) is introduced to prevent ice growth in the downward direction. Finally, the box is filled with water molecules (turquoise). (B) sbwAFP visualized as a cartoon drawing (yellow). For a better representation of the ice-binding site, the corresponding amino acids are shown as a licorice representation and in different colors. Threonine residues are depicted in red, valine in blue, and isoleucine in green. To get an impression of the dimension, the surface is indicated as a gray shadow.*

5.3.3 Determination of T_{min} after Binding of sbwAFP

The temperature T_{min} is defined here as the lowest temperature at which the system does not freeze completely. To determine T_{min}, the box is simulated at different temperatures below the melting point and the state of the system is observed. In addition to the visual assessment if the system is freezing or not, the progression of the density is examined to see density changes due to the ice growth. Moreover, the simulation with the lowest temperature, which remains in a liquid state, was repeated three times in total and extended to 300 ns. These simulations will be abbreviated in the further course of this paper as Sim 1, Sim 2, and Sim 3.

5.3.4 Visualization of the Ice Surface and Determination of the Curvature Radius

For the visualization of the ice surface and for the examination of the radius of curvature of the ice crystal in between the bound molecules, slabs are cut out of the simulation box in several directions. The advantage of using slabs is that the desired plane is visualized without superimposition of water molecules in the planes behind and in front. An easy and fast method to create these slabs is the use of the clipping plane tool in VMD. This tool allows cutting the three-dimensional box along a plane which is defined by its vector, and slabs with a thickness of 0.7–1 nm are created. Hence, the cuts can be set freely within the simulation box, it is possible to obtain horizontal (xz-plane) and vertical (yz-plane) slabs. The horizontal slabs provide an overview of the ice surface and allow the identification of the geometry of the ice surface landscape. To visualize the curvature of the ice surface, the vertical slabs are used. All vertical slabs, which are analyzed, are shown in Figure 5.4A) and alphabetically numbered. In order to calculate the radius based on the vertical slabs, the chord length s and the height of a circular segment h (Eq 5.3, Figure 5.4B) are used.

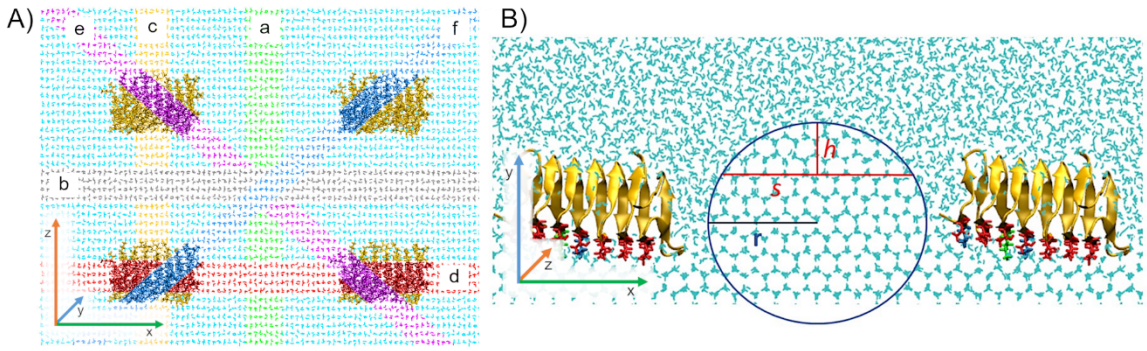

Figure 5.4. *(A) Slabs that are generated and observed during the simulation. The slab of the xz-plane is shown from the top. (B) Exemplary image of the slab d (xy-plane) viewed from the front of the box. The radius r can be obtained by measuring the length s of the chord and the corresponding height h.*

Eq 5.3: Calculation of the radius of a circular segment.

$$r = \frac{4h^2 + s^2}{8h} \tag{5.3}$$

Where $r = radius$:
$h = height$
$s = chord\ length$

The precision of this method is estimated by calculating the radius three times at different heights and chord lengths. These radii result in three melting temperatures $T_m(x)$, according to the Gibbs–Thomson equation. The greatest deviations occur when a clear phase boundary cannot be identified. Taking this into account, the largest measured standard deviation is 0.574 K of 96 slabs in total. To get a better overview over the deviation of this method, the smallest deviation and the third quartile are determined. The third quartile states that 75% of all deviations are less than or equal to this value. They are 0.007 and 0.234 K, respectively. Moreover, the deviation of the individual temperature ranges is far greater than the standard deviation caused by the determination method. In conclusion, we can state that the performed determination method is a simple and quick analysis with adequate accuracy. An alternative would be the calculation and usage of an order parameter to create an artificial cut off for the separation between ice and water. However, the selection of the cut off value itself can influence the structure of the ice surface, especially since it is a highly dynamic interface and the computational time increases drastically for the analysis.

Depending on the ice surface geometry, the Gibbs–Thomson equation is adapted resulting in Eq 5.4 for a cylindrical and Eq 5.5 for an arbitrary elliptical geometry. Subsequently, the mean value and the corresponding standard deviation are calculated. When using two different radii in the Gibbs–Thomson equation (Eq 5.5), the average value of the radii is used.

The radii depend on the dynamic and the geometry of the ice surface. Since the simulation at T_{min} is repeated three times, a static evaluation at fixed times is performed to analyze differences between identical starting setups. In addition to the static analysis, a dynamic analysis of the radii is carried out. Here, the radii are measured over the course of the simulation, whenever the curvature is at its maximum.

5.3.5 Calculation of the Expected TH with the Gibbs–Thomson Equation

With the calculated radii of curvature, the expected depression of the melting temperature $T_m(x)$ is calculated with the Gibbs–Thomson equation (Eq 5.1). The parameters used are shown in Table A3.1 in the Appendix. [416,419] They depend on the used water model and are specific for the pyramidal plane bound by the AFP in the simulation. Depending on the geometry of the ice surface, the geometry factor of the Gibbs–Thomson equation is adapted. The depressed melting temperature $T_m(x)$ of a cylindrical surface with a radius *r* can be calculated according to Eq 5.4.

Eq 5.4: Gibbs–Thomson equation for a cylindrical surface geometry.

$$T_m(x) = T_m^{\infty} - \frac{M\ \sigma\ T_m^{\infty}}{\rho\ \Delta H_f\ r} \tag{6.4}$$

Where: $T_m(x) = depressed\ melting\ point$
$T_m^{\infty} = bulk\ melting\ temperature$
$M = molar\ mass\ of\ ice$
$\sigma = ice - water\ surface\ tension$
$\rho = density\ of\ the\ solid$
$\Delta H_f = enthalpy\ of\ fusion$
$r = radius\ of\ curvature$

whereas $T_m(x)$ of an arbitrary elliptical geometry can be calculated with Eq 5.5. This applies also for a spherical structure since this is a special case of an ellipse where both radii are of the same length.

Eq 5.5: Gibbs–Thomson equation for an elliptical surface geometry with principal radii r_1 and r_2.

$$T_m(x) = T_m^{\infty} - \frac{M\ \sigma\ T_m^{\infty}}{\rho\ \Delta H_f} \times \left(\frac{1}{r_1} + \frac{1}{r_2}\right) \tag{5.5}$$

Where: $T_m(x) = depressed\ melting\ point$
$T_m^{\infty} = bulk\ melting\ temperature$
$M = molar\ mass\ of\ ice$
$\sigma = ice - water\ surface\ tension$
$\rho = density\ of\ the\ solid$
$\Delta H_f = enthalpy\ of\ fusion$
$r_1 = principal\ radius\ 1$
$r_2 = principal\ radius\ 2$

Since many different slabs were evaluated, the ice crystal surface is analyzed in detail and the critical radius determining the extent of the melting point depression can be identified.

5.4 Results and Discussion

5.4.1 Determination of T_{min} after Binding of sbwAFP

For the determination of T_{min} different temperatures were simulated for at least 200 ns. The simulation results were analyzed at first visually and the state of the system was observed. Second, a detailed analysis of the density curve was carried out.

The starting configuration is identical for each simulation (Figure 5.5A), the protein is oriented with its ice-binding site towards the ice surface and is able to move freely within the box. At the beginning, the ice grows in the *y*-direction and the distance to the protein becomes smaller. During the first 50 ns, the protein is able to bind to the growing ice crystal. Directly after the binding process, no curvature is visible (Figure 5.5B). Remarkably, the protein binds in each of the eight simulations performed but the binding orientation is slightly different, which may influence the ice formation. In some simulations, the protein binds parallel to the *x*-axis and in other cases it is shifted. This can exemplarily be seen in Figure 5.5B,D where the proteins are shifted on one side in the direction of the *y*-axis. In contrast, in Figure 5.5C, the protein is bound to the ice surface parallel to the *x*-axis. An important aspect regarding the binding behavior is the interaction strength between the protein and the ice surface. "AFPs that adsorb strongly will have higher surface concentrations and a larger thermal hysteresis gap" (Kumari et al. 2020, page 2444). [420] The simulative determination of this interaction strength proves to be difficult, since the dynamic of the ice surface has a non-negligible influence on the adsorption of the protein. This in turn depends on the force field and the water model used. Therefore, a comparison and an estimation of which combination of force field and water model provides the most accurate results or whether the influence of the force fields is not decisive at all should be included in future studies.

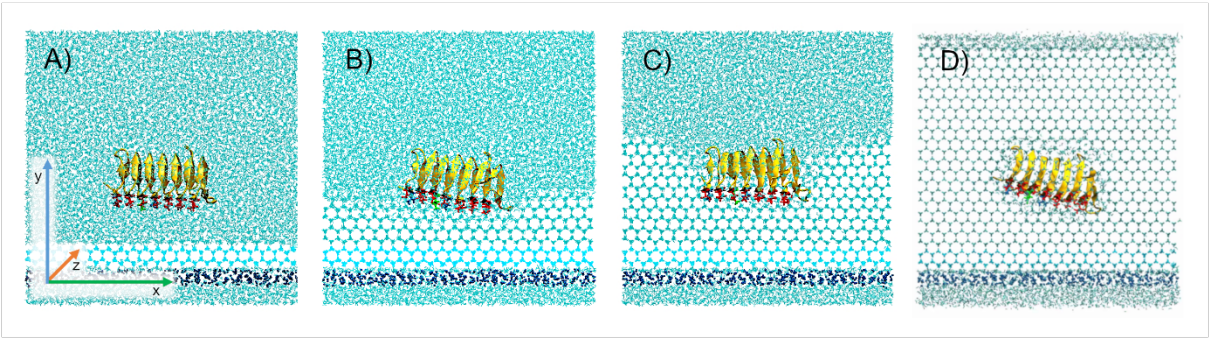

Figure 5.5. *Basic course of the simulation and possible system states. (A) Starting configuration, which is the same for all simulations. (B) AFP is able to bind to the growing ice surface. The picture is taken at a temperature of 262.5 K (Sim 3). (C) After the binding process, ice continues to grow and a curvature is formed (262.5 K, Sim 1). (D) If the temperature is too low, the protein is overgrown and trapped in the ice (262.2 K). Depending on the actual degree of supercooling, the endpoint of the simulation is either (C) or (D).*

After the protein has bound to the ice surface, the ice crystal continues to grow and a curvature is formed. With increasing curvature, the radius and thus the melting temperature decreases and the growing ice front is stopped if the set simulation temperature equals with the melting temperature (Figure 5.5C). If the simulation temperature is lower and larger radii of curvature can be formed, the AFP is overgrown and trapped inside the ice crystal (Figure 5.5D).

According to the visual analysis of the simulation box, the lowest temperature at which the system does not freeze completely is at 262.5 K. At even lower temperatures (262.2, 262.0, 261.5, and 260 K), the system is able to freeze and the protein is trapped in the ice crystal.

In addition to the visual observation, the density and the height of the ice layers were examined to identify whether the system at the given temperature freezes or not. The development of the density with and without AFPs is shown in Figure 5.6. We assume that the ice growth rate is proportional to the decrease in density. Without AFPs, the system freezes within 100 ns at a temperature of 265 K. Due to the inserted ice grid, the density at the start of the simulation is already somewhat lower than that for pure water. In the further course of the simulation, the density decreases almost linearly until the box is frozen in the y-direction. In case no AFP is present, a lowest density of 925 kg/m^3 is reached (Figure 5.6A). In contrast, the presence of sbwAFP increases this value to about 935 kg/m^3, assuming that the temperature is low enough for the ice to overgrow the protein (Figure 5.6B). Three phases can be identified that always occur in our simulations when the system with AFPs freezes completely. Figure 5.6B shows the density progression of a system at 262.2 K that freezes in the course of the simulation. The three phases are alphabetically numbered from a to c. During phase a, the density decreases linearly due to the ice formation. After binding of the protein, ice growth is impaired and the ice can no longer grow with a straight surface. The pinning of the ice surface results in a curvature and a reduced ice formation velocity (phase b). This means that the ice still continues to grow with a curved surface. As long as this curvature is not strong enough to stop the ice growth, the ice is able to grow over the protein and a continuous layer can form. In this case, the growth rate of the ice can increase again as can be seen in phase c. The system then freezes up to a density value of approximately 930 kg/m^3. This relation holds true for all simulations below 262.5 K.

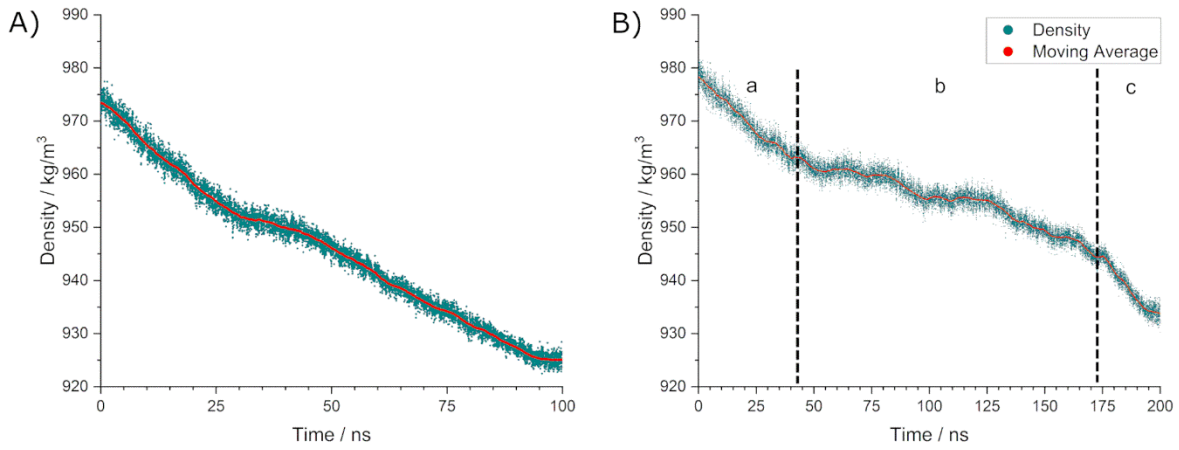

Figure 5.6. *(A) Progression of the density at 265 K without AFPs. At the beginning, the density is around 975 kg/m3 and decreases linearly during the simulation. At 95 ns, the box is frozen and the density reaches a threshold of 925 kg/m3. (B) System with AFPs at a temperature of 262.2 K. The density progression can be divided into three phases a–c. In the first phase (a) from 0 to 45 ns the ice crystal grows and the protein binds to the ice surface. Afterward, in the second phase (b), the curvature develops but cannot stop the formation of ice. The velocity of the ice formation is reduced. When the protein is engulfed and the first ice layer above the protein is formed, the hindrance of ice formation is lower and thus the ice formation rate increases again. This can be seen in the third phase (c).*

At moderate supercooling, the resulting curvature prevents freezing and the course of the density approaches a threshold value. The threshold value depends on temperature, since at higher temperatures the critical radius of curvature is larger and is therefore reached earlier. This limits the maximum amount of ice in the system. For example, at a temperature of 262.5 K, a lowest density of approx. 960 kg/m^3 is reached (Figure 5.7), whereas at 265 K, the density does not decrease below 970 kg/m^3.

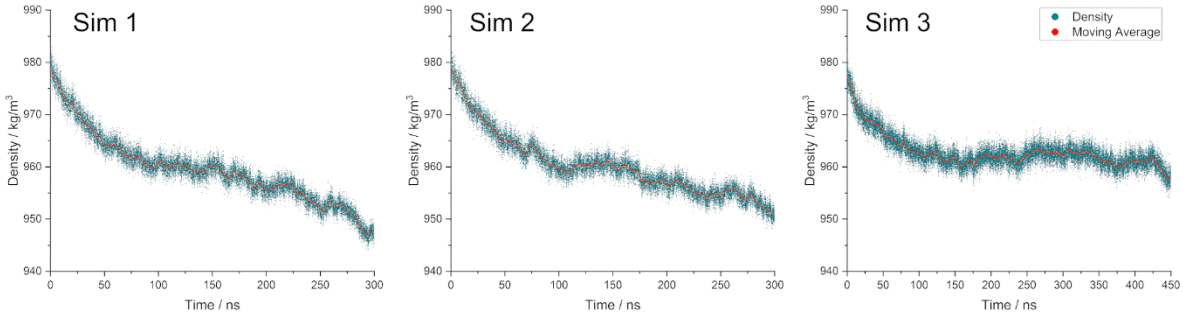

Figure 5.7. *Density progression of the three simulations at 262.5 K. The first two simulations, Sim 1 (left) and Sim 2 (middle), seem to reach a threshold around 150 ns, but the density continues to decrease in the further course of the simulation. Sim 3 (right) is stable at a density around 960 kg/m3 for a simulation period of 450 ns.*

The simulation at 262.5 K was repeated three times in total. Hereinafter referred to as Sim 1, Sim 2, and Sim 3. This was done to see differences between individual simulations at the same

temperature, to evaluate the impact on the resulting curvature and to make sure that 262.5 K is the critical temperature T_{min}. Figure 5.7 shows the progression of the density of the three simulations at 262.5 K. Although all simulations have the same initial conditions, the ice formation and therefore the density progression is not identical. One influence that may play a role here is the previously mentioned slightly different binding configuration of the protein. For Sim 1 and Sim 2, the course of the density is quite similar. It reaches apparently a constant value around 150 ns but afterward it decreases again. Even though a longer simulation might have led to an overgrowth of the protein, this could not be observed in the simulations presented here. In contrast, Sim 3 approaches the threshold slightly above 960 kg/m^3 and stays constant for the rest of the 450 ns of the simulation. To ensure that the density reached a constant value, the simulation was extended from 300 to 450 ns. The initial ice formation seems to be the same for all three simulations, since the density converges to a value of 960 kg/m^3 during the first 150 ns. In this context, the simulation time needed to produce reliable information is important. As seen in the density progressions of Sim 1 and Sim 2, the system would have been stable at around 150 ns without further simulation. This may lead to wrong assumptions when systems with antifreeze molecules are simulated in a too short range. This shows the principal need of relatively long simulation times for well-founded statements.

We can conclude from the detailed simulation analyses that the lowest temperature at which the system does not freeze completely is close to $T_{min} \approx 262.5$ K. Hence, Sim 1 and Sim 2 tend to freeze for longer simulation times; the temperature T_{min} may be slightly higher. These three simulations are analyzed in more detail below for the surface geometry and the different radii.

5.4.2 Preanalysis of the Three-Dimensional Ice Surface at T_{min}

Before the critical radius can be determined, the general structure of the ice surface needs to be examined. A good way to get an overview over the geometry of the ice surface is to analyze horizontal (*xz*-plane) slabs through the simulation box (Figure 5.8). Because of its regular structure, ice can easily be distinguished from the disordered water molecules. All three simulations at 262.5 K show the same cylindrical ice pattern at the surface.

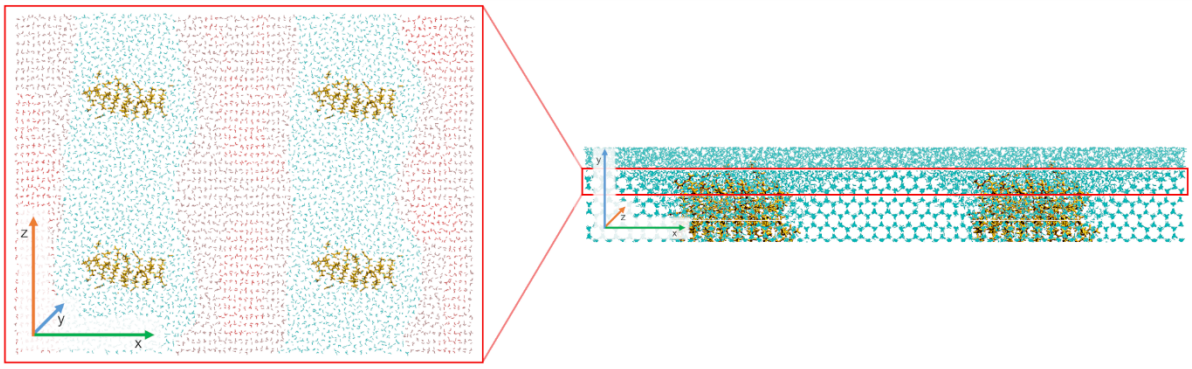

Figure 5.8. *Top view of a horizontal slice to visualize the geometry of the ice surface. The water molecules are roughly divided into ice (red) and water (cyan). To spatially classify the slice, the front view of the box is depicted on the right.*

To make the cylindrical shape obvious, the length axis of the cylinder is analyzed with the help of slab a (Figure 5.4A). No curvature can be identified in the *z*-direction of slab a during all simulations and at different simulation times (Figure A3.3).

Due to the shape of the surface, the critical radius, which determines the depression of the melting temperature, has to be on the cylinder and perpendicular to the longitudinal axis (*z*-direction). In addition, it can be seen from Figure 5.8 that the cylinder is not exactly uniformly shaped and different curvature radii are present in the *x*-direction. The shortest radius is directly between the two AFP molecules and corresponds to slab d, whereas slab b is located at the widest point of the cylinder (Figure 5.4A). Again, this is the same for all three simulations.

5.4.3 Analysis of the Radii of Curvature and Calculation of $T_m(x)$ with the Gibbs–Thomson Equation

Now, the different radii are determined and inserted into the Gibbs–Thomson equation. In this way, the expected melting temperature $T_m(x)$ at this location is determined. In the case of the critical radius, this should correspond to the temperature T_{min} already determined. The geometry of the ice surface plays a critical role in the calculation of $T_m(x)$ with the Gibbs–Thomson equation. As already shown, a cylindrical surface between the proteins with a longitudinal axis in the *z*-direction can be seen and one may assume that the critical radius is to be found on the cylinder perpendicular to the longitudinal axis. We investigated this aspect in more detail for the three simulations Sim 1, Sim 2, and Sim 3 at $T_{min} = 262.5$ K. Therefore, all reasonable radii in the system are examined, not only those on the cylinder. First, the static analysis at specific time points provides information about the temporal behavior of the various radii in the system. For example, radii, which are permanently very short, can be neglected, since the

resulting melting temperature $T_m(x)$ at this point is always below the ambient temperature. Second, the radii that cannot be excluded are subjected to a dynamic analysis in which they are measured at a maximum curvature.

Static Analysis

At first, the slabs c and d directly between the proteins are examined (Figure A3.4). For slab d located between the proteins in the *x*-direction (Figure A3.4A), the cylindrical version of the Gibbs–Thomson equation (Eq 5.4) can be used. The resulting radii of curvature are comparably short and the melting temperature is below the ambient temperature (Table A3.2).

In contrast, slab c between the proteins in the *z*-direction (Figure A3.4B) is not part of the cylindrical surface geometry and therefore the cylindrical geometry factor cannot be used. For the calculation of the melting temperature with Eq 5.5, we need the radius of curvature perpendicular to slab c in the *x*-direction. This is delivered by the surface analysis of slab b (Figure A3.5).

It turns out that a minimum height of the ice surface with a negative radius of slab b is directly between the proteins. For the calculation of the corresponding melting temperature, Eq 5.5 was used with the two perpendicular radii at the cross-section (c and b). As the radius in the *x*-direction is negative, the calculation of melting temperatures leads to comparably high melting temperatures (Table 5.1). Due to the negative radius, there is a high tendency for water molecules to adsorb to the surface at this point. Nevertheless, by filling this area, the radius increases to zero (flat surface) and the radius in the *z*-direction dominates the melting temperature. Yet, the radius in the *z*-direction is too small to be the critical radius. One can see this by elaboration of the measured radii for different simulation times (Table A3.2). For these reasons we assume that the critical radius cannot be located at this position.

Table 5.1. *Melting Temperatures of several slabs at different locations, calculated with the cylindrical (Eq 6.4) or the elliptical Gibbs–Thomson equation (Eq 6.5).*

Simulation	Time / ns	Slab	Temperature $T_m(x)$ / K	Equation
1	200	d	261.47 ± 0.36	6.4
2	200	d	261.15 ± 0.49	6.4
3	200	d	262.10 ± 0.17	6.4
1	200	b+c	262.63	6.5
2	200	b+c	270.79	6.5
3	200	b+c	266.87	6.5
1	200	e	264.64 ± 0.16	6.4
2	200	e	263.42 ± 0.31	6.4
3	200	e	264.58 ± 0.19	6.4
1	200	f	264.22 ± 0.24	6.4
2	200	f	263.70 ± 0.09	6.4
3	200	f	264.37 ± 0.13	6.4
1	200	e+f	259.07	6.5
2	200	e+f	257.33	6.5
3	200	e+f	259.16	6.5
1	175	b	262.97 ± 0.18	6.4
1	200	b	265.52 ± 0.12	6.4
2	175	b	264.18 ± 0.17	6.4
2	200	b	265.50 ± 0.32	6.4
3	175	b	265.63 ± 0.08	6.4
3	200	b	264.98 ± 0.01	6.4

A similar problem arises for the diagonals, slabs e and f. They are located at the cylinder, but to use the cylindrical Gibbs–Thomson equation, they need to be perpendicular to the length axis of the cylinder. If Eq 5.4 is used erroneously, the radii will be incorrectly prolonged leading to an unfeasible high melting temperature as shown in Table 5.1. On the other hand, one can state that slabs e and f are approximately perpendicular and calculate the melting temperature with these two radii and Eq 5.5. This results in comparably low values for the melting temperature

(Table 5.1) and thus provides evidence that in this system the longest distance between the proteins is not decisive for the melting point depression.

The last slab to be analyzed is the most promising, which is slab b. It is perpendicular to the longitudinal axis and at the same time the widest point of the cylinder along slab a. In addition, the usage of the cylindrical Gibbs–Thomson equation is perfectly applicable in this case.

As seen in Table 5.1, most of the calculated melting temperatures are above $T_{min} = 262.5$ K. This means that the curvature would still be able to grow and the maximum melting point depression is not reached yet.

Only the melting temperature $T_m(x)$ at 175 ns in Sim 1 seems to be in the right order of magnitude. In addition, these values suggest that there are large differences between the simulations. However, keeping in mind that the ice surface is in a dynamic equilibrium, it is not surprising that the radii of curvature are changing over time and cannot be expected to be the same between different simulations at fixed times. It can be concluded from the static analysis that the individual simulations show differences and therefore fixed time points cannot be directly compared with each other. Although the overall ice formation seems to be similar based on the density curves, the formation and variation of the curvature development are different in each simulation. The curvature may be formed the same way with a similar radius, but this is a coincidence for a fixed time point. Another reason for the deviations of the three simulations at 262.5 K may be the slightly different binding orientations of the AFP, since this could have an impact on the ice formation and the surface topology. Therefore, a dynamic analysis of the most promising surface area of slab b is shown in the next section.

Dynamic Analysis

In the dynamic analysis, the development of slab b was examined throughout the simulation. During the simulation time, the ice curvature at slab b builds up until a certain extent but then starts to melt again (Figure 5.9). This happens repetitively throughout all simulations and during the whole simulation time, showing impressively the dynamic equilibrium. In contrast, the curvature of all other slabs is formed without the curvature melting away completely and may be approximated as continuously growing until the maximum curvature is reached. This does not mean that the ice surface here is rigid and that there is no dynamic equilibrium between melting and freezing. Nevertheless, it stands out that the ice formation and the ice surface in slab b is far more dynamic than in the other slabs.

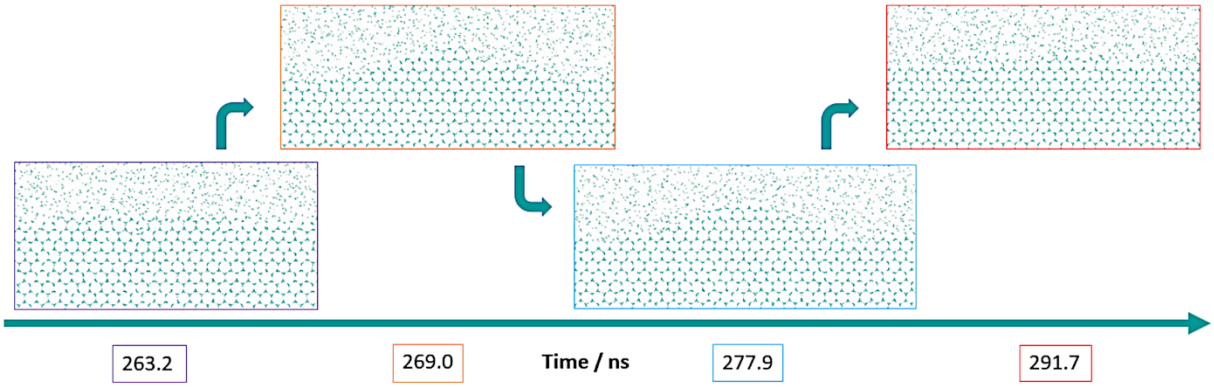

Figure 5.9. *Formation of the curvature between 263 and 292 ns at slab b (yz-plane) of Sim 3. At 263 ns, no curvature is visible. In the further course of the simulation, the curvature starts to form and is stable for around 20 ns. During this time, minor fluctuations happen, but no significant growth or melting is observed. After 30 ns, the curvature is completely melted and the ice formations starts again to form a new curvature.*

The ice formation at the position of slab b was recorded, and the radius of curvature was determined whenever it reaches a maximum. This should yield a melting temperature in the range of the previously determined T_{min}.

The resulting melting temperatures $T_m(x)$ shown in Table 5.2 were calculated with the cylindrical Gibbs–Thomson equation (Eq 5.4). They are very close to the observed T_{min} of 262.5 K. However, the values tend to be somewhat higher, which would be in agreement with the previous observation that Sim 1 and Sim 2 could freeze during longer simulations.

Table 5.2. *Melting point at Position b determined at maximum curvature.*

Simulation	Time / ns	Slab	Temperature $T_m(x)$ / K
1	172.7	b	263.21 ± 0.29
2	122.9	b	262.75 ± 0.09
2	178.9	b	262.46 ± 0.22
3	217.2	b	262.94 ± 0.08

Because of these findings, we assume that the critical radius is located at the position of slab b. To summarize the results of the dynamic analysis, it can be said that the length of the radii and the resulting melting temperatures at slab b are in very good agreement with T_{min}. It is noteworthy that the critical radius is not found between the proteins and is located on the free, unoccupied ice crystal surface. Contrary to Naullage et al., [409] the critical radius in our simulation is not located at the widest distance in the distribution, since this would be the diagonal

between the proteins. Instead, one could say that the critical radius is located at the largest distance of the formed geometric structure on the ice surface.

In addition, it is important for us to emphasize once again that the simulations reproduce the Gibbs–Thomson effect well, but a comparison of the simulation with experimentally measured TH is not possible. Reasons for this have already been given, such as the unknown surface occupancy of the AFP on the ice crystal and the distribution of the distances between the proteins or the fact that the ice growth is only investigated at one specific ice crystal plane. As already mentioned before, the determination of the affinity of the protein to the single crystal surface is of great importance. Due to the specification of the box size, this interaction is not correctly reproduced in the simulation. It is obvious by repeated simulation whether a protein binds better or not, but in the case that it binds, the surface occupancy is predetermined by the box. Therefore, it would be desirable to be able to determine this binding strength unambiguously. Kumari et al. also proposed a new method to compare the adsorption behavior of different AFPs or toward different ice crystal planes. [420] This method should be evaluated in more detail. In combination with other MD simulations, this could provide further insights into the functioning of AFPs and molecules with similar properties. Furthermore, the current incompatibility of experiments and simulations could be improved in the future.

5.5 Conclusions

As a general result of our investigation, we can state that the geometry of the ice surface is extremely important and may not be guessed upfront the simulation. Due to the rectangular arrangement of the protein and its images, an ellipsoidal curvature was expected but a cylindrical ice surface has been observed in all simulations on the surface. For this reason, it is not purposeful to estimate a maximum radius just from the distances between the proteins. We showed that the critical radius is on a slab where no protein is adsorbed. By simulating different temperatures, the minimum temperature at which the resulting curvature prevents ice growth was determined and is at $T_{min} = 262.5$ K. This is in good agreement with the value calculated with the Gibbs–Thomson equation at the critical radius. For the identification of the critical radius, it is important that the simulation time is sufficient and that the dynamics of the ice front is taken into account. We showed that in our case the critical radius was the most dynamic one and not located at the longest distance between the adsorbed molecules. Therefore, it is necessary to determine this radius over the course of the simulation.

Overall, our results show on the one hand that the Gibbs–Thomson effect can be taken as the basis of TH and that MD simulations are suitable for the prediction of the melting point depression. The simulations could provide the possibility to compare different AFPs or mutants based on their TH in an identical system with same distances between the proteins. The force field used could also have an influence on the adsorption of the water molecules to the ice structure in the simulation. This should be evaluated in future studies. However, it is still not possible to compare an experimentally determined TH with a value obtained by simulation.

6 Investigation of κ-Carrageenan's Ice-Binding Properties Using Molecular Dynamics Simulation

6.1 Abstract

Recrystallization of ice crystals during storage of frozen food, cells, or medical samples causes serious damage to the stored material. To mitigate this damage, additives such as κ-carrageenan, a polysaccharide derived from algae, can be employed. Experimental results demonstrated that κ-carrageenan strongly inhibits ice recrystallization and alters the ice crystal morphology, suggesting ice-binding properties. However, a binding of κ-carrageenan to ice crystals has not yet been shown, and the underlying mechanism of its recrystallization inhibition activity remains unclear. In this study, molecular dynamics simulations using different κ-carrageenan molecules and ice planes were performed to shed light on this. The results revealed that κ-carrageenan is able to interact with the basal plane and primary and secondary prism planes, but the binding appears to be reversible, at least for the investigated molecular sizes. In addition, the formation of a double helix did not affect the binding affinity. Hydrogen bond formation and the integration of κ-carrageenan's oxygen atoms into the ice lattice structure facilitate the interaction with the ice crystal. These findings provide further insights into the recrystallization inhibition of polysaccharides and foster the tailored design of effective freeze-protection molecules.

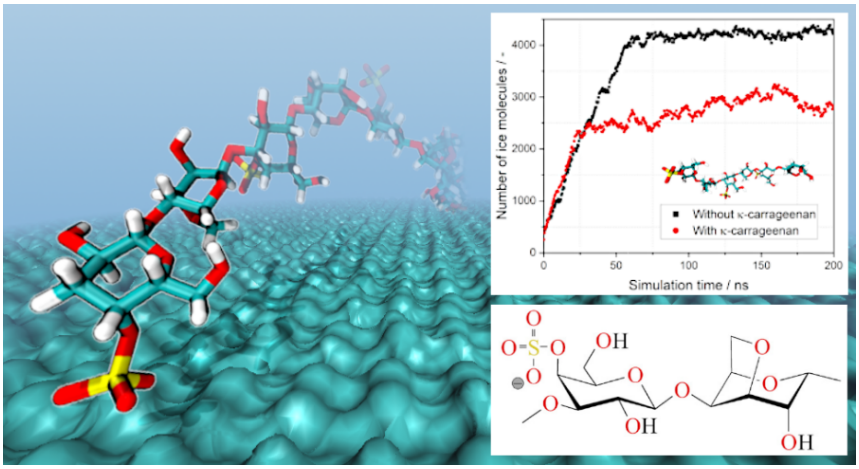

Figure 6.1. *Graphical abstract.*

6.2 Introduction

Frozen storage preserves biological products such as food [421] and enables cryopreservation of cells, tissues, and organs in medicine [372,422]. However, ice crystal formation and ice growth can lead to mechanical stress and physical damage to the cells [83]. A major damaging mechanism during storage is the recrystallization of ice crystals [5,423,424]. During the process of ice recrystallization, smaller ice crystals dissolve and water molecules migrate to larger crystals, which continue to grow as the process progresses leading to a coarsening of the ice crystal structure [376]. Additives can be employed to alter ice recrystallization and growth. Ice-binding proteins (IBP), found in various organisms, exhibit highly potent ice recrystallization inhibition (IRI) activity [99,159]. IBPs induce microcurvatures by binding to the ice surface, preventing further ice growth [128,425]. Due to these curvatures, the local melting temperature decreases and the temperature range over which ice crystal growth is inhibited are termed thermal hysteresis. Ice crystals have different crystal planes (Figure 6.2) and growth directions, which can be subdivided into primary and secondary prism planes and the basal plane [125]. It is known that the different surface structures of these planes can lead to different binding behaviors of IBP, which is reflected in changes in the ice crystal shape [403,426]. In addition, ice binding prevents recrystallization by creating similar microstructures across the surfaces of the individual ice crystals. The ability of IBP to specifically bind to ice crystals is essential for their effectiveness, even at micromolar concentrations [25,427]. Besides ice plane specificity, the binding kinetics of IBPs onto the ice surface are another important factor [428]. There are multiple mechanisms or even combinations of mechanisms discussed for IBPs to bind to the ice crystal surface. While some IBP influence the surrounding water structure [194,196,429,430], a structural match with the ice lattice can also be important for binding [182]. Furthermore, studies have revealed that formation of hydrogen bonds and hydrophobic interactions are crucial for the interaction between the protein and ice crystal surface [431]. Midya and Bandyopadhyay demonstrated that the binding of IBP to ice crystals occurs through the freezing of interfacial water molecules on both surfaces. Efficient inhibition of recrystallization appears to require effective binding to the ice surface and disruption of ordered interfacial water molecules [432]. Short polymers resembling antifreeze glycoproteins appear to show enhanced ice-binding capabilities with increasing l-alanine content and incorporation of succinate groups [433].

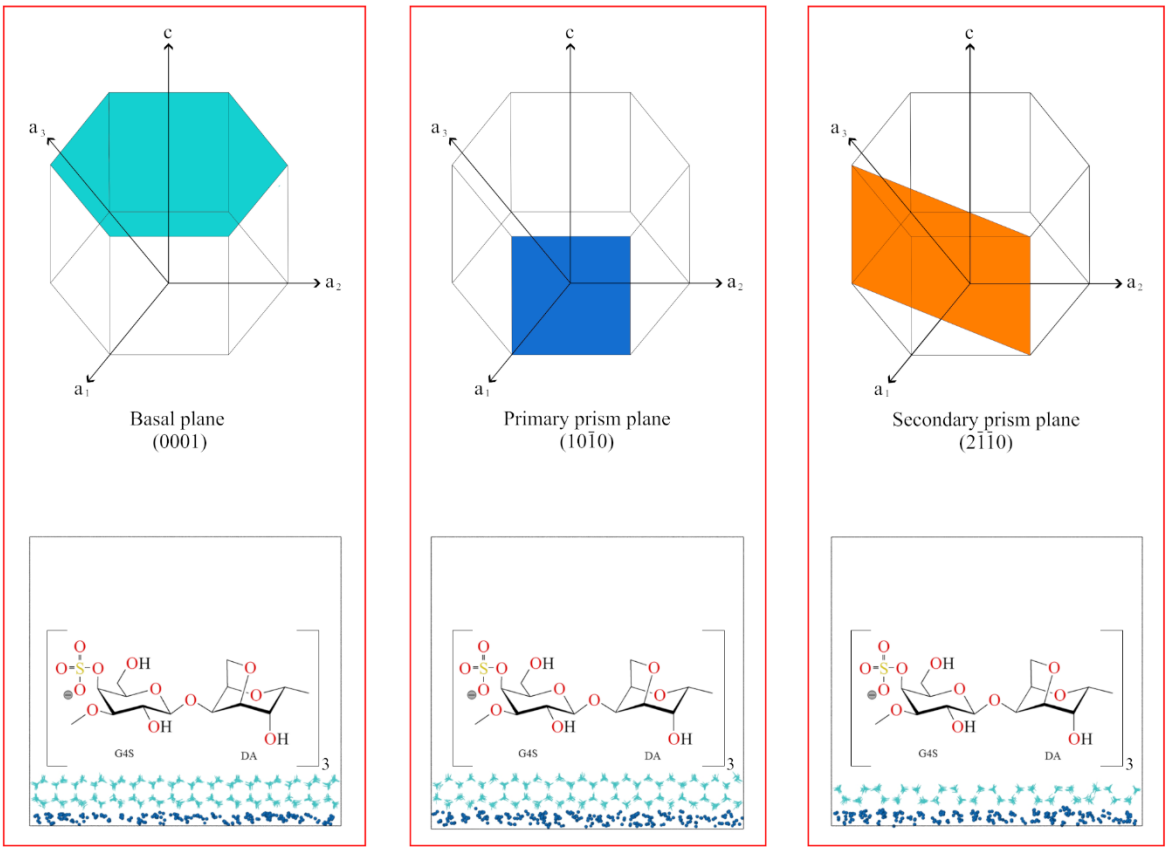

Figure 6.2. *Illustration of different ice crystal planes (upper part) and the corresponding simulation setups (lower part) to study the interaction of κ-carrageenan with the basal plane (left), the primary prism plane (middle), and the secondary prism plane (right).*

Whether binding of IBP to ice is reversible or irreversible is still under debate. Microfluidic experiments [200] and nanoscopy of individual molecules [206] demonstrate irreversible binding for the hyperactive *Tenebrio molitor* AFP and type III AFP, while antifreeze glycoproteins and winter flounder AFP bind reversibly [203,206]. Notably, reversible binding seems sufficient for potent IRI activity, but not for thermal hysteresis [206].

Besides IBPs, numerous nonprotein substances with similar properties have been discovered [38,107,116,210,211,389]. These are typically more cost-effective to produce and thus are more readily available. A highly promising alternative is κ-carrageenan, a linear polysaccharide derived from red algae that is composed of repeating disaccharide units of β-D-galactopyranose (G-unit) and 3,6-anhydro-α-D-galactopyranose (DA-unit). The G-unit has a sulfate group at position O-4, resulting in one negative charge per disaccharide unit [384,385,434]. κ-Carrageenan's helical structure enables thermo-reversible gel formation with the gel properties depending on the available cations. Potassium ions yield firm and brittle gels [339,435], while calcium

ions form an elastic gel [339,436]. The gelation is a complex, not fully understood process involving a transition from a random coil structure to a helical conformation upon cation addition. The tertiary structure results from the intramolecular self-aggregation of a single helical strand into a double helix. Subsequently, several of these double helices can aggregate into quaternary structures [263,387]. However, recent studies by Westberry et al. indicate that κ-carrageenan adopts a helical conformation independent of salt addition, yet it does accelerate double helix formation [437,438].

While widely used as thickener and stabilizer, κ-carrageenan has recently found applications in foams, biofilms, and encapsulation [439–441]. In addition to its gelling and film-building properties, κ-carrageenan also influences the growth and recrystallization of ice crystals. Upon κ-carrageenan addition, smaller ice crystals form, and their further growth is inhibited over time. The inhibition of ice recrystallization increases with increasing κ-carrageenan concentration at comparatively low levels [25,38] and is influenced by the hydrocolloids molecular weight [442]. A reduction in molecular size results in larger crystals and reduced IRI activity [43]. However, the IRI activity of κ-carrageenan decreases once gelation or development of a gel-like character occurs [41]. Furthermore, a change in ice crystal morphology toward a rectangular shape can be observed while κ-carrageenan is present [44]. These aspects lead to the assumption that the IRI activity of κ-carrageenan is likely based on a surface binding effect rather than on a viscosity change. While certain studies suggest that the addition of non-ice-binding hydrocolloids to ice cream reduces the recrystallization and influences the rearrangement of water molecules [90,377,378], others report conflicting results. Investigations of commercially available carrageenans did not show an influence of viscosity on recrystallization [38]. Similar results were obtained for nanocellulose [92].

Surface-active linear polymers seem to interact differently with ice than IBPs. Poly(vinyl alcohol) (PVA), an extensively studied synthetic linear polymer with IRI activity, binds to the ice surface independently of its three-dimensional conformation [214] and binds to the primary prism plane [113,213,407,409] similar to antifreeze glycoproteins [143], despite their structural differences. This suggests that linear polymers need a certain degree of flexibility for effective ice binding.

In addition, the formation of hydrogen bonds between PVA and ice appears to be the primary driving force of the binding to the ice surface [214,389,443]. While short molecules containing three hydroxyl groups can interact with ice, stable binding requires around eight hydroxyl

groups [217] and experimentally measurable IRI activity requires 10–20 units [215]. The reversible nature of this interaction underscores the importance of the binding rate [217]. In the case of κ-carrageenan, both sulfate groups and the numerous hydroxyl groups contribute to its hydrogen bonding capability acting as potential binding sites for interaction with the ice surface.

Besides ice binding, gelation, and viscosity related effects, other theories attempt to explain the recrystallization inhibition of polysaccharides. Tam et al. proposed that polysaccharides may disrupt the ice-like ordering of water molecules at the ice–water interface, preventing the attachment of water molecules [444]. Low-molecular-weight polyethylene glycol demonstrated recrystallization inhibition activity in experiments using the splat assay and has positive effects on preserving stem cells during cryopreservation [445,446].

Due to the difficulty in visualizing the processes at the ice crystal surface, this study employs MD simulations, a prominent tool in ice-binding molecule research [126,127,407,438,444], to investigate the potential binding of κ-carrageenan to ice crystals, based on the following hypotheses:

Given the strong IRI activity of κ-carrageenan and its ability to induce morphologic changes in ice crystal shapes [25,44], it is postulated that this substance binds to the ice surface.

Hyperactive IBPs bind to multiple ice planes, exhibiting high thermal hysteresis [447]. Therefore, κ-carrageenan, which lacks thermal hysteresis [44], is assumed to bind to a single ice crystal plane.

In addition, longer κ-carrageenan molecules are hypothesized to bind more strongly due to their larger number of potential binding sites, supported by observations of higher IRI activity in longer molecules [41]. Assuming κ-carrageenan is able to bind to ice, this interaction likely involves hydrogen bond formation and structural adaptation to the ice lattice, similar to PVA [214,217].

Since gel formation eliminates the IRI activity of κ-carrageenan [41], it is hypothesized that the aggregation of κ-carrageenan strands into a double helix may reduce the flexibility of the molecule needed to adapt to the ice lattice, negatively affecting the binding process. Conversely, recent studies demonstrated an enhanced IRI activity in case of κ- and ι-carrageenan by substituting bound ions with helix-stabilizing ions [448].

To examine these hypotheses, simulations of κ-carrageenan containing three and six disaccharide units, including a double helix, were performed under varying ice-growth directions and temperatures. The analysis included ice-growth kinetics, molecular fluctuations via root-mean-square deviation and root-mean-square fluctuation, hydrogen bond metrics, and visual inspection.

6.3 Materials and Methods

6.3.1 General Methodology

MD simulations employ Newton's laws of motion to predict the trajectories of atoms and molecules. This requires the calculations of the forces acting on each atom, described by a set of mathematical equations generally known as the force field. Consequently, the accuracy of the force field is crucial, as any errors will lead to inaccurate or incorrect atomic trajectories. The simulated system encompasses two distinct components that require accurate characterization through a force field: the polysaccharide κ-carrageenan and a multitude of water molecules. κ-Carrageenan was characterized by the latest GLYCAM06 force field specifically developed for describing carbohydrates [298]. The parametrization is identical to the approach published by Westberry et al [437,438]. A plethora of models for the description of water is available. Due to the importance of ice formation within the simulated system, the TIP4P/Ice model was used [413]. The four-site representation is specifically optimized to accurately reproduce the phase-transition behavior of water resulting in a melting point of 269.1 K [449]. (75) However, diverging melting points for a given water model are often found in the literature, which is due to the use of different determination methods. In case of TIP4P/Ice, a range from 268 to 272 K is reported [413,417,450–452].

All simulations in this study were performed using the GROMACS 2021.2 software package [453,454]. Subsequently, the resulting trajectories were visualized using Visual Molecular Dynamics (VMD) software [330] and OVITO [455].

6.3.2 Simulation Setup

The binding of molecules to ice crystals is influenced by the crystal's surface structure, necessitating the investigation of different crystal planes facing the molecule. Therefore, various initial crystals were prepared with the GenIce tool [456] and the ice growth in the direction of the basal plane, primary prism plane, and secondary prism plane was examined (Figure 6.2). For example, when the ice crystal grows with its basal plane oriented toward the molecule, it is

defined as “growth in the direction of the basal plane”. The distinct ice lattice arrangements and the size of the κ-carrageenan molecule required different box sizes for the simulations. The dimensions of these boxes are presented in Table A4.1 of the Appendix. For simulating the double helix, identical box sizes were applied as those used for the simulations of κ-carrageenan composed of three units.

Since ice crystal nucleation is a random process that would occur with a very low probability under the simulated conditions, an initial ice crystal is used to promote ice growth along the specific growth direction of interest. To prevent downward ice growth, a layer of water molecules beneath the initial ice crystal was immobilized by using position restraints. This is crucial to avoid the ice crystal from extending beyond the simulation box’s lower boundary, which could potentially encase the κ-carrageenan molecule from above. The studied κ-carrageenan molecule, consisting of three disaccharide units adopting a helical conformation, was positioned with its center of mass (COM) ∼2 nm above the initial ice crystal surface. To neutralize the overall charge of the simulated system, three sodium ions were added to compensate for the negative charge of the three sulfate groups present in the investigated κ-carrageenan molecule. In addition to the initial ice crystal and immobilized water layer with about 200–300 molecules, the simulation box also includes 6000 water molecules. The lower panels presented in Figure 6.2 illustrate the initial configurations used in these simulations.

Considering the computational costs and information obtained from the small molecule, simulations of the κ-carrageenan composed of six disaccharide units focused exclusively on the secondary prism plane. The larger system shares the same fundamental setup as the smaller system, with its dimensions given in Table 6.1. It features an immobilized water layer of 800 molecules, an initial ice crystal consisting of 441 molecules and a distance of 2 nm between κ-carrageenan and the ice surface. An additional 16,873 water molecules complete the system (Figure A4.1).

Table 6.1. *Average ice-growth rates in the control systems in absence of κ-carrageenan across three different simulations with corresponding standard deviation.*

Growth direction / -	Temperature / K	Ice-growth rate / molecules·ns^{-1}·nm^{-2}
Basal plane	262.5	1.53 ± 0.12
Primary prism plane	262.5	2.67 ± 0.38
Secondary prism plane	262.5	2.64 ± 0.17
Basal plane	265	1.01 ± 0.17
Primary prism plane	265	2.26 ± 0.03
Secondary prism plane	265	2.24 ± 0.31
Primary prism plane	268	0.72 ± 0.25
Secondary prism plane	268	0.94 ± 0.30

To achieve a double helix structure, two κ-carrageenan strands, each containing three disaccharide units, were placed in a water-filled box with six sodium ions to neutralize the system's charge. Following the formation of a stable helix structure, this configuration was utilized in simulations of systems containing either a primary or secondary prism plane.

6.3.3 Simulation Protocols

Each simulation employed an all-atom representation, explicitly calculating the forces acting on each atom within the system. The LeapFrog integrator was chosen as the integration method due to its stability and reliability. The LINCS algorithm was employed to constrain hydrogen bonds throughout all simulations, which enabled an integration time step of 2 fs during the production simulations [315]. To prepare the κ-carrageenan molecules for simulation, Ambertools21 [457] was used with the preparation files obtained from Westberry et al [437,438]. Afterward, the resulting files were converted into GROMACS compatible file format using acpype [458,459]. The simulation box was first set up, followed by minimizing the system's energy employing the steepest decent method. A v-rescale thermostat is used to maintain constant temperature and achieve a canonical ensemble (NVT) [325]. The effect of the thermostat on latent heat release and consequently the ice-growth speed has been the subject of debate. However, recent studies demonstrated a minimal impact of temperature regulation by using a thermostat on ice-growth rates [460]. Subsequently, a pressure regulation was introduced using a Berendsen barostat to achieve an isothermal–isobaric ensemble (NpT) [328]. For enhanced pressure regulation during the production simulations, a Parinello–Rahman barostat was used

[327]. Considering the periodic boundary conditions, anisotropic pressure coupling must be employed to ensure proper ice crystal growth. The pressure was kept constant at a value of 1 bar by applying an anisotropic pressure coupling with a coupling constant of 2 ps. In addition, long-range electrostatic interactions were calculated by the Particle-Mesh Ewald method [304]. To ensure the reproducibility of the results, the production simulations are performed three times for each system. The effect of the temperature was investigated by examining different levels of undercooling. Based on the melting point of the water model of 269.1 K, the following three temperatures were chosen: 268, 265, and 262.5 K. A temperature of 268 K was chosen to examine the behavior of κ-carrageenan under the conditions of slow ice growth. Based on previous simulations of an IBP, 262.5 K was identified as the lowest temperature at which the protein was not trapped inside the ice crystal [127]. Additionally, 265 K was chosen as the intermediate temperature. To investigate uninhibited ice growth, control simulations were performed without κ-carrageenan. The control simulations run for varying lengths between 150 and 250 ns, depending on the time needed to achieve an entirely frozen simulation box. All simulations involving κ-carrageenan with three disaccharide units were conducted for 250 ns. To investigate the reversibility of the binding interaction, one simulation was extended to 1 μs. Due to the larger box sizes in the system with κ-carrageenan containing six disaccharide units, the simulations were run for 300 ns. In total, 23 systems were simulated, including controls and triplicate repetitions.

6.3.4 Methods of Analysis

To obtain the ice-growth rate, the number of ice molecules was calculated at 500 ps intervals throughout the simulation. This analysis was performed using OVITO version 3.10.0 [455] and its built-in CHILL+ algorithm [461]. To determine the ice-growth rates, the number of ice molecules was plotted against the simulation time, and the slope was calculated. To account for the different box sizes, these rates were normalized by the area perpendicular to the ice-growth direction. This analysis was performed on the distinct stages of ice growth that could be observed during the simulations. The segmentation was done based on the temporal changes in the number of ice molecules and visual inspection. The specific location of the carrageenan molecule, either adsorbed at the interface or dissolved in bulk water, played a crucial role in defining the different stages of the simulation.

To analyze the number and lifespan of hydrogen bond interactions, the module gmx h-bond was employed. Two geometric criteria must be satisfied for the establishment of a hydrogen bond. The distance between the acceptor and donor atoms must be less than or equal to 0.35

nm [462,463]. Moreover, the angle formed between the hydrogen donor and acceptor must be less than or equal to 30°. Accurately analyzing the lifespan of hydrogen bonds is a difficult process, and most methods provide only approximate results. Nevertheless, to obtain the highest possible accuracy, the method of Luzar and Chandler was employed [463,464]. This approach considers the rate at which hydrogen bonds break and reform. The calculated autocorrelation function tracks how likely a hydrogen bond is to be present later, based on whether it was existing before.

To gain further insight into the movement and flexibility of the κ-carrageenan molecule and its individual atoms, the root-mean-square deviation (RMSD) and the root-mean-square fluctuation (RMSF) were calculated. The RMSD was computed using the gmx rms module, which determines the average displacement of all atoms of the κ-carrageenan molecule compared with their initial positions in the reference. Figure 6.2 depicts the reference structure at the start of the simulation. In contrast, the RMSF value provides information on the individual movements of the atoms within the κ-carrageenan molecule and was calculated with the gmx rmsf module. Consistent with the RMSD analysis, the reference structure is the conformation at the beginning of the simulation as depicted in Figure 6.2. Both, RMSD and RMSF values are measures of molecular structural changes but differ in the way they are calculated. While the RMSD value is calculated for an individual time point during the simulation, the RMSF value is an average over the entire simulation. Although RMSD and RMSF values do not provide a standalone conclusion, they can be valuable tools in conjunction with other data and were therefore calculated for every simulation performed.

6.4 Results and Discussion

6.4.1 Ice-Growth Rates in the Control Systems

In general, the systems of the controls without κ-carrageenan demonstrated uniform ice growth as expected, with higher ice-growth rates at lower temperatures, as shown in Table 6.1. At the same temperature, ice growth along the *c*-axis in the direction of the basal plane exhibited slower growth rates compared to the prism facets, which grew at similar rates. While the growth rates are influenced by multiple parameters, including the temperature, the slower basal growth aligns with previous findings [465]. Given the relatively weaker interaction of κ-carrageenan with the basal plane, this plane was not included in simulations at 268 K, resulting in its absence from Table 6.1.

6.4.2 Ice Binding of Three Units of κ-Carrageenan and Influence on the Ice-Growth Rate

General Behavior and Ice Binding

Using MD simulations, Weng et al. demonstrated that already short PVA molecules with 5 repeating units are capable of binding to the ice surface [407], even though these do not exhibit IRI activity in experiments. Therefore, κ-carrageenan may behave similarly, and short molecules are adequate for investigating the ice-binding properties.

The presence of κ-carrageenan consistently affected the ice crystal growth regardless of temperature or the direction of ice growth. Fundamentally, systems containing κ-carrageenan can exhibit different behaviors, which are, in general, described below. All of these behaviors have been observed at some point in different simulation.

Initially, the κ-carrageenan molecule is not in spatial proximity to the initial ice crystal, allowing unrestricted ice growth (unrestricted ice-growth phase). Subsequently, upon contact of the molecule with the growing ice surface, the simulation's course can diverge based on the simulation temperature and κ-carrageenans' ability to interact with the respective ice surface. If no interaction takes place, the growing ice crystal displaces the molecule until the simulation box is completely frozen (displacement phase). Otherwise, if κ-carrageenan can establish a binding with the respective ice plane, ice growth can occur only at unoccupied sites, leading to the formation of a curved ice surface, as with IBPs. The curvature results in a depression of the melting temperature at this surface, a phenomenon known as Gibbs–Thomson effect [126,127]. Depending on the actual temperature, this curvature might prevent further ice growth by depressing the melting temperature to the simulation or actual temperature (ice-growth inhibition phase). However, at lower temperatures, κ-carrageenan becomes progressively trapped within the ice crystal, restricting the attachment of water molecules and temporarily slowing the ice-growth rate (ice-trapping phase). Once fully trapped, the molecule no longer affects ice growth, and growth rates return to unrestricted levels. At elevated temperatures, κ-carrageenan may not maintain a stable attachment to the ice front, leading to the detachment from the surface, allowing unrestricted ice growth. This phase may be followed by another interaction phase. The κ-carrageenan molecule can attach itself to the ice surface in two primary binding orientations. Horizontal binding occurs when the molecule aligns parallel to the ice surface, while in a vertical binding orientation, the molecule binds perpendicular to the surface.

A consolidated overview of all simulations with κ-carrageenan composed of three disaccharide units is given in Table 6.2. It quantifies the number of interactions between κ-carrageenan and

the ice surface during the 250 ns long simulations. An interaction is defined as any instance where the molecule is located at the ice surface exerting an influence on the ice-growth rate, which corresponds to an ice-growth inhibition phase. Furthermore, the table indicates whether κ-carrageenan could stop further ice growth or if the molecule was trapped inside the ice crystal with a previous ice-trapping phase. Additionally, the binding orientation is specified for molecules bound to the ice surface.

Table 6.2. *Summary of simulation results for a system with a κ-carrageenan molecule consisting of three disaccharide units.*

Ice growth direction	Temperature / K	Simulation number	Number of interactions with the ice surface	Ice growth stopped	Molecule trapped in ice crystal	Binding orientation
Basal plane	262.5	1	0	no	no	-
		2	1	no	yes	vertical
		3	1	no	yes	horizontal
	265	1	0	no	no	-
		2	1	no	yes	vertical
		3	1	no	yes	vertical
Primary prism plane	262.5	1	1	no	yes	horizontal
		2	1	no	yes	vertical
		3	1	no	yes	horizontal
	265	1	1	yes	no	horizontal
		2	1	no	yes	vertical
		3	2	yes	no	horizontal
	268	1	2	no	no	-
		2	2	no	no	-
		3	0	no	no	-
Secondary prism plane	262.5	1	1	no	yes	vertical
		2	1	no	yes	horizontal
		3	1	no	yes	horizontal
	265	1	1	yes	no	horizontal
		2	1	no	yes	vertical
		3	1	no	yes	vertical
	268	1	1	no	no	-
		2	1	no	no	-
		3	2	no	no	-

In the first simulation at 262.5 K, κ-carrageenan was unable to bind to the ice surface growing in the direction of the basal plane and was displaced to the top of the simulation box. While κ-carrageenan was able to bind to the ice surface in most of the simulations performed, the resulting curvature was insufficient to inhibit further ice growth and the molecule was trapped inside the ice crystal. This was consistently observed at 262.5 K. At higher temperatures of 265 K, κ-carrageenan repeatedly bound to the primary prism plane and in simulations 1 and 3 completely stopped ice growth.

κ-carrageenan effectively bound to all simulated crystal planes at 262.5 and 265 K. The orientation of the bound molecule significantly influenced ice-growth inhibition. Vertical binding at 265 K resulted in a trapped molecule, while horizontal binding effectively inhibited ice growth. Increasing the temperature to 268 K caused κ-carrageenan to lose its binding ability with the ice surface.

A graphical representation of the ice growth in all simulations containing κ-carrageenan composed of three disaccharide units is given in Figure A4.2 of the Appendix.

Most ice-binding molecules interact with a preferred ice crystal plane. It is commonly assumed that binding to multiple planes is one of the key factors for high thermal hysteresis activity. However, recent studies suggest that interacting with multiple planes does not necessarily lead to high thermal hysteresis activity [466]. This aligns with previous investigations of κ-carrageenan, where no thermal hysteresis activity was measurable [44]. However, the simulations indicated that κ-carrageenan exhibits different binding affinities toward distinct ice planes. In one-third of the simulations of ice growth in the direction of the basal plane, the molecule failed to attach to the ice surface and was displaced by the advancing ice front until it reached the top of the box (Table 6.2). This was consistently observed at both 262.5 and 265 K as shown in Figure A4.4. In contrast, for the primary and secondary prism planes, κ-carrageenan has successfully bound to the ice surface. These findings indicate that the interaction between κ-carrageenan and the basal plane is weaker compared to the prism planes. Consequently, simulations of the ice growth in the direction of the basal plane were not conducted at an elevated temperature of 268 K.

Effect of κ-Carrageenan on Ice Growth during the Overgrowth Process

To exemplify the mechanism of overgrowth and the influence of bound κ-carrageenan on the ice-growth rate, the results of the first simulation at 262.5 K with ice growth along the direction of the primary prism plane are illustrated in Figure 6.3.

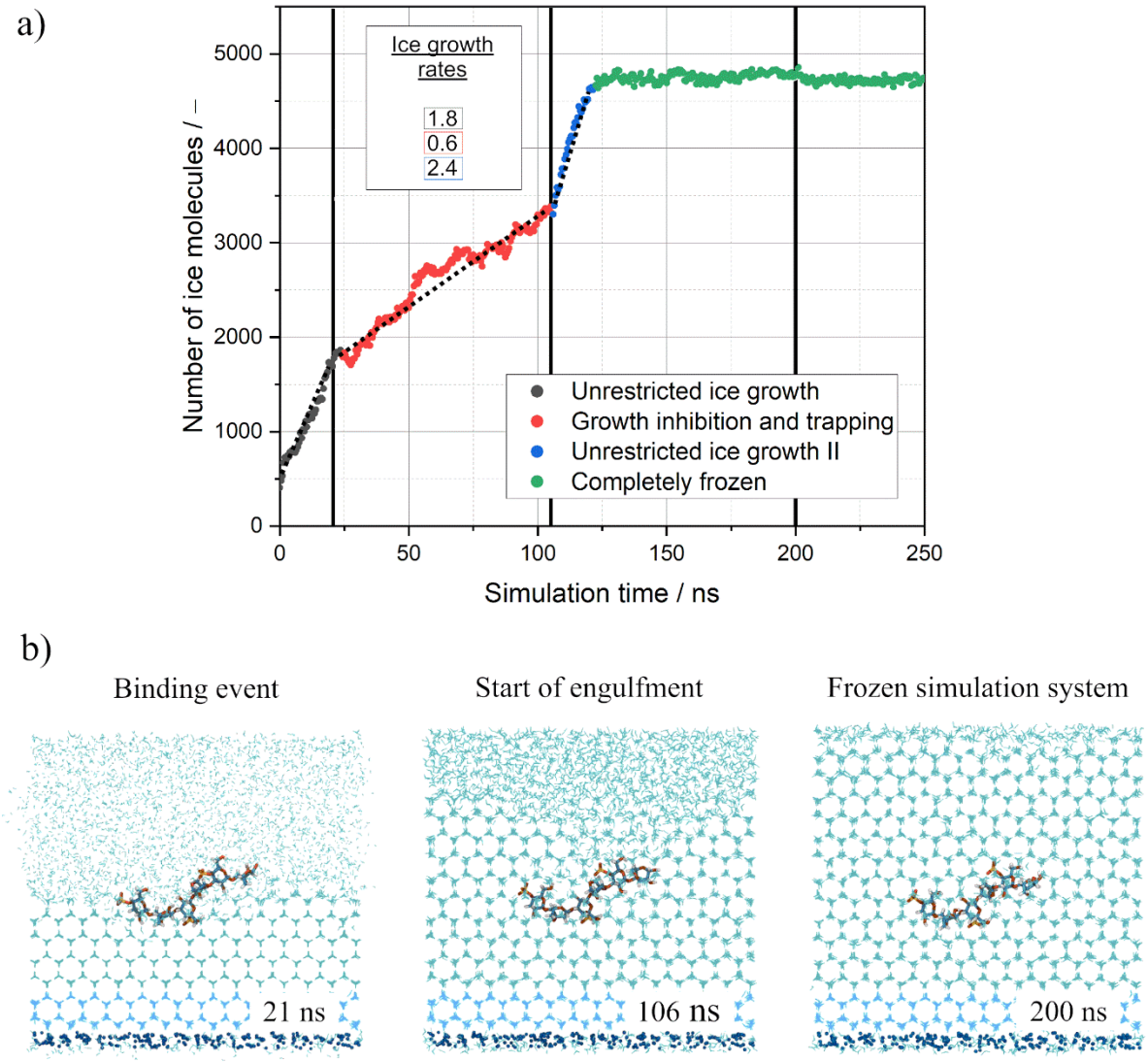

Figure 6.3. *(a) Evolution of ice growth in the direction of the primary prism plane at 262.5 K. The different phases of ice growth are color-coded, and the dashed line represents the slope of each phase. Additionally, the diagram includes the corresponding ice-growth rates in molecules·ns^{-1}·nm^{-2}. In panel (b), a visual timeline of the characteristic events is shown. The initial ice binding of κ-carrageenan (left), the end of the ice-trapping phase (middle), and the final state of the fully frozen simulation box (right) are depicted.*

Initially, the presence of κ-carrageenan had a minimal effect on ice growth as shown by the gray line in Figure 6.3a, with an initial growth rate of 1.8 molecules·ns^{-1}·nm^{-2}, compared to the controls growth rate of 2.67 ± 0.38 molecules·ns^{-1}·nm^{-2} (unrestricted ice-growth phase). Subsequently, at a simulation time of 21 ns, the molecule bound to the ice surface, as illustrated in the left image in Figure 6.3b. This caused a reduction in the ice-growth rate to 0.6 molecules·ns^{-1}·nm^{-2} (red line, Figure 6.3a) and the formation of the characteristic curved surface (ice-trapping phase). This is most evident in the image in the middle of Figure 6.3b at the end of this phase. Once 106 ns had passed, the ice crystal enveloped the bound κ-carrageenan, allowing unrestricted ice growth at a rate of 2.4 molecules·ns^{-1}·nm^{-2} as indicated by the blue line in

Figure 6.3a (unrestricted ice-growth phase). As indicated by the green line in Figure 6.3a, the ice growth stopped completely after approximately 120 ns when the box is completely frozen. The frozen state of the system is visualized by the image on the right in Figure 6.3b. Based on this simulation, the ice surface is visualized in Figure A4.3 to demonstrate that the ice crystal enveloped the bound molecule and finally closed directly above it.

All systems simulated at a temperature of 262.5 K froze entirely, irrespective of the ice-growth direction and κ-carrageenan presence.

Influence of the Binding Orientation on Ice Growth

Moreover, the binding orientation of the molecule notably affected the ice-growth rate. This was evident at 262.5 and 265 K. In the case of vertical binding, only a minimal ice surface area was covered, allowing for a higher ice-growth rate and faster overgrowth. To visualize this, Figure 6.4 presents the two different binding orientations of κ-carrageenan and the corresponding ice growth along the secondary prism plane at 265 K. Figure 6.4a illustrates simulation 1, where the κ-carrageenan molecule attached to the ice surface at 17 ns and aligned horizontally. While in Figure 7.4b illustrating the second simulation, κ-carrageenan adopted a vertical binding orientation. The two corresponding ice-growth patterns shown in Figure 6.4c demonstrate the influence of the binding orientation on ice growth. Without κ-carrageenan, the growth rate was around 2.24 molecules·ns^{-1}·nm^{-2} and decreased to 0.15 molecules·ns^{-1}·nm^{-2} upon horizontal binding (ice-growth inhibition phase). Furthermore, the ice growth seemed to cease after 150 ns, as evident by the plateau in the ice growth (Figure 6.4c, gray squares). This suggests that the ice growth was completely inhibited. In contrast, a vertical binding orientation as observed in the second simulation resulted in a less pronounced decrease with an ice-growth rate, dropping to a value of 0.24 molecules·ns^{-1}·nm^{-2} after the binding of κ-carrageenan (ice-trapping phase). Despite the binding of κ-carrageenan, further ice growth could not be prevented within the simulation box, resulting in a completely frozen system. The control's ice-growth rate is provided in Table 6.1, while the ice-growth profiles for all simulative conditions are given in Figure A4.2 in the Appendix.

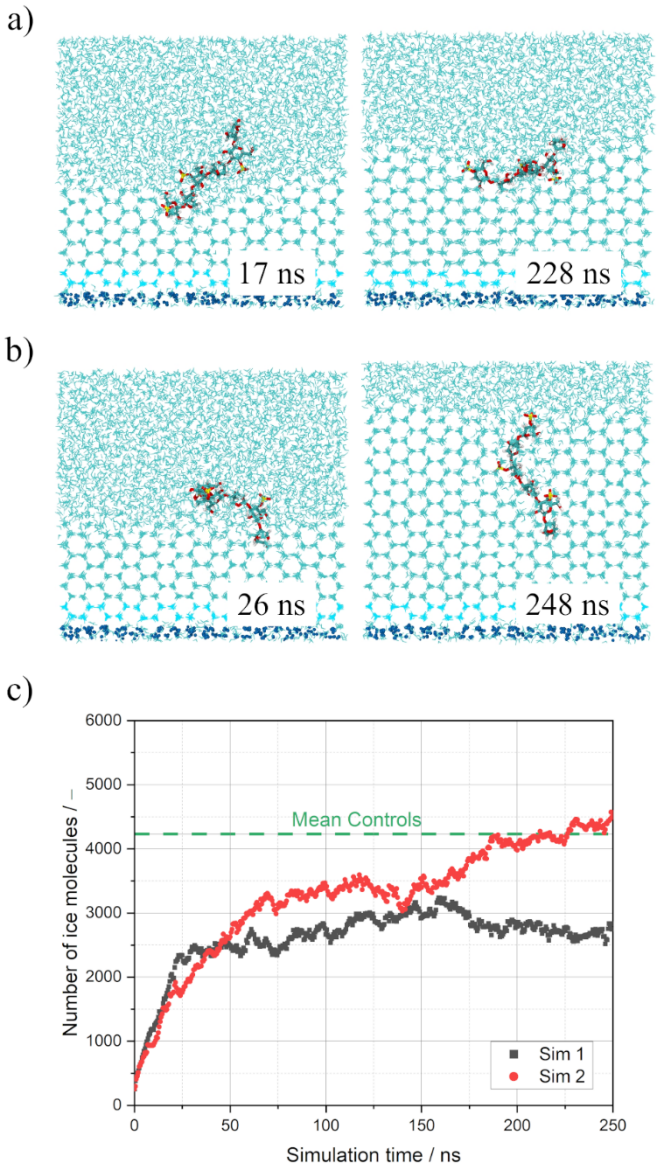

Figure 6.4. *Impact of κ-carrageenan binding orientation on ice growth in the direction of the secondary prism plane at 265 K. (a) In Sim 1, κ-carrageenan binds horizontally. The images depict the first interaction with the secondary prims plane at 17 ns (left) and close to the end of the simulation at 228 ns (right). Images in panel (b) present the vertical binding orientation in Sim 2. Correspondingly, panel (c) shows the ice growth during those two simulations. Additionally, the green dashed line represents the average number of ice molecules of the frozen controls.*

Across all simulations in the direction of the secondary prism plane, κ-carrageenan was able to bind to the ice surface within the first 50 ns of the simulation. In two of the three simulations, κ-carrageenan adopted a vertical binding orientation and was not able to fully stop the ice growth (Table 6.2).

Similarly, κ-carrageenan bound to the primary prism plane in all three simulations exhibited behavior consistent with the previous observations made for the ice growth in the direction of

the secondary prism plane. In two-out-of-three instances, it adopted a horizontal binding orientation, successfully preventing ice growth (the ice-growth inhibition phase). Moreover, a vertical binding orientation was observed in the second simulation suggesting the molecule may not effectively inhibit ice growth (Figure A4.5).

Loss of κ-Carrageenan's Ice-Growth Inhibition Activity at Higher Temperatures

While a temperature increase to 268 K generally reduced the ice-growth rates (Table 6.1), the behavior of κ-carrageenan changed drastically. To illustrate the general ability of κ-carrageenan to affect the ice growth at 268 K, the third simulation in the direction of the secondary prism plane was examined and is presented in Figure 6.5. The evolution of ice growth is depicted in Figure 6.5a, while Figure 6.5b provides the corresponding simulation snapshots. Initially, the molecule bound temporarily to the ice surface from 8 to 20 ns, resulting in a reduction of the ice-growth rate to 0.47 molecules·ns^{-1}·nm^{-2} (ice-growth inhibition phase I, gray triangles). After the detachment, the ice crystal grew freely until a further temporary attachment occurred between 51 and 84 ns (ice-growth inhibition phase II, blue triangles). This again led to a reduction of the ice-growth rate to 0.3 molecules·ns^{-1}·nm^{-2}.

The simulations clearly demonstrated that κ-carrageenan was no longer able to stop the ice crystal growth at 268 K, neither in the direction of the primary prism plane nor in the direction of the secondary prism plane. In all simulations, the molecule attempted to interact with the corresponding ice surface but had a negligible influence on ice growth (Table 6.2 and Figure A4.6). Consistent with these observations, the ice-growth rates were close to the values of the controls without κ-carrageenan. For the primary prism plane, the control's ice-growth rate was 0.72 ± 0.25 molecules·ns^{-1}·nm^{-2} (Table 6.1). Due to the short durations of the interactions of the molecule, the ice-growth rate decreased slightly to 0.47 molecules·ns^{-1}·nm^{-2} in the first simulation and 0.65 molecules·ns^{-1}·nm^{-2} in the third simulation (Figure A4.2). Ice-growth rates in the direction of the secondary prism plane showed comparable values in the presence of κ-carrageenan.

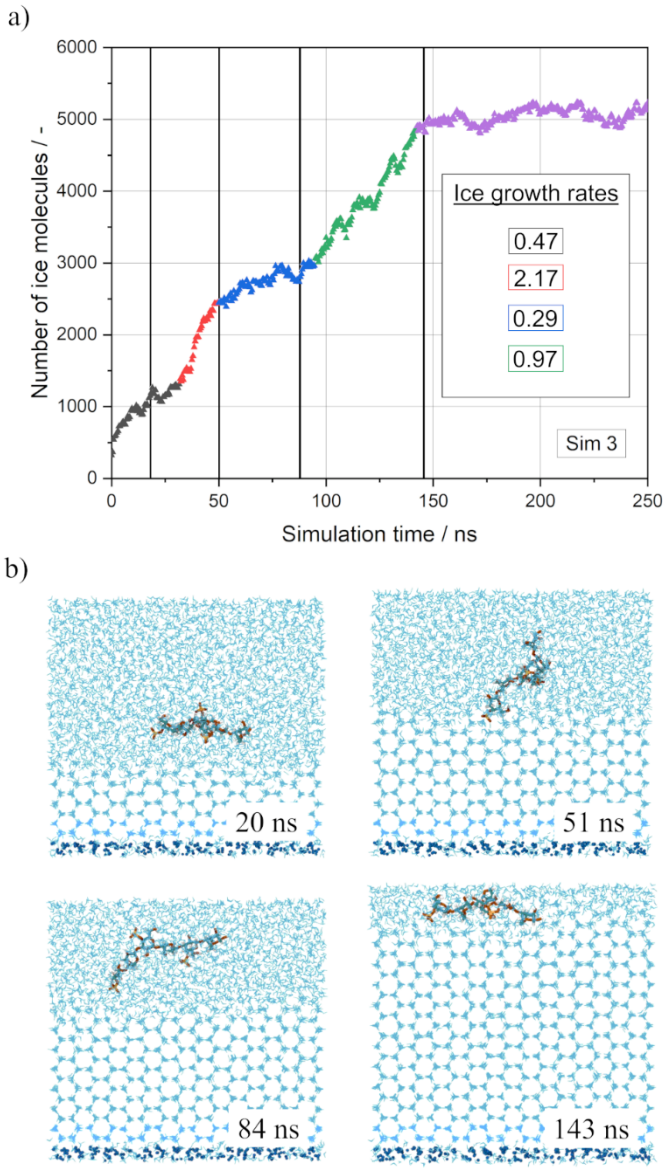

Figure 6.5. *Progression of ice growth in the direction of the secondary prism plane at 268 K (a) and corresponding snapshots of the simulation box (b). Initially, κ-carrageenan attempted to bind to the ice surface but detached at 20 ns, resulting in an accelerated ice growth until a second interaction occurred at 51 ns. This interaction slowed down ice growth, but the molecule detached again around 84 ns. No further interactions were observed, and the simulation box froze completely after 143 ns. Ice-growth rates are given in molecules·ns^{-1}·nm^{-2}.*

Comparing the Structural Dynamics of κ-Carrageenan at 265 and 268 K

To further illustrate the differences between the simulations at 265 and 268 K, the RMSD values and *y*-coordinate of κ-carrageenan can be evaluated and are presented in Figure 6.6. Conformational changes in κ-carrageenan can be inferred from the RMSD value, while the values of the *y*-coordinate provide evidence of possible interactions or binding to the ice surface. During the first simulation in the direction of the secondary prism plane at 265 K, the RMSD value shown in Figure 6.6a exhibited a rapid increase from 0.15 to 0.45 nm within the first 20 ns. Subsequently, the interaction of κ-carrageenan with the ice surface occurred leading to a stabilization

of the RMSD value at this level. At 50 ns, a subtle rearrangement of the molecule took place, which resulted in a stable binding position and conformation. This is reflected by a drop of the RMSD value to 0.4 nm. Throughout the remaining simulation time until 250 ns, the molecule adhered stable to the ice surface and inhibited further ice growth. Consequently, the RMSD value remained constant at 0.4 nm. This behavior was further evident in the trajectory of the COM of κ-carrageenan in the *y*-direction presented in Figure 6.6b. As ice growth proceeds along the *y*-axis, a stable binding of the molecule to the ice surface can be identified by constant values of the *y*-coordinate. Starting at 50 ns, this was clearly observed as the molecule consistently resides at a height of 3 nm. In contrast, the third simulation at 268 K exhibited a highly fluctuating RMSD value, as shown in Figure 6.6c, suggesting a flexible molecule undergoing continuous positional and conformational changes. These fluctuations decrease over the course of the simulation due to restricted mobility of κ-carrageenan by the growing ice crystal. Around 150 ns, the molecule was confined at the top of the simulation box leading to a constant RMSD value. Accordingly, the *y*-coordinate illustrated in Figure 6.6d displayed an almost steady increase. In addition, the previously mentioned short interaction with the ice surface between 50 and 84 ns is evident as the *y*-coordinate values show a minor increase during this interval. However, the reason behind κ-carrageenan's inability to stable bind to the ice surface at 268 K remains elusive. Higher temperatures not only result in slower ice-growth rates but also increase the flexibility and mobility of the molecule. This may cause the κ-carrageenan molecule to change its position or conformation too quickly to attach to the growing ice surface.

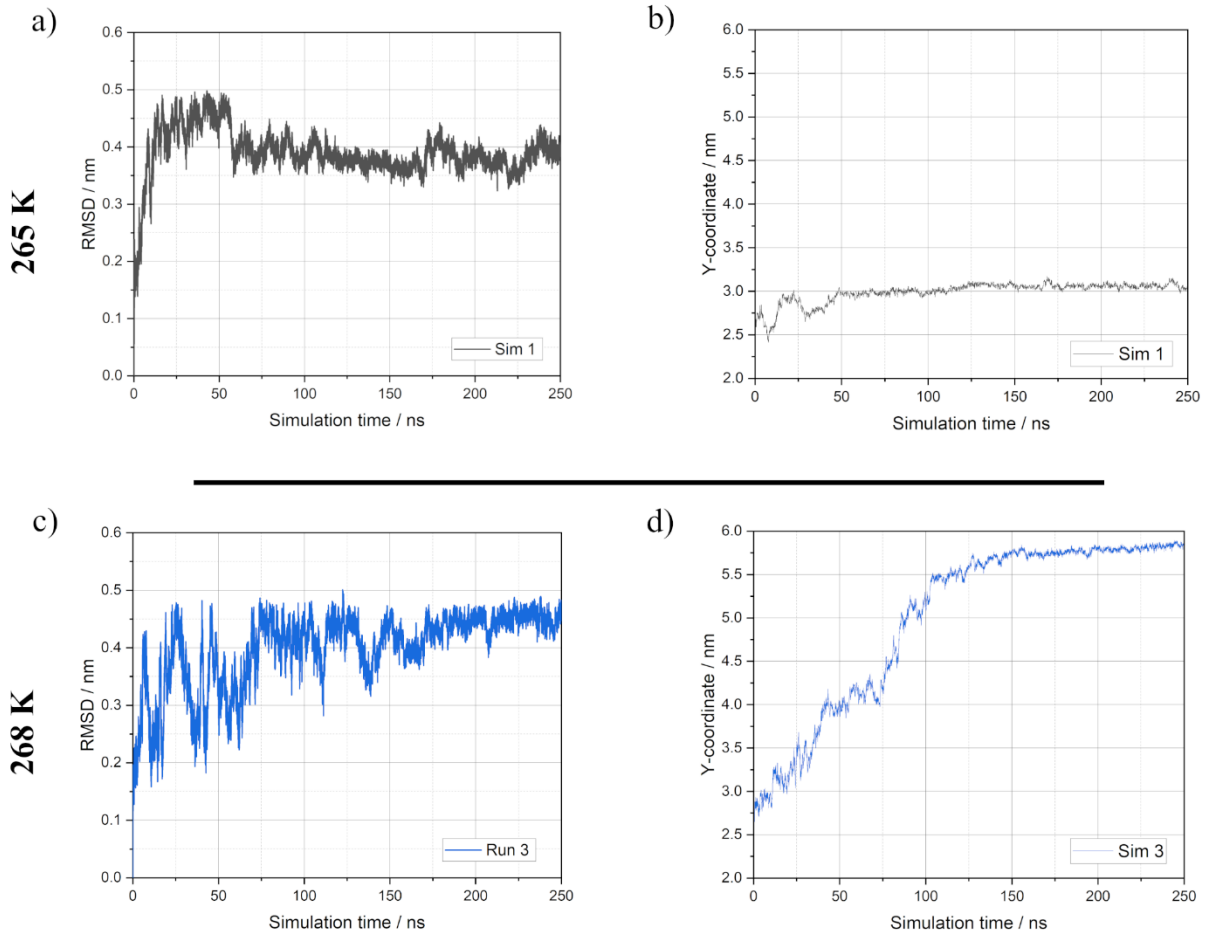

Figure 6.6. *Top and bottom rows display RMSD and y-coordinate values from simulations with ice growth in the direction of the secondary prism plane at 265 and 268 K, respectively.*

Summary

To summarize this section, the simulations of a κ-carrageenan containing three disaccharide units yield several notable findings. Despite its short molecular length, κ-carrageenan is capable of interacting with the ice crystal surface as hypothesized in the Introduction. Contrary to the hypothesis, the interaction involved not just one but the basal plane and both prism planes. However, the interaction with the basal plane is less pronounced compared to those of the primary and secondary prism planes. The simulation study also revealed that the binding orientation of the molecule is important for inhibiting ice growth. In this regard, it is crucial to note that the simulations involve an artificial system with well-defined dimensions. Due to the applied PBC, the distance between κ-carrageenan and its mirror image is smaller for a horizontal binding orientation compared to a vertical binding orientation. This aspect must be taken into account when comparing different sized systems or the thermal hysteresis obtained from simu-

lations with experimental data. Nevertheless, the binding orientation and consequently the covered surface area have been shown to correlate with the antifreeze activity of ice-binding proteins [199], which is further supported by the simulation of κ-carrageenan. Remarkably, the interaction between κ-carrageenan and the ice crystal exhibited a temperature dependency, with no stable binding observed at a temperature of 268 K, regardless of the ice-growth direction. This contrasting binding behavior clearly distinguishes κ-carrageenan from PVA, which is able to irreversibly bind to the prismatic plane even in the absence of further ice growth [213,217]. Therefore, one may assume that the binding affinity of each individual structural unit of κ-carrageenan interacting with the ice surface is rather weak. Consequently, a longer molecule compromising more of these structural units may still bind to the ice surface at elevated temperatures.

6.4.3 Influence of Molecular Size on the Ice-Binding Behavior

To investigate the binding of a larger molecule to the ice surface, the ice growth in the direction of the secondary prism plane at a temperature of 265 K was studied. A summary of the simulation results, including κ-carrageenan composed of six disaccharide units is provided in Table 6.3. All simulations demonstrated that κ-carrageenan bound to the ice surface but only after a first, temporary interaction. The bound κ-carrageenan molecule maintained consistently a horizontal binding orientation without being trapped inside the ice crystal. Moreover, Figure A4.7 illustrates the exact ice-growth profiles and growth rates. This figure illustrates once more the initial interaction phase and subsequent growth reduction in the ice-growth rate.

Table 6.3. *Overview of the results obtained for κ-carrageenan composed of six disaccharide units and the double helix with ice growth toward the secondary prism plane.*

Ice growth direction	Temperature / K	Simulation number	Number of interactions with the ice surface	Ice growth stopped	Molecule trapped in ice crystal	Binding orientation
Six unit κ -carrageenan	265	1	2	no [a]	no	horizontal
		2	2	no [a]	no	horizontal
		3	2	no [a]	no	horizontal
Double helix	265	1	1	yes	no	horizontal
		2	1	no	yes	vertical
		3	2	yes	no	horizontal

[a] *The late permanent binding of κ-carrageenan to the ice surface makes it difficult to definitely conclude whether it is able to stop ice growth.*

To exemplify the behavior of the longer κ-carrageenan molecule, the second simulation is visualized in Figure A4.8. Initially, unrestricted ice growth was observed as the κ-carrageenan molecule was not yet in close contact with the ice surface. Therefore, the ice-growth rate of 1.93 molecules·ns^{-1}·nm^{-2} was close to the growth rate of the control without a κ-carrageenan of 2.14 ± 0.06 molecules·ns^{-1}·nm^{-2} (unrestricted ice-growth phase I). At 19 ns, the molecule established a stable binding to the ice surface, which persisted until 158 ns. Due to this interaction, the ice-growth rate dropped tremendously to 0.18 molecules·ns^{-1}·nm^{-2} (ice-growth inhibition phase I). The κ-carrageenan molecule subsequently detached from the ice surface, leading to a restoration of ice growth at a rate of 1.71 molecules·ns^{-1}·nm^{-2} (unrestricted ice-growth phase II). Starting from 214 ns, κ-carrageenan was able to reattach to the ice surface forming a stable binding (ice-growth inhibition phase II). Consequently, the ice-growth rate decreased again to 0.17 molecules·ns^{-1}·nm^{-2} and the characteristic curved ice surface developed. The established interaction between the molecule and ice surface lasted throughout the rest of the simulation up to 300 ns. A similar pattern was evident in the other two simulations. When the

ice-growth rates during ice-growth inhibition phases were compared between the small and large systems, only minor differences were observed. Both the small and large κ-carrageenan molecules lead to a substantial reduction of the ice-growth rate in the range 0.17–0.22 molecules·ns^{-1}·nm^{-2}. However, only the six-unit κ-carrageenan consistently displayed a two-step binding behavior and horizontal binding orientation. This may be attributed to the increased number of potential binding sites in the larger molecule. These results do not confirm the hypothesis that longer molecules bind more strongly to the ice surface.

With the aim to gain further insights into κ-carrageenans's interaction with the ice surface, a detailed analysis of the initial interaction phase from 14 to 127 ns of the second simulation was performed. The greater number of potential binding sites on the six-unit molecule allowed for a more thorough analysis. To illustrate the sequence of interactions, Figure 6.7 presents the corresponding simulation snapshots arranged in chronological order. For better visualization, the molecular segments interacting with the ice surface are color-coded. The initial interaction led to the most stable binding during this interaction period and involved the leftmost G-unit of the molecule (colored red). Following the initial interaction, the opposite end of the molecule (colored blue) attempted to bind to the ice surface. This connection via the DA-unit was maintained until around 71 ns, but subsequently, this end of the molecule detached from the ice surface. Simultaneously, a more central G-unit of the molecule (colored green) endeavored to bind to the ice surface. However, this segment was not able to establish a stable interaction with the ice surface. As the simulation progressed, no further segments of the κ-carrageenan strand interacted with the ice surface. At around 127 ns, even the previously firmly bound left portion of the molecule (colored red) detached, causing the molecule to drift away from the ice surface.

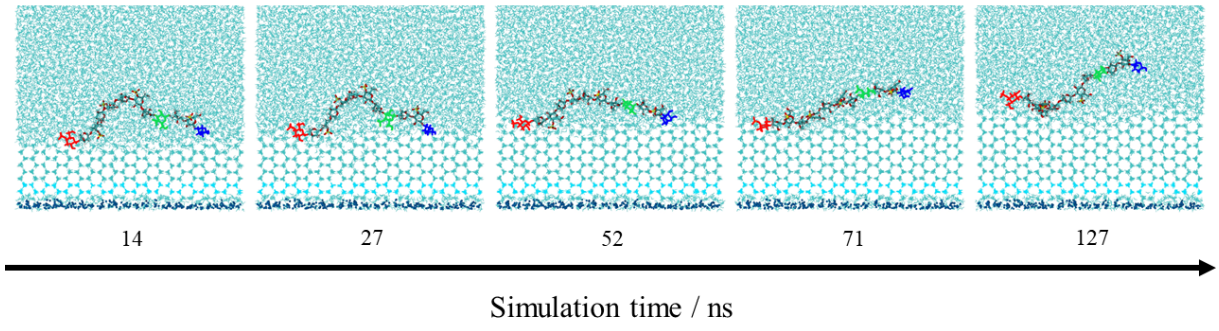

Figure 6.7. *Simulation snapshots captured in the growth direction of the secondary prism plane at 265 K to visualize the interaction of κ-carrageenan with the ice surface between 14 and 127 ns.*

Generally, the interaction behavior of κ-carrageenan exhibits similarities to the zipper mechanism described by Naullage and Molinero for PVA [217]. After an initial attachment at a random binding site, additional interactions of nearby binding sites occur [217]. In the case of κ-carrageenan, these additional binding sites were not able to establish a permanent interaction with the ice surface. Furthermore, the molecule was not able to form a stable initial interaction at a higher temperature of 268 K independent of its size with three or six disaccharide units. This further supports the assumption that the interaction strength of the respective binding site is weaker compared with PVA. Moreover, the ice-growth rate may also influence the binding ability of κ-carrageenan. At 268 K, the ice-growth rate was substantially lower, and no binding was observed. The initial interaction shown in Figure 6.7 resulted in a decrease in ice-growth rate potentially preventing further interactions of the remaining binding sites. Figure A4.7 provides the ice-growth pattern and exact growth rates. Particularly at slow ice-growth rates, the dynamic nature of the ice surface, due to the continuous attachment and detachment of water molecules, seems to present a challenge for the κ-carrageenan seeking to bind. In addition, κ-carrageenan might necessitate the formation of ice crystal curvatures to remain in its position and prevent displacement. This curvature formation may be too slow at higher temperatures or at close distances to an already bound molecular segment.

Additionally, Figure 6.8 illustrates the effect of the longer κ-carrageenan molecule on the ice surface structure, which is particularly evident in the results of the third simulation. For instance, the ice surface demonstrated deep indentations attributed to the bound κ-carrageenan at 290 ns. The molecule initially interacted with the ice surface via the G-unit at the molecule's left end similar to the second simulation illustrated in Figure 6.7, allowing further ice growth in unoccupied regions. Subsequently, interactions with the molecule's right end influenced ice crystal growth, resulting in an additional, smaller indentation as depicted in the front view picture of Figure 6.8. Furthermore, the role of molecular flexibility to achieve efficient binding is evident in Figure 6.8. The initially bound left segment of the molecule stands upright, while the rest of the molecule is oriented parallel to the ice surface. The molecule ability to bend its structure prevents it from being easily trapped within the growing ice crystal. In all simulations at 265 K where the small κ-carrageenan exhibited a vertical binding orientation, it became trapped within the ice crystal. Due to the flexibility and increased number of binding sites in the longer molecule, this vertical entrapment seems less likely. This simulation also demonstrated the ability of the κ-carrageenan strand to adapt to the structural features of the ice lattice to enable an interaction with the ice crystal.

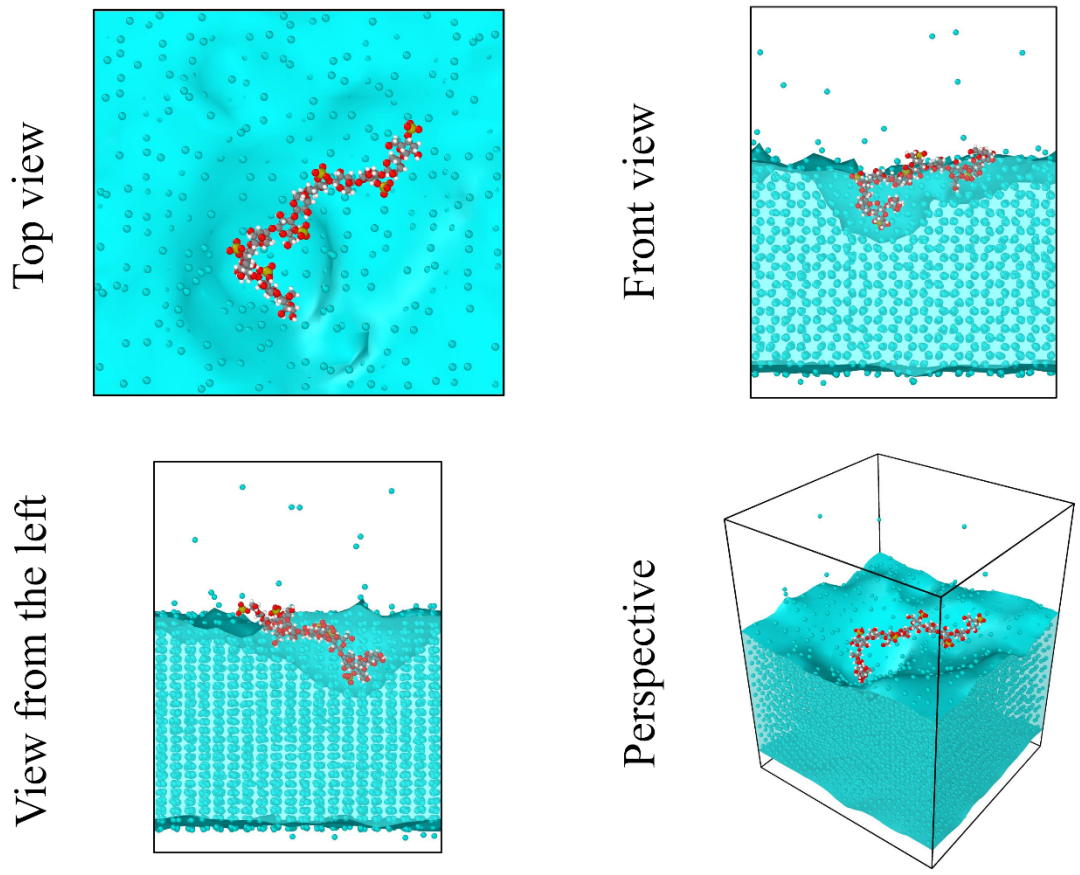

Figure 6.8. *Visualization of the ice surface structure at a temperature of 265 K and 290 ns with ice growth along the secondary prism plane. The water molecules categorized as hexagonal ice by the CHILL+ algorithm are depicted as cyan spheres.*

Aside from the previously described flexibility and the more dynamic, temporary binding behavior, there were no substantial differences evident between the two κ-carrageenan molecules. The six-unit κ-carrageenan was able to bind to the ice crystal surface in all three simulations. A strongly curved ice surface was formed, suggesting the inhibition of further ice growth. However, this could not be proven within the simulation time of 300 ns. Despite the higher number of potential binding sites, the interaction with the ice surface of the secondary prism plane was not significantly improved. Furthermore, the variation in molecular length had no significant impact on the ice-growth rates after the binding of the κ-carrageenan to the ice crystal surface. Both systems exhibited growth rates in the range of 0.15–0.22 molecules·ns^{-1}·nm^{-2} with ice growth along the secondary prism plane at 265 K. Despite the elongation of the simulated κ-carrageenan by three disaccharide units, the molecule was likely still too short to show its full potential. According to Leiter et al., κ-carrageenan demonstrated the highest IRI activity with its molecular weight being above 300 kDa [43]. Smaller molecules tend to exhibit a decreased IRI activity.

6.4.4 Influence of Double Helix Formation on the Ice-Binding Behavior

The gel formation of κ-carrageenan or furcellaran, a structurally similar polysaccharide, substantially decreases their IRI activity [41,124]. Therefore, the formation of double helix structures might potentially reduce the ice-binding ability of κ-carrageenan. To further investigate this, simulations were performed involving a double helix composed of two κ-carrageenan strands. Each strand contained three disaccharide units. At first, a stable double helix conformation was generated by simulating these two strands in a water-filled box at a temperature of 268 K without the addition of excess ions. Besides visual inspection, the progression of the RMSD value was analyzed to identify the time point when a stable conformation was formed. The RMSD value was calculated using the initial confirmation of the two strands as a reference and reached a stable level after 400 ns, as depicted in the left panel of Figure A4.9. To ensure the stability of the double helix conformation, the simulation was extended to 1000 ns. The conformation remained unaltered throughout the additional simulation time and was exported at the end of the simulation, as illustrated in the right image of Figure A4.9. This conformation was used as the initial structure for the subsequent simulations to investigate the ice-binding ability of the κ-carrageenan double helix.

The results of the simulation with ice growth along the secondary prism plane at 265 K are summarized in Table 6.3. The progression of ice growth along with the corresponding ice-growth rates is shown in Figure A4.10. In all three simulations, the double helix was able to interact with the ice surface inhibiting ice growth. The double helix maintained a parallel orientation relative to the ice crystal surface throughout the simulations. While in the first and second simulation, the double helix structure demonstrated efficient ice-growth inhibition, in the third simulation, the double helix showed a less pronounced effect on ice growth, with ice continuing to grow throughout the simulation period. Remarkably, the double helix demonstrated stability and both κ-carrageenan strands maintained close proximity even when in contact with the ice crystal. During two-out-of-three simulations, the double helix was able to stably attach to the ice surface and remained in place, resisting displacement by subsequent ice growth. This is shown in Figure 6.9. In this simulation, the double helix bound to the ice surface after about 25 ns, impeding further ice growth (the ice-growth inhibition phase). The ice-growth rate dropped to 0.11 molecules$\cdot$ns$^{-1}\cdot$nm^{-2}, which is marginally below that of the single-stranded κ-carrageenan. This is likely attributed to the larger surface area occupied by the bound double helix. Consequently, with the same simulation box size, fewer water molecules were able to join the ice lattice. Despite the subsequent rotation of the double helix on the ice surface, ice growth remained negligible.

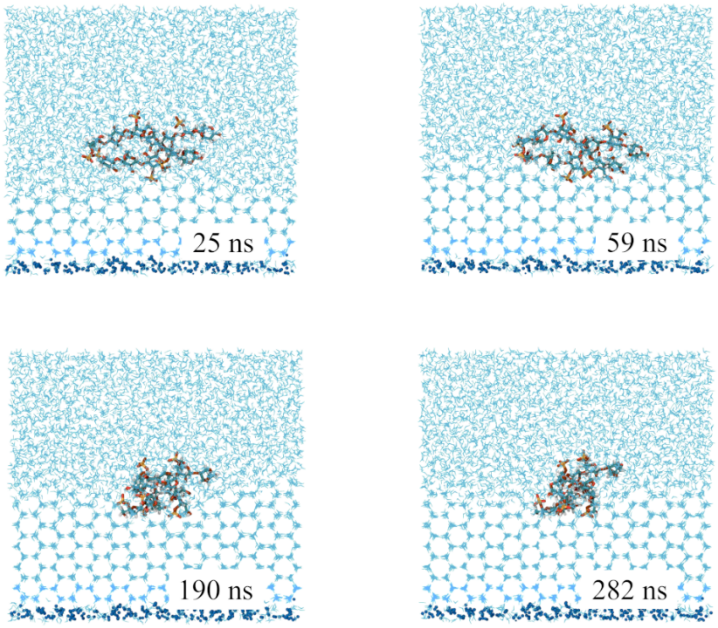

Figure 6.9. *Series of snapshots are provided to visualize the progression of the second simulation. The double helix initially interacted with the ice surface at 25 ns. Subsequently, the double helix exhibited rotational motion but remained attached to the ice surface throughout the simulation.*

Additionally, the progression of the *y*-coordinate of the COM is presented in Figure A4.11. Despite its strong influence on the ice-growth rate, κ-carrageenan exhibited a nonstable interaction with the ice surface in the third simulation. After the initial binding at about 25 ns, the double helix was displaced while still located at the surface after 240 ns.

The hypothesis that the aggregation into a double helix would negatively impact the binding of κ-carrageenan to ice was not supported by the simulations. Despite the double helix formation, the molecules were still able to interact with the ice surface. This finding aligns with the observation that associated helix-stabilizing ions can enhance IRI activity of κ- and ι-carrageenan [448].

6.4.5 Ice-Binding Mechanism of κ-Carrageenan

The precise mechanism of binding of κ-carrageenan to ice is still not fully understood. For instance, the bound κ-carrageenan molecule exhibits a certain degree of flexibility and mobility, raising the question of whether the binding is of a reversible nature. Additionally, the specific atomic interactions that facilitate this binding remain unknown. These uncertainties are addressed in the following sections of this study.

Reversible or Irreversible Binding?

In the introduction, it is highlighted that ice-binding proteins can bind reversibly or irreversibly depending on the type of protein. Based upon the previous findings in this study, a reversible binding mechanism for κ-carrageenan may be plausible. Since a reversible binding was not clearly observed within the simulation period of 250 ns, the first simulation of ice growth in the direction of the secondary prism plane at 265 K was extended to 1000 ns. Considering the stable binding of the three-unit κ-carrageenan to the ice surface and the reduced computational costs of the small system, this system was selected for further analysis. In the case of an irreversible binding to the ice surface, one expects no or only minimal changes in the position of the bound molecule and, depending on the temperature, an inhibition of further ice growth. Hence, the ice growth, the *y*-coordinate, the RMSD value of the molecule, and snapshots from the simulation were evaluated. Figure 6.10 depicts the progression of ice formation on the left graph, while the right graph illustrates the progression of the *y*-coordinate. Despite the previously made assumption that κ-carrageenan might fully inhibit ice growth, further simulation revealed continuous ice growth, albeit at very low rates of 0.04 molecules·ns^{-1}·nm^{-2} (left graph of Figure 6.10). Initially, the *y*-position of κ-carrageenan remained stable at a height of 3 nm for approximately 500 ns (right graph of Figure 6.10). However, during the subsequent 500 ns, the molecule exhibited an upward shift of 0.75 nm, suggesting a loss of a stable interaction.

Furthermore, the analysis of RMSD values and the corresponding simulation snapshots, given in Figure A4.12, further supports these findings. While the RMSD value settled around 0.4 nm, it experienced two peaks during 500–600 and 700–800 ns (left graph of Figure A4.12). The analysis of the snapshots revealed that these RMSD fluctuations were associated with conformational changes and the dislocation of the molecule (Figure A4.12).

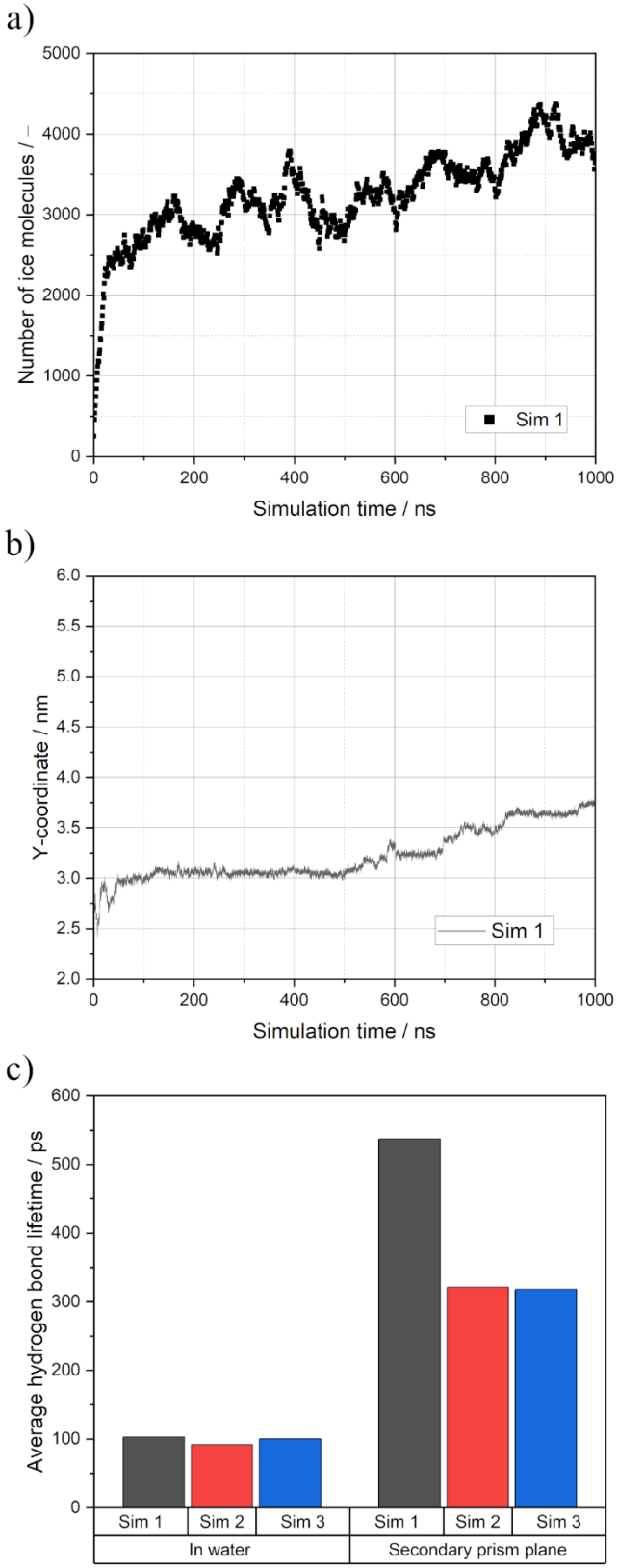

Figure 6.10. *Shown are the results of the extended simulation with ice growth along the secondary prism plane at 265 K. Panel (a) illustrates the ice growth, while the panel (b) graph presents the y-coordinate of the COM of the κ-carrageenan molecule as a function of simulation time. In addition, panel (c) compares the average hydrogen bond lifetimes at 265 K for systems containing six-unit κ-carrageenan in water without ice crystal (bars on the left) and in systems with ice growth and bound κ-carrageenan (bars on the right).*

Moreover, none of the simulations containing the κ-carrageenan molecule with six disaccharide units displayed irreversible binding throughout the entire 300 ns simulation duration. In addition, the bound double helix exhibited rotational freedom after binding to the ice surface (Figure 6.9) and, in one of the three simulations, detached from the ice surface after a certain period (Figure A4.11). All of these observations strongly suggest that κ-carrageenan engages in reversible binding with the ice crystal surface. The inability to determine a thermal hysteresis for κ-carrageenan [44], despite its strong IRI activity, further supports that κ-carrageenan binds reversibly to ice crystals. However, it is important to reiterate that reversible binding has only been demonstrated for very short molecules of κ-carrageenan up to six disaccharide units. Larger molecules, with their increased number of interaction sites, might be able to establish longer lasting interactions with the ice surface or even irreversible binding.

Hydrogen Bond Analysis

As previously described in the Introduction, hydrogen bonding seems crucial for the interaction between polymers and the ice surface; the number and lifetime of hydrogen bonds formed between water molecules and κ-carrageenan were analyzed throughout all simulations. Given the abundance of hydroxyl groups in κ-carrageenan, the formation of numerous hydrogen bonds is expected. Nevertheless, variations in the stability of these bonds, particularly between the unbound and bound states of κ-carrageenan, are anticipated. The results obtained for κ-carrageenan composed of six disaccharide units will be presented, as this molecule was also simulated in water without ice crystal growth at 265 K. Additionally, the higher number of hydroxyl groups compared to the three disaccharide variant should make differences more apparent. Nevertheless, the hydrogen bond analysis was conducted across all systems.

No significant difference in the average number of hydrogen bonds in the systems with carrageenan bound to ice and the systems without ice was evident, with values of 81.3 ± 0.25 and 81.3 ± 0.24, respectively. These findings indicate that the number of hydrogen bonds remains at a consistently high level, regardless of whether κ-carrageenan is bound to the ice crystal or not.

Although the number of hydrogen bonds was similar, the stability of these bonds varied considerably between bound and unbound κ-carrageenan, revealing crucial differences in their interaction with water or ice. As illustrated in Figure 6.10c, the average hydrogen bond lifetimes in the systems with unbound κ-carrageenan and without ice growth were substantially shorter with 98 ± 6 ps than in the systems exhibiting ice growth and bound κ-carrageenan with 392 ± 126 ps. The larger deviations observed between the simulations involving ice binding can be

attributed to the varying binding durations of κ-carrageenan to the ice surface. Moreover, the results obtained for both the smaller κ-carrageenan and double helix in systems with ice binding were in a comparable range. It should be noted that the stabilization of the double helix involves approximately three hydrogen bonds between the individual κ-carrageenan strands, slightly reducing the hydrogen bond capacity of the helix. Nevertheless, this minimal reduction did not affect the binding ability of the double helix to the ice surface. This suggests that the aggregation into a double helical structure has no negative influence on κ-carrageenans' ability to interact with ice crystals via hydrogen bonds, at least for the short helix simulated in this study. Consistent with expectations, hydrogen bonds generally appear as a critical aspect in ice binding of κ-carrageenan and maintaining its interaction with the ice surface.

Detailed Analysis at the Atomic Level

The precise identification of atoms or groups of atoms involved in the interaction with the ice surface remains elusive. Yet, it is highly likely that they are either donors or acceptors of hydrogen bond formation. Regardless of its helical conformation, the flexibility of the κ-carrageenan strand enables an adaptation to the ice surface structure to some degree. This assumption is further supported by the fact that κ-carrageenan can interact with all investigated ice planes, including basal, primary, and secondary prism planes. By analyzing the RMSF value of atoms in each system, the most flexible atom regions of κ-carrageenan were identified. Subsequently, the alignment of these regions with the positions of water molecules within the ice lattice was examined to gain insights into the polymer–ice interaction. For clarity, the presentation will focus on the results obtained from the smaller system, which are identical with those of the larger system.

In Figure 6.11a, the RMSF values for the atoms of κ-carrageenan composed of three disaccharide units and ice growth in the direction of primary and secondary prism planes (red and blue curves) are plotted. Additionally, the atoms with high RMSF values exhibiting the greatest flexibility are highlighted in different colors in Figure 6.11b. Reoccurring peaks are observed at particular atom positions, for example, atoms 47–50, 56–58, 90–92, and 98–100. Furthermore, the molecule's terminal regions consistently exhibited enhanced flexibility. The most mobile atoms of the molecule exhibited high RMSF values and belonged to the sulfate and neighboring CH_2OH group, both part of the G-unit (Figure 6.11b). Given the presence of oxygen atoms in both groups, it is plausible that hydrogen bonds are formed at these positions. Notably, the hydroxyl group of the DA-unit forms hydrogen bonds with the surrounding water molecules and internally with the sulfate group of the neighboring G-unit. This might be one reason for

the lower RMSF values of these hydroxyl groups compared to those of the CH_2OH group of the G-unit. This is illustrated in Figure A4.13, where hydrogen bonds in the water shell around κ-carrageenan are illustrated.

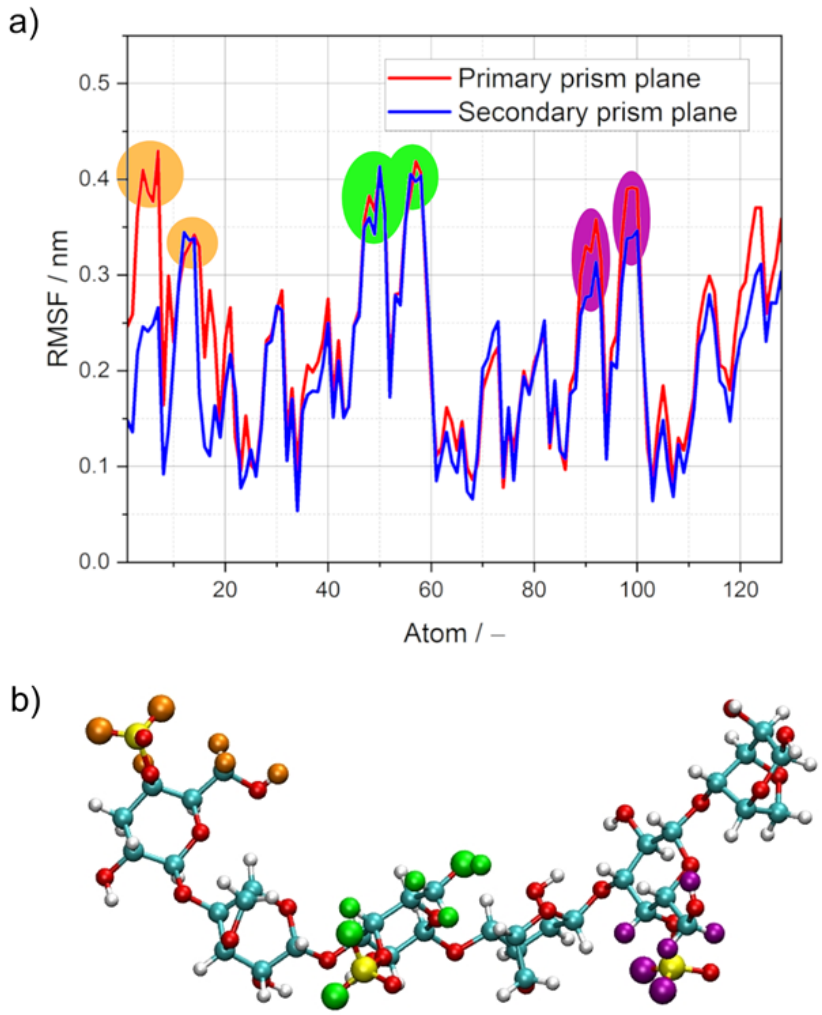

Figure 6.11. *(a) RMSF values of κ-carrageenan containing three disaccharide units, calculated for the growth direction along the primary prism plane (red curve) and the secondary prism plane (blue curve) at a temperature of 265 K. (b) κ-Carrageenan molecule with highlighted atoms (orange, green, and purple) corresponding to the respective peaks in the RMSF values of panel (a).*

Further details of the interaction between κ-carrageenan and the ice surface can be gained by analyzing the bound state and identifying specific atoms or molecular sections involved in the interaction. A three-dimensional analysis using VMD was performed to locate oxygen atoms of κ-carrageenan that replaced water molecules within the ice lattice. Each oxygen atom was checked against the lattice position from different perspectives. Those oxygen atoms occupying a lattice site were colored green and are shown in Figure A4.14. The simulation at 265 K with

ice growth along the secondary prism plane was chosen as an example of this analysis. A distinct cluster of four oxygen atoms belonging to κ-carrageenan's left-hand terminal G-unit is aligned with ice lattice positions. Analysis of the corresponding simulation data reveals that this molecular region initiated contact with the ice surface, effectively anchoring the molecule and preventing it from diffusing away (as seen in Figure 6.4a). In contrast, the right side of the κ-carrageenan displayed greater mobility. Lattice positions were frequently occupied by oxygen atoms in the sulfate groups and G-unit. Additionally, oxygen atoms belonging to the DA-unit were observed at these positions. In most cases, the sulfur atoms did not align with the lattice positions. In general, the overall structure of the κ-carrageenan molecule attempts to adapt to the ice lattice structure. Similar trends were observed for various growth directions and in simulations involving κ-carrageenan with six disaccharide units, as exemplarily illustrated in Figure A4.15.

In summary, the interaction of κ-carrageenan with ice seems to be a reversible process, at least for the investigated molecular sizes. The reversible nature of the binding behavior was maintained in the case of a molecule twice as large and the double helix. In addition, the formation of hydrogen bonds is a key factor in this interaction. These hydrogen bonds exhibited an exceptionally long lifetime once the molecule was attached to the ice surface. Moreover, the binding mechanism to the ice surface involved the occupation of lattice positions by oxygen atoms of κ-carrageenan and the molecule's ability to conform to these lattice positions. Thus, the hypothesis that hydrogen bonding and lattice matching play a significant role in the interaction mechanism between κ-carrageenan and ice can be confirmed.

Further Investigations and Outlook

Lee et al. showed that hyperbranched polyglycerols influence the thickness of the quasi-liquid layer (QLL) and thus altering ice crystal growth [390]. This effect was also investigated in this study for κ-carrageenan by analyzing the density profile in the *y*-direction to determine the QLL thickness. No significant influence of κ-carrageenan on QLL was observed. As an example, the thickness of the QLL was 0.66 nm when κ-carrageenan was bound to the ice surface, as determined from the extended simulation at 265 K with ice growth along the secondary prism plane at 800 ns. The corresponding density profile is depicted in Figure A4.16. This falls within the range of 0.69 ± 0.044 nm for the QLL thickness in a system without κ-carrageenan. Moreover, the formation of clathrate structures or ice-like water in the vicinity of ice-binding proteins can mediate their attachment onto the ice crystal surface [194,196,430,467]. To investigate this, systems including the six-unit κ-carrageenan were analyzed by using the CHILL+ algorithm.

However, no evidence was found that κ-carrageenan is able to promote the formation of such ordered water structures, neither in systems with nor without ice growth.

Through extensive simulations, this study provides new insights into the ice-binding mechanism of κ-carrageenan, which may also be applicable to other polysaccharides. Future studies should experimentally verify the ice binding using techniques such as fluorescence-based ice plane affinity [403] or super-resolution microscopy [206]. However, these methods need further development, so they can be applied to polysaccharides.

To further investigate the reversibility of ice binding, simulating a much longer molecule would be beneficial. The increased number of binding sites in a longer molecule might facilitate binding, even at slower ice-growth rates.

Furthermore, previous research by Hale et al. demonstrated that the addition of helix-stabilizing ions can enhance the IRI activity of κ- and ι-carrageenan [448]. By utilizing MD simulations, the influence of these ions on the polysaccharide's structure and conformational changes resulting in an altered ice-binding behavior can be elucidated. Given the flat and rigid ice-binding site of IBPs, these ions may introduce a conformational change in the polysaccharide structure, which is favored for ice binding [101].

Moreover, by computationally comparing the binding mechanism between κ- and ι-carrageenan, further insights into the molecular features responsible for ice binding of these polysaccharides may be gained. Although ι-carrageenan possesses an additional sulfate group on the DA-unit, experiments indicate a lower IRI activity of ι-carrageenan in comparison to κ-carrageenan [44].

To isolate the effects of the individual disaccharide's subunits on ice binding, the simulation of an artificial molecule entirely composed of DA- or G-units may yield further insights. This may enable the identification of the unique contributions of each subunit to the ice-binding process.

6.5 Conclusions

Simulation results demonstrated that κ-carrageenan is able to bind to multiple ice surfaces, including the basal plane and primary and secondary prism planes but with a less pronounced affinity toward the basal plane. In addition, the ability of κ-carrageenan to inhibit ice growth depends on the binding orientation, whether the molecule binds parallel or perpendicular to the ice surface. Importantly, within the molecular size range studied, the attachment of κ-carrageenan to the ice crystal surface is reversible. Even when the molecular length is increased from

three to six disaccharide units, the reversible binding behavior is not altered. Similar to the zipper mechanism proposed for PVA, the κ-carrageenan molecule initiated binding and attempted to progress along the strand, but neighboring units failed to establish interactions with the ice surface for longer time periods. At an elevated temperature of 268 K, which is approximately 2 K below the melting point of the water model, ice crystal growth slowed, and no binding occurred. Moreover, the aggregation of two κ-carrageenan strands with three disaccharide units into a double helical structure did not negatively affect the binding to the surface of the secondary prism plane. The interaction between the respective ice surface and κ-carrageenan is facilitated by the formation of hydrogen bonds. While many hydrogen bonds were formed in general between κ-carrageenan and ice or water molecules, the hydrogen bond lifetime was significantly prolonged in the case of κ-carrageenan binding to the ice surface. Additionally, the flexibility of κ-carrageenan allows its oxygen atoms to occupy a specific position within the ice lattice, while the overall molecular structure can adapt itself to the ice surface structure. To experimentally verify the ice binding of κ-carrageenan and its binding planes, future studies should employ methods such as fluorescence-based ice plane affinity after refinement for use with polysaccharides. This study improves our understanding of the interaction between κ-carrageenan and ice crystals and may facilitate the design and development of tailored applications for this biopolymer.

7 General Discussion and Outlook

This thesis aims to elucidate the intricate molecular mechanisms governing the ice recrystallization inhibition activity of carrageenan polysaccharides. Employing a combined approach of experimental techniques and molecular dynamics simulations, the fundamental principles underlying this phenomenon are investigated. This research investigates several key questions as outlined in **Chapter 1.1.1**, including the interaction mechanism of carrageenan polysaccharides affecting ice recrystallization. Additionally, the study explores whether carrageenan molecules directly interact with the ice crystal surface and to identify the functional groups and structural motifs responsible for their IRI activity.

The following general discussion presents a synthesis of the research findings, integrating data obtained from experimental (**Chapters 2–4**) and computational (**Chapters 5–6**) approaches. A critical analysis of these findings is conducted in this section and the potential implications for the application of IRI-active carrageenans are discussed. Furthermore, the hypotheses presented in **Chapter 1.1.2** are revisited, undergoing either falsification or confirmation, and summarized in Table 7.1.To conclude, potential directions for future research are outlined.

Previous studies have demonstrated that the structure of carrageenans significantly affects their functional properties. An extensively investigated functional property, the gel formation, varies greatly between κ- and ι-carrageenan and their hybrids [274,382]. Consequently, the specific composition of carrageenan impacts its application. Using recombinantly produced carrageenases, **Chapter 2** presents a novel method for structurally analyzing carrageenans and their hybrids. Enzymatic digestion and HPLC-MS/HPSEC-RI result in successfull characterization of all samples. A substantial discrepancy between the manufacturers labeling and the actual structure are observed in most of the commcercial carrageenan samples. Notably, none of the λ-carrageenan samples exhibit the expected structural characteristics; instead they contain κ-, ι-, and ν-units, indicating they are hybrid carrageenans. In addition, the samples exhibit differences in the type of associated cations and the overall ion concentration. Structural differences, especially the proportion of κ-units, directly affect the gelling properties. Improved gelation is observed with increasing κ-unit content, providing substantial support for *Hypothesis 1* (Table 7.1). Moreover, the presence of ν-units in κ/ι hybrids is observed to hinder gelation. This clearly demonstrates how crucial carrageenan's structure is to its functional properties, highlighting that this structural information should be determined prior to utilizing commercial carrageenans for certain applications.

Given that **Chapter 2** demonstrates the influence of carrageenan structure on the gelling properties, it can be inferred that other functional properties, such as IRI activity, are also structure-dependent. For this reasen, **Chapter 3** examines the IRI activity of previously selected and structurally characterized commercial carrageenans. In addition, monocationic forms of the carrageenan samples are produced to understand the influence of associated cations on IRI activity. Even low concentrations of added ions can affect the IRI activity of κ-carrageenan, as shown by Leiter et al. [41,42]. Consequently, the associated cations may also influence its IRI activity. Consistent with prior findings of uncharacterized carrageenans, the studied κ-carrageenan generally possesses superior IRI acitivity compared to ι-carrageenan [44]. For the hybrid carrageenans, a positive correlation between the content of κ-units and the IRI activity is evident. Moreover, the arrangement of the κ-units within the carrageenan molecule has a substantial impact. Consecutive placement of κ-units demonstrates a greater ability to inhibit recrystallization processes than a more scattered distribution. As hypothesized, also the type of associated cations exhibits an influence on the IRI activity. Helix-stabilizing ions enhance the ice recrystallization inhibition properties of both κ- and ι-carrageenans, as well as hybrid carrageenans. Potassium stabilizes κ-carrageenan, while ι-carrageenan is stabilized by calcium. Thus, *Hypothesis 2*, stating that both varying structural units and associated cations influence IRI activity, can be confirmed (Table 7.1). Additionally, *Hypothesis 3*, proposing that hybrid carrageenans exhibit higher IRI activity as their κ-unit content rises, is also supported by these findings (Table 7.1).

The findings presented in **Chapter 2** and **Chapter 3** provide valuable insights into the potential of carrageenans as ice recrystallization inhibitors. A thourough structural analysis of the used carrageenan is crucial as manufacturers' declarations may be inaccurate and variations in structure can have a profound impact on the functional properties. Inaccurate declarations may be responsible for contradicting results in scientific studies due to the lack of further structural analysis. Given that carrageenans are commonly employed in food systems containing certain salt concentrations or proteins such as casein, the likelihood of gel formation in these environments becomes a critical factor to consider. For instance, κ-carrageenan is typically used to stabilize ice cream through gel formation. Thus, the polymer has no influence on the recrystallization of ice crystals. In order to eliminate gel formation and to exploit IRI activity, κ-carrageenan hybrids containing ν-units can be employed while maintaining strong ice recrystallization inhibition. The utilization of a κ-ν hybrid carrageenan emerges as a viable alternative of-

fering comparable advantages at reduced costs. This approach circumvents the need for genetically modified organisms to produce IBPs while carrageenans possess pre-existing regulatory approval as food additives.

The underlying mechanism of carrageenan-mediated IRI activity remains elusive, and consequently, the specific structural characteristics essential for this effect have not been identified. Given the inverse relationship between sulfate content and IRI activity, observed from ι- to κ-carrageenan, it is plausible that the sulfate groups contribute to the observed IRI activity. Therefore, **Chapter 4** investigates the IRI activity of furcellaran. Structurally resembling κ-carrageenan, furcellaran exhibits a lower sulfate content of 16–18% [258] compared to 25–30% [386] in κ-carrageenan. Following structural characterization and sulfate content verification, the polysaccharide was confirmed to be furcellaran, exhibiting ice recrystallization inhibiting properties. Notably, the observed IRI activity of furcellaran is found to be comparable to that of κ-carrageenan. Consequently, reducing sulfate content did not result in a significant enhancement of IRI activity. Despite influencing the structure and flexibility of carrageenans, the sulfate groups do not appear to directly affect the IRI mechanism. Thus, *Hypothesis 4* is only partially supported and cannot be fully confirmed (Table 7.1). Consitent with an ice-binding mechanism already discussed in the literature [25,43,44], the characteristic rectangular ice crystal morphology is observed upon furcellaran addition. It is evident that the ice recrystallization inhibiting effect increases up to a concentration of 1 g/L within the investigated range. However, with further increases in furcellaran concentration, the IRI activity decreases again. Previous studies have demonstrated that salt addition to κ-carrageenan solutions results in the formation of a gel or gel-like character, which eliminates the ability of κ-carrageenan to inhibit recrystallization processes [41]. With regard to furcellaran, **Chapter 4** demonstrates that increasing the polymer concentration to 3 g/L or higher resulted in gel formation and a decreased IRI activity. Although the ion concentration of the furcellaran sample was not precisely measured, it is theoretically possible that the concomitant increase in ion concentration with rising polymer concentration may contribute to gel formation.

Given the limitations of experimental techniques studying the atomic-level interactions of IBMs at the ice surface and understanding their binding mechanism, MD simulations offer a viable alternative. The simulation published by Kuiper et al. in 2015 marked a significant breakthrough by providing the first visual representation of an IBP binding to a growing ice crystal at the atomistic scale [126]. A key finding of this simulation is the clear visualization of the ice surface's curvature and the crucial role of the Gibbs-Thomson effect in inhibiting further crystal

growth. Consequently, **Chapter 5** conducts a detailed analysis of the ice crystal surface structure following the binding of an IBP, aiming to demonstate that the simulation results are in agreement with the Gibbs-Thomson equation. The findings of **Chapter 5** confirm the suitability of MD simulations for the investigation of IBPs and that the Gibbs-Thomson equation can be accurately reproduced. *Hypothesis 5* can therefore be confirmed (Table 7.1). A detailed analysis reveals that the ice surface structure and the critical radius linked to maximum depression of the systems melting temperature cannot be predicted a priori based on the intermolecular distances of the bound molecules. At the critical radius, the ice crystal surface exhibits dramatic fluctuations, with the formed curvature repeatedly melting. In contrast to the assumption that the longest intermolecular distance determines the maximum melting point depression, this chapter's results suggest that this correlation may not always hold. Moreover, it is evident that the size of the simulation box, coupled with the periodic boundary conditions determines the distance between the simulated molecule and its periodic image. This inherent limitation prevents the accurate determination of macroscopic properties of IBPs such as their thermal hysteresis. Experimental systems exhibit greater complexity characterized by multiple ice crystal growth directions which is challenging to replicate in MD simulations due to the limited computational capabilities. Additionally, the precise distances between bound molecules within the actual system remain elusive.

Using MD simulations, **Chapter 6** investigates the origin of carrageenans IRI activity and whether a direct interaction with the ice crystal surface is responsible for this activity. To understand the mechanism behind recrystallization inhibition, different κ-carrageenan molecules are simulated in ice-growing systems. Based on experimental data indicating no thermal hysteresis, it is assumed that κ-carrageenan interacts with a single ice plane. Due to the uncertainty regarding the specific ice plane, the basal, primary, and secondary prism planes are all examined in various simulations. Across all ice planes investigated, the simulations demonstrate that κ-carrageenan consistently interacts with the ice crystal surface. Upon prolonged binding to the ice surface, characteristic curvatures develop, consistent with the Gibbs-Thomson effect. These findings strongly suggest that the IRI activity of carrageenans arise from the direct interaction with ice crystals, similar to IBPs. This verifies *Hypothesis 6*, but *Hypothesis 7*, which posits a single ice crystal plane for interaction, is not supported (Table 7.1).

Notably, the interaction is temperature-sensitive, as neither the κ-carrageenan composed of 3 nor 6 disaccharide units can form a stable interaction with the ice surface at low ice growth

rates when temperatures are higher. This may be attributed to a combination of a slower ice growth rate and the higher mobility of the κ-carrageenan molecule.

In addition, the molecule's flexibility might be the key to its ability to conform to the varying structures of the different ice lattice structures. A detailed analysis of bound κ-carrageenan clearly indicates that its molecular conformation deforms substantially to align with the specific arrangement of water molecules within the ice lattice. The hydroxyl groups' oxygen atoms, which are part of the saccharides, appear to be the primary points of interaction with the ice crystal, as they frequently occupy lattice positions. Although oxygen atoms of the sulfate groups can occasionally be found in these positions, this occurrence is less frequent. Therefore, the simulation data provides further evidence that while the sulfate groups contribute to the molecule's overall structure and flexibility, they are not essential for its the attachment to the ice crystal surface. Moreover, hydrogen bonding between κ-carrageenan and the water molecules within the ice lattice plays an important role in the binding process. Upon successful binding, the lifetime of the hydrogen bonds substantially increases. These findings confirm *Hypothesis 8* (Table 7.1).

Furthermore, the binding of κ-carrageenan to ice crystals remains unchanged even when its length is doubled from 3 to 6 disaccharide units. Thus, *Hypothesis 9* is not supported (Table 7.1). Nevertheless, it's important to consider that a molecule with six units is still relatively short, and further elongation might still enhance its binding affinity.

Another important finding is the inability of the simulated κ-carrageenan molecules to establish a permanent bond with the ice surface. Despite significantly influencing ice growth, the bound molecule is slowly but consistently displaced by the growing ice crystal. This behavior is not observed for the insect IBP investigated in **Chapter 5**. These findings indicate that binding occurs through a reversible mechanism reminiscent of the binding mechanism observed in antifreeze glycoproteins [203,206,380]. In addition, the lack of thermal hysteresis in case κ-carrageenan further supports a reversible binding mechanism. This aligns with the experimental work of Tas et al., demonstrating that reversible binding is sufficient for IRI activity but not for thermal hysteresis [206].

Given that both κ-carrageenan [41] and furcellaran [124] exhibit reduced IRI activity upon gel formation, the initial aggregation step into double helices may also negatively affect ice binding. However, this does not apply to a κ-carrageenan double helix composed of two strands, each with 3 disaccharide units. Despite its reduced flexibility, the investigated double helix can

still interact with the ice crystal surface and the individual strands maintain sufficient adaptability for adsorption. Consequently, *Hypothesis 10* cannot be confirmed either.

Its important to note that the results presented in **Chapter 6** are restricted to the smaller molecules examined, in the first place. Larger molecules might behave differently, and experimentally employed carrageenans commonly exhibit sizes above 300 kDa.

Table 7.1. *Overview and evaluation of Hypotheses.*

Hypothesis	Hypothesis formulation	Evaluation
H 1	*The structural variations alter the gel formation and the gel strength of hybrid carrageenans. An icrease in the proportion of κ-units is associated with an enhanced gel strength.*	
H 2	*It is hypothesized that the IRI activity of carrageenan polysaccharides is directly affect by their structural variations, including associated cations.*	
H 3	*A higher proportion of κ-units in hybrid carrageenans is expected to enhance their IRI activity,resulting in reduced mean ice crystal sizes after a given storage period.*	
H 4	*Since a higher sulfate content in carrageenans, as observed in ι-carrageenan, lowers IRI activity, it is hypothesized that furcellaran will exhibit IRI activity and, given its lower sulfate content, may exhibit improved IRI activity.*	
H 5	*The Gibbs-Thomson induced melting point depression of a curved ice surface due to a bound molecule can be accurately modeled by MD simulations.*	
H 6	*κ-carrageenan can directly interact with the ice crystal surface.*	
H 7	*κ-carrageenan, lacking thermal hysteresis, binds to a single ice crystal plane.*	
H 8	*The interaction between κ-carrageenan and the ice surface is mediated by hydrogen bond formation and the structural adaption of the molecule to the ice lattice.*	
H 9	*The greater number of potential binding sites in longer molecules is proposed to result in stronger ice-binding affinity.*	
H 10	*Considering that gel formation eliminates the IRI activity of κ-carrageenan, it is reasonable to hypothesize that even aggregation of individual strands can negatively impact κ-carrageenan's interaction with the ice surface.*	

7.1 Outlook and Future Perspectives

Despite analyst prediction of the IBP market as a high-growth sector, the reality has fallen short of these expectations. While awareness of their benefits in food and medicine is rising, the market faces substantial difficulties attributed to insufficient availability and high prices.

The incorporation of ice-binding molecules in ice cream products results in a smother and creamier texture, attributed to the formation of smaller ice crystal sizes. Simultaneously, ice crystal growth through recrystallization processes is inhibited. Consequently, the ice cream exhibits enhanced stability during the storage period and reduduced susceptibility to quality degradation caused by temperature fluctuations. This is a significant advantage in regions with hot climates, where maintaining a consistent cold chain is challenging. Moreover, it increases the product's robustness within the retail distribution environment, particularly mitigiating the impact of frequent temperature fluctuations that occur when products are moved in and out of refrigerated displays. In addition, the formation of smaller ice crystal sizes enables an increase in water content without compromising the desired ice crystal size distribution in the final product. As a result, the formulation can be adjusted, such as reducing fat content or incorporating higher levels of fruit. The finer distribution of ice crystals in posicles reduces the number of interconnected crystals and, thereby, potential fracture points. Unilever has been using yeast-based recombinantly produced IBPs to improve the stability and texture of their ice cream. However, the acceptance of genetically modified additives in food is notably low, especially in Europe. Currently, Unilever does not use any of these recombinant proteins in its European products.

Conseuquently, alternative materials such as carrageenan, which are naturally sourced, efficient and affordable, are required. While gelation and the resulting loss of IRI activity has been a challenge in the application of κ-carrageenan in various food products, hybrid carrageenans might offer a potential solution. As demonstrated in **Chapter 2 and 4,** a small portion of ν-units can prevent gel formation without compromising IRI activity. Therefore, future research is needed to validate these findings in real-world food systems.

By employing MD simulations, **Chapter 6** provided evidence suggesting that the IRI activity of κ-carrageenan arises from a reversible binding to the ice crystal surface. To further validate these findings, experimental verification should be conducted, whenever feasible. For instance, IBPs can be easily labeled with fluorescent tags to enable fluorescence-based ice plane affinity analysis, which provides insights into the ice-binding activity but also the preferred adsorption

plane of IBPs. Consequently, fluorescent labeling of κ-carrageenan is required. Although labelling is not as straightforward as with IBPs, Heilig et al. employed covalently linked FITC to stain a κ-carrageenan gel [468]. To date, no studies explored the application of fluorescence-based ice plane affinity analysis to substances, such as carrageenan, despite the potential feasibility of such an approach. However, as part of this work, ice shell purification experiments were conducted to examine the ice-binding activity of κ-carrageenan. This technique, commonly used for the isolation of IBPs, involves the formation of a thin ice layer within a round-bottom flask. Subsequently, the IBP-containing sample is added and the flask is rotated in a chilled bath. As the ice grows, only molecules with ice-binding properties adsorb to the ice surface. At the end of this process, the remaining solution is removed, and the ice layer, containing the IBPs, is melted. The results of this method using a κ-carrageenan and a winter flounder AFP type I solution demonstrated a higher incorporation of κ-carrageenan into the ice layer compared to the AFP. Nevertheless, the concentration of both substances were relatively low, presenting a significant challenge for accurate quantification. The enrichment of κ-carrageenan may be attributed to its potential interaction with the basal, primary and secondary prims planes, as shown in **Chapter 6**, while winter flounder AFP type I only interacts with a single ice crystal plane. Despite providing initial experimental evidence, these observations require further investigation to improve the accuracy and reliability of these findings.

To improve the comparability between simulation results and experimental data, additional simulations should be performed with even longer κ-carrageenan molecules. To mitigate the increasing computational costs, the system's height can be decreased without affecting the results.

Combining the findings from **Chapter 4 and 6**, the data suggests that the sulfate groups do not directly contribute to the adsorption of carrageenans onto ice. To gain additional insights into the role of the sulfate groups, β-carrageenan might be a promising candidate for simulative and experimental studies. Unlike other carrageenans, β-carrageenan does not contain sulfate groups and is composed of β-D-galactopyranose (G-unit) and 3,6-anhydro-α-D-galactopyranose (DA-unit) repeating disaccharide units. Nevertheless, prior to conducting any experiments, it is necessary to find a supplier and to verify the molecular structure of β-carrageenan. Additionally, the IRI experiments, including data analysis, typically require around 2 weeks. Thus, a simulation study is substantially easier and faster to conduct.

In conclusion, this work offers numerous new insights into the IRI activity of carrageenans and the underlying mechanisms. These results provide a robust foundation for future experimental

and computational investigations to achieve even deeper insights. Furthermore, these findings may be applied to other polysaccharides with IRI activity, enabling to explain their effects and potentially identify new IRI agents. By gaining a more comprehensive understanding of the general impact of molecular structure on IRI activity and the precise IRI mechanism, will improve the targeted selection and development of carrageenans and other substances for specific applications.

Appendix

A1. Supplementary Data to Chapter 2

Table A1.1. *Primer sequences used for gene amplification for ligation-independent cloning.*

Gene locus	Primer	Primer sequence (5' → 3')
ZGAL_236	forward	TACTTCCAATCCATGCAACAACCTACGAA-GACTTCAAATCCGAAC
	reverse	TATCCACCTTTACTGTTACTCCACGAGTATCTTTTTT-GAAACCTCTCC
ZGAL_4265	forward	TACTTCCAATCCATGGTTCCAACTGAATTGAGGGCCG
	reverse	TATCCACCTTTACTGTCAGTTACACGAAGTAA-TACTACCTAGATTTTGGTTAC

Table A1.2. *Molecular weight and polydispersity (determined by HPSEC-RI/MALLS) of the carrageenans used in this study.*

Sample	M_W, kDa	Polydispersity index
KC1	1013 ± 35	1.9
KC2	965 ± 23	2.3
KC3	925 ± 25	1.7
IC1	999 ± 16	1.9
IC2	621 ± 25	2.3
IC3	523 ± 61	1.7
IC4	866 ± 5	1.8
IC5	915 ± 3	2.0
LC1	923 ± 8	2.0
LC2	641 ± 9	1.8
LC3	1787 ± 18	2.0
LC4	1499 ± 2	2.2
LC5	1013 ± 35	1.7
LC6	965 ± 23	2.7
C1	925 ± 25	2.1
C2	999 ± 16	2.0

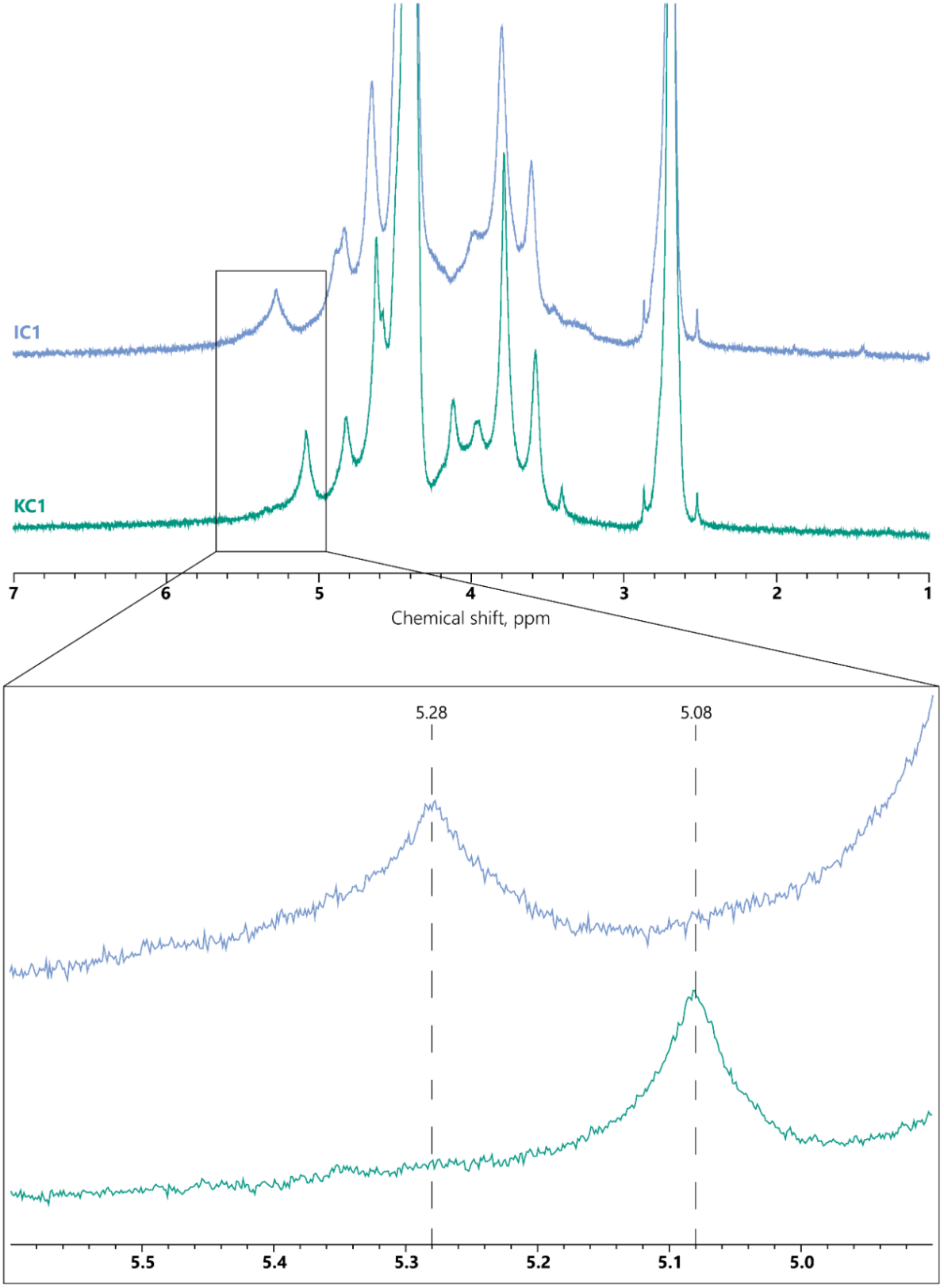

Figure A1.1. *^{1}H NMR spectra oft he commercial carrageenans KC1 and IC1.*

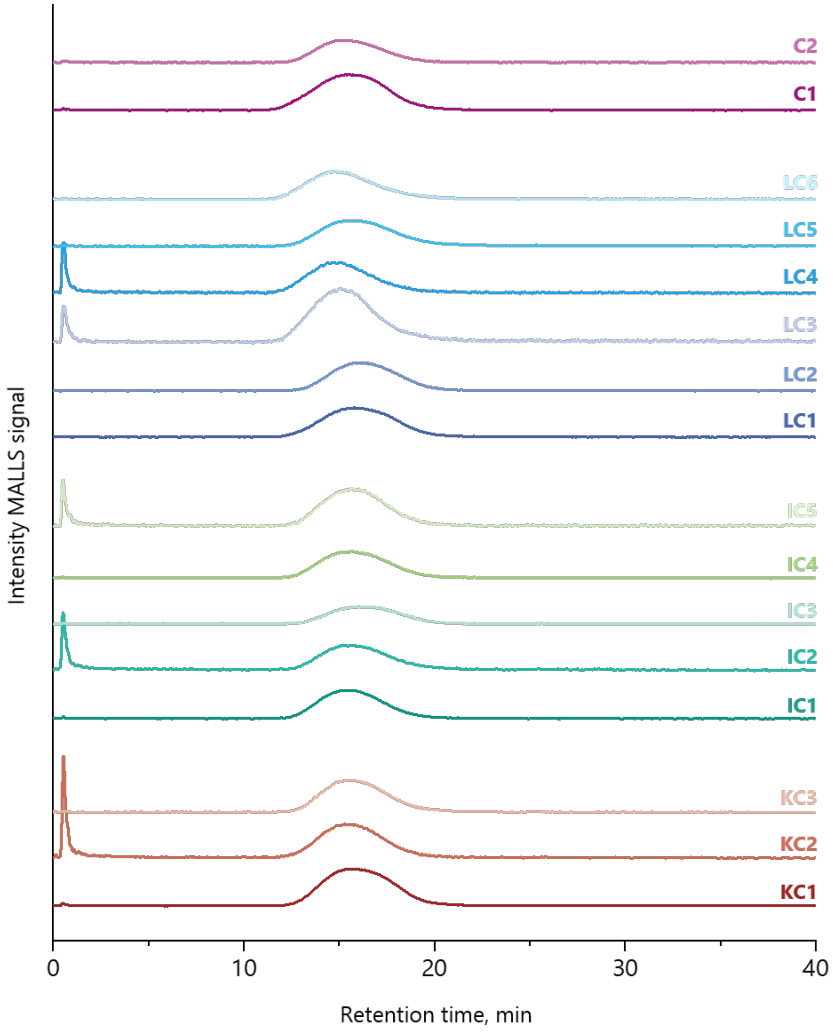

Figure A1.2. *HPSEC-MALLS chromatograms of the commercial used in this study.*

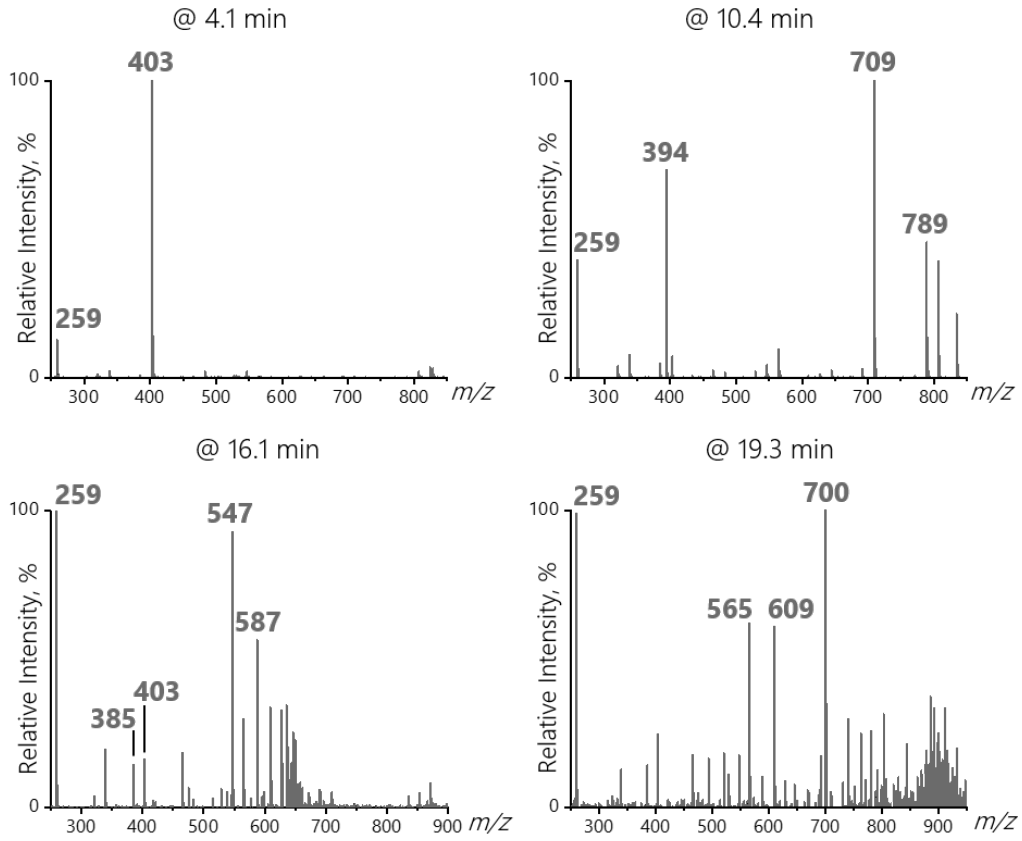

Figure A1.3. *Mass spectra of the oligosaccharides enzymatically released from KC1 after κ-carrageenase treatment. The analysis was conducted using HPLC-MS in negative full scan mode. The retention times of the oligosaccharides are indicated above the mass spectra.*

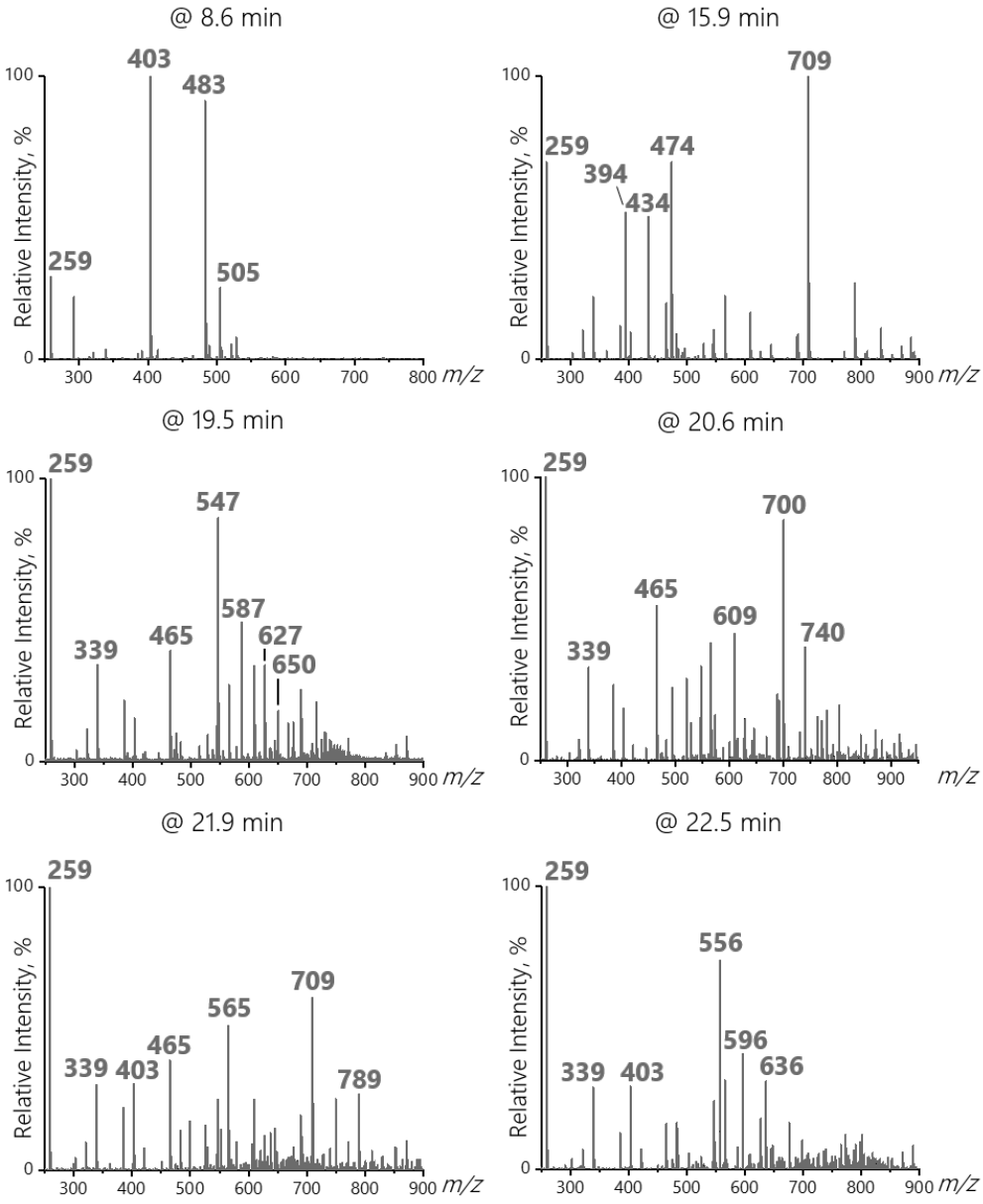

Figure A1.4. *Mass spectra of the oligosaccharides enzymatically released from IC1 after ι-carrageenase treatment. The analysis was conducted using HPLC-MS in negative full scan mode. The retention times of the oligosaccharides are indicated above the mass spectra.*

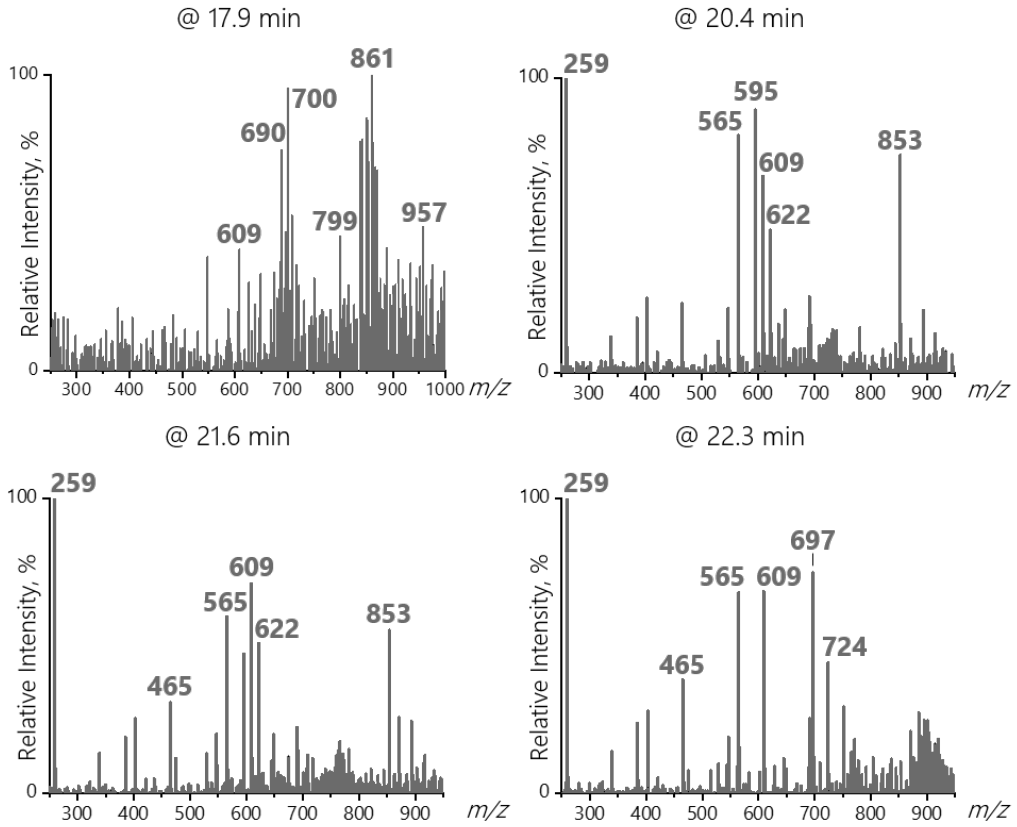

Figure A1.5. *Mass spectra of the oligosaccharides eluting between 17.9 min and 22.3 min, enzymatically released from LC2 after κ-carrageenase treatment. The analysis was conducted using HPLC-MS in negative full scan mode. The retention times of the oligosaccharides are indicated above the mass spectra.*

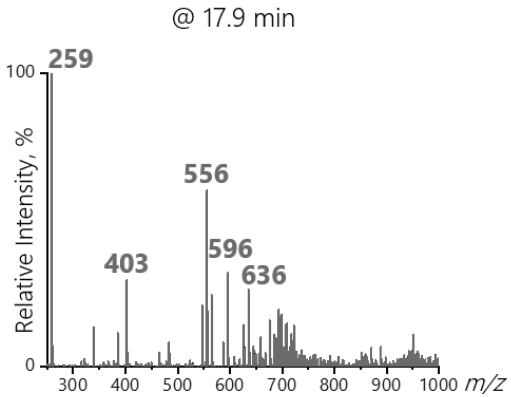

Figure A1.6. *Mass spectra of the oligosaccharide eluting at 17.9 min, enzymatically released from LC1 after κ-carrageenase treatment. The analysis was conducted using HPLC-MS in negative full scan mode. The retention times of the oligosaccharides are indicated above the mass spectra.*

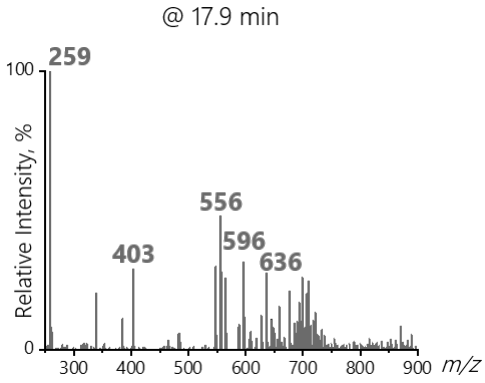

Figure A1.7. *Mass spectra of the oligosaccharide eluting at 17.9 min, enzymatically released from C1 after κ-carrageenase treatment. The analysis was conducted using HPLC-MS in negative full scan mode. The retention times of the oligosaccharides are indicated above the mass spectra.*

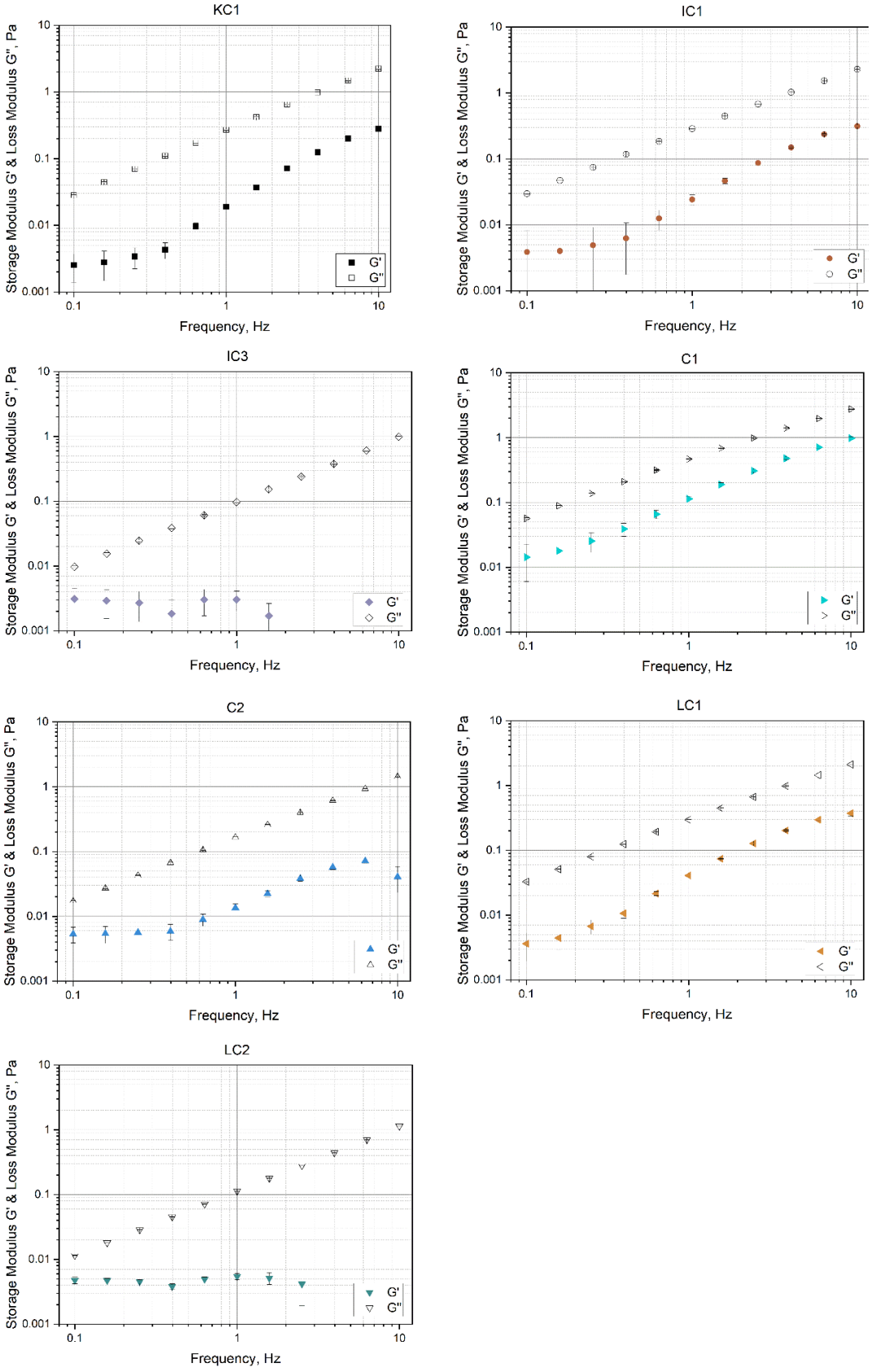

Figure A1.8. *Storage Modulus G' and loss modulus G'' of the seven rheologically analyzed commercial carrageenan samples. The filled symbols correspond to the storage modulus G', while the empty symbols represent the loss modulus G''. The samples were prepared without $CaCl_2$ addition and exhibit a predominantly viscous behavior.*

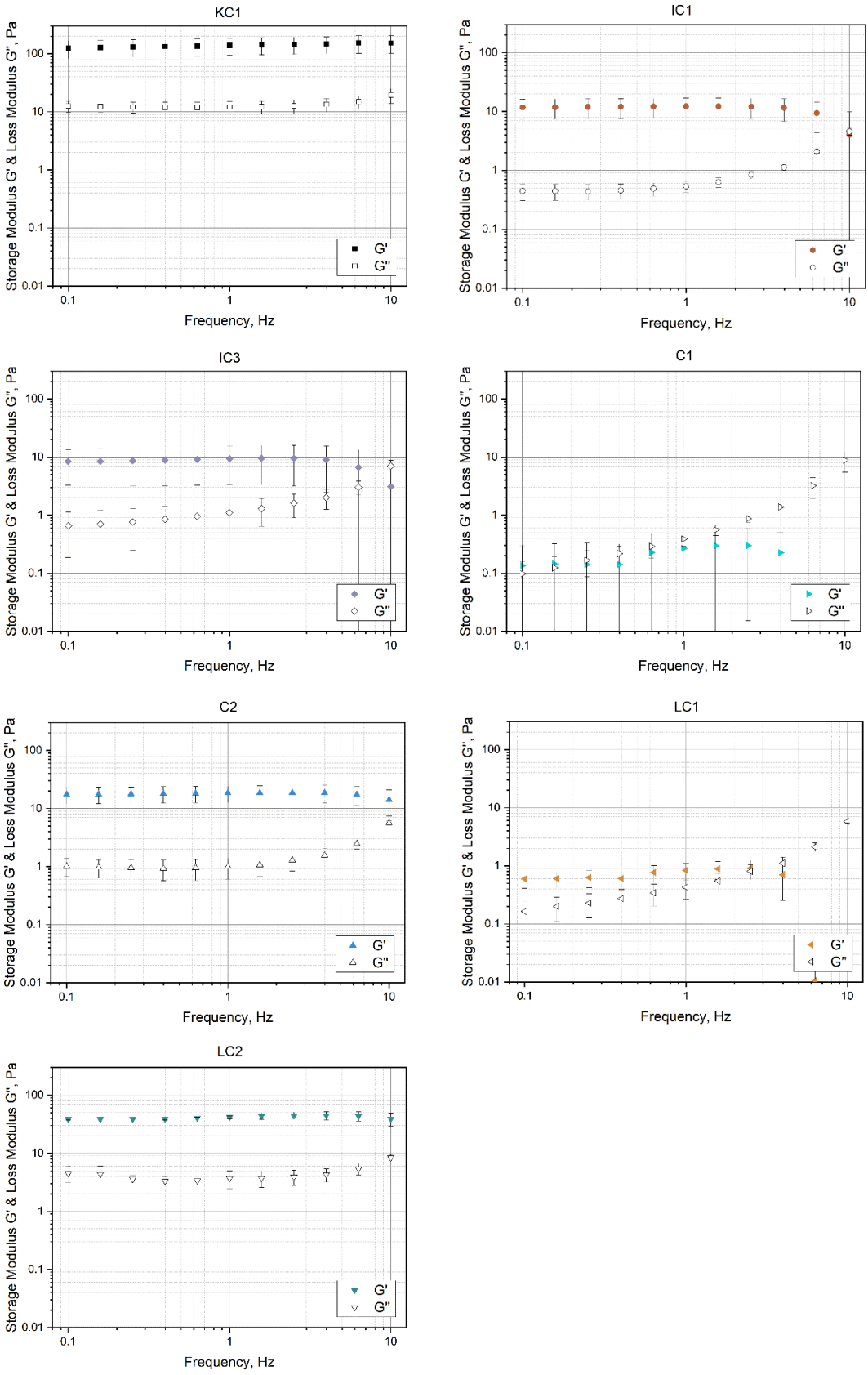

Figure A1.9. *Storage Modulus G' and loss modulus G'' of the seven commercially available carrageenan samples analyzed rheologically with the addition of $CaCl_2$. The filled symbols correspond to the storage modulus G', while the empty symbols represent the loss modulus G''. With exception of samples C1 and LC1, all other measured samples exhibit gel formation, although the gel strengths vary.*

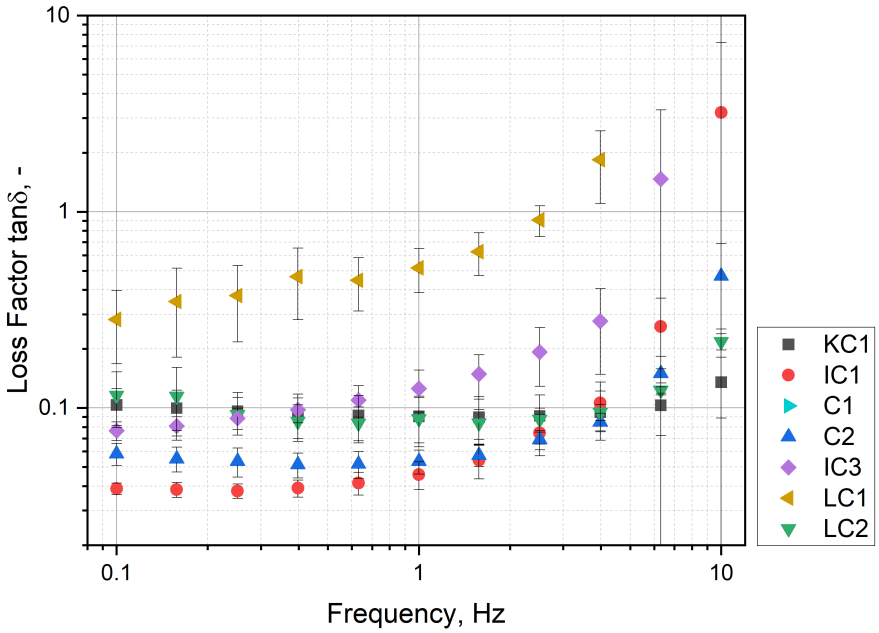

Figure A1.10. *Loss factors of the different commercial carrageenan samples in 0.1 M $CaCl_2$ solution measured at a frequency range between 0.1 and 10 Hz at an amplitude γ of 2%.*

A2. Supplementary Data to Chapter 3

Table A2.1. *Chemical shifts of the anomeric protons used to assign the different carrageenan types.*

Structural unit	**^{1}H chemical shift**
κ	5.09 ppm
ι	5.29 ppm
ν	5.49 ppm

Table A2.2. *Contents of K^+, Ca^{2+}, Na^+, and sulfate (determined by ICP-OES) of the carrageenans used in this study before and after cation exchange and alkaline modification (κνC1m).*

Sample	K^+, % (w/w)	Na^+, % (w/w)	Ca^{2+}, % (w/w)	Sulfate, % (w/w)
κC	6.84	0.10	0.82	18.1
κC K	16.14	0.01	0.01	16.3
κC Na	0.20	8.22	0.01	20.0
κC Ca	0.99	0.02	4.30	20.4
ιC	4.45	0.07	4.00	28.2
ιC K	13.42	0.03	0.02	27.5
ιC Na	0.21	7.83	0.02	30.2
ιC Ca	0.29	0.09	5.85	26.4
ικC	5.71	0.09	2.65	21.7
ικC K	13.18	0.02	0.01	26.9
ικC Ca	0.44	0.05	5.61	26.0
κιC1	4.18	2.39	0.11	17.4
κιC1 K	12.81	0.02	0.01	24.3
κιC1 Ca	0.50	0.05	5.39	24.3
κιC2	5.73	0.30	2.33	21.9
κιC2 K	14.76	0.02	0.01	18.9
κιC2 Na	0.33	6.84	0.01	23.1
κιC2 Ca	0.78	0.05	4.64	21.8
κινC1	0.98	0.25	5.48	29.4
κινC1 K	13.46	0.04	0.02	29.5
κινC1 Na	0.06	7.84	0.03	30.3
κινC1 Ca	0.11	0.14	6.03	27.8
κινC1m K	11.35	0.05	0.01	22.9
κινC1m Na	n.d.	9.06	0.12	25.2
κινC2	1.69	5.58	0.37	28.9
κινC2 K	13.42	0.03	0.02	29.2
κινC2 Ca	0.17	0.12	6.48	29.9

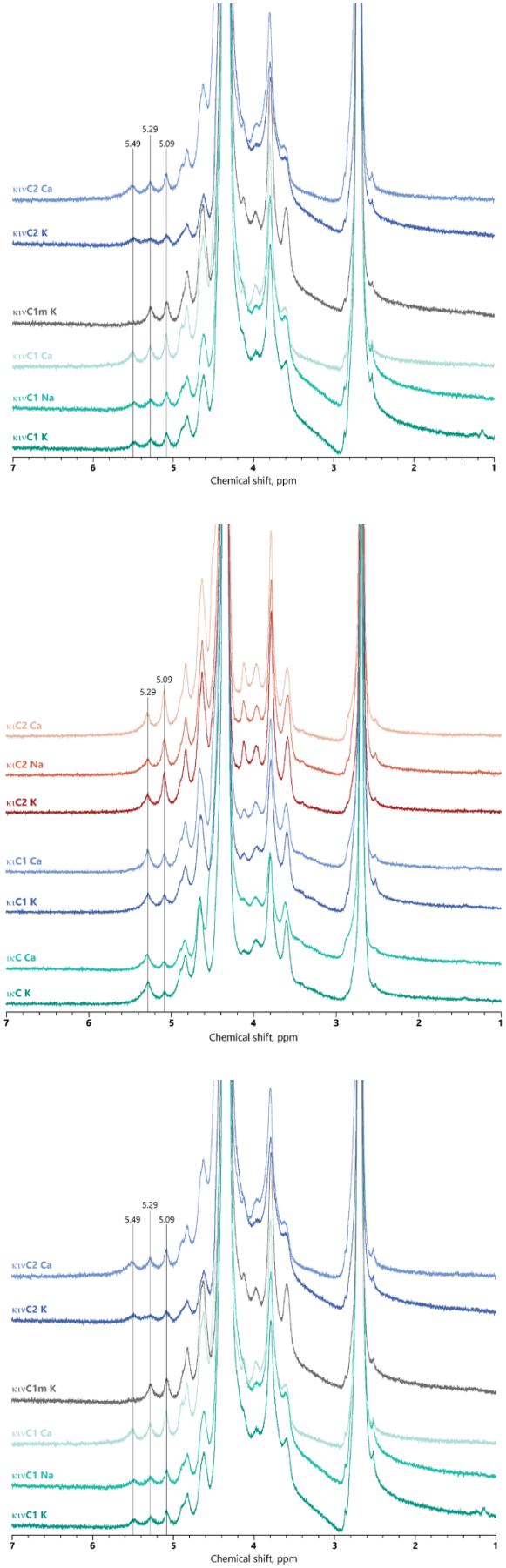

Figure A2.1. *^{1}H NMR spectra of the carrageenans used in this study.*

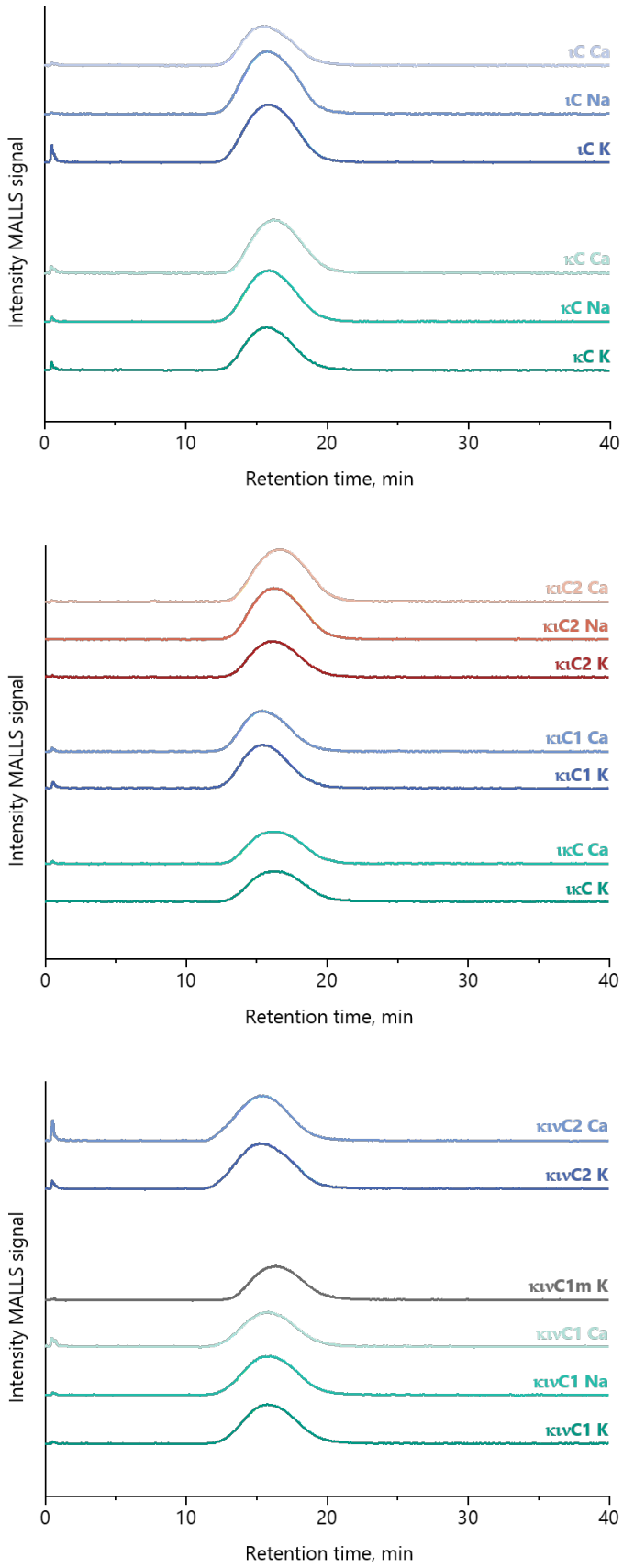

Figure A2.2. *HPSEC-MALS chromatograms of the carrageenans used in this study.*

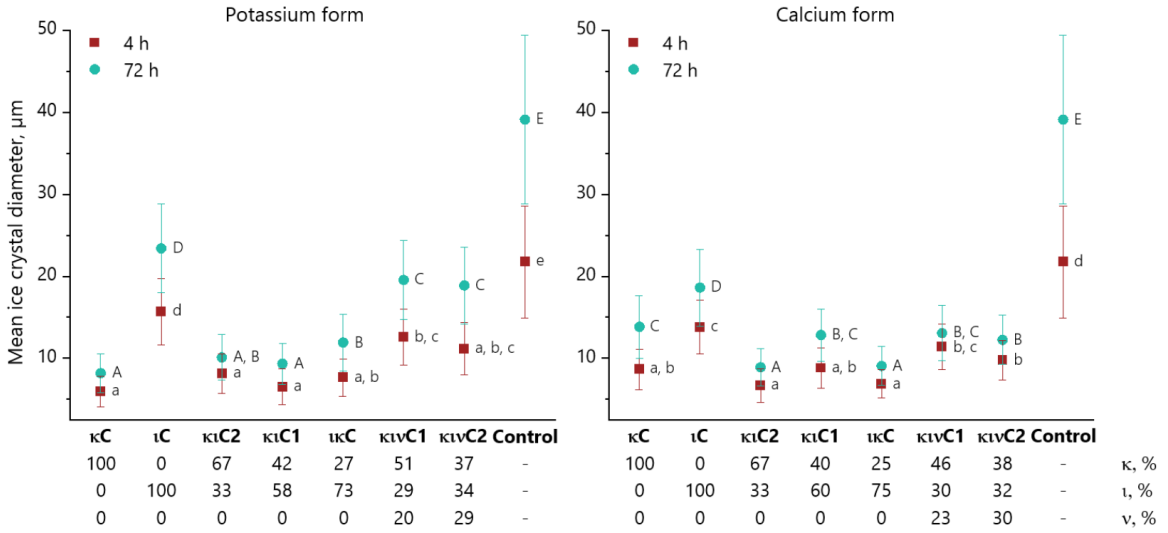

Figure A2.3. *Mean ice crystal diameter (n = 4) after 4 h and 72 h at -12 °C of a 49% sucrose solution with 1 mg/mL of the potassium and calcium forms of the carrageenans used in this study. The control sample refers to a sucrose solution without carrageenan addition. The statistical analysis was conducted by using one-way analysis of variance (ANOVA) with post-hoc Tukey test (α = 0.05). In case of heterogeneity of variances, Welch ANOVA was applied.*

A3. Supplementary Data to Chapter 5

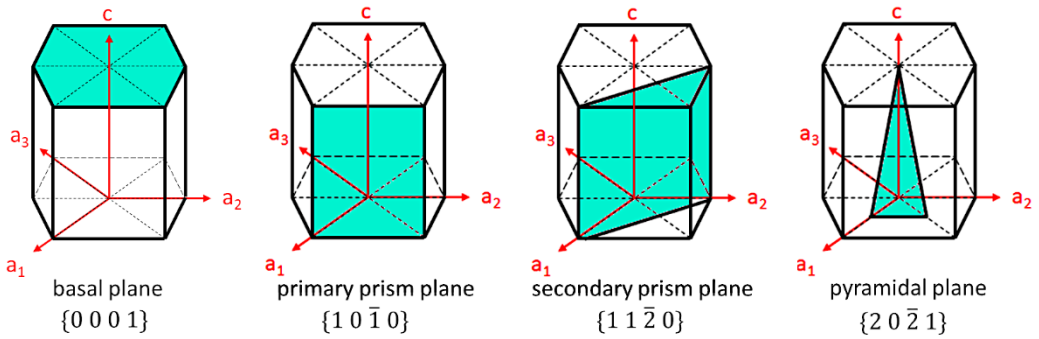

Figure A3.1. *Possible ice binding planes for AFP. The specific plane is shown in turquoise with the corresponding miller index.*

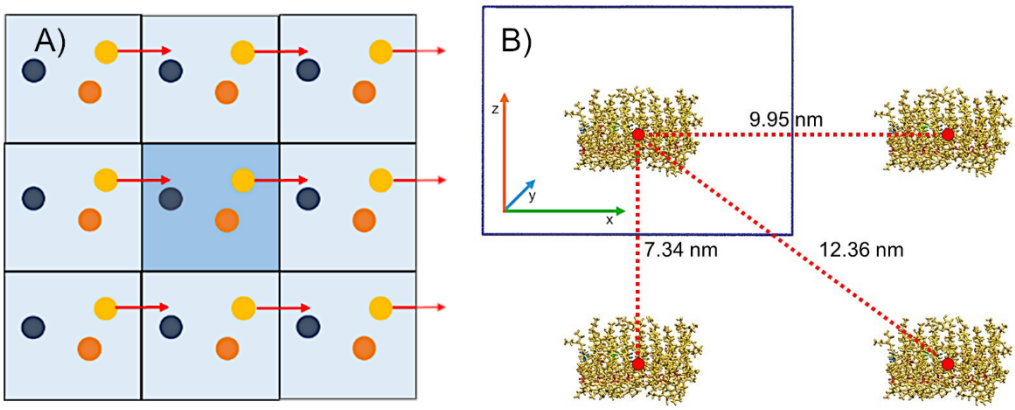

Figure A3.2. *A) Simplified, two dimensional drawing of periodic boundary conditions in MD simulations. The original simulation box is shown in darker blue in the center and contains three example atoms (yellow, orange and dark blue). The simulation box is duplicated and placed around the original simulation box, depicted in light blue. Due to the periodic boundary an atom that leaves the box (yellow at the right side), re-enters from the other side (left). In our case, leaving and entering "atoms" are water molecules. B) Geometry created by connecting four simulation boxes with one adsorbed sbwAFP in each box. The size of the original simulation-box is shown by the blue box. Logically, the distance between the centers of mass of the proteins (red dotted lines) is equal to the corresponding box length in x- and z-direction respectively. The longest distance between AFP in this arrangement is the diagonal with 12.36 nm.*

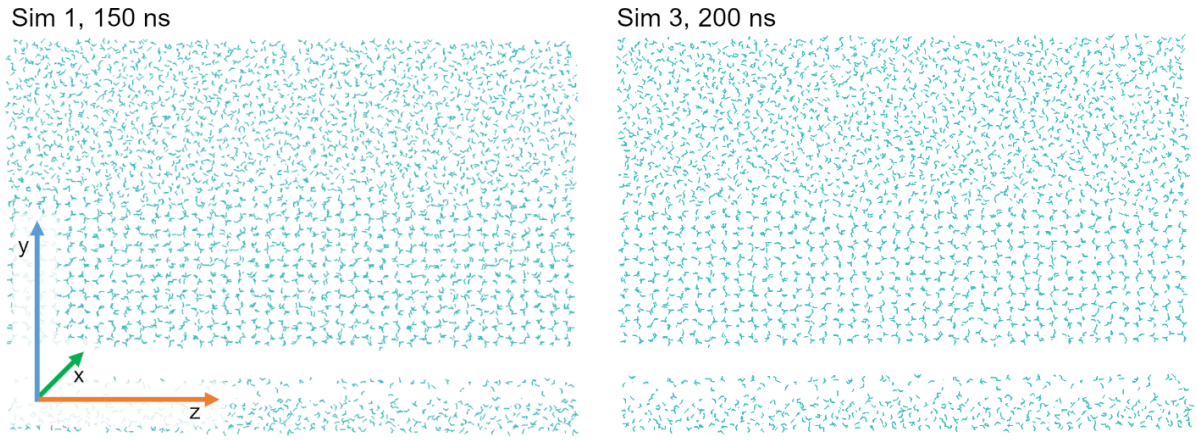

Figure A3.3. *Slab a of two different simulations at different time points. Both slices show a straight ice surface. This is also true for Sim 2 and other times. It is worth mentioning, that no curvature is formed despite the fact that the ice layer grows.*

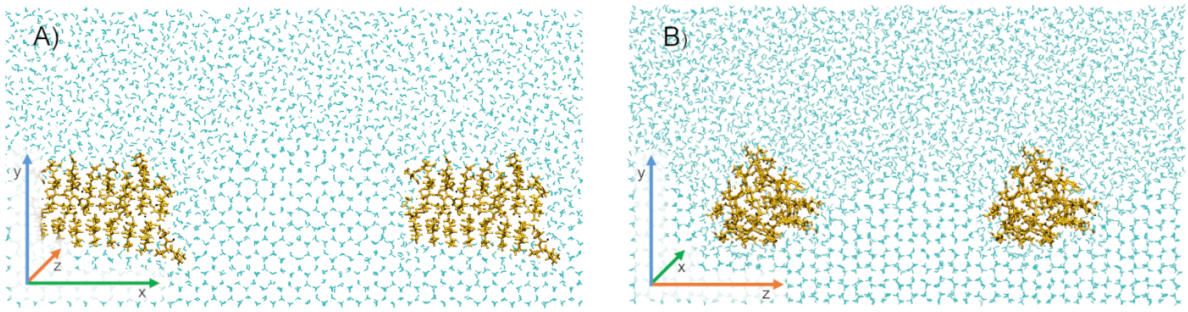

Figure A3.4. *A) Slab d of Sim 2 at 200 ns. The ice surface between the proteins is strongly curved and the top of the ice surface is slightly above the protein. B) Slab c of Sim 1 at 175 ns. The height of the curvature is lower and below the height of the protein.*

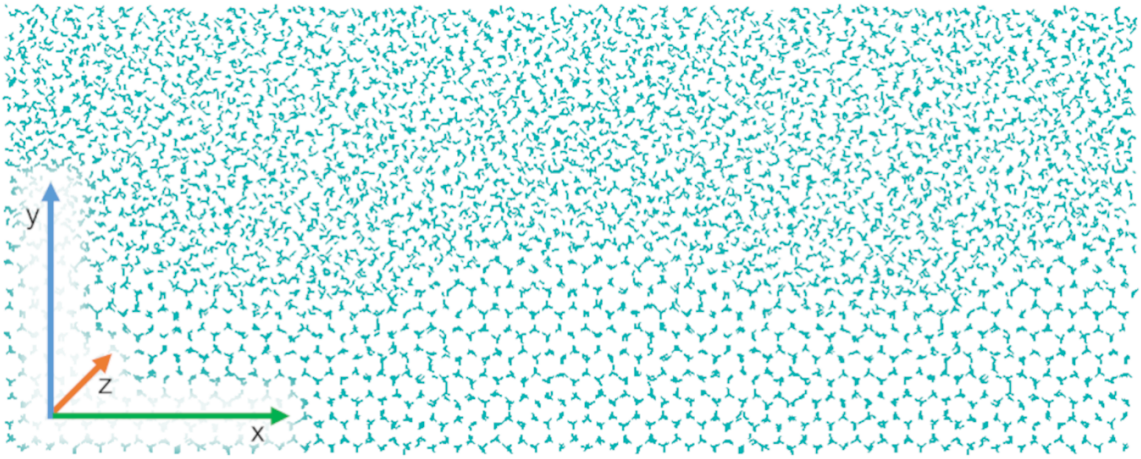

Figure A3.5. *Slab b of Sim 3 at 200 ns. In the center, the curvature has formed, which leads to negative curvatures flanking the elevation in the center. The minima of these negative curvatures are between the proteins in z-direction.*

Table A3.1. *TIP4P/Ice parameters.*

Property	**Value**
Bulk melting temperature T_m^{∞} [416]	269.8 K
Surface tension of the secondary prism plane σ [419]	0.0316 $\frac{J}{m^2}$
Enthalpy of fusion ΔH_f [419]	1.29 $\frac{kcal}{mol}$ or 5397.36 $\frac{J}{mol}$
Density of TIP4P/Ice ice [416]	906 $\frac{kg}{m^3}$
Molecular weight of water and ice M	0.018 $\frac{kg}{mol}$

Table A3.2. *Radii and corresponding melting temperatures of the static analysis calculated with the cylindrical Gibbs-Thomson equation.*

Simulation	Slab	Time / ns	Radius / nm	Temperature $T_m(x)$ / K
1	b	150	7.63	265.69
1	b	150	7.29	265.50
1	b	150	7.40	265.56
1	b	175	4.51	262.84
1	b	175	4.54	262.89
1	b	175	4.73	263.17
1	b	200	7.10	265.38
1	b	200	7.45	265.59
1	b	200	7.44	265.58
1	c	150	3.75	261.43
1	c	150	3.62	261.12
1	c	150	3.80	261.55
1	c	175	3.24	260.12
1	c	175	3.19	259.97
1	c	175	3.35	260.44
1	c	200	2.62	257.80
1	c	200	2.68	258.08
1	c	200	2.63	257.86
1	d	150	3.65	261.19
1	d	150	3.76	261.45
1	d	150	3.60	261.09
1	d	175	3.14	259.79
1	d	175	3.08	259.61
1	d	175	3.25	260.13
1	d	200	3.64	261.18
1	d	200	3.96	261.87
1	d	200	3.72	261.36
1	e	150	6.87	265.23

1	e	150	6.84	265.22
1	e	150	6.97	265.30
1	e	175	5.53	264.12
1	e	175	5.54	264.14
1	e	175	5.40	263.99
1	e	200	5.94	264.51
1	e	200	6.03	264.60
1	e	200	6.31	264.82
1	f	150	6.18	264.72
1	f	150	5.99	264.56
1	f	150	6.11	264.67
1	f	175	4.89	263.38
1	f	175	5.20	263.76
1	f	175	5.08	263.62
1	f	200	5.51	264.10
1	f	200	5.47	264.06
1	f	200	5.91	264.49
2	b	150	6.87	265.23
2	b	150	7.12	265.39
2	b	150	7.26	265.48
2	b	175	5.78	264.37
2	b	175	5.47	264.06
2	b	175	5.53	264.12
2	b	200	6.74	265.14
2	b	200	7.52	265.63
2	b	200	7.73	265.74
2	c	150	2.99	259.29
2	c	150	3.12	259.73
2	c	150	3.24	260.11
2	c	175	3.18	259.95
2	c	175	3.35	260.43

2	c	175	3.42	260.61
2	c	200	3.72	261.36
2	c	200	3.74	261.40
2	c	200	3.89	261.74
2	d	150	2.63	257.85
2	d	150	2.63	257.86
2	d	150	2.66	258.00
2	d	175	4.24	262.39
2	d	175	4.36	262.60
2	d	175	4.48	262.80
2	d	200	3.49	260.80
2	d	200	3.54	260.93
2	d	200	3.88	261.71
2	e	150	4.53	262.87
2	e	150	4.59	262.96
2	e	150	4.52	262.86
2	e	175	4.56	262.91
2	e	175	4.55	262.91
2	e	175	4.59	262.96
2	e	200	4.71	263.13
2	e	200	4.89	263.38
2	e	200	5.19	263.75
2	f	150	5.02	263.55
2	f	150	4.86	263.35
2	f	150	5.01	263.54
2	f	175	6.12	264.67
2	f	175	6.48	264.96
2	f	175	5.91	264.49
2	f	200	5.06	263.59
2	f	200	5.21	263.78
2	f	200	5.16	263.71

3	b	150	6.05	264.61
3	b	150	6.23	264.76
3	b	150	6.37	264.88
3	b	175	7.42	265.57
3	b	175	7.49	265.61
3	b	175	7.69	265.72
3	b	200	6.52	264.98
3	b	200	6.52	264.99
3	b	200	6.50	264.97
3	c	150	3.28	260.22
3	c	150	3.71	261.34
3	c	150	3.57	261.00
3	c	175	2.79	258.57
3	c	175	2.95	259.16
3	c	175	2.86	258.83
3	c	200	3.15	259.83
3	c	200	3.39	260.54
3	c	200	3.14	259.82
3	d	150	3.15	259.84
3	d	150	3.27	260.21
3	d	150	3.45	260.70
3	d	175	3.19	259.96
3	d	175	3.31	260.31
3	d	175	3.40	260.56
3	d	200	4.01	261.98
3	d	200	4.04	262.04
3	d	200	4.18	262.29
3	e	150	6.43	264.92
3	e	150	6.40	264.89
3	e	150	6.48	264.95
3	e	175	5.85	264.43

3	e	175	6.08	264.63
3	e	175	5.90	264.48
3	e	200	5.82	264.40
3	e	200	6.00	264.57
3	e	200	6.25	264.78
3	f	150	5.71	264.31
3	f	150	5.75	264.34
3	f	150	5.72	264.31
3	f	175	5.89	264.47
3	f	175	6.16	264.70
3	f	175	6.32	264.84
3	f	200	5.71	264.31
3	f	200	5.94	264.52
3	f	200	5.69	264.28

Table A3.3. *Radii and melting temperatures when slab c and b are combined. For the calculation, the elliptical Gibbs-Thomson equation is used.*

Simulation	**Time / ns**	**Average radius for slab b / nm**	**Average radius for slab c / nm**	**Temperature $T_m(x)$ / K**
1	150	-3.09	3.72	271.51
1	175	-4.05	3.26	267.94
1	200	-6.65	2.64	262.63
2	150	-4.70	3.11	266.40
2	175	-4.68	3.32	267.05
2	200	-3.38	3.78	270.79
3	150	-4.67	3.52	267.59
3	175	-4.65	2.87	265.61
3	200	-4.61	3.23	266.87

Table A3.4. *Radii and melting temperatures when slab e and f are combined. For the calculation, the elliptical Gibbs-Thomson equation is used.*

Simulation	Time / ns	Average radius for slab e / nm	Average radius for slab f / nm	Temperature $T_m(x)$ / K
1	150	6.89	6.09	260.10
1	175	5.49	5.06	257.88
1	200	6.09	5.63	259.07
2	150	4.55	4.96	256.58
2	175	4.57	6.17	257.84
2	200	4.93	5.14	257.33
3	150	6.43	5.73	259.44
3	175	5.94	6.12	259.39
3	200	6.02	5.78	259.16

Table A3.5. *Radii and corresponding melting temperatures at the position of slab b during the dynamic analysis. The melting temperatures are calculated with the cylindrical version of the Gibbs-Thomson equation.*

Simulation	Slab	Time / ns	Radius / nm	Temperature $T_m(x)$ / K
1	b	93	4.86	263.34
1	b	93	4.65	263.05
1	b	93	4.79	263.25
1	b	117.1	6.00	264.57
1	b	117.1	5.68	264.28
1	b	117.1	5.69	264.28
1	b	172.7	4.82	263.29
1	b	172.7	4.54	262.89
1	b	172.7	4.93	263.44
1	b	218.6	5.08	263.62
1	b	218.6	5.17	263.73
1	b	218.6	5.05	263.59
1	b	262.1	6.73	265.13

1	b	262.1	7.19	265.44
1	b	262.1	6.93	265.27
2	b	91.9	7.42	265.57
2	b	91.9	7.32	265.51
2	b	91.9	7.12	265.39
2	b	93.7	5.19	263.76
2	b	93.7	4.99	263.51
2	b	93.7	4.96	263.48
2	b	111.6	6.94	265.28
2	b	111.6	6.83	265.21
2	b	111.6	6.84	265.21
2	b	122.9	4.47	262.78
2	b	122.9	4.39	262.65
2	b	122.9	4.49	262.82
2	b	178.9	4.42	262.71
2	b	178.9	4.16	262.26
2	b	178.9	4.25	262.42
2	b	238.2	5.60	264.19
2	b	238.2	5.54	264.13
2	b	238.2	5.65	264.25
2	b	263.9	6.17	264.71
2	b	263.9	5.89	264.47
2	b	263.9	6.11	264.66
3	b	81.8	4.11	262.17
3	b	81.8	4.14	262.23
3	b	81.8	4.13	262.21
3	b	96.4	5.76	264.36
3	b	96.4	5.55	264.14
3	b	96.4	5.82	264.40
3	b	131.0	4.92	263.42
3	b	131.0	5.03	263.56

3	b	131.0	4.91	263.41
3	b	191.1	5.21	263.78
3	b	191.1	5.50	264.09
3	b	191.1	5.03	263.55
3	b	217.2	4.52	262.86
3	b	217.2	4.58	262.94
3	b	217.2	4.64	263.03
3	b	236.2	6.12	264.67
3	b	236.2	6.24	264.77
3	b	236.2	6.57	265.02
3	b	348.8	4.96	263.47
3	b	348.8	4.77	263.22
3	b	348.8	4.73	263.16
3	b	365.7	5.56	264.15
3	b	365.7	5.51	264.10
3	b	365.7	5.53	264.13
3	b	382.5	5.97	264.54
3	b	382.5	5.92	264.50
3	b	382.5	6.12	264.67
3	b	401.7	6.87	265.23
3	b	401.7	6.51	264.98
3	b	401.7	6.70	265.12

A4. Supplementary Data to Chapter 6

Table A4.1. *Box dimensions of the individual simulation setups*

	3 units κ-carrageenan			6 units κ-carrageenan		
	X / nm	**Y / nm**	**Z / nm**	**X / nm**	**Y / nm**	**Z / nm**
Basal plane	6.26	6.10	6.32	-	-	-
Primary prism plane	6.35	6.29	5.15	-	-	-
Secondary prism plane	6.35	5.99	5.15	7.82	10.18	7.35

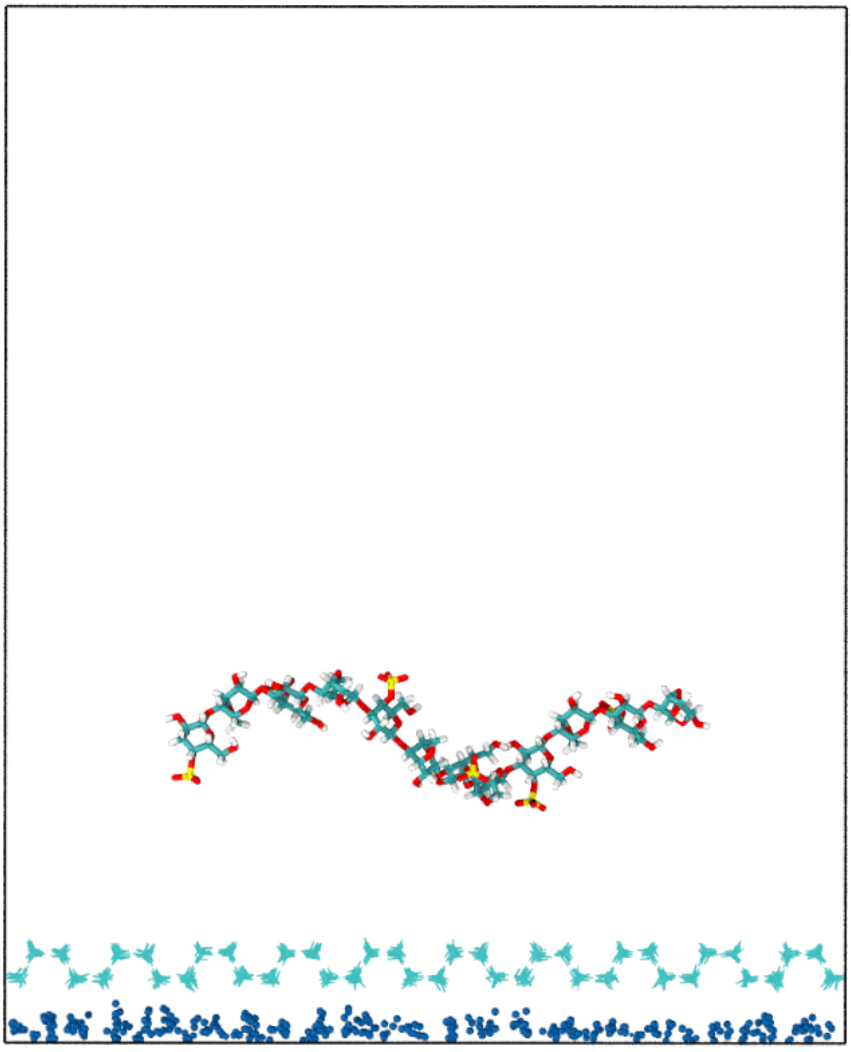

Figure A4.1. *Setup of the simulation box with a κ-carrageenan molecule containing 6 disaccharide units. The box encompasses the polysaccharide positioned approximately 2 nm above the initial ice crystal (cyan). Beneath the ice crystal, a layer of immobilized water molecules (blue) is introduced.*

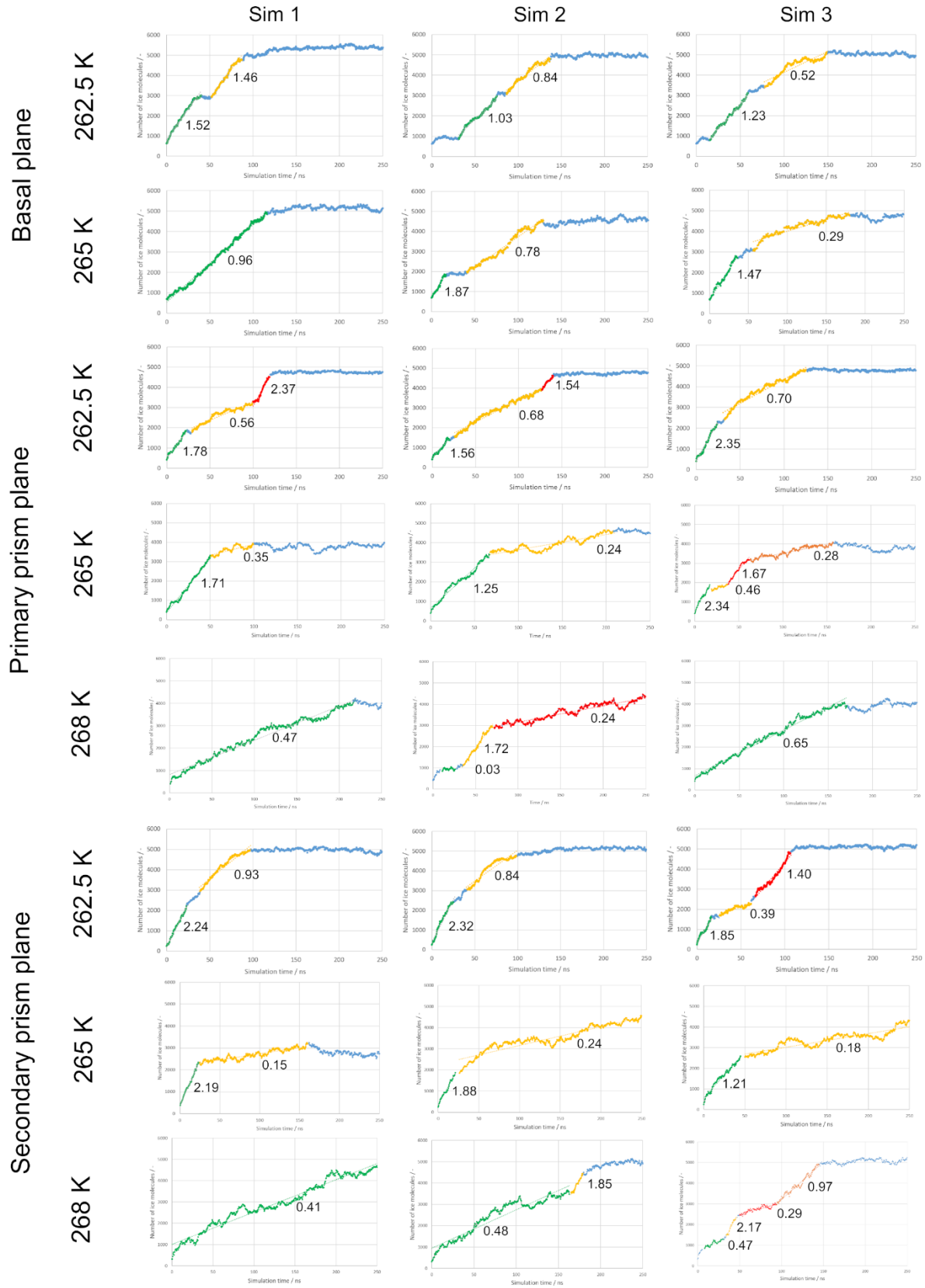

Figure A4.2. *Simple plots illustrating ice growth for all simulations involving κ-carrageenan composed of 3 disaccharide units. The ice growth rate in each phase is indicated by the number on the right side of the curve and measured in molecules*ns^{-1}*nm^{-2}.*

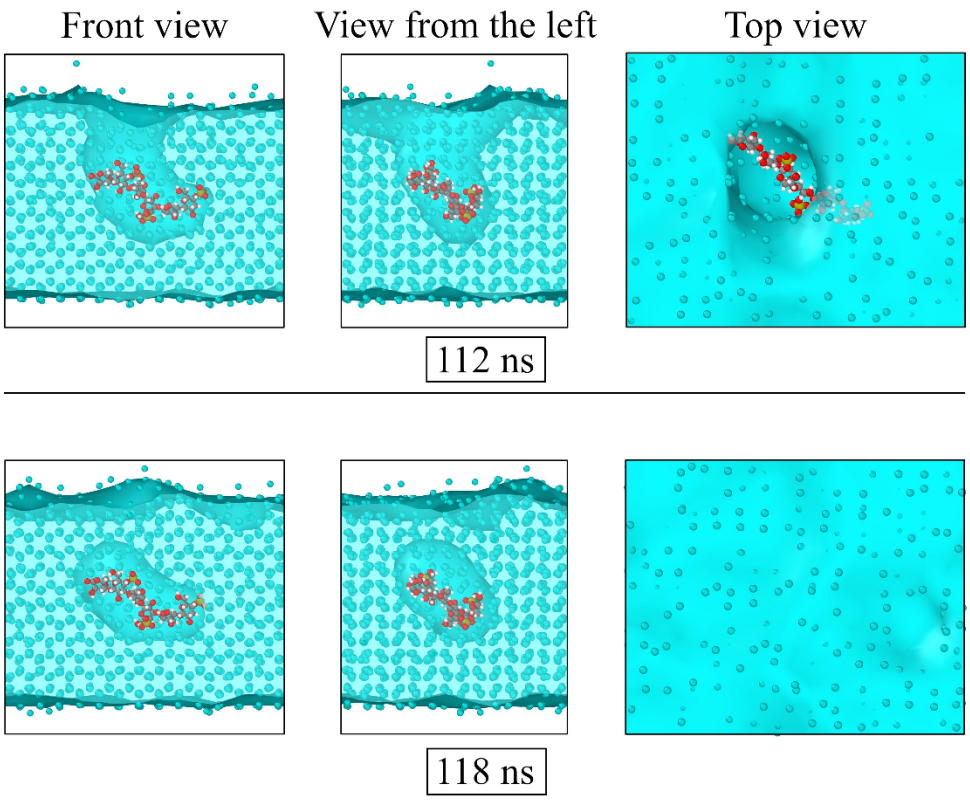

Figure A4.3. *Ice surface of the primary prism plane shown shortly before (top row) and after (bottom row) the bound κ-carrageenan is overgrown at a temperature of 262.5 K.*

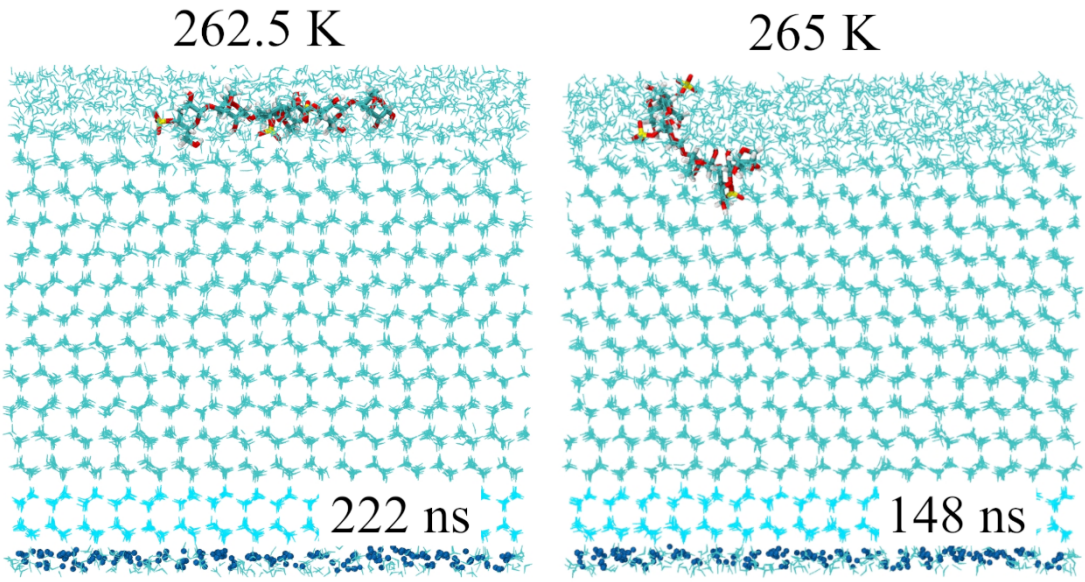

Figure A4.4. *Snapshots of the simulations with ice growth in basal plane direction at 262.5 and 265 K. In both simulations, the advancing ice front constantly displaced the κ-carrageenan molecule, preventing its binding to the ice surface.*

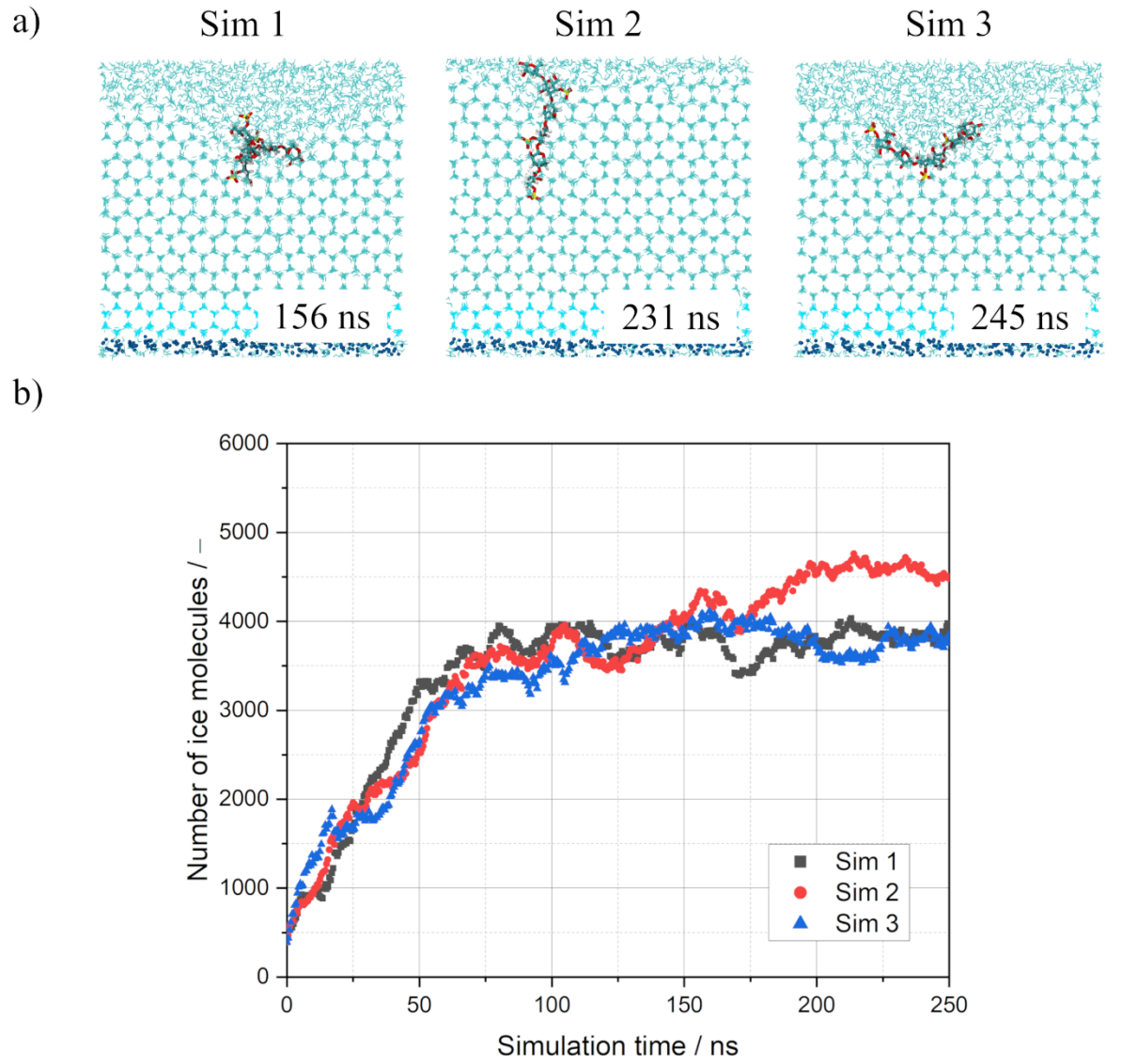

Figure A4.5. *Shown are the different binding orientations of κ-carrageenan [a)] in growth direction of the primary prism plane at 265 K and the progression of ice growth of the three simulations [b)]. Two out of three simulations displayed horizontal binding of the molecule to the primary prism plane, resulting in an inhibition of ice growth. Even after binding, the simulation with vertical bound κ-carrageenan exhibited slow ice growth.*

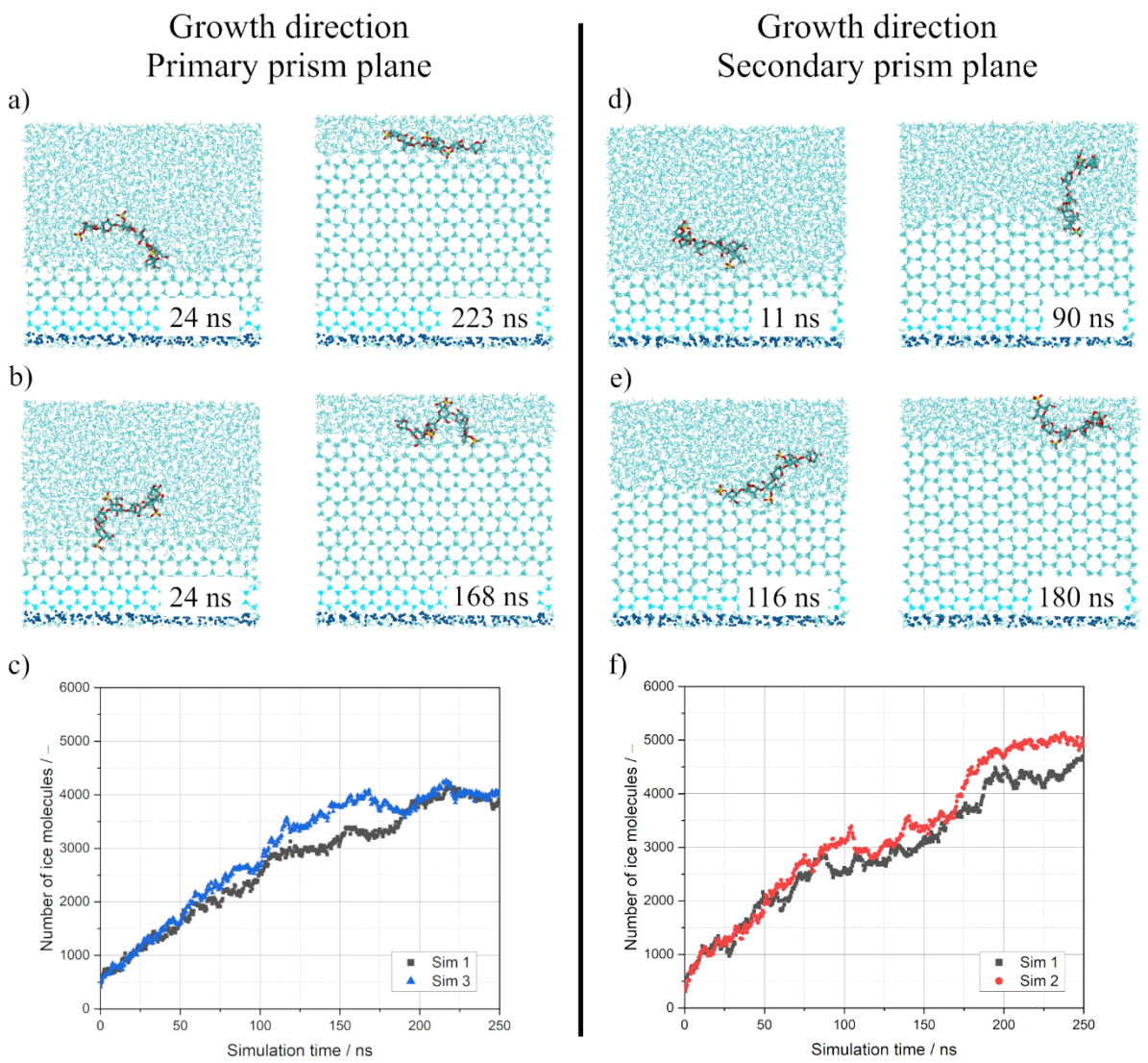

Figure A4.6. *Illustration of the attempted interaction of κ-carrageenan with the ice surface and its influence on ice growth at 268 K. In simulations 1 [a)] and 3 [b)], the molecule briefly attaches to the ice surface of the primary prism plane, but fails to interact with it for an extended time period. The corresponding ice growth profiles [c)] indicate no considerable influence on ice crystal growth. A similar behavior is observed for the secondary prism plane. In d) and e) κ-carrageenan tries to interact with the secondary prism plane, in simulation 1 and 2, respectively. This interaction is again of short duration resulting in no substantial influence on ice growth, as seen in the corresponding diagram in f).*

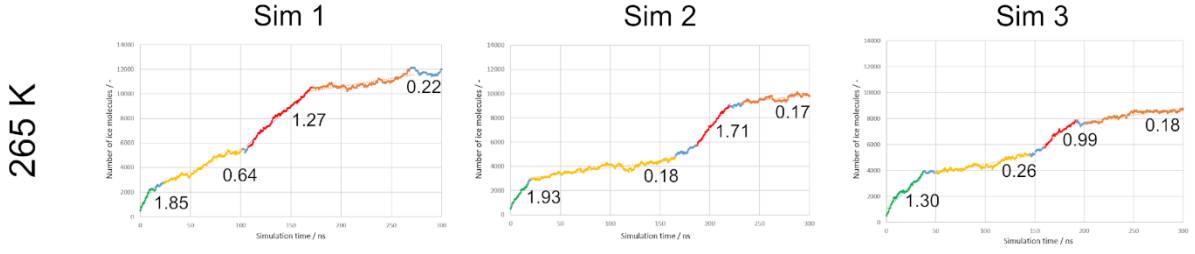

Figure A4.7. *Simple plots illustrating ice growth for all simulations involving κ-carrageenan composed of 6 disaccharide units. The ice growth rate in each phase is indicated by the number on the right side of the curve and measured in molecules*ns^{-1}*nm^{-2}.*

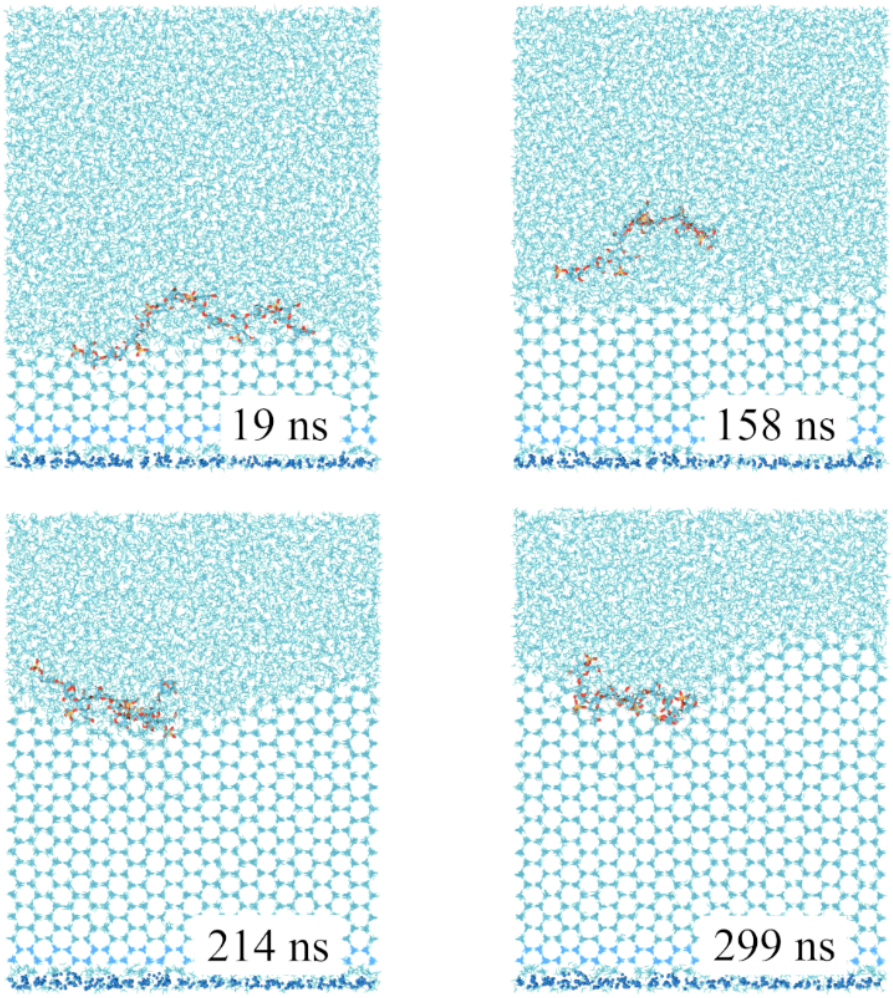

Figure A4.8. *Progression of ice growth along the secondary prism plane during the second simulation at a temperature of 265 K. For further comprehension, snapshots from the simulations are presented to illustrate characteristic aspects.*

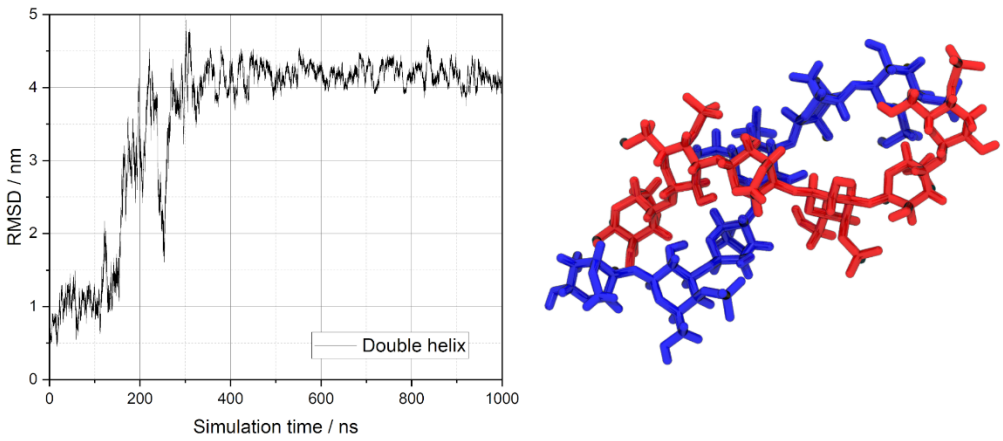

Figure A4.9. *The RMSD values during the double helix formation simulated without ion excess at a temperature of 270 K are presented in the left image. The right image illustrates the stable double helix conformation formed by two κ-carrageenan strands (blue and red) each containing three disaccharide units.*

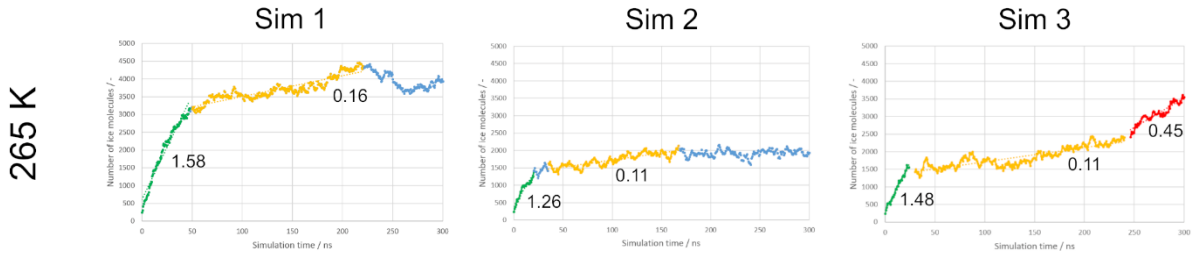

Figure A4.10. *Simple plots illustrating ice growth for all simulations involving the κ-carrageenan double helix. The ice growth rate in each phase is indicated by the number on the right side of the curve and measured in molecules*ns^{-1}*nm^{-2}.*

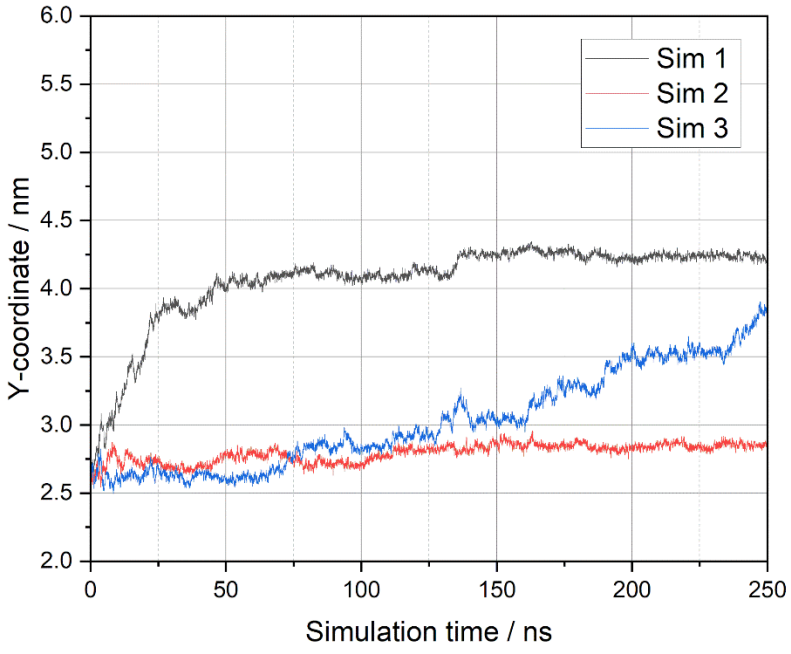

Figure A4.11. *Progression of the y-coordinate of the COM of the double helix during the simulations at 265 K with ice growth in direction of the secondary prism plane.*

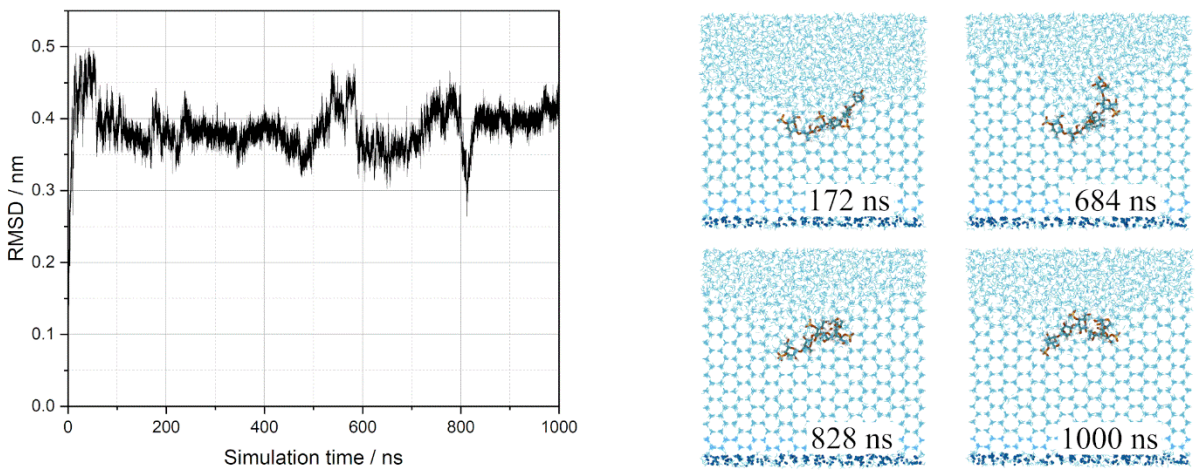

Figure A4.12. *The left graph illustrates the RMSD value, while the right panel provides a visual representation of the system during the simulation with ice growth in direction of the secondary prism plane at 265 K.*

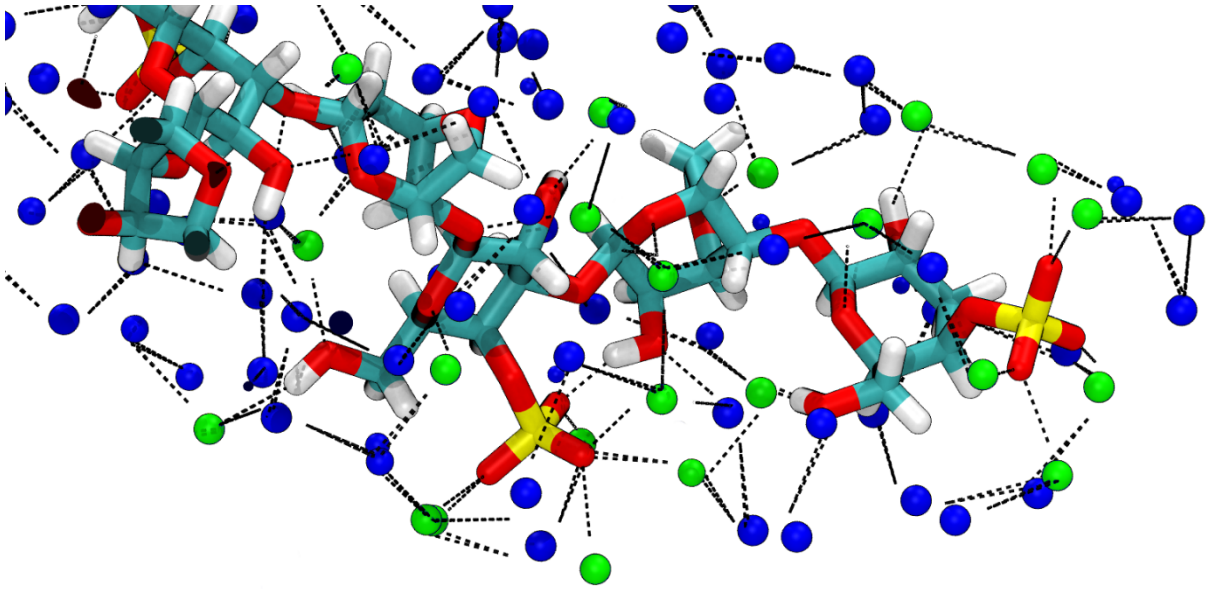

Figure A4.13. *Visualization of the hydrogen bond network involving the hydration layer and κ-carrageenan. Hydrogen bonds are represented as black dashed lines, while water molecules forming hydrogen bonds with κ-carrageenan are depicted as green spheres.*

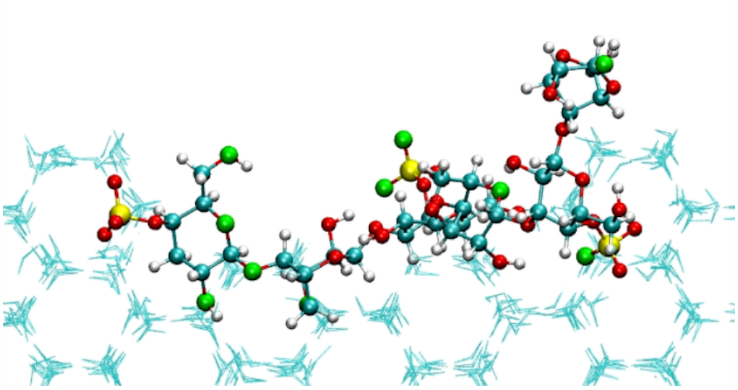

Figure A4.14. *Snapshots of κ-carrageenan obtained from the first simulation with ice growth along the secondary prism plane at 265 K. After a simulation time of 200 ns, a 3D analysis was performed and oxygen atoms of κ-carrageenan occupying ice lattice positions were colored green. Water molecules within the ice lattice are represented as cyan lines.*

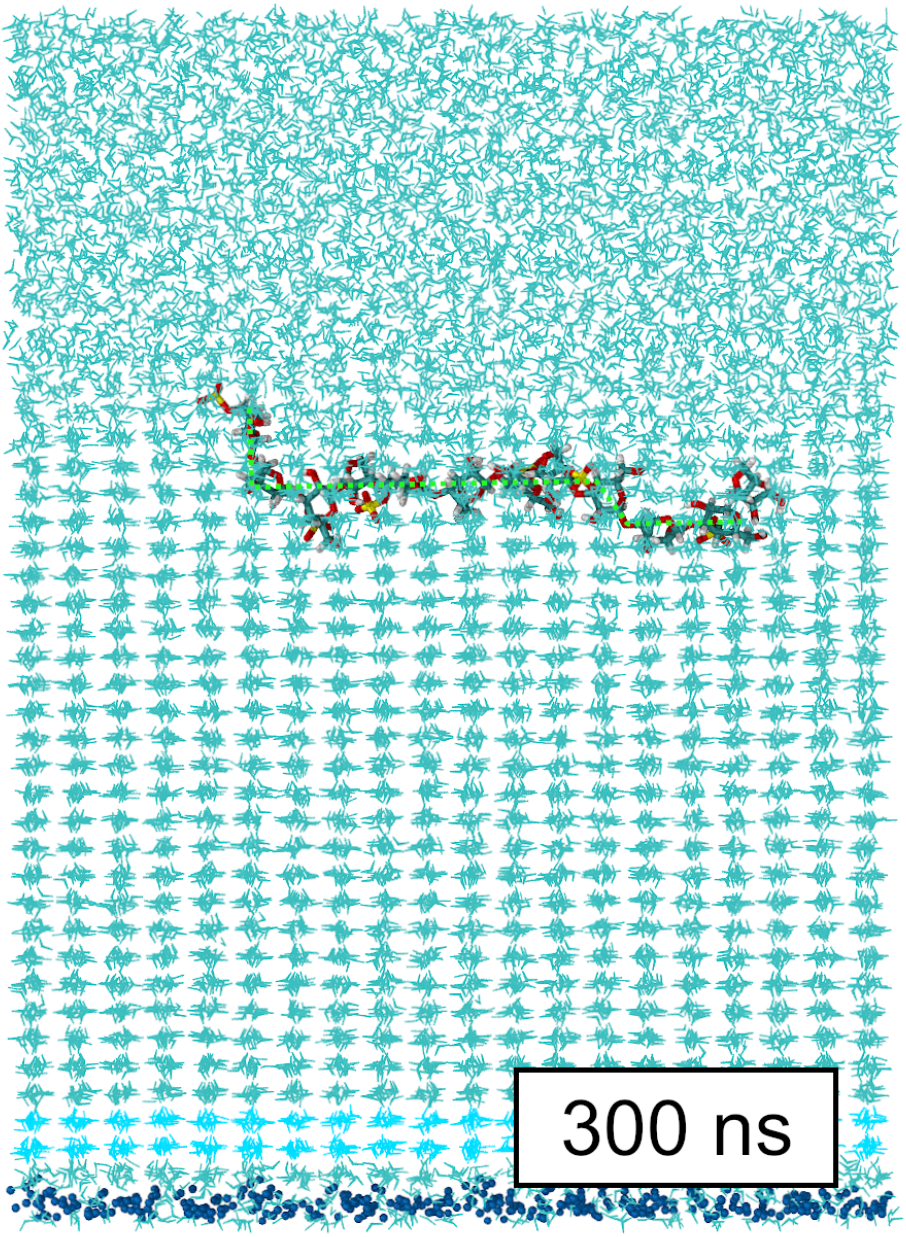

Figure A4.15. *Snapshot of the simulation with 6-unit κ-carrageenan and ice growth along the secondary prism plane at 265 K. The image illustrates the significant conformational changes the molecule exhibits as it interacts with the ice lattice, evidenced by its pronounced structural bends.*

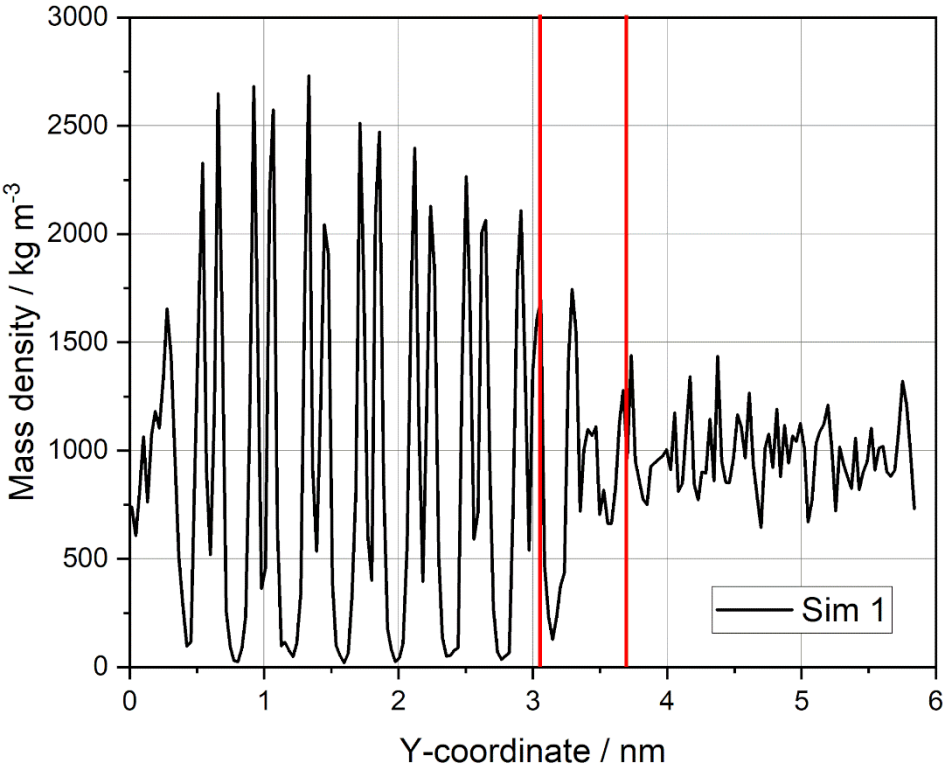

Figure A4.16. *Mass density profile along the y-axis of the first simulation at 265 K including κ-carrageenan composed of 3 disaccharide units. The red vertical lines indicate the boundaries of the quasi-liquid layer.*

A5. Acknowledgements

A5.1. Acknowledgements to Chapter 2

This work was supported by Deutsche Forschungsgemeinschaft (WE 6416/2-1). The authors are grateful to Prof. Gisela Guthausen for her support with the NMR measurements and to Dr. Elisabeth Eiche for her support with the ICP-OES measurements. In addition, the authors would like to thank Lydia Schütz for her invaluable contributions in conducting the rheological measurements.

A5.2. Acknowledgements to Chapter 3

This work was supported by Deutsche Forschungsgemeinschaft (WE 6416/2-1). The authors are grateful to Prof. Gisela Guthausen for her support with the NMR measurements and to Dr. Elisabeth Eiche for her support with the ICP-OES measurements.

A5.3. Acknowledgements to Chapter 4

The authors would like to thank Lydia Schütz for her support with the rheological measurements. Additionally, we would like to thank Martin Daescu and Nina Weis for their support in carrying out recrystallization experiments and Prof. Gisela Guthausen for her support with the NMR measurements.

A5.4. Acknowledgements to Chapter 6

We would like to thank Benjamin Westberry for generously providing the Glycam parameters for κ-carrageenan.

Bibliography

1. Statista. Private Haushalte - Ausstattung mit Gefrierschrank bis 2022 | Statista. Available online: https://de.statista.com/statistik/daten/studie/410662/umfrage/private-haushalte-in-deutschland-mit-gefrierschrank/ (accessed on 13 November 2024).
2. Statista. Pro-Kopf-Verbrauch von Tiefkühlkost in Deutschland bis 2023 | Statista. Available online: https://de.statista.com/statistik/daten/studie/37571/umfrage/pro-kopf-verbrauch-von-tiefkuehlkost/ (accessed on 13 November 2024).
3. Statista. Pro-Kopf-Konsum von Speiseeis bis 2023 | Statista. Available online: https://de.statista.com/statistik/daten/studie/20152/umfrage/entwicklung-des-eiskonsums-in-deutschland-seit-2001/ (accessed on 13 November 2024).
4. Statista. Absatzverteilung von Tiefkühlkost nach Produktgruppen 2023 | Statista (accessed on 13 November 2024).
5. Mazur, P. Freezing of living cells: mechanisms and implications. *The American journal of physiology* **1984**, 247, C125-42, doi:10.1152/ajpcell.1984.247.3.C125.
6. Tan, M.; Mei, J.; Xie, J. The Formation and Control of Ice Crystal and Its Impact on the Quality of Frozen Aquatic Products: A Review. *Crystals* **2021**, 11, 68, doi:10.3390/cryst11010068.
7. Li, D.; Zhu, Z.; Sun, D.-W. Effects of freezing on cell structure of fresh cellular food materials: A review. *Trends in Food Science & Technology* **2018**, 75, 46–55, doi:10.1016/j.tifs.2018.02.019.
8. Scott, K.L.; Lecak, J.; Acker, J.P. Biopreservation of red blood cells: past, present, and future. *Transfusion medicine reviews* **2005**, 19, 127–142, doi:10.1016/j.tmrv.2004.11.004.
9. Donhowe, D.P.; Hartel, R.W. Recrystallization of ice in ice cream during controlled accelerated storage. *International Dairy Journal* **1996**, 6, 1191–1208, doi:10.1016/S0958-6946(96)00029-5.
10. Zhang, B.; Cao, H.-J.; Wei, W.; Ying, X.-G. Influence of temperature fluctuations on growth and recrystallization of ice crystals in frozen peeled shrimp (Litopenaeus vannamei) pre-soaked with carrageenan oligosaccharide and xylooligosaccharide. *Food Chem.* **2020**, 306, 125641, doi:10.1016/j.foodchem.2019.125641.
11. Martino, M.N.; Zaritzky, N.E. Ice recrystallization in a model system and in frozen muscle tissue. *Cryobiology* **1989**, 26, 138–148, doi:10.1016/0011-2240(89)90044-8.

12. Bevilacqua, A.E.; Zaritzky, N.E. Ice Recrystallization in Frozen Beef. *Journal of Food Science* **1982**, 47, 1410–1414, doi:10.1111/j.1365-2621.1982.tb04950.x.
13. Alizadeh, E.; Chapleau, N.; Lamballerie, M. de; Le-Bail, A. Effect of different freezing processes on the microstructure of Atlantic salmon (Salmo salar) fillets. *Innovative Food Science & Emerging Technologies* **2007**, 8, 493–499, doi:10.1016/j.ifset.2006.12.003.
14. Luscher, C.; Schlüter, O.; Knorr, D. High pressure–low temperature processing of foods: impact on cell membranes, texture, color and visual appearance of potato tissue. *Innovative Food Science & Emerging Technologies* **2005**, 6, 59–71, doi:10.1016/j.ifset.2002.05.001.
15. Sun, D.-W.; Li, B. Microstructural change of potato tissues frozen by ultrasound-assisted immersion freezing. *Journal of Food Engineering* **2003**, 57, 337–345, doi:10.1016/S0260-8774(02)00354-0.
16. Zhang, Z.; Sun, D.-W.; Zhu, Z.; Cheng, L. Enhancement of Crystallization Processes by Power Ultrasound: Current State of the Art and Research Advances. *Comp Rev Food Sci Food Safe* **2015**, 14, 303 ‐ 316, doi:10.1111/1541-4337.12132.
17. Xanthakis, E.; Havet, M.; Chevallier, S.; Abadie, J.; Le-Bail, A. Effect of static electric field on ice crystal size reduction during freezing of pork meat. *Innovative Food Science & Emerging Technologies* **2013**, 20, 115–120, doi:10.1016/j.ifset.2013.06.011.
18. Dalvi-Isfahan, M.; Hamdami, N.; Le-Bail, A. Effect of freezing under electrostatic field on the quality of lamb meat. *Innovative Food Science & Emerging Technologies* **2016**, 37, 68–73, doi:10.1016/j.ifset.2016.07.028.
19. Otero, L.; Rodríguez, A.C.; Pérez-Mateos, M.; Sanz, P.D. Effects of Magnetic Fields on Freezing: Application to Biological Products. *Comp Rev Food Sci Food Safe* **2016**, 15, 646–667, doi:10.1111/1541-4337.12202.
20. Dalvi-Isfahan, M.; Hamdami, N.; Xanthakis, E.; Le-Bail, A. Review on the control of ice nucleation by ultrasound waves, electric and magnetic fields. *Journal of Food Engineering* **2017**, 195, 222–234, doi:10.1016/j.jfoodeng.2016.10.001.
21. Dempsey, P.; Bansal, P. The art of air blast freezing: Design and efficiency considerations. *Applied Thermal Engineering* **2012**, 41, 71–83, doi:10.1016/j.applthermaleng.2011.12.013.
22. Hou, Q.; Cheng, Y.; Kang, D.; Zhang, W.; Zhou, G. Quality changes of pork during frozen storage: comparison of immersion solution freezing and air blast freezing. *International Journal of Food Science & Technology* **2020**, 55, 109–118, doi:10.1111/ijfs.14257.

23. Espinoza Rodezno, L.A.; Sundararajan, S.; Solval, K.M.; Chotiko, A.; Li, J.; Zhang, J.; Alfaro, L.; Bankston, J.D.; Sathivel, S. Cryogenic and air blast freezing techniques and their effect on the quality of catfish fillets. *LWT - Food Science and Technology* **2013**, 54, 377–382, doi:10.1016/j.lwt.2013.07.005.
24. James, C.; Purnell, G.; James, S.J. A Review of Novel and Innovative Food Freezing Technologies. *Food Bioprocess Technol* **2015**, 8, 1616–1634, doi:10.1007/s11947-015-1542-8.
25. Gaukel, V.; Leiter, A.; Spieß, W.E. Synergism of different fish antifreeze proteins and hydrocolloids on recrystallization inhibition of ice in sucrose solutions. *Journal of Food Engineering* **2014**, 141, 44–50, doi:10.1016/j.jfoodeng.2014.05.016.
26. DeVries, A.L. Glycoproteins as biological antifreeze agents in antarctic fishes. *Science* **1971**, 172, 1152–1155, doi:10.1126/science.172.3988.1152.
27. Kristiansen, E.; Zachariassen, K.E. The mechanism by which fish antifreeze proteins cause thermal hysteresis. *Cryobiology* **2005**, 51, 262–280, doi:10.1016/j.cryobiol.2005.07.007.
28. Knight, C.A.; DeVries, A.L.; Oolman, L.D. Fish antifreeze protein and the freezing and recrystallization of ice. *Nature* **1984**, 308, 295–296, doi:10.1038/308295a0.
29. Ustun, N.S.; Turhan, S. Antifreeze Proteins: Characteristics, Function, Mechanism of Action, Sources and Application to Foods. *Journal of Food Processing and Preservation* **2015**, 39, 3189–3197, doi:10.1111/jfpp.12476.
30. Liu, M.; Liang, Y.; Zhang, H.; Wu, G.; Wang, L.; Qian, H.; Qi, X. Production of a recombinant carrot antifreeze protein by Pichia pastoris GS115 and its cryoprotective effects on frozen dough properties and bread quality. *LWT - Food Science and Technology* **2018**, 96, 543–550, doi:10.1016/j.lwt.2018.05.074.
31. WO2015082488A1 - Ice structuring protein - Google Patents. Available online: https://patents.google.com/patent/WO2015082488A1/en (accessed on 13 November 2024).
32. Knight, J.G.; Mather, D.W.; Holdsworth, D.K.; Ermen, D.F. Acceptance of GM food--an experiment in six countries. *Nat. Biotechnol.* **2007**, 25, 507–508, doi:10.1038/nbt0507-507.
33. Statista. Meinungen zum Konsum gentechnisch veränderten Lebensmitteln weltweit 2018 | Statista. Available online: https://de.statista.com/statistik/daten/studie/959754/umfrage/meinungen-zum-konsum-gentechnisch-veraenderten-lebensmitteln-weltweit/ (accessed on 13 November 2024).

34. Ruiter, G.A. de; Rudolph, B. Carrageenan biotechnology. *Trends in Food Science & Technology* **1997**, 8, 389–395, doi:10.1016/S0924-2244(97)01091-1.
35. Usov, A. Structural analysis of red seaweed galactans of agar and carrageenan groups. *Food Hydrocolloids* **1998**, 12, 301–308, doi:10.1016/S0268-005X(98)00018-6.
36. van de Velde, F. Structure and function of hybrid carrageenans. *Food Hydrocolloids* **2008**, 22, 727–734, doi:10.1016/j.foodhyd.2007.05.013.
37. van de Velde, F.; Antipova, A.S.; Rollema, H.S.; Burova, T.V.; Grinberg, N.V.; Pereira, L.; Gilsenan, P.M.; Tromp, R.H.; Rudolph, B.; Grinberg, V.Y. The structure of kappa/iota-hybrid carrageenans II. Coil-helix transition as a function of chain composition. *Carbohydrate Research* **2005**, 340, 1113–1129, doi:10.1016/j.carres.2005.02.015.
38. Kiran-Yildirim, B.; Hale, J.; Wefers, D.; Gaukel, V. Ice recrystallization inhibition of commercial κ-, ι-, and λ-carrageenans. *Journal of Food Engineering* **2021**, 290, 110269, doi:10.1016/j.jfoodeng.2020.110269.
39. Gaukel, V. Untersuchungen zum Einfluss von Antigefrierproteinen auf die Rekristallisation von Eis während der Gefrierlagerung, dargestellt an Modelllösungen für Eiskrem. Zugl.: Hohenheim, Univ., Diss., 2004, Als Ms. gedr; *GCA-Verlag: Herdecke*, **2004**, ISBN 3898631702.
40. Rinaudo, M. Main properties and current applications of some polysaccharides as biomaterials. *Polymer International* **2008**, 57, 397–430, doi:10.1002/pi.2378.
41. Leiter, A.; Emmer, P.; Gaukel, V. Influence of gelation on ice recrystallization inhibition activity of κ-carrageenan in sucrose solution. *Food Hydrocolloids* **2018**, 76, 194–203, doi:10.1016/j.foodhyd.2016.11.028.
42. Leiter, A.; Ludwig, A.; Gaukel, V. Influence of heating temperature, pH and ions on recrystallization inhibition activity of κ-carrageenan in sucrose solution. *Journal of Food Engineering* **2017**, 195, 14–20, doi:10.1016/j.jfoodeng.2016.09.016.
43. Leiter, A.; Mailänder, J.; Wefers, D.; Bunzel, M.; Gaukel, V. Influence of acid hydrolysis and dialysis of κ-carrageenan on its ice recrystallization inhibition activity. *Journal of Food Engineering* **2017**, 209, 26–35, doi:10.1016/j.jfoodeng.2017.04.013.
44. Kiran‐Yildirim, B.; Gaukel, V. Ice Crystal Growth in Sucrose Solutions Containing Kappa- and Iota-Carrageenans. *Chem Eng & Technol* **2020**, 43, 1040‐1047, doi:10.1002/ceat.201900644.
45. Rischer, H.; Szilvay, G.R.; Oksman-Caldentey, K.-M. Cellular agriculture - industrial biotechnology for food and materials. *Curr. Opin. Biotechnol.* **2020**, 61, 128–134, doi:10.1016/j.copbio.2019.12.003.

46. Hartel, R.W. Crystallization in foods. Handbook of industrial crystallization, 2nd ed.; *Butterworth-Heinemann: Boston*, **2002**; pp 287–304, ISBN 9780750670128.
47. Cook, K.; Hartel, R.W. Mechanisms of Ice Crystallization in Ice Cream Production. *Comp Rev Food Sci Food Safe* **2010**, 9, 213–222, doi:10.1111/j.1541-4337.2009.00101.x.
48. Tan, K.-C.; Ho, W.; Katz, J.I.; Feng, S.-J. A study of the occurrence of supercooling of water. *American Journal of Physics* **2016**, 84, 293–300, doi:10.1119/1.4939792.
49. Maeda, N. Brief Overview of Ice Nucleation. *Molecules* **2021**, 26, doi:10.3390/molecules26020392.
50. Kashchiev, D.; van Rosmalen, G.M. Review: Nucleation in solutions revisited. *Cryst. Res. Technol.* **2003**, 38, 555–574, doi:10.1002/crat.200310070.
51. Kiani, H.; Sun, D.-W. Water crystallization and its importance to freezing of foods: A review. *Trends in Food Science & Technology* **2011**, 22, 407–426, doi:10.1016/j.tifs.2011.04.011.
52. McCabe, W.L.; Smith, J.C.; Harriot, P. Unit operations of chemical engineering, 5. ed.; *McGraw-Hill: New York*, **1993**, ISBN 0-07-044844-2.
53. Schwartzberg, H.G.; Rao, M.A. Biotechnology and food process engineering: Papers presented at a symposium held June 23 - 24, 1989; *Dekker: New York*, **1990**, ISBN 9780824783631.
54. Debenedetti, P.G. Supercooled and glassy water. *J. Phys.: Condens. Matter* **2003**, 15, R1669-R1726, doi:10.1088/0953-8984/15/45/R01.
55. Handbook of frozen food processing and packaging; Sun, D.-W., Ed., 2nd ed (Online-Ausg.); *Boca Raton FL: Taylor & Francis*, **2012**, ISBN 9781283350174.
56. Erdemir, D.; Lee, A.Y.; Myerson, A.S. Nucleation of crystals from solution: classical and two-step models. *Acc. Chem. Res.* **2009**, 42, 621–629, doi:10.1021/ar800217x.
57. Zachariassen, K.E.; Kristiansen, E. Ice nucleation and antinucleation in nature. *Cryobiology* **2000**, 41, 257–279, doi:10.1006/cryo.2000.2289.
58. Aich, R.; Pal, P.; Chakraborty, S.; Jana, B. Preferential Ordering and Organization of Hydration Water Favor Nucleation of Ice by Ice-Nucleating Proteins over Antifreeze Proteins. *The journal of physical chemistry. B* **2023**, 127, 6038–6048, doi:10.1021/acs.jpcb.3c01641.
59. Whaley, D.; Damyar, K.; Witek, R.P.; Mendoza, A.; Alexander, M.; Lakey, J.R. Cryopreservation: An Overview of Principles and Cell-Specific Considerations. *Cell Transplant.* **2021**, 30, 963689721999617, doi:10.1177/0963689721999617.

60. Seki, S.; Mazur, P. The dominance of warming rate over cooling rate in the survival of mouse oocytes subjected to a vitrification procedure. *Cryobiology* **2009**, 59, 75–82, doi:10.1016/j.cryobiol.2009.04.012.
61. Hoffmann, N.E.; Bischof, J.C. The cryobiology of cryosurgical injury. *Urology* **2002**, 60, 40–49, doi:10.1016/s0090-4295(02)01683-7.
62. Mazur, P. The role of intracellular freezing in the death of cells cooled at supraoptimal rates. *Cryobiology* **1977**, 14, 251–272, doi:10.1016/0011-2240(77)90175-4.
63. Chang, T.; Zhao, G. Ice Inhibition for Cryopreservation: Materials, Strategies, and Challenges. *Adv. Sci. (Weinh)* **2021**, 8, 2002425, doi:10.1002/advs.202002425.
64. Zanotto, E.D.; Mauro, J.C. The glassy state of matter: Its definition and ultimate fate. *Journal of Non-Crystalline Solids* **2017**, 471, 490–495, doi:10.1016/j.jnoncrysol.2017.05.019.
65. Rahman, M.; Guizani, N.; Al-Khaseibi, M.; Ali Al-Hinai, S.; Al-Maskri, S.S.; Al-Hamhami, K. Analysis of cooling curve to determine the end point of freezing. *Food Hydrocolloids* **2002**, 16, 653–659, doi:10.1016/S0268-005X(02)00031-0.
66. Huang, H.; He, X.; Yarmush, M.L. Advanced technologies for the preservation of mammalian biospecimens. *Nat. Biomed. Eng.* **2021**, 5, 793–804, doi:10.1038/s41551-021-00784-z.
67. Han, Z.; Rao, J.S.; Gangwar, L.; Namsrai, B.-E.; Pasek-Allen, J.L.; Etheridge, M.L.; Wolf, S.M.; Pruett, T.L.; Bischof, J.C.; Finger, E.B. Vitrification and nanowarming enable long-term organ cryopreservation and life-sustaining kidney transplantation in a rat model. *Nat Commun* **2023**, 14, 3407, doi:10.1038/s41467-023-38824-8.
68. Fahy, G.M.; Wowk, B. Principles of cryopreservation by vitrification. *Methods in molecular biology (Clifton, N.J.)* **2015**, 1257, 21–82, doi:10.1007/978-1-4939-2193-5_2.
69. Elliott, G.D.; Wang, S.; Fuller, B.J. Cryoprotectants: A review of the actions and applications of cryoprotective solutes that modulate cell recovery from ultra-low temperatures. *Cryobiology* **2017**, 76, 74–91, doi:10.1016/j.cryobiol.2017.04.004.
70. Cen, H.; Lu, R.; Mendoza, F.; Beaudry, R.M. Relationship of the optical absorption and scattering properties with mechanical and structural properties of apple tissue. *Postharvest Biology and Technology* **2013**, 85, 30–38, doi:10.1016/j.postharvbio.2013.04.014.
71. Ordaz-Ortiz, J.J.; Marcus, S.E.; Knox, J.P. Cell wall microstructure analysis implicates hemicellulose polysaccharides in cell adhesion in tomato fruit pericarp parenchyma. *Molecular Plant* **2009**, 2, 910–921, doi:10.1093/mp/ssp049.

72. Kaale, L.D.; Eikevik, T.M. A histological study of the microstructure sizes of the red and white muscles of Atlantic salmon (Salmo salar) fillets during superchilling process and storage. *Journal of Food Engineering* **2013**, 114, 242–248, doi:10.1016/j.jfoodeng.2012.08.003.
73. Marshall, W.F.; Young, K.D.; Swaffer, M.; Wood, E.; Nurse, P.; Kimura, A.; Frankel, J.; Wallingford, J.; Walbot, V.; Qu, X.; et al. What determines cell size? *BMC Biol.* **2012**, 10, 101, doi:10.1186/1741-7007-10-101.
74. Jensen, K.H.; Zwieniecki, M.A. Physical limits to leaf size in tall trees. *Phys. Rev. Lett.* **2013**, 110, 18104, doi:10.1103/PhysRevLett.110.018104.
75. Roos, Y.H. Glass transition temperature and its relevance in food processing. *Annu. Rev. Food Sci. Technol.* **2010**, 1, 469–496, doi:10.1146/annurev.food.102308.124139.
76. Boily, J.-F. Solubility. *Encyclopedia of Geochemistry* **2017**, 1–9, doi:10.1007/978-3-319-39193-9_72-1.
77. Blanshard, J.M.; Muhr, A.H.; Gough, A. Crystallization from concentrated sucrose solutions. *Adv. Exp. Med. Biol.* **1991**, 302, 639–655, doi:10.1007/978-1-4899-0664-9_35.
78. Singh, V.K. 8 - Phase equilibria and formation of clinker phases. In The Science and Technology of Cement and Other Hydraulic Binders; Singh, V.K., Ed.; *Elsevier Science & Technology: San Diego*, **2023**; pp 253–323, ISBN 978-0-323-95080-0.
79. Donhowe, D.P.; Hartel, R.W. Recrystallization of ice during bulk storage of ice cream. *International Dairy Journal* **1996**, 6, 1209–1221, doi:10.1016/S0958-6946(96)00030-1.
80. Lin, M.; Cao, H.; Li, J. Control strategies of ice nucleation, growth, and recrystallization for cryopreservation. *Acta Biomaterialia* **2023**, 155, 35–56, doi:10.1016/j.actbio.2022.10.056.
81. Adapa, S.; Schmidt, K.A.; Jeon, I.J.; Herald, T.J.; Flores, R.A. Mechanisms of ice crystallization and recrystallization in ice cream: A review. *Food Reviews International* **2000**, 16, 259–271, doi:10.1081/FRI-100100289.
82. Zhu, Z.; Zhou, Q.; Sun, D.-W. Measuring and controlling ice crystallization in frozen foods: A review of recent developments. *Trends in Food Science & Technology* **2019**, 90, 13–25, doi:10.1016/j.tifs.2019.05.012.
83. Fennema, O.; Powrie, W.D. Fundamentals of Low-Temperature Food Preservation. In Advances in Food Research; Chichester, C.O., Mrak, E.M., Stewart, G.F., Eds.; *Academic Press*, **1964**; pp 219–347, ISBN 0065-2628.

84. Wagner, C. Theorie der Alterung von Niederschlägen durch Umlösen (Ostwald‐Reifung). Zeitschrift für Elektrochemie, *Berichte der Bunsengesellschaft für physikalische Chemie* **1961**, 65, 581–591, doi:10.1002/bbpc.19610650704.
85. Hagiwara, T.; Hartel, R.W. Effect of Sweetener, Stabilizer, and Storage Temperature on Ice Recrystallization in Ice Cream. *Journal of Dairy Science* **1996**, 79, 735–744, doi:10.3168/jds.S0022-0302(96)76420-2.
86. Flores, A.A.; Goff, H.D. Recrystallization in Ice Cream After Constant and Cycling Temperature Storage Conditions as Affected by Stabilizers. *Journal of Dairy Science* **1999**, 82, 1408–1415, doi:10.3168/jds.S0022-0302(99)75367-1.
87. Budke, C.; Heggemann, C.; Koch, M.; Sewald, N.; Koop, T. Ice recrystallization kinetics in the presence of synthetic antifreeze glycoprotein analogues using the framework of LSW theory. *The Journal of Physical Chemistry B* **2009**, 113, 2865–2873, doi:10.1021/jp805726e.
88. Chinard, F.P. Colligative properties. *J. Chem. Educ.* **1955**, 32, 377, doi:10.1021/ed032p377.
89. Harper, E.K.; Shoemaker, C.F. Effect of Locust Bean Gum and Selected Sweetening Agents on Ice Recrystallization Rates. *Journal of Food Science* **1983**, 48, 1801–1803, doi:10.1111/j.1365-2621.1983.tb05088.x.
90. Regand, A.; Goff, H. Structure and ice recrystallization in frozen stabilized ice cream model systems. *Food Hydrocolloids* **2003**, 17, 95–102, doi:10.1016/S0268-005X(02)00042-5.
91. Herrera, M.L.; M'Cann, J.I.; Ferrero, C.; Hagiwara, T.; Zaritzky, N.E.; Hartel, R.W. Thermal, Mechanical, and Molecular Relaxation Properties of Frozen Sucrose and Fructose Solutions Containing Hydrocolloids. *Food Biophysics* **2007**, 2, 20–28, doi:10.1007/s11483-007-9025-8.
92. Li, T.; Li, M.; Zhong, Q.; Wu, T. Effect of Fibril Length on the Ice Recrystallization Inhibition Activity of Nanocelluloses. *Carbohydrate polymers* **2020**, 240, 116275, doi:10.1016/j.carbpol.2020.116275.
93. Ndoye, F.T.; Alvarez, G. Characterization of ice recrystallization in ice cream during storage using the focused beam reflectance measurement. *Journal of Food Engineering* **2015**, 148, 24–34, doi:10.1016/j.jfoodeng.2014.09.014.
94. Miller-Livney, T.; Hartel, R.W. Ice Recrystallization in Ice Cream: Interactions Between Sweeteners and Stabilizers. *Journal of Dairy Science* **1997**, 80, 447–456, doi:10.3168/jds.S0022-0302(97)75956-3.

95. Goff, H.D.; Ferdinando, D.; Schorsch, C. Fluorescence microscopy to study galactomannan structure in frozen sucrose and milk protein solutions. *Food Hydrocolloids* **1999**, 13, 353–362, doi:10.1016/S0268-005X(99)00017-X.
96. Blond, G. Velocity of linear crystallization of ice in macromolecular systems. *Cryobiology* **1988**, 25, 61–66, doi:10.1016/0011-2240(88)90021-1.
97. Muhr, A.H.; Blanschard, J.M.V. Effect of polysaccharide stabilizers on the rate of growth of ice. *International Journal of Food Science & Technology* **1986**, 21, 683–710, doi:10.1111/ijfs1986216683.
98. Martin, D.R.; Ablett, S.; Darke, A.; Sutton, R.L.; Sahagian, M. Diffusion of Aqueous Sugar Solutions as Affected by Locust Bean Gum Studied by NMR. *Journal of Food Science* **1999**, 64, 46–49, doi:10.1111/j.1365-2621.1999.tb09858.x.
99. Bar Dolev, M.; Braslavsky, I.; Davies, P.L. Ice-Binding Proteins and Their Function. *Annual review of biochemistry* **2016**, 85, 515–542, doi:10.1146/annurev-biochem-060815-014546.
100. Kawahara, H. Cryoprotectants and Ice-Binding Proteins. In *Psychrophiles; Margesin, R., Ed.; Springer International Publishing: Cham*, **2017**; pp 237–257, ISBN 978-3-319-57056-3.
101. Davies, P.L. Ice-binding proteins: a remarkable diversity of structures for stopping and starting ice growth. *Trends in Biochemical Sciences* **2014**, 39, 548–555, doi:10.1016/j.tibs.2014.09.005.
102. Lifshitz, I.M.; Slyozov, V.V. The kinetics of precipitation from supersaturated solid solutions. *Journal of Physics and Chemistry of Solids* **1961**, 19, 35–50, doi:10.1016/0022-3697(61)90054-3.
103. Jain, S.C.; Hughes, A.E. Ostwald ripening and its application to precipitates and colloids in ionic crystals and glasses. *J Mater Sci* **1978**, 13, 1611–1631, doi:10.1007/BF00548725.
104. Kahlweit, M. Ostwald ripening of precipitates. *Advances in Colloid and Interface Science* **1975**, 5, 1–35, doi:10.1016/0001-8686(75)85001-9.
105. van Westen, T.; Groot, R.D. Predicting the Kinetics of Ice Recrystallization in Aqueous Sugar Solutions. *Crystal Growth & Design* **2018**, 18, 2405–2416, doi:10.1021/acs.cgd.8b00038.
106. Knight, C.A.; Hallett, J.; DeVries, A.L. Solute effects on ice recrystallization: an assessment technique. *Cryobiology* **1988**, 25, 55–60, doi:10.1016/0011-2240(88)90020-x.

107. Sun, X.; Guo, R.; Kou, Y.; Song, H.; Zhan, T.; Wu, J.; Song, L.; Zhang, H.; Xie, F.; Wang, J.; et al. Inhibition of ice recrystallization by tamarind (Tamarindus indica L.) seed polysaccharide and molecular weight effects. *Carbohydrate polymers* **2023**, 301, 120358, doi:10.1016/j.carbpol.2022.120358.
108. Wu, S.; Zhu, C.; He, Z.; Xue, H.; Fan, Q.; Song, Y.; Francisco, J.S.; Zeng, X.C.; Wang, J. Ion-specific ice recrystallization provides a facile approach for the fabrication of porous materials. *Nat Commun* **2017**, 8, 15154, doi:10.1038/ncomms15154.
109. Warren, M.T.; Galpin, I.; Bachtiger, F.; Gibson, M.I.; Sosso, G.C. Ice Recrystallization Inhibition by Amino Acids: The Curious Case of Alpha- and Beta-Alanine. *J. Phys. Chem. Lett.* **2022**, 13, 2237–2244, doi:10.1021/acs.jpclett.1c04080.
110. Diaz-Dussan, D.; Peng, Y.-Y.; Sengupta, J.; Zabludowski, R.; Adam, M.K.; Acker, J.P.; Ben, R.N.; Kumar, P.; Narain, R. Trehalose-Based Polyethers for Cryopreservation and Three-Dimensional Cell Scaffolds. *Biomacromolecules* **2020**, 21, 1264–1273, doi:10.1021/acs.biomac.0c00018.
111. Le Tri, D.; Childers, C.L.; Adam, M.K.; Ben, R.N.; Storey, K.B.; Biggar, K.K. Characterization of ice recrystallization inhibition activity in the novel freeze-responsive protein Fr10 from freeze-tolerant wood frogs, Rana sylvatica. *J. Therm. Biol.* **2019**, 84, 426–430, doi:10.1016/j.jtherbio.2019.07.030.
112. Knight, C.A.; Wen, D.; Laursen, R.A. Nonequilibrium antifreeze peptides and the recrystallization of ice. *Cryobiology* **1995**, 32, 23–34, doi:10.1006/cryo.1995.1002.
113. Budke, C.; Koop, T. Ice recrystallization inhibition and molecular recognition of ice faces by poly(vinyl alcohol). *Chemphyschem* **2006**, 7, 2601–2606, doi:10.1002/cphc.200600533.
114. Worrall, D.; Elias, L.; Ashford, D.; Smallwood, M.; Sidebottom, C.; Lillford, P.; Telford, J.; Holt, C.; Bowles, D. A carrot leucine-rich-repeat protein that inhibits ice recrystallization. *Science* **1998**, 282, 115–117, doi:10.1126/science.282.5386.115.
115. Delesky, E.A.; Srubar, W.V. Ice-binding proteins and bioinspired synthetic mimics in non-physiological environments. *iScience* **2022**, 25, 104286, doi:10.1016/j.isci.2022.104286.
116. Drori, R.; Li, C.; Hu, C.; Raiteri, P.; Rohl, A.L.; Ward, M.D.; Kahr, B. A Supramolecular Ice Growth Inhibitor. *Journal of the American Chemical Society* **2016**, 138, 13396–13401, doi:10.1021/jacs.6b08267.

117. Gaukel, V.; Spieß, W.E.L. Einfluss von Antigefrierproteinen auf die Rekristallisation von Eis in Modelllösungen für Eiskrem. *Chemie Ingenieur Technik* **2004**, 76, 454–458, doi:10.1002/cite.200400068.
118. Tomczak, M.M.; Marshall, C.B.; Gilbert, J.A.; Davies, P.L. A facile method for determining ice recrystallization inhibition by antifreeze proteins. *Biochem. Biophys. Res. Commun.* **2003**, 311, 1041–1046, doi:10.1016/j.bbrc.2003.10.106.
119. Gilbert, J.A.; Hill, P.J.; Dodd, C.E.R.; Laybourn-Parry, J. Demonstration of antifreeze protein activity in Antarctic lake bacteria. *Microbiology (Reading)* **2004**, 150, 171–180, doi:10.1099/mic.0.26610-0.
120. Graham, L.A.; Agrawal, P.; Oleschuk, R.D.; Davies, P.L. High-capacity ice-recrystallization endpoint assay employing superhydrophobic coatings that is equivalent to the 'splat' assay. *Cryobiology* **2018**, 81, 138–144, doi:10.1016/j.cryobiol.2018.01.011.
121. Olijve, L.L.C.; Oude Vrielink, A.S.; Voets, I.K. A Simple and Quantitative Method to Evaluate Ice Recrystallization Kinetics Using the Circle Hough Transform Algorithm. *Crystal Growth & Design* **2016**, 16, 4190–4195, doi:10.1021/acs.cgd.5b01637.
122. Biggs, C.I.; Stubbs, C.; Graham, B.; Fayter, A.E.R.; Hasan, M.; Gibson, M.I. Mimicking the Ice Recrystallization Activity of Biological Antifreezes. When is a New Polymer "Active"? *Macromol. Biosci.* **2019**, 19, e1900082, doi:10.1002/mabi.201900082.
123. Liu, X.; Pan, Y.; Liu, F.; He, Y.; Zhu, Q.; Liu, Z.; Zhan, X.; Tan, S. A Review of the Material Characteristics, Antifreeze Mechanisms, and Applications of Cryoprotectants (CPAs). *Journal of Nanomaterials* **2021**, 2021, 1–14, doi:10.1155/2021/9990709.
124. Gerhäuser, J.; Hale, J.; Wefers, D.; Gaukel, V. Furcellaran: Impact of Concentration, Rheological Properties, and Structure on Ice Recrystallization Inhibition Activity. *Biomacromolecules* **2024**, 25, 4535–4544, doi:10.1021/acs.biomac.4c00541.
125. Voets, I.K. From ice-binding proteins to bio-inspired antifreeze materials. *Soft Matter* **2017**, 13, 4808–4823, doi:10.1039/c6sm02867e.
126. Kuiper, M.J.; Morton, C.J.; Abraham, S.E.; Gray-Weale, A. The biological function of an insect antifreeze protein simulated by molecular dynamics. *eLife* **2015**, 4, doi:10.7554/eLife.05142.
127. Gerhäuser, J.; Gaukel, V. Detailed Analysis of the Ice Surface after Binding of an Insect Antifreeze Protein and Correlation with the Gibbs-Thomson Equation. *Langmuir : the ACS journal of surfaces and colloids* **2021**, 37, 11716–11725, doi:10.1021/acs.langmuir.1c01620.

128. Raymond, J.A.; DeVries, A.L. Adsorption inhibition as a mechanism of freezing resistance in polar fishes. *Proceedings of the National Academy of Sciences of the United States of America* **1977**, 74, 2589–2593, doi:10.1073/pnas.74.6.2589.
129. Graham, L.A.; Liou, Y.C.; Walker, V.K.; Davies, P.L. Hyperactive antifreeze protein from beetles. *Nature* **1997**, 388, 727–728, doi:10.1038/41908.
130. Cziko, P.A.; DeVries, A.L.; Evans, C.W.; Cheng, C.-H.C. Antifreeze protein-induced superheating of ice inside Antarctic notothenioid fishes inhibits melting during summer warming. *Proceedings of the National Academy of Sciences of the United States of America* **2014**, 111, 14583–14588, doi:10.1073/pnas.1410256111.
131. Braslavsky, I.; Drori, R. LabVIEW-operated novel nanoliter osmometer for ice binding protein investigations. *JoVE (Journal of Visualized Experiments)* **2013**, e4189, doi:10.3791/4189.
132. Inada, T.; Lu, S.-S. Thermal hysteresis caused by non-equilibrium antifreeze activity of poly(vinyl alcohol). *Chemical Physics Letters* **2004**, 394, 361–365, doi:10.1016/j.cplett.2004.07.021.
133. Baskaran, A.; Kaari, M.; Venugopal, G.; Manikkam, R.; Joseph, J.; Bhaskar, P.V. Anti freeze proteins (Afp): Properties, sources and applications - A review. *Int. J. Biol. Macromol.* **2021**, 189, 292–305, doi:10.1016/j.ijbiomac.2021.08.105.
134. Drori, R.; Davies, P.L.; Braslavsky, I. Experimental correlation between thermal hysteresis activity and the distance between antifreeze proteins on an ice surface. *RSC Adv.* **2015**, 5, 7848–7853, doi:10.1039/C4RA12638F.
135. Vorontsov, D.A.; Sazaki, G.; Furukawa, Y.; Titaeva, E.K.; Kim, E.L. Adsorption Kinetics of Type-III Antifreeze Protein on Ice Crystal Surfaces. *Langmuir : the ACS journal of surfaces and colloids* **2023**, 39, 8612–8622, doi:10.1021/acs.langmuir.3c00299.
136. Gaede-Koehler, A.; Kreider, A.; Canfield, P.; Kleemeier, M.; Grunwald, I. Direct measurement of the thermal hysteresis of antifreeze proteins (AFPs) using sonocrystallization. *Anal. Chem.* **2012**, 84, 10229–10235, doi:10.1021/ac301946w.
137. Tyshenko, M.G.; Doucet, D.; Davies, P.L.; Walker, V.K. The antifreeze potential of the spruce budworm thermal hysteresis protein. *Nat. Biotechnol.* **1997**, 15, 887–890, doi:10.1038/nbt0997-887.
138. Drori, R.; Celik, Y.; Davies, P.L.; Braslavsky, I. Ice-binding proteins that accumulate on different ice crystal planes produce distinct thermal hysteresis dynamics. *J. R. Soc. Interface* **2014**, 11, 20140526, doi:10.1098/rsif.2014.0526.

139. Sun, X.; Griffith, M.; Pasternak, J.J.; Glick, B.R. Low temperature growth, freezing survival, and production of antifreeze protein by the plant growth promoting rhizobacterium Pseudomonas putida GR12-2. *Can. J. Microbiol.* **1995**, 41, 776–784, doi:10.1139/m95-107.
140. Chen, X.; Wu, J.; Cai, X.; Wang, S. Production, structure-function relationships, mechanisms, and applications of antifreeze peptides. *Comp Rev Food Sci Food Safe* **2021**, 20, 542–562, doi:10.1111/1541-4337.12655.
141. Fomich, M.; Día, V.P.; Premadasa, U.I.; Doughty, B.; Krishnan, H.B.; Wang, T. Ice Recrystallization Inhibition Activity of Soy Protein Hydrolysates. *J. Agric. Food Chem.* **2023**, 71, 11587–11598, doi:10.1021/acs.jafc.2c08701.
142. Gaukel, V. Verfahrenstechnische Aspekte der Produktgestaltung am Beispiel ausgewählter Lebensmittelverarbeitungsprozesse. *Karlsruher Institut für Technologie (KIT)* **2021** KITopen-ID: 1000135539.
143. Olijve, L.L.C.; Meister, K.; DeVries, A.L.; Duman, J.G.; Guo, S.; Bakker, H.J.; Voets, I.K. Blocking rapid ice crystal growth through nonbasal plane adsorption of antifreeze proteins. *Proceedings of the National Academy of Sciences of the United States of America* **2016**, 113, 3740–3745, doi:10.1073/pnas.1524109113.
144. Bar-Dolev, M.; Celik, Y.; Wettlaufer, J.S.; Davies, P.L.; Braslavsky, I. New insights into ice growth and melting modifications by antifreeze proteins. *J. R. Soc. Interface* **2012**, 9, 3249–3259, doi:10.1098/rsif.2012.0388.
145. Diao, Y.; Hao, T.; Liu, X.; Yang, H. Advances in single ice crystal shaping materials: From nature to synthesis and applications in cryopreservation. *Acta Biomaterialia* **2024**, 174, 49–68, doi:10.1016/j.actbio.2023.11.035.
146. Sun, X.; Guo, R.; Zhan, T.; Kou, Y.; Ma, X.; Song, H.; Song, L.; Li, X.; Zhang, H.; Xie, F.; et al. Self-assembly of tamarind seed polysaccharide via enzymatic depolymerization and degalactosylation enhanced ice recrystallization inhibition activity. *Int. J. Biol. Macromol.* **2023**, 252, 126352, doi:10.1016/j.ijbiomac.2023.126352.
147. Yu, S.O.; Brown, A.; Middleton, A.J.; Tomczak, M.M.; Walker, V.K.; Davies, P.L. Ice restructuring inhibition activities in antifreeze proteins with distinct differences in thermal hysteresis. *Cryobiology* **2010**, 61, 327–334, doi:10.1016/j.cryobiol.2010.10.158.
148. Urrutia, M.E.; Duman, J.G.; Knight, C.A. Plant thermal hysteresis proteins. *Biochim. Biophys. Acta* **1992**, 1121, 199–206, doi:10.1016/0167-4838(92)90355-H.

149. Gruneberg, A.K.; Graham, L.A.; Eves, R.; Agrawal, P.; Oleschuk, R.D.; Davies, P.L. Ice recrystallization inhibition activity varies with ice-binding protein type and does not correlate with thermal hysteresis. *Cryobiology* **2021**, 99, 28–39, doi:10.1016/j.cryobiol.2021.01.017.
150. Białkowska, A.; Majewska, E.; Olczak, A.; Twarda-Clapa, A. Ice Binding Proteins: Diverse Biological Roles and Applications in Different Types of Industry. *Biomolecules* **2020**, 10, doi:10.3390/biom10020274.
151. DeVries, A.L.; Wohlschlag, D.E. Freezing resistance in some Antarctic fishes. *Science* **1969**, 163, 1073–1075, doi:10.1126/science.163.3871.1073.
152. Bouvet, V.; Ben, R.N. Antifreeze glycoproteins: structure, conformation, and biological applications. *Cell Biochem Biophys* **2003**, 39, 133–144, doi:10.1385/CBB:39:2:133.
153. Barrett, J. Thermal hysteresis proteins. *The International Journal of Biochemistry & Cell Biology* **2001**, 33, 105–117, doi:10.1016/S1357-2725(00)00083-2.
154. Clarke, C.J.; Buckley, S.L.; Lindner, N. Ice structuring proteins - a new name for antifreeze proteins. *Cryo Letters* **2002**, 23, 89–92.
155. Lukas, M.; Schwidetzky, R.; Eufemio, R.J.; Bonn, M.; Meister, K. Toward Understanding Bacterial Ice Nucleation. *The journal of physical chemistry. B* **2022**, 126, 1861–1867, doi:10.1021/acs.jpcb.1c09342.
156. DeVries, A.L. Fish Antifreeze Proteins. In Antifreeze Proteins Volume 1: Environment, Systematics and Evolution, 1st ed. 2020; Ramløv, H., Friis, D.S., *Eds.; Springer International Publishing; Imprint Springer: Cham*, **2020**; pp 85–129, ISBN 978-3-030-41929-5.
157. Biggar, K.K.; Kotani, E.; Furusawa, T.; Storey, K.B. Expression of freeze-responsive proteins, Fr10 and Li16, from freeze-tolerant frogs enhances freezing survival of BmN insect cells. *FASEB journal : official publication of the Federation of American Societies for Experimental Biology* **2013**, 27, 3376–3383, doi:10.1096/fj.13-230573.
158. Uko, M.P.; Umana, S.I.; Iwatt, I.J.; Udoekong, N.S.; Mgbechidinma, C.L.; Adie, F.U.; Akan, O.D. Microbial ice-binding structures: A review of their applications. *Int. J. Biol. Macromol.* **2024**, 275, 133670, doi:10.1016/j.ijbiomac.2024.133670.
159. Bredow, M.; Walker, V.K. Ice-Binding Proteins in Plants. *Front. Plant Sci.* **2017**, 8, 2153, doi:10.3389/fpls.2017.02153.
160. Duman, J.G.; Newton, S.S. Insect Antifreeze Proteins. In Antifreeze Proteins Volume 1: Environment, Systematics and Evolution, 1st ed. 2020; Ramløv, H., Friis, D.S., *Eds.; Springer International Publishing; Imprint Springer: Cham*, **2020**; pp 131–187, ISBN 978-3-030-41929-5.

161. Scholander, P.F.; van Dam, L.; Kanwisher, J.W.; Hammel, H.T.; Gordon, M.S. Supercooling and osmoregulation in arctic fish. *J. Cell. Comp. Physiol.* **1957**, 49, 5–24, doi:10.1002/jcp.1030490103.
162. Duman, J.G.; Xu, L.; Neven, L.G.; Tursman, D.; Wu, D.W. Hemolymph Proteins Involved in Insect Subzero-Temperature Tolerance: Ice Nucleators and Antifreeze Proteins. In Insects at Low Temperature; Lee, R., *Ed.; Springer: New York*, NY, **1991**; pp 94–127, ISBN 978-1-4757-0190-6.
163. Pearce, R. Plant Freezing and Damage. *Annals of Botany* **2001**, 87, 417–424, doi:10.1006/anbo.2000.1352.
164. Murray, B.J.; O'Sullivan, D.; Atkinson, J.D.; Webb, M.E. Ice nucleation by particles immersed in supercooled cloud droplets. *Chem. Soc. Rev.* **2012**, 41, 6519–6554, doi:10.1039/C2CS35200A.
165. Lorv, J.S.H.; Rose, D.R.; Glick, B.R. Bacterial ice crystal controlling proteins. *Scientifica* **2014**, 2014, 976895, doi:10.1155/2014/976895.
166. Lindow, S.E. The Role of Bacterial ICE Nucleation in Frost Injury to Plants. *Annu. Rev. Phytopathol.* **1983**, 21, 363–384, doi:10.1146/annurev.py.21.090183.002051.
167. Cochet, N.; Widehem, P. Ice crystallization by Pseudomonas syringae. *Appl Microbiol Biotechnol* **2000**, 54, 153–161, doi:10.1007/s002530000377.
168. Lindow, S.E.; Arny, D.C.; Upper, C.D. Bacterial ice nucleation: a factor in frost injury to plants. *Plant Physiol* **1982**, 70, 1084–1089, doi:10.1104/pp.70.4.1084.
169. Amato, P.; Joly, M.; Schaupp, C.; Attard, E.; Möhler, O.; Morris, C.E.; Brunet, Y.; Delort, A.-M. Survival and ice nucleation activity of bacteria as aerosols in a cloud simulation chamber. *Atmos. Chem. Phys.* **2015**, 15, 6455–6465, doi:10.5194/acp-15-6455-2015.
170. Pöschl, U.; Martin, S.T.; Sinha, B.; Chen, Q.; Gunthe, S.S.; Huffman, J.A.; Borrmann, S.; Farmer, D.K.; Garland, R.M.; Helas, G.; et al. Rainforest Aerosols as Biogenic Nuclei of Clouds and Precipitation in the Amazon. *American Association for the Advancement of Science [Online]*, September 17, **2010**. Available online: https://www.science.org/doi/10.1126/science.1191056?url_ver=Z39.88-2003&rfr_id=ori:rid:crossref.org&rfr_dat=cr_pub%20%200pubmed (accessed on 14 November 2024).
171. DeLeon-Rodriguez, N.; Lathem, T.L.; Rodriguez-R, L.M.; Barazesh, J.M.; Anderson, B.E.; Beyersdorf, A.J.; Ziemba, L.D.; Bergin, M.; Nenes, A.; Konstantinidis, K.T. Microbiome of the upper troposphere: species composition and prevalence, effects of tropical storms, and atmospheric implications. *Proceedings of the National Academy of Sciences of the United States of America* **2013**, 110, 2575–2580, doi:10.1073/pnas.1212089110.

172. Fröhlich-Nowoisky, J.; Kampf, C.J.; Weber, B.; Huffman, J.A.; Pöhlker, C.; Andreae, M.O.; Lang-Yona, N.; Burrows, S.M.; Gunthe, S.S.; Elbert, W.; et al. Bioaerosols in the Earth system: Climate, health, and ecosystem interactions. *Atmospheric Research* **2016**, 182, 346–376, doi:10.1016/j.atmosres.2016.07.018.
173. Roeters, S.J.; Golbek, T.W.; Bregnhøj, M.; Drace, T.; Alamdari, S.; Roseboom, W.; Kramer, G.; Šantl-Temkiv, T.; Finster, K.; Pfaendtner, J.; et al. Ice-nucleating proteins are activated by low temperatures to control the structure of interfacial water. *Nat Commun* **2021**, 12, 1183, doi:10.1038/s41467-021-21349-3.
174. Hartmann, S.; Ling, M.; Dreyer, L.S.A.; Zipori, A.; Finster, K.; Grawe, S.; Jensen, L.Z.; Borck, S.; Reicher, N.; Drace, T.; et al. Structure and Protein-Protein Interactions of Ice Nucleation Proteins Drive Their Activity. *Frontiers in Microbiology* **2022**, 13, 872306, doi:10.3389/fmicb.2022.872306.
175. Garnham, C.P.; Campbell, R.L.; Davies, P.L. Anchored clathrate waters bind antifreeze proteins to ice. *Proceedings of the National Academy of Sciences of the United States of America* **2011**, 108, 7363–7367, doi:10.1073/pnas.1100429108.
176. Krembs, C.; Eicken, H.; Junge, K.; Deming, J. High concentrations of exopolymeric substances in Arctic winter sea ice: implications for the polar ocean carbon cycle and cryoprotection of diatoms. *Deep Sea Research Part I: Oceanographic Research Papers* **2002**, 49, 2163–2181, doi:10.1016/S0967-0637(02)00122-X.
177. Deming, J.W. Psychrophiles and polar regions. *Current Opinion in Microbiology* **2002**, 5, 301–309, doi:10.1016/S1369-5274(02)00329-6.
178. Janech, M.G.; Krell, A.; Mock, T.; Kang, J.-S.; Raymond, J.A. Ice-binding proteins from sea ice diatoms (Bacillariophyceae) 1. *Journal of Phycology* **2006**, 42, 410 – 416, doi:10.1111/j.1529-8817.2006.00208.x.
179. Raymond, J.A.; Fritsen, C.; Shen, K. An ice-binding protein from an Antarctic sea ice bacterium. *FEMS Microbiol Ecol* **2007**, 61, 214–221, doi:10.1111/j.1574-6941.2007.00345.x.
180. Guo, S.; Garnham, C.P.; Whitney, J.C.; Graham, L.A.; Davies, P.L. Re-evaluation of a bacterial antifreeze protein as an adhesin with ice-binding activity. *PLOS ONE* **2012**, 7, e48805, doi:10.1371/journal.pone.0048805.
181. DeLuca, C.I.; Davies, P.L.; Ye, Q.; Jia, Z. The effects of steric mutations on the structure of type III antifreeze protein and its interaction with ice. *Journal of Molecular Biology* **1998**, 275, 515–525, doi:10.1006/jmbi.1997.1482.

182. Yang, D.S.; Hon, W.C.; Bubanko, S.; Xue, Y.; Seetharaman, J.; Hew, C.L.; Sicheri, F. Identification of the ice-binding surface on a type III antifreeze protein with a "flatness function" algorithm. *Biophysical Journal* **1998**, 74, 2142–2151, doi:10.1016/S0006-3495(98)77923-8.

183. Jia, Z.; Davies, P.L. Antifreeze proteins: an unusual receptor-ligand interaction. Trends in Biochemical Sciences 2002, 27, 101–106, doi:10.1016/S0968-0004(01)02028-X.

184. Dalal, P.; Sönnichsen, F.D. Source of the ice-binding specificity of antifreeze protein type I. *J. Chem. Inf. Comput. Sci.* **2000**, 40, 1276–1284, doi:10.1021/ci000449b.

185. DeVries, A.L. Antifreeze peptides and glycopeptides in cold-water fishes. *Annual Review of Physiology* **1983**, 45, 245–260, doi:10.1146/annurev.ph.45.030183.001333.

186. Haymet, A.D.; Ward, L.G.; Harding, M.M.; Knight, C.A. Valine substituted winter flounder 'antifreeze': preservation of ice growth hysteresis. *FEBS Letters* **1998**, 430, 301–306, doi:10.1016/S0014-5793(98)00652-8.

187. Antson, A.A.; Smith, D.J.; Roper, D.I.; Lewis, S.; Caves, L.S.; Verma, C.S.; Buckley, S.L.; Lillford, P.J.; Hubbard, R.E. Understanding the mechanism of ice binding by type III antifreeze proteins. *Journal of Molecular Biology* **2001**, 305, 875–889, doi:10.1006/jmbi.2000.4336.

188. Sönnichsen, F.D.; DeLuca, C.I.; Davies, P.L.; Sykes, B.D. Refined solution structure of type III antifreeze protein: hydrophobic groups may be involved in the energetics of the protein-ice interaction. *Structure* **1996**, 4, 1325–1337, doi:10.1016/S0969-2126(96)00140-2.

189. Leinala, E.K.; Davies, P.L.; Doucet, D.; Tyshenko, M.G.; Walker, V.K.; Jia, Z. A beta-helical antifreeze protein isoform with increased activity. Structural and functional insights. *Journal of Biological Chemistry* **2002**, 277, 33349–33352, doi:10.1074/jbc.M205575200.

190. Graether, S.P.; Kuiper, M.J.; Gagné, S.M.; Walker, V.K.; Jia, Z.; Sykes, B.D.; Davies, P.L. Beta-helix structure and ice-binding properties of a hyperactive antifreeze protein from an insect. *Nature* **2000**, 406, 325–328, doi:10.1038/35018610.

191. Liou, Y.C.; Tocilj, A.; Davies, P.L.; Jia, Z. Mimicry of ice structure by surface hydroxyls and water of a beta-helix antifreeze protein. *Nature* **2000**, 406, 322–324, doi:10.1038/35018604.

192. Sun, T.; Lin, F.-H.; Campbell, R.L.; Allingham, J.S.; Davies, P.L. An antifreeze protein folds with an interior network of more than 400 semi-clathrate waters. *Science* **2014**, 343, 795–798, doi:10.1126/science.1247407.

193. Shi, J.; Fulford, M.; Li, H.; Marzook, M.; Reisjalali, M.; Salvalaglio, M.; Molteni, C. Investigating the quasi-liquid layer on ice surfaces: a comparison of order parameters. *Phys. Chem. Chem. Phys.* **2022**, 24, 12476–12487, doi:10.1039/D2CP00752E.

194. Meister, K.; Strazdaite, S.; DeVries, A.L.; Lotze, S.; Olijve, L.L.C.; Voets, I.K.; Bakker, H.J. Observation of ice-like water layers at an aqueous protein surface. *Proceedings of the National Academy of Sciences of the United States of America* **2014**, 111, 17732–17736, doi:10.1073/pnas.1414188111.

195. Midya, U.S.; Bandyopadhyay, S. Hydration behavior at the ice-binding surface of the Tenebrio molitor antifreeze protein. *The journal of physical chemistry. B* **2014**, 118, 4743–4752, doi:10.1021/jp412528b.

196. Nutt, D.R.; Smith, J.C. Dual function of the hydration layer around an antifreeze protein revealed by atomistic molecular dynamics simulations. *Journal of the American Chemical Society* **2008**, 130, 13066–13073, doi:10.1021/ja8034027.

197. Ebbinghaus, S.; Meister, K.; Born, B.; DeVries, A.L.; Gruebele, M.; Havenith, M. Antifreeze glycoprotein activity correlates with long-range protein-water dynamics. *Journal of the American Chemical Society* **2010**, 132, 12210–12211, doi:10.1021/ja1051632.

198. Hudait, A.; Moberg, D.R.; Qiu, Y.; Odendahl, N.; Paesani, F.; Molinero, V. Preordering of water is not needed for ice recognition by hyperactive antifreeze proteins. *Proceedings of the National Academy of Sciences of the United States of America* **2018**, 115, 8266–8271, doi:10.1073/pnas.1806996115.

199. Scholl, C.L.; Davies, P.L. Protein engineering of antifreeze proteins reveals that their activity scales with the area of the ice-binding site. *FEBS Letters* **2023**, 597, 538–546, doi:10.1002/1873-3468.14552.

200. Celik, Y.; Drori, R.; Pertaya-Braun, N.; Altan, A.; Barton, T.; Bar-Dolev, M.; Groisman, A.; Davies, P.L.; Braslavsky, I. Microfluidic experiments reveal that antifreeze proteins bound to ice crystals suffice to prevent their growth. *Proceedings of the National Academy of Sciences of the United States of America* **2013**, 110, 1309–1314, doi:10.1073/pnas.1213603110.

201. Drori, R.; Davies, P.L.; Braslavsky, I. When are antifreeze proteins in solution essential for ice growth inhibition? *Langmuir : the ACS journal of surfaces and colloids* **2015**, 31, 5805–5811, doi:10.1021/acs.langmuir.5b00345.

202. Meister, K.; DeVries, A.L.; Bakker, H.J.; Drori, R. Antifreeze Glycoproteins Bind Irreversibly to Ice. *Journal of the American Chemical Society* **2018**, 140, 9365–9368, doi:10.1021/jacs.8b04966.

203. Mochizuki, K.; Molinero, V. Antifreeze Glycoproteins Bind Reversibly to Ice via Hydrophobic Groups. *Journal of the American Chemical Society* **2018**, 140, 4803–4811, doi:10.1021/jacs.7b13630.
204. Sun, Y.; Giubertoni, G.; Bakker, H.J.; Liu, J.; Wagner, M.; Ng, D.Y.W.; DeVries, A.L.; Meister, K. Disaccharide Residues are Required for Native Antifreeze Glycoprotein Activity. *Biomacromolecules* **2021**, 22, 2595–2603, doi:10.1021/acs.biomac.1c00313.
205. Zhang, W.; Liu, H.; Fu, H.; Shao, X.; Cai, W. Revealing the Mechanism of Irreversible Binding of Antifreeze Glycoproteins to Ice. *The journal of physical chemistry. B* **2022**, 126, 10637–10645, doi:10.1021/acs.jpcb.2c06183.
206. Tas, R.P.; Hendrix, Marco M. R. M.; Voets, I.K. Nanoscopy of single antifreeze proteins reveals that reversible ice binding is sufficient for ice recrystallization inhibition but not thermal hysteresis. *Proceedings of the National Academy of Sciences of the United States of America* **2023**, 120, e2212456120, doi:10.1073/pnas.2212456120.
207. Friis, D.S.; Ramløv, H. Mutational Studies on Antifreeze Proteins. In Antifreeze Proteins Volume 2: Biochemistry, Molecular Biology and Applications, 1st ed. 2020; Ramløv, H., Friis, D.S., *Eds.; Springer International Publishing; Imprint Springer: Cham*, **2020**; pp 327–354, ISBN 978-3-030-41948-6.
208. Walters, K.R.; Serianni, A.S.; Voituron, Y.; Sformo, T.; Barnes, B.M.; Duman, J.G. A thermal hysteresis-producing xylomannan glycolipid antifreeze associated with cold tolerance is found in diverse taxa. *J Comp Physiol B* **2011**, 181, 631–640, doi:10.1007/s00360-011-0552-8.
209. Walters, K.R.; Serianni, A.S.; Sformo, T.; Barnes, B.M.; Duman, J.G. A nonprotein thermal hysteresis-producing xylomannan antifreeze in the freeze-tolerant Alaskan beetle Upis ceramboides. *Proceedings of the National Academy of Sciences of the United States of America* **2009**, 106, 20210–20215, doi:10.1073/pnas.0909872106.
210. Deville, S.; Viazzi, C.; Guizard, C. Ice-structuring mechanism for zirconium acetate. *Langmuir : the ACS journal of surfaces and colloids* **2012**, 28, 14892–14898, doi:10.1021/la302275d.
211. Geng, H.; Liu, X.; Shi, G.; Bai, G.; Ma, J.; Chen, J.; Wu, Z.; Song, Y.; Fang, H.; Wang, J. Graphene Oxide Restricts Growth and Recrystallization of Ice Crystals. *Angewandte Chemie* **2017**, 129, 1017–1021, doi:10.1002/ange.201609230.
212. Inada, T.; Lu, S.-S. Inhibition of Recrystallization of Ice Grains by Adsorption of Poly(Vinyl Alcohol) onto Ice Surfaces. *Crystal Growth & Design* **2003**, 3, 747–752, doi:10.1021/cg0340300.

213. Naullage, P.M.; Lupi, L.; Molinero, V. Molecular Recognition of Ice by Fully Flexible Molecules. *J. Phys. Chem. C* **2017**, 121, 26949–26957, doi:10.1021/acs.jpcc.7b10265.
214. Bachtiger, F.; Congdon, T.R.; Stubbs, C.; Gibson, M.I.; Sosso, G.C. The atomistic details of the ice recrystallisation inhibition activity of PVA. *Nat Commun* **2021**, 12, 1323, doi:10.1038/s41467-021-21717-z.
215. Congdon, T.; Notman, R.; Gibson, M.I. Antifreeze (glyco)protein mimetic behavior of poly(vinyl alcohol): detailed structure ice recrystallization inhibition activity study. *Biomacromolecules* **2013**, 14, 1578–1586, doi:10.1021/bm400217j.
216. Congdon, T.R.; Notman, R.; Gibson, M.I. Influence of Block Copolymerization on the Antifreeze Protein Mimetic Ice Recrystallization Inhibition Activity of Poly(vinyl alcohol). *Biomacromolecules* **2016**, 17, 3033–3039, doi:10.1021/acs.biomac.6b00915.
217. Naullage, P.M.; Molinero, V. Slow Propagation of Ice Binding Limits the Ice-Recrystallization Inhibition Efficiency of PVA and Other Flexible Polymers. *Journal of the American Chemical Society* **2020**, 142, 4356–4366, doi:10.1021/jacs.9b12943.
218. Penders, B. Cool and Safe. Bulletin of Science, *Technology & Society* **2011**, 31, 472–481, doi:10.1177/0270467611422836.
219. Safety of 'Ice Structuring Protein (ISP) - Scientific Opinion of the Panel on Dietetic Products, Nutrition and Allergies and of the Panel on Genetically Modified Organisms. *EFSA Journal* **2008**, 6, 768, doi:10.2903/j.efsa.2008.768.
220. Regand, A.; Goff, H.D. Ice recrystallization inhibition in ice cream as affected by ice structuring proteins from winter wheat grass. *Journal of Dairy Science* **2006**, 89, 49–57, doi:10.3168/jds.S0022-0302(06)72068-9.
221. Payne, S.R.; Sandford, D.; Harris, A.; Young, O.A. The effects of antifreeze proteins on chilled and frozen meat. *Meat Science* **1994**, 37, 429–438, doi:10.1016/0309-1740(94)90058-2.
222. Feng, X.; Yu, X.; Yang, Y.; Tang, X. Improving the freeze-thaw stability of fish myofibrils and myofibrillar protein gels: Current methods and future perspectives. *Food Hydrocolloids* **2023**, 144, 109041, doi:10.1016/j.foodhyd.2023.109041.
223. Zhang, B.; Yang, H.-C.; Tang, H.; Hao, G.-J.; Zhang, Y.-Y.; Deng, S.-G. Insights into Cryoprotective Roles of Carrageenan Oligosaccharides in Peeled Whiteleg Shrimp (Litopenaeus vannamei) during Frozen Storage. *J. Agric. Food Chem.* **2017**, 65, 1792–1801, doi:10.1021/acs.jafc.6b05651.

224. Zhang, C.; Zhang, H.; Wang, L.; Guo, X. Effect of carrot (Daucus carota) antifreeze proteins on texture properties of frozen dough and volatile compounds of crumb. *LWT - Food Science and Technology* **2008**, 41, 1029–1036, doi:10.1016/j.lwt.2007.07.010.
225. Xu, H.-N.; Huang, W.; Jia, C.; Kim, Y.; Liu, H. Evaluation of water holding capacity and breadmaking properties for frozen dough containing ice structuring proteins from winter wheat. *Journal of Cereal Science* **2009**, 49, 250–253, doi:10.1016/j.jcs.2008.10.009.
226. Zhu, B.; Xiong, A.-S.; Peng, R.-H.; Xu, J.; Jin, X.-F.; Meng, X.-R.; Yao, Q.-H. Over-expression of ThpI from Choristoneura fumiferana enhances tolerance to cold in Arabidopsis. *Mol Biol Rep* **2010**, 37, 961–966, doi:10.1007/s11033-009-9759-0.
227. Lin, X.; Wisniewski, M.E.; Duman, J.G. Expression of Two Self-enhancing Antifreeze Proteins from the Beetle Dendroides canadensis in Arabidopsis thaliana. *Plant Mol Biol Rep* **2011**, 29, 802–813, doi:10.1007/s11105-011-0287-4.
228. van Eenennaam, A.L.; Muir, W.M. Transgenic salmon: a final leap to the grocery shelf? *Nat. Biotechnol.* **2011**, 29, 706–710, doi:10.1038/nbt.1938.
229. Qadeer, S.; Khan, M.A.; Ansari, M.S.; Rakha, B.A.; Ejaz, R.; Iqbal, R.; Younis, M.; Ullah, N.; DeVries, A.L.; Akhter, S. Efficiency of antifreeze glycoproteins for cryopreservation of Nili-Ravi (Bubalus bubalis) buffalo bull sperm. *Animal Reproduction Science* **2015**, 157, 56–62, doi:10.1016/j.anireprosci.2015.03.015.
230. Jo, J.W.; Jee, B.C.; Lee, J.R.; Suh, C.S. Effect of antifreeze protein supplementation in vitrification medium on mouse oocyte developmental competence. *Fertility and Sterility* **2011**, 96, 1239–1245, doi:10.1016/j.fertnstert.2011.08.023.
231. Nishijima, K.; Tanaka, M.; Sakai, Y.; Koshimoto, C.; Morimoto, M.; Watanabe, T.; Fan, J.; Kitajima, S. Effects of type III antifreeze protein on sperm and embryo cryopreservation in rabbit. *Cryobiology* **2014**, 69, 22–25, doi:10.1016/j.cryobiol.2014.04.014.
232. Capicciotti, C.J.; Kurach, J.D.R.; Turner, T.R.; Mancini, R.S.; Acker, J.P.; Ben, R.N. Small molecule ice recrystallization inhibitors enable freezing of human red blood cells with reduced glycerol concentrations. *Sci Rep* **2015**, 5, 9692, doi:10.1038/srep09692.
233. Deller, R.C.; Vatish, M.; Mitchell, D.A.; Gibson, M.I. Glycerol-Free Cryopreservation of Red Blood Cells Enabled by Ice-Recrystallization-Inhibiting Polymers. *ACS Biomater. Sci. Eng.* **2015**, 1, 789–794, doi:10.1021/acsbiomaterials.5b00162.
234. Chao, H.; Davies, P.L.; Carpenter, J.F. Effects of antifreeze proteins on red blood cell survival during cryopreservation. *J Exp Biol* **1996**, 199, 2071–2076, doi:10.1242/jeb.199.9.2071.

235. Amir, G.; Rubinsky, B.; Basheer, S.Y.; Horowitz, L.; Jonathan, L.; Feinberg, M.S.; Smolinsky, A.K.; Lavee, J. Improved viability and reduced apoptosis in sub-zero 21-hour preservation of transplanted rat hearts using anti-freeze proteins. *J. Heart Lung Transplant.* **2005**, 24, 1915–1929, doi:10.1016/j.healun.2004.11.003.
236. Ideta, A.; Aoyagi, Y.; Tsuchiya, K.; Nakamura, Y.; Hayama, K.; Shirasawa, A.; Sakaguchi, K.; Tominaga, N.; Nishimiya, Y.; Tsuda, S. Prolonging hypothermic storage (4 C) of bovine embryos with fish antifreeze protein. *J. Reprod. Dev.* **2015**, 61, 1–6, doi:10.1262/jrd.2014-073.
237. Rubinsky, L.; Raichman, N.; Lavee, J.; Frenk, H.; Ben-Jacob, E.; Bickler, P.E. Antifreeze protein suppresses spontaneous neural activity and protects neurons from hypothermia/re-warming injury. *Neuroscience Research* **2010**, 67, 256–259, doi:10.1016/j.neures.2010.04.004.
238. Koushafar, H.; Rubinsky, B. Effect of antifreeze proteins on frozen primary prostatic adenocarcinoma cells. Urology 1997, 49, 421–425, doi:10.1016/S0090-4295(96)00572-9.
239. Bragg, M.; Hutchison, T.; Merret, J. Effect of ice accretion on aircraft flight dynamics. In 38th Aerospace Sciences Meeting and Exhibit. *38th Aerospace Sciences Meeting and Exhibit, Reno,NV,U.S.A*, 10 January 2000 - 13 January **2000**; American Institute of Aeronautics and Astronautics: Reston, Virigina, 01102000.
240. Titov, D.E.; Ugarov, G.G.; Soshinov, A.G. Monitoring the Intensity of Ice Formation on Overhead Electric Power Lines and Contact Networks. *Power Technol Eng* **2015**, 49, 78–82, doi:10.1007/s10749-015-0578-2.
241. Laforte, J.L.; Allaire, M.A.; Laflamme, J. State-of-the-art on power line de-icing. *Atmospheric Research* **1998**, 46, 143–158, doi:10.1016/S0169-8095(97)00057-4.
242. Esser-Kahn, A.P.; Trang, V.; Francis, M.B. Incorporation of antifreeze proteins into polymer coatings using site-selective bioconjugation. *Journal of the American Chemical Society* **2010**, 132, 13264–13269, doi:10.1021/ja103038p.
243. Gwak, Y.; Park, J.; Kim, M.; Kim, H.S.; Kwon, M.J.; Oh, S.J.; Kim, Y.-P.; Jin, E. Creating Anti-icing Surfaces via the Direct Immobilization of Antifreeze Proteins on Aluminum. *Sci Rep* **2015**, 5, 12019, doi:10.1038/srep12019.
244. Qu, Z.; Guo, S.; Sproncken, C.C.M.; Surís-Valls, R.; Yu, Q.; Voets, I.K. Enhancing the Freeze-Thaw Durability of Concrete through Ice Recrystallization Inhibition by Poly(vinyl alcohol). *ACS Omega* **2020**, 5, 12825–12831, doi:10.1021/acsomega.0c00555.
245. Stephen, A.M. Food Polysaccharides and Their Applications, *2nd ed.; Taylor and Francis: Hoboken*, **2010**, ISBN 9781420015164.

246. Slaughter, B.V.; Khurshid, S.S.; Fisher, O.Z.; Khademhosseini, A.; Peppas, N.A. Hydrogels in regenerative medicine. *Advanced Materials* **2009**, 21, 3307–3329, doi:10.1002/adma.200802106.
247. Richbourg, N.R.; Peppas, N.A. The swollen polymer network hypothesis: Quantitative models of hydrogel swelling, stiffness, and solute transport. *Progress in Polymer Science* **2020**, 105, 101243, doi:10.1016/j.progpolymsci.2020.101243.
248. Peppas, N.A.; Hilt, J.Z.; Khademhosseini, A.; Langer, R. Hydrogels in Biology and Medicine: From Molecular Principles to Bionanotechnology. *Advanced Materials* **2006**, 18, 1345–1360, doi:10.1002/adma.200501612.
249. Udo, T.; Mummaleti, G.; Mohan, A.; Singh, R.K.; Kong, F. Current and emerging applications of carrageenan in the food industry. *Food Res. Int.* **2023**, 173, 113369, doi:10.1016/j.foodres.2023.113369.
250. Campo, V.L.; Kawano, D.F.; Da Silva, D.B.; Carvalho, I. Carrageenans: Biological properties, chemical modifications and structural analysis – A review. *Carbohydrate polymers* **2009**, 77, 167–180, doi:10.1016/j.carbpol.2009.01.020.
251. Cheng, C.; Chen, S.; Su, J.; Zhu, M.; Zhou, M.; Chen, T.; Han, Y. Recent advances in carrageenan-based films for food packaging applications. *Front. Nutr.* **2022**, 9, 1004588, doi:10.3389/fnut.2022.1004588.
252. Hemilä, H.; Chalker, E. Carrageenan nasal spray may double the rate of recovery from coronavirus and influenza virus infections: Re-analysis of randomized trial data. *Pharmacology Res & Perspec* **2021**, 9, doi:10.1002/prp2.810.
253. Souza, H.K.S.; Kraiem, W.; Ben Yahia, A.; Aschi, A.; Hilliou, L. From Seaweeds to Hydrogels: Recent Progress in Kappa-2 Carrageenans. *Materials* **2023**, 16, 5387, doi:10.3390/ma16155387.
254. Porse, H.; Rudolph, B. The seaweed hydrocolloid industry: 2016 updates, requirements, and outlook. *J Appl Phycol* **2017**, 29, 2187–2200, doi:10.1007/s10811-017-1144-0.
255. Knutsen, S.H.; Myslabodski, D.E.; Larsen, B.; Usov, A.I. A Modified System of Nomenclature for Red Algal Galactans. 1437-4323 **1994**, 37, 163–170, doi:10.1515/botm.1994.37.2.163.
256. Jouanneau, D.; Guibet, M.; Boulenguer, P.; Mazoyer, J.; Smietana, M.; Helbert, W. New insights into the structure of hybrid κ-/μ-carrageenan and its alkaline conversion. *Food Hydrocolloids* **2010**, 24, 452–461, doi:10.1016/j.foodhyd.2009.11.012.
257. Tuvikene, R.; Truus, K.; Robal, M.; Volobujeva, O.; Mellikov, E.; Pehk, T.; Kollist, A.; Kailas, T.; Vaher, M. The extraction, structure, and gelling properties of hybrid galactan

from the red alga Furcellaria lumbricalis (Baltic Sea, Estonia). *J Appl Phycol* **2010**, 22, 51–63, doi:10.1007/s10811-009-9425-x.

258. Laos, K.; Ring, S.G. Note: Characterisation of furcellaran samples from Estonian Furcellaria lumbricalis (Rhodophyta). *J Appl Phycol* **2005**, 17, 461–464, doi:10.1007/s10811-005-1635-2.
259. Morris, E.R.; REES, D.A.; Robinson, G. Cation-specific aggregation of carrageenan helices: Domain model of polymer gel structure. *Journal of Molecular Biology* **1980**, 138, 349–362, doi:10.1016/0022-2836(80)90291-0.
260. Smidsrød, O.; Grasdalen, H. Some physical properties of carrageenan in solution and gel state. *Carbohydrate polymers* **1982**, 2, 270–272, doi:10.1016/0144-8617(82)90029-7.
261. Funami, T.; Hiroe, M.; Noda, S.; Asai, I.; Ikeda, S.; Nishinari, K. Influence of molecular structure imaged with atomic force microscopy on the rheological behavior of carrageenan aqueous systems in the presence or absence of cations. *Food Hydrocolloids* **2007**, 21, 617–629, doi:10.1016/j.foodhyd.2006.07.013.
262. Meunier, V.; Nicolai, T.; Durand, D. Structure and Kinetics of Aggregating κ-Carrageenan Studied by Light Scattering. *Macromolecules* **2000**, 33, 2497–2504, doi:10.1021/ma991433t.
263. Schefer, L.; Adamcik, J.; Diener, M.; Mezzenga, R. Supramolecular chiral self-assembly and supercoiling behavior of carrageenans at varying salt conditions. *Nanoscale* **2015**, 7, 16182–16188, doi:10.1039/c5nr04525h.
264. Ueda, K.; Itoh, M.; Matsuzaki, Y.; Ochiai, H.; Imamura, A. Observation of the Molecular Weight Change during the Helix−Coil Transition of κ-Carrageenan Measured by the SEC−LALLS Method. *Macromolecules* **1998**, 31, 675–680, doi:10.1021/ma970846w.
265. Takemasa, M.; Nishinari, K. The effect of the linear charge density of carrageenan on the ion binding investigated by differential scanning calorimetry, dc conductivity, and kHz dielectric relaxation. *Colloids and Surfaces B: Biointerfaces* **2004**, 38, 231–240, doi:10.1016/j.colsurfb.2004.02.025.
266. Grasdalen, H.; Smidsroed, O. Iodide-specific formation of .kappa.-carrageenan single helixes. Iodine-127 NMR spectroscopic evidence for selective site binding of iodide anions in the ordered conformation. *Macromolecules* **1981**, 14, 1842–1845, doi:10.1021/ma50007a051.

267. Zhang, W.; Piculell, L.; Nilsson, S. Effects of specific anion binding on the helix-coil transition of lower charged carrageenans. NMR data and conformational equilibria analyzed within the Poisson-Boltzmann cell model. *Macromolecules* **1992**, 25, 6165–6172, doi:10.1021/ma00049a012.

268. Lai, V.; Wong, P.-L.; Lii, C.-Y. Effects of Cation Properties on Sol‐gel Transition and Gel Properties of κ‐carrageenan. *Journal of Food Science* **2000**, 65, 1332‐1337, doi:10.1111/j.1365-2621.2000.tb10607.x.

269. Morris, V.J.; Chilvers, G.R. Rheological studies of specific cation forms of kappa carrageenan gels. *Carbohydrate polymers* **1983**, 3, 129–141, doi:10.1016/0144-8617(83)90003-6.

270. MacArtain, P.; Jacquier, J.; Dawson, K. Physical characteristics of calcium induced κ-carrageenan networks. *Carbohydrate polymers* **2003**, 53, 395–400, doi:10.1016/S0144-8617(03)00120-6.

271. Michel, A.S.; Mestdagh, M.M.; Axelos, M.A. Physico-chemical properties of carrageenan gels in presence of various cations. *Int. J. Biol. Macromol.* **1997**, 21, 195–200, doi:10.1016/S0141-8130(97)00061-5.

272. Watase, M.; Nishinari, K. Effect of alkali metal ions on the viscoelasticity of concentrated kappa-carrageenan and agarose gels. *Rheol Acta* **1982**, 21, 318–324, doi:10.1007/BF01515719.

273. Bhattacharyya, T.; Palla, C.S.; Dethe, D.H.; Joshi, Y.M. Rheological investigation of the network structure in mixed gels of Kappa and Iota Carrageenan. *Food Hydrocolloids* **2024**, 146, 109298, doi:10.1016/j.foodhyd.2023.109298.

274. Bui, V.T.N.T.; Nguyen, B.T.; Nicolai, T.; Renou, F. Mixed iota and kappa carrageenan gels in the presence of both calcium and potassium ions. *Carbohydrate polymers* **2019**, 223, 115107, doi:10.1016/j.carbpol.2019.115107.

275. Parker, A.; Brigand, G.; Miniou, C.; Trespoey, A.; Vallée, P. Rheology and fracture of mixed ι- and κ-carrageenan gels: Two-step gelation. *Carbohydrate polymers* **1993**, 20, 253–262, doi:10.1016/0144-8617(93)90097-N.

276. Rochas, C.; Rinaudo, M.; Landry, S. Relation between the molecular structure and mechanical properties of carrageenan gels. *Carbohydrate polymers* **1989**, 10, 115–127, doi:10.1016/0144-8617(89)90061-1.

277. Rochas, C.; Rinaudo, M.; Landry, S. Role of the molecular weight on the mechanical properties of kappa carrageenan gels. *Carbohydrate polymers* **1990**, 12, 255–266, doi:10.1016/0144-8617(90)90067-3.

278. Meunier, V.; Nicolai, T.; Durand, D.; Parker, A. Light Scattering and Viscoelasticity of Aggregating and Gelling κ-Carrageenan. *Macromolecules* **1999**, 32, 2610–2616, doi:10.1021/ma981319v.
279. MORITAKA, H.; TAKAHASHI, M.; KUBOTA, K. Effects of Cooling Rate and Sodium Chloride on Polysaccharide Gelation. *Food Science and Technology Research* **2007**, 13, 345–350, doi:10.3136/fstr.13.345.
280. van de Velde, F.; Ruiter, G.A. de. Carrageenan. In Biopolymers: Biology, chemistry, biotechnology, applications; Vandamme, E.J., Baets, S. de, Steinbüchel, A., *Eds.; Wiley-VCH: Weinheim*, **2001**, ISBN 9783527302901.
281. Azizi-Lalabadi, M.; Moghaddam, N.R.; Jafari, S.M. 9 - Pasteurization in the food industry. In Thermal Processing of Food Products by Steam and Hot Water: Unit Operations and Processing Equipment in the Food Industry; Jafari, S.M., *Ed.; Elsevier Science & Technology: San Diego,* **2023**; pp 247–273, ISBN 978-0-12-818616-9.
282. Budiaman, E.R.; Fennema, O. Linear Rate of Water Crystallization as Influenced by Temperature of Hydrocolloid Suspensions. *Journal of Dairy Science* **1987**, 70, 534–546, doi:10.3168/jds.S0022-0302(87)80038-3.
283. Kumar, G.; Mishra, R.R.; Verma, A. Introduction to Molecular Dynamics Simulations. Forcefields for Atomistic-Scale Simulations. *Materials and Applications* **2022**, 99, 1–19, doi:10.1007/978-981-19-3092-8_1.
284. Zimmerman, M.I.; Porter, J.R.; Ward, M.D.; Singh, S.; Vithani, N.; Meller, A.; Mallimadugula, U.L.; Kuhn, C.E.; Borowsky, J.H.; Wiewiora, R.P.; et al. SARS-CoV-2 simulations go exascale to predict dramatic spike opening and cryptic pockets across the proteome. *Nat. Chem.* **2021**, 13, 651–659, doi:10.1038/s41557-021-00707-0.
285. Arantes, P.R.; Saha, A.; Palermo, G. Fighting COVID-19 Using Molecular Dynamics Simulations. *ACS Cent. Sci.* **2020**, 6, 1654–1656, doi:10.1021/acscentsci.0c01236.
286. Padhi, A.K.; Rath, S.L.; Tripathi, T. Accelerating COVID-19 Research Using Molecular Dynamics Simulation. *The journal of physical chemistry. B* **2021**, 125, 9078–9091, doi:10.1021/acs.jpcb.1c04556.
287. Harbison, A.M.; Fogarty, C.A.; Phung, T.K.; Satheesan, A.; Schulz, B.L.; Fadda, E. Fine-tuning the spike: role of the nature and topology of the glycan shield in the structure and dynamics of the SARS-CoV-2 S. *Chem. Sci.* **2022**, 13, 386–395, doi:10.1039/D1SC04832E.

288. Badar, M.S.; Shamsi, S.; Ahmed, J.; Alam, M.A. Molecular Dynamics Simulations: Concept, Methods, and Applications. *Transdisciplinarity* **2022**, 5, 131–151, doi:10.1007/978-3-030-94651-7_7.
289. Liang, J.J.; Pitsillou, E.; Hung, A.; Karagiannis, T.C. A repository of COVID-19 related molecular dynamics simulations and utilisation in the context of nsp10-nsp16 antivirals. *J. Mol. Graph. Model.* **2024**, 126, 108666, doi:10.1016/j.jmgm.2023.108666.
290. Casalino, L.; Gaieb, Z.; Goldsmith, J.A.; Hjorth, C.K.; Dommer, A.C.; Harbison, A.M.; Fogarty, C.A.; Barros, E.P.; Taylor, B.C.; McLellan, J.S.; et al. Beyond Shielding: The Roles of Glycans in the SARS-CoV-2 Spike Protein. *ACS Cent. Sci.* **2020**, 6, 1722–1734, doi:10.1021/acscentsci.0c01056.
291. Alder, B.J.; Wainwright, T.E. Phase Transition for a Hard Sphere System. *J. Chem. Phys.* **1957**, 27, 1208–1209, doi:10.1063/1.1743957.
292. Barker, J.A.; Watts, R.O. Structure of water; A Monte Carlo calculation. *Chemical Physics Letters* **1969**, 3, 144–145, doi:10.1016/0009-2614(69)80119-3.
293. McCammon, J.A.; Gelin, B.R.; Karplus, M. Dynamics of folded proteins. *Nature* **1977**, 267, 585–590, doi:10.1038/267585a0.
294. Schwerdtfeger, P.; Wales, D.J. 100 Years of the Lennard-Jones Potential. *J. Chem. Theory Comput.* **2024**, 20, 3379–3405, doi:10.1021/acs.jctc.4c00135.
295. Stephan, S.; Staubach, J.; Hasse, H. Review and comparison of equations of state for the Lennard-Jones fluid. *Fluid Phase Equilibria* **2020**, 523, 112772, doi:10.1016/j.fluid.2020.112772.
296. Morse, P.M. Diatomic Molecules According to the Wave Mechanics. II. *Vibrational Levels. Phys. Rev.* **1929**, 34, 57–64, doi:10.1103/PhysRev.34.57.
297. Buckingham, R.A. The classical equation of state of gaseous helium, neon and argon. *Proc. R. Soc. Lond. A* **1938**, 168, 264–283, doi:10.1098/rspa.1938.0173.
298. Kirschner, K.N.; Yongye, A.B.; Tschampel, S.M.; Gonzales-Outeirino, J.; Daniels, C.R.; Foley, B.L.; Woods, R.J. GLYCAM06: a generalizable biomolecular force field. *Carbohydrates. Journal of computational chemistry* **2008**, 29, 622–655, doi:10.1002/jcc.20820.
299. Jorgensen, W.L.; Maxwell, D.S.; Tirado-Rives, J. Development and Testing of the OPLS All-Atom Force Field on Conformational Energetics and Properties of Organic Liquids. *Journal of the American Chemical Society* **1996**, 118, 11225–11236, doi:10.1021/ja9621760.

300. Wang, L.-P.; Martinez, T.J.; Pande, V.S. Building Force Fields: An Automatic, Systematic, and Reproducible Approach. *J. Phys. Chem. Lett.* **2014**, 5, 1885–1891, doi:10.1021/jz500737m.
301. Unke, O.T.; Chmiela, S.; Sauceda, H.E.; Gastegger, M.; Poltavsky, I.; Schütt, K.T.; Tkatchenko, A.; Müller, K.-R. Machine Learning Force Fields. *Chemical Reviews* **2021**, 121, 10142–10186, doi:10.1021/acs.chemrev.0c01111.
302. Kolafa, J.; Perram, J.W. Cutoff Errors in the Ewald Summation Formulae for Point Charge Systems. *Molecular Simulation* **1992**, 9, 351–368, doi:10.1080/08927029208049126.
303. Wells, B.A.; Chaffee, A.L. Ewald Summation for Molecular Simulations. *J. Chem. Theory Comput.* **2015**, 11, 3684–3695, doi:10.1021/acs.jctc.5b00093.
304. Essmann, U.; Perera, L.; Berkowitz, M.L.; Darden, T.; Lee, H.; Pedersen, L.G. A smooth particle mesh Ewald method. *J. Chem. Phys.* **1995**, 103, 8577–8593, doi:10.1063/1.470117.
305. Lynden-Bell, R.M. Water and Life: The Unique Properties of H2O, *1st ed.; Taylor & Francis Group: Baton Rouge*, **2010**, ISBN 9781439803578.
306. Berendsen, H.J.C.; Postma, J.P.M.; van Gunsteren, W.F.; Hermans, J. Interaction Models for Water in Relation to Protein Hydration. In Intermolecular Forces: Proceedings of the Fourteenth Jerusalem Symposium on Quantum Chemistry and Biochemistry Held in Jerusalem, Israel, April 13-16, 1981; Pullman, B., *Ed.; Springer: Dordrecht*, **1981**; pp 331–342, ISBN 978-94-015-7658-1.
307. Jorgensen, W.L.; Chandrasekhar, J.; Madura, J.D.; Impey, R.W.; Klein, M.L. Comparison of simple potential functions for simulating liquid water. *J. Chem. Phys.* **1983**, 79, 926–935, doi:10.1063/1.445869.
308. Mahoney, M.W.; Jorgensen, W.L. A five-site model for liquid water and the reproduction of the density anomaly by rigid, nonpolarizable potential functions. *J. Chem. Phys.* **2000**, 112, 8910–8922, doi:10.1063/1.481505.
309. Lamoureux, G.; Harder, E.; Vorobyov, I.V.; Roux, B.; MacKerell, A.D. A polarizable model of water for molecular dynamics simulations of biomolecules. *Chemical Physics Letters* **2006**, 418, 245–249, doi:10.1016/j.cplett.2005.10.135.
310. Verlet, L. Computer "Experiments" on Classical Fluids. I. Thermodynamical Properties of Lennard-Jones Molecules. *Phys. Rev.* **1967**, 159, 98–103, doi:10.1103/PhysRev.159.98.

311. Grubmüller, H.; Heller, H.; Windemuth, A.; Schulten, K. Generalized Verlet Algorithm for Efficient Molecular Dynamics Simulations with Long-range Interactions. *Molecular Simulation* **1991**, 6, 121–142, doi:10.1080/08927029108022142.
312. Martys, N.S.; Mountain, R.D. Velocity Verlet algorithm for dissipative-particle-dynamics-based models of suspensions. *Phys. Rev. E* **1999**, 59, 3733–3736, doi:10.1103/PhysRevE.59.3733.
313. Leimkuhler, B.J.; Reich, S.; Skeel, R.D. Integration Methods for Molecular Dynamics. In Mathematical approaches to biomolecular structure and dynamics: Based on the proceedings of the IMA Summer Program on "Molecular Biology"; Friedman, A., Gulliver, R., Mesirov, J.P., Schulten, K., Sumners, D.W., *Eds.; Springer: New York*, NY, **1996**; pp 161–185, ISBN 978-0-387-94838-6.
314. Ciccotti, G.; Ryckaert, J.P. Molecular dynamics simulation of rigid molecules. *Computer Physics Reports* **1986**, 4, 346–392, doi:10.1016/0167-7977(86)90022-5.
315. Hess, B.; Bekker, H.; Berendsen, H.J.C.; Fraaije, J.G.E.M. LINCS: A linear constraint solver for molecular simulations. *J. Comput. Chem.* **1997**, 18, 1463–1472, doi:10.1002/(SICI)1096-987X(199709)18:12<1463:AID-JCC4>3.0.CO;2-H.
316. Tuckerman, M.E.; Martyna, G.J. Understanding Modern Molecular Dynamics: Techniques and Applications. *The journal of physical chemistry. B* **2000**, 104, 159–178, doi:10.1021/jp992433y.
317. Snyder, H.D.; Kucukkal, T.G. Computational Chemistry Activities with Avogadro and ORCA. *J. Chem. Educ.* **2021**, 98, 1335–1341, doi:10.1021/acs.jchemed.0c00959.
318. Makarewicz, T.; Kaźmierkiewicz, R. Molecular dynamics simulation by GROMACS using GUI plugin for PyMOL. *Journal of Chemical Information and Modeling* **2013**, 53, 1229–1234, doi:10.1021/ci400071x.
319. Jo, S.; Cheng, X.; Lee, J.; Kim, S.; Park, S.-J.; Patel, D.S.; Beaven, A.H.; Lee, K.I.; Rui, H.; Park, S.; et al. CHARMM-GUI 10 years for biomolecular modeling and simulation. *J. Comput. Chem.* **2017**, 38, 1114–1124, doi:10.1002/jcc.24660.
320. Akshaya, J.; Rahul, G.; Rishi Karthigayan, S.; Rishekesan, S.V.; Harischander, A.; Sachin Kumar, S.; Soman, K.P. A comparison between steepest descent and non-linear conjugate gradient algorithms for binding energy minimization of organic molecules. *J. Phys.: Conf. Ser.* **2023**, 2484, 12004, doi:10.1088/1742-6596/2484/1/012004.
321. Nakano, A. Parallel multilevel preconditioned conjugate-gradient approach to variable-charge molecular dynamics. *Computer Physics Communications* **1997**, 104, 59–69, doi:10.1016/S0010-4655(97)00041-6.

322. Aviat, F.; Levitt, A.; Stamm, B.; Maday, Y.; Ren, P.; Ponder, J.W.; Lagardère, L.; Piquemal, J.-P. Truncated Conjugate Gradient: An Optimal Strategy for the Analytical Evaluation of the Many-Body Polarization Energy and Forces in Molecular Simulations. *J. Chem. Theory Comput.* **2017**, 13, 180–190, doi:10.1021/acs.jctc.6b00981.
323. Ray, J.R.; Zhang, H. Correct microcanonical ensemble in molecular dynamics. *Phys. Rev. E* **1999**, 59, 4781–4785, doi:10.1103/physreve.59.4781.
324. Brown, D.; Clarke, J. A comparison of constant energy, constant temperature and constant pressure ensembles in molecular dynamics simulations of atomic liquids. *Molecular Physics* **1984**, 51, 1243–1252, doi:10.1080/00268978400100801.
325. Bussi, G.; Donadio, D.; Parrinello, M. Canonical sampling through velocity rescaling. *J. Chem. Phys.* **2007**, 126, 14101, doi:10.1063/1.2408420.
326. Nosé, S.; Klein, M.L. Constant pressure molecular dynamics for molecular systems. *Molecular Physics* **1983**, 50, 1055–1076, doi:10.1080/00268978300102851.
327. Parrinello, M.; Rahman, A. Polymorphic transitions in single crystals: A new molecular dynamics method. *J. Appl. Phys.* **1981**, 52, 7182–7190, doi:10.1063/1.328693.
328. Berendsen, H.J.C.; Postma, J.P.M.; van Gunsteren, W.F.; DiNola, A.; Haak, J.R. Molecular dynamics with coupling to an external bath. *J. Chem. Phys.* **1984**, 81, 3684–3690, doi:10.1063/1.448118.
329. Martyna, G.J.; Tuckerman, M.E.; Tobias, D.J.; Klein, M.L. Explicit reversible integrators for extended systems dynamics. *Molecular Physics* **1996**, 87, 1117–1157, doi:10.1080/00268979600100761.
330. Humphrey, W.; Dalke, A.; Schulten, K. VMD: visual molecular dynamics. *Journal of molecular graphics* **1996**, 14, 33-8, 27-8, doi:10.1016/0263-7855(96)00018-5.
331. Warnecke, A.; Sandalova, T.; Achour, A.; Harris, R.A. PyTMs: a useful PyMOL plugin for modeling common post-translational modifications. *BMC Bioinformatics* **2014**, 15, 370, doi:10.1186/s12859-014-0370-6.
332. Naughton, F.B.; Alibay, I.; Barnoud, J.; Barreto-Ojeda, E.; Beckstein, O.; Bouysset, C.; Cohen, O.; Gowers, R.J.; MacDermott-Opeskin, H.; Matta, M.; et al. MDAnalysis 2.0 and beyond: fast and interoperable, community driven simulation analysis. *Biophysical Journal* **2022**, 121, 272a-273a, doi:10.1016/j.bpj.2021.11.1368.
333. Tribello, G.A.; Bonomi, M.; Branduardi, D.; Camilloni, C.; Bussi, G. PLUMED 2: New feathers for an old bird. *Computer Physics Communications* **2014**, 185, 604–613, doi:10.1016/j.cpc.2013.09.018.

334. van der Spoel, D.; Lindahl, E.; Hess, B.; Groenhof, G.; Mark, A.E.; Berendsen, H.J.C. GROMACS: fast, flexible, and free. *J. Comput. Chem.* **2005**, 26, 1701–1718, doi:10.1002/jcc.20291.

335. Phillips, J.C.; Braun, R.; Wang, W.; Gumbart, J.; Tajkhorshid, E.; Villa, E.; Chipot, C.; Skeel, R.D.; Kalé, L.; Schulten, K. Scalable molecular dynamics with NAMD. *J. Comput. Chem.* **2005**, 26, 1781–1802, doi:10.1002/jcc.20289.

336. Robal, M.; Brenner, T.; Matsukawa, S.; Ogawa, H.; Truus, K.; Rudolph, B.; Tuvikene, R. Monocationic salts of carrageenans: Preparation and physico-chemical properties. *Food Hydrocolloids* **2017**, 63, 656–667, doi:10.1016/j.foodhyd.2016.09.032.

337. Guibet, M.; Boulenguer, P.; Mazoyer, J.; Kervarec, N.; Antonopoulos, A.; Lafosse, M.; Helbert, W. Composition and distribution of carrabiose moieties in hybrid kappa-/iota-carrageenans using carrageenases. *Biomacromolecules* **2008**, 9, 408–415, doi:10.1021/bm701109r.

338. Jouanneau, D.; Boulenguer, P.; Mazoyer, J.; Helbert, W. Enzymatic degradation of hybrid iota-/nu-carrageenan by Alteromonas fortis iota-carrageenase. *Carbohydrate Research* **2010**, 345, 934–940, doi:10.1016/j.carres.2010.02.014.

339. Hermansson, A.-M.; Eriksson, E.; Jordansson, E. Effects of potassium, sodium and calcium on the microstructure and rheological behaviour of kappa-carrageenan gels. *Carbohydrate polymers* **1991**, 16, 297–320, doi:10.1016/0144-8617(91)90115-S.

340. Engster, M.; Abraham, R. Cecal response to different molecular weights and types of carrageenan in the guinea pig. *Toxicology and Applied Pharmacology* **1976**, 38, 265–282, doi:10.1016/0041-008X(76)90134-4.

341. Bhattacharyya, S.; Xue, L.; Devkota, S.; Chang, E.; Morris, S.; Tobacman, J.K. Carrageenan-induced colonic inflammation is reduced in Bcl10 null mice and increased in IL-10-deficient mice. *Mediators of Inflammation* **2013**, 2013, 397642, doi:10.1155/2013/397642.

342. Shang, Q.; Sun, W.; Shan, X.; Jiang, H.; Cai, C.; Hao, J.; Li, G.; Yu, G. Carrageenan-induced colitis is associated with decreased population of anti-inflammatory bacterium, Akkermansia muciniphila, in the gut microbiota of C57BL/6J mice. *Toxicology Letters* **2017**, 279, 87–95, doi:10.1016/j.toxlet.2017.07.904.

343. Mi, Y.; Chin, Y.X.; Cao, W.X.; Chang, Y.G.; Lim, P.E.; Xue, C.H.; Tang, Q.J. Native κ-carrageenan induced-colitis is related to host intestinal microecology. *Int. J. Biol. Macromol.* **2020**, 147, 284–294, doi:10.1016/j.ijbiomac.2020.01.072.

344. Munyaka, P.M.; Sepehri, S.; Ghia, J.-E.; Khafipour, E. Carrageenan Gum and Adherent Invasive Escherichia coli in a Piglet Model of Inflammatory Bowel Disease: Impact on Intestinal Mucosa-associated Microbiota. *Frontiers in Microbiology* **2016**, 7, 462, doi:10.3389/fmicb.2016.00462.
345. Wu, W.; Zhou, J.; Xuan, R.; Chen, J.; Han, H.; Liu, J.; Niu, T.; Chen, H.; Wang, F. Dietary κ-carrageenan facilitates gut microbiota-mediated intestinal inflammation. *Carbohydrate polymers* **2022**, 277, 118830, doi:10.1016/j.carbpol.2021.118830.
346. Carlucci, M.J.; Ciancia, M.; Matulewicz, M.C.; Cerezo, A.S.; Damonte, E.B. Antiherpetic activity and mode of action of natural carrageenans of diverse structural types. *Antiviral Research* **1999**, 43, 93–102, doi:10.1016/S0166-3542(99)00038-8.
347. Carlucci, M.J.; Scolaro, L.A.; Noseda, M.D.; Cerezo, A.S.; Damonte, E.B. Protective effect of a natural carrageenan on genital herpes simplex virus infection in mice. *Antiviral Research* **2004**, 64, 137–141, doi:10.1016/j.antiviral.2004.07.001.
348. Jang, Y.; Shin, H.; Lee, M.K.; Kwon, O.S.; Shin, J.S.; Kim, Y.; Kim, C.W.; Lee, H.-R.; Kim, M. Antiviral activity of lambda-carrageenan against influenza viruses and severe acute respiratory syndrome coronavirus 2. *Sci Rep* **2021**, 11, 821, doi:10.1038/s41598-020-80896-9.
349. Younes, M.; Aggett, P.; Aguilar, F.; Crebelli, R.; Filipič, M.; Frutos, M.J.; Galtier, P.; Gott, D.; Gundert-Remy, U.; Kuhnle, G.G.; et al. Re-evaluation of carrageenan (E 407) and processed Eucheuma seaweed (E 407a) as food additives. *EFSA Journal* **2018**, 16, e05238, doi:10.2903/j.efsa.2018.5238.
350. van de Velde, F.; Pereira, L.; Rollema, H.S. The revised NMR chemical shift data of carrageenans. *Carbohydrate Research* **2004**, 339, 2309–2313, doi:10.1016/j.carres.2004.07.015.
351. Lecacheux, D.; Panaras, R.; Brigand, G.; Martin, G. Molecular weight distribution of carrageenans by size exclusion chromatography and low angle laser light scattering. *Carbohydrate polymers* **1985**, 5, 423–440, doi:10.1016/0144-8617(85)90003-7.
352. Jol, C.N.; Neiss, T.G.; Penninkhof, B.; Rudolph, B.; Ruiter, G.A. de. A novel high-performance anion-exchange chromatographic method for the analysis of carrageenans and agars containing 3,6-anhydrogalactose. *Anal. Biochem.* **1999**, 268, 213–222, doi:10.1006/abio.1998.3059.
353. Ficko-Blean, E.; Préchoux, A.; Thomas, F.; Rochat, T.; Larocque, R.; Zhu, Y.; Stam, M.; Génicot, S.; Jam, M.; Calteau, A.; et al. Carrageenan catabolism is encoded by a complex

regulon in marine heterotrophic bacteria. *Nat Commun* **2017**, 8, 1685, doi:10.1038/s41467-017-01832-6.

354. Aslanidis, C.; Jong, P.J. de. Ligation-independent cloning of PCR products (LIC-PCR). *Nucleic Acids Res* **1990**, 18, 6069–6074, doi:10.1093/nar/18.20.6069.
355. Mao, B.; Divoux, T.; Snabre, P. Normal force controlled rheology applied to agar gelation. *J. Rheol.* **2016**, 60, 473–489, doi:10.1122/1.4944994.
356. Slootmaekers, D.; Mandel, M.; Reynaers, H. Dynamic light scattering by kappa- and lambda-carrageenan solutions. *Int. J. Biol. Macromol.* **1991**, 13, 17–25, doi:10.1016/0141-8130(91)90005-F.
357. Hjerde, T.; Smidsrd, O.; Christensen, B.E. Analysis of the conformational properties of κ- and ι-carrageenan by size-exclusion chromatography combined with low-angle laser light scattering. *Biopolymers* **1999**, 49, 71–80, doi:10.1002/(SICI)1097-0282(199901)49:1<71:AID-BIP7>3.0.CO;2-H.
358. Spichtig, V.; Austin, S. Determination of the low molecular weight fraction of food-grade carrageenans. *Journal of Chromatography B* **2008**, 861, 81–87, doi:10.1016/j.jchromb.2007.11.012.
359. Guenet, J.-M. Thermoreversible gelation of polymers and biopolymers. (No Title).
360. Picout, D.R.; Ross-Murphy, S.B. Rheology of biopolymer solutions and gels. *TheScientificWorldJournal* **2003**, 3, 105–121, doi:10.1100/tsw.2003.15.
361. Ross-Murphy, S.B. Structure–property relationships in food biopolymer gels and solutions. *J. Rheol.* **1995**, 39, 1451–1463, doi:10.1122/1.550610.
362. Kamińska-Dwórznicka, A.; Janczewska-Dupczyk, A.; Kot, A.; Łaba, S.; Samborska, K. The impact of ι- and κ-carrageenan addition on freezing process and ice crystals structure of strawberry sorbet frozen by various methods. *Journal of Food Science* **2020**, 85, 50–56, doi:10.1111/1750-3841.14987.
363. Hale, J.; Gerhäuser, J.; Gaukel, V.; Wefers, D. Commercially available carrageenans show broad variation in their structure, composition, and functionality. *Eur Food Res Technol* **2024**, 250, 2989–3003, doi:10.1007/s00217-024-04605-w.
364. Mangione, M.R.; Giacomazza, D.; Bulone, D.; Martorana, V.; Cavallaro, G.; San Biagio, P.L. K(+) and Na(+) effects on the gelation properties of kappa-Carrageenan. *Biophysical Chemistry* **2005**, 113, 129–135, doi:10.1016/j.bpc.2004.08.005.
365. Polowsky, P.J.; Janaswamy, S. Hydrocolloid-based nutraceutical delivery systems: Effect of counter-ions on the encapsulation and release. *Food Hydrocolloids* **2015**, 43, 658–663, doi:10.1016/j.foodhyd.2014.07.033.

366. Ciancia, M.; Noseda, M.D.; Matulewicz, M.C.; Cerezo, A.S. Alkali-modification of carrageenans: mechanism and kinetics in the kappa/iota-, mu/nu- and lambda-series. *Carbohydrate polymers* **1993**, 20, 95–98, doi:10.1016/0144-8617(93)90083-G.
367. Doyle, J.P.; Giannouli, P.; Rudolph, B.; Morris, E.R. Preparation, authentication, rheology and conformation of theta carrageenan. *Carbohydrate polymers* **2010**, 80, 648–654, doi:10.1016/j.carbpol.2009.10.029.
368. Rochas, C.; Rinaudo, M. Activity coefficients of counterions and conformation in kappa-carrageenan systems. *Biopolymers* **1980**, 19, 1675-1687, doi:10.1002/bip.1980.360190911.
369. Nilsson, S.; Piculell, L.; Joensson, B. Helix-coil transitions of ionic polysaccharides analyzed within the Poisson-Boltzmann cell model. 1. Effects of polyion concentration and counterion valency. *Macromolecules* **1989**, 22, 2367–2375, doi:10.1021/ma00195a063.
370. Archer, D.L. Freezing: an underutilized food safety technology? *International journal of food microbiology* **2004**, 90, 127–138, doi:10.1016/s0168-1605(03)00215-0.
371. Fennema, O. An over-all view of low temperature food preservation. *Cryobiology* **1966**, 3, 197–213, doi:10.1016/s0011-2240(66)80013-5.
372. Pegg, D.E. Principles of cryopreservation. *Methods in molecular biology (Clifton, N.J.)* **2007**, 368, 39–57, doi:10.1007/978-1-59745-362-2_3.
373. Russell, A.B.; Cheney, P.E.; Wantling, S.D. Influence of freezing conditions on ice crystallisation in ice cream. *Journal of Food Engineering* **1999**, 39, 179–191, doi:10.1016/S0260-8774(98)00161-7.
374. Zhang, B.; Zhao, J.; Chen, S.; Zhang, X.; Wei, W. Influence of trehalose and alginate oligosaccharides on ice crystal growth and recrystallization in whiteleg shrimp (Litopenaeus vannamei) during frozen storage with temperature fluctuations. *International Journal of Refrigeration* **2019**, 99, 176–185, doi:10.1016/j.ijrefrig.2018.11.015.
375. Gutierrez, M.S.C.; Araujo, L.C. de; Silvera Junior, V. An empirical model to estimate the growth of ice crystals for storage of Tilapia at variable temperature conditions. *Food Sci. Technol* **2019**, 39, 567–572, doi:10.1590/fst.31717.
376. Hartel, R.W. Mechanisms and kinetics of recrystallization in ice cream. The Properties of Water in Foods ISOPOW 6; *Springer, Boston, MA*, **1998**; pp 287–319.
377. Goff, H.D.; Caldwell, K.B.; Stanley, D.W.; Maurice, T.J. The Influence of Polysaccharides on the Glass Transition in Frozen Sucrose Solutions and Ice Cream. *Journal of Dairy Science* **1993**, 76, 1268–1277, doi:10.3168/jds.S0022-0302(93)77456-1.

378. Hartel, R.W. Ice crystallization during the manufacture of ice cream. *Trends in Food Science & Technology* **1996**, 7, 315–321, doi:10.1016/0924-2244(96)10033-9.
379. Rahman, A.T.; Arai, T.; Yamauchi, A.; Miura, A.; Kondo, H.; Ohyama, Y.; Tsuda, S. Ice recrystallization is strongly inhibited when antifreeze proteins bind to multiple ice planes. *Sci Rep* **2019**, 9, 2212, doi:10.1038/s41598-018-36546-2.
380. Zepeda, S.; Yokoyama, E.; Uda, Y.; Katagiri, C.; Furukawa, Y. In Situ Observation of Antifreeze Glycoprotein Kinetics at the Ice Interface Reveals a Two-Step Reversible Adsorption Mechanism. *Crystal Growth & Design* **2008**, 8, 3666–3672, doi:10.1021/cg800269w.
381. Adar, C.; Sirotinskaya, V.; Bar Dolev, M.; Friehmann, T.; Braslavsky, I. Falling water ice affinity purification of ice-binding proteins. *Sci Rep* **2018**, 8, 11046, doi:10.1038/s41598-018-29312-x.
382. Loureiro, R.R.; Cornish, M.L.; Neish, I.C. Applications of Carrageenan: With Special Reference to Iota and Kappa Forms as Derived from the Eucheumatoid Seaweeds. Tropical Seaweed Farming Trends, Problems and Opportunities; *Springer, Cham*, **2017**; pp 165–171.
383. Rupert, R.; Rodrigues, K.F.; Thien, V.Y.; Yong, W.T.L. Carrageenan From Kappaphycus alvarezii (Rhodophyta, Solieriaceae): Metabolism, Structure, Production, and Application. *Frontiers in Plant Science* **2022**, 13, 859635, doi:10.3389/fpls.2022.859635.
384. Imeson, A. Food Stabilisers, Thickeners and Gelling Agents; *John Wiley & Sons Ltd: Hoboken*, **2011**, ISBN 9781405132671.
385. Millane, R.P.; Chandrasekaran, R.; Arnott, S.; Dea, I.C. The molecular structure of kappa-carrageenan and comparison with iota-carrageenan. *Carbohydrate Research* **1988**, 182, 1–17, doi:10.1016/0008-6215(88)84087-4.
386. Muthukumar, J.; Chidambaram, R.; Sukumaran, S. Sulfated polysaccharides and its commercial applications in food industries-A review. *Journal of Food Science and Technology* **2021**, 58, 2453–2466, doi:10.1007/s13197-020-04837-0.
387. Diener, M.; Adamcik, J.; Sánchez-Ferrer, A.; Jaedig, F.; Schefer, L.; Mezzenga, R. Primary, Secondary, Tertiary and Quaternary Structure Levels in Linear Polysaccharides: From Random Coil, to Single Helix to Supramolecular Assembly. *Biomacromolecules* **2019**, 20, 1731–1739, doi:10.1021/acs.biomac.9b00087.
388. Mangione, M.R.; Giacomazza, D.; Bulone, D.; Martorana, V.; San Biagio, P.L. Thermoreversible gelation of kappa-carrageenan: relation between conformational transition

and aggregation. *Biophysical Chemistry* **2003**, 104, 95–105, doi:10.1016/S0301-4622(02)00341-1.

389. Burkey, A.A.; Riley, C.L.; Wang, L.K.; Hatridge, T.A.; Lynd, N.A. Understanding Poly(vinyl alcohol)-Mediated Ice Recrystallization Inhibition through Ice Adsorption Measurement and pH Effects. *Biomacromolecules* **2018**, 19, 248–255, doi:10.1021/acs.biomac.7b01502.
390. Lee, S.Y.; Kim, M.; Won, T.K.; Back, S.H.; Hong, Y.; Kim, B.-S.; Ahn, D.J. Janus regulation of ice growth by hyperbranched polyglycerols generating dynamic hydrogen bonding. *Nat Commun* **2022**, 13, 6532, doi:10.1038/s41467-022-34300-x.
391. Food Hydrocolloids; Glicksman, M., Ed.; *CRC Press: Boca Raton*, *Florida, London, England, New York*, **2019**, ISBN 9780429290374.
392. Riedel, L. Brechungsvermögen und Gefriertemperaturen von Fruchtsäften in Abhängigkeit von der Konzentration. *Z Lebensm Unters Forch* **1949**, 89, 289–299, doi:10.1007/BF01984301.
393. Yu, G.; Yang, B.; Ren, W.; Zhao, X.; Zhang, J.; Barrow, C. A comparative analysis of four kinds of polysaccharides purified from Furcellaria lumbricalis. *J Ocean Univ. China* **2007**, 6, 16–20, doi:10.1007/s11802-007-0016-7.
394. Kratochvílová, I.; Golan, M.; Pomeisl, K.; Richter, J.; Sedláková, S.; Šebera, J.; Mičová, J.; Falk, M.; Falková, I.; Řeha, D.; et al. Theoretical and experimental study of the antifreeze protein AFP752, trehalose and dimethyl sulfoxide cryoprotection mechanism: correlation with cryopreserved cell viability. *RSC Adv.* **2017**, 7, 352–360, doi:10.1039/C6RA25095E.
395. Duman, J.G. Antifreeze and ice nucleator proteins in terrestrial arthropods. *Annual Review of Physiology* **2001**, 63, 327–357, doi:10.1146/annurev.physiol.63.1.327.
396. Muñoz, P.A.; Márquez, S.L.; González-Nilo, F.D.; Márquez-Miranda, V.; Blamey, J.M. Structure and application of antifreeze proteins from Antarctic bacteria. *Microb Cell Fact* **2017**, 16, 138, doi:10.1186/s12934-017-0737-2.
397. Muldrew, K.; McGann, L.E. Mechanisms of intracellular ice formation. *Biophysical Journal* **1990**, 57, 525–532, doi:10.1016/S0006-3495(90)82568-6.
398. Celik, Y.; Graham, L.A.; Mok, Y.-F.; Bar, M.; Davies, P.L.; Braslavsky, I. Superheating of ice crystals in antifreeze protein solutions. *Proceedings of the National Academy of Sciences of the United States of America* **2010**, 107, 5423–5428, doi:10.1073/pnas.0909456107.

399. Scotter, A.J.; Marshall, C.B.; Graham, L.A.; Gilbert, J.A.; Garnham, C.P.; Davies, P.L. The basis for hyperactivity of antifreeze proteins. *Cryobiology* **2006**, 53, 229–239, doi:10.1016/j.cryobiol.2006.06.006.
400. Hanada, Y.; Nishimiya, Y.; Miura, A.; Tsuda, S.; Kondo, H. Hyperactive antifreeze protein from an Antarctic sea ice bacterium Colwellia sp. has a compound ice-binding site without repetitive sequences. *FEBS J.* **2014**, 281, 3576–3590, doi:10.1111/febs.12878.
401. Davies, P.L.; Hew, C.L. Biochemistry of fish antifreeze proteins. *FASEB journal : official publication of the Federation of American Societies for Experimental Biology* **1990**, 4, 2460–2468, doi:10.1096/fasebj.4.8.2185972.
402. Knight, C.A.; DeVries, A.L. Melting Inhibition and Superheating of Ice by an Antifreeze Glycopeptide. *American Association for the Advancement of Science [Online]*, August 4, **1989**. Available online: https://www.science.org/doi/10.1126/science.245.4917.505 (accessed on 25 November 2024).
403. Basu, K.; Garnham, C.P.; Nishimiya, Y.; Tsuda, S.; Braslavsky, I.; Davies, P. Determining the ice-binding planes of antifreeze proteins by fluorescence-based ice plane affinity. *Journal of Visualized Experiments : JoVE* **2014**, e51185, doi:10.3791/51185.
404. Pertaya, N.; Marshall, C.B.; Celik, Y.; Davies, P.L.; Braslavsky, I. Direct visualization of spruce budworm antifreeze protein interacting with ice crystals: basal plane affinity confers hyperactivity. *Biophysical Journal* **2008**, 95, 333–341, doi:10.1529/biophysj.107.125328.
405. Ramløv, H.; DeVries, A.L.; Wilson, P.W. Antifreeze glycoproteins from the antarctic fish Dissostichus mawsoni studied by differential scanning calorimetry (DSC) in combination with nanolitre osmometry. *Cryo Letters* **2005**, 26, 73–84.
406. Hassa-Roudsari, M.; Goff, H.D. A new quantitative method to measure activity of ice structuring proteins using differential scanning calorimetry. *Cryo Letters* **2012**, 33, 118–125.
407. Weng, L.; Stott, S.L.; Toner, M. Molecular Dynamics at the Interface between Ice and Poly(vinyl alcohol) and Ice Recrystallization Inhibition. *Langmuir : the ACS journal of surfaces and colloids* **2018**, 34, 5116–5123, doi:10.1021/acs.langmuir.7b03243.
408. Nada, H.; Furukawa, Y. Antifreeze proteins: computer simulation studies on the mechanism of ice growth inhibition. *Polym J* **2012**, 44, 690–698, doi:10.1038/pj.2012.13.
409. Naullage, P.M.; Qiu, Y.; Molinero, V. What Controls the Limit of Supercooling and Superheating of Pinned Ice Surfaces? *J. Phys. Chem. Lett.* **2018**, 9, 1712–1720, doi:10.1021/acs.jpclett.8b00300.

410. Midya, U.S.; Bandyopadhyay, S. Operation of Kelvin Effect in the Activities of an Antifreeze Protein: A Molecular Dynamics Simulation Study. *The journal of physical chemistry. B* **2018**, 122, 3079–3087, doi:10.1021/acs.jpcb.8b00846.
411. Nada, H.; Furukawa, Y. Growth inhibition at the ice prismatic plane induced by a spruce budworm antifreeze protein: a molecular dynamics simulation study. *Phys. Chem. Chem. Phys.* **2011**, 13, 19936–19942, doi:10.1039/C1CP21929D.
412. Berendsen, H.; van der Spoel, D.; van Drunen, R. GROMACS: A message-passing parallel molecular dynamics implementation. *Computer Physics Communications* **1995**, 91, 43–56, doi:10.1016/0010-4655(95)00042-E.
413. Abascal, J.L.F.; Sanz, E.; García Fernández, R.; Vega, C. A potential model for the study of ices and amorphous water: TIP4P/Ice. *J. Chem. Phys.* **2005**, 122, 234511, doi:10.1063/1.1931662.
414. Kaminski, G.A.; Friesner, R.A.; Tirado-Rives, J.; Jorgensen, W.L. Evaluation and Reparametrization of the OPLS-AA Force Field for Proteins via Comparison with Accurate Quantum Chemical Calculations on Peptides. *The journal of physical chemistry. B* **2001**, 105, 6474–6487, doi:10.1021/jp003919d.
415. Sæthre, B.S.; van der Spoel, D.; Hoffmann, A.C. Free energy of separation of structure II clathrate hydrate in water and a light oil. *The journal of physical chemistry. B* **2012**, 116, 5933–5940, doi:10.1021/jp300230p.
416. Conde, M.M.; Rovere, M.; Gallo, P. High precision determination of the melting points of water TIP4P/2005 and water TIP4P/Ice models by the direct coexistence technique. *J. Chem. Phys.* **2017**, 147, 244506, doi:10.1063/1.5008478.
417. García Fernández, R.; Abascal, J.L.F.; Vega, C. The melting point of ice Ih for common water models calculated from direct coexistence of the solid-liquid interface. *J. Chem. Phys.* **2006**, 124, 144506, doi:10.1063/1.2183308.
418. Chakraborty, S.; Jana, B. Molecular Insight into the Adsorption of Spruce Budworm Antifreeze Protein to an Ice Surface: A Clathrate-Mediated Recognition Mechanism. *Langmuir : the ACS journal of surfaces and colloids* **2017**, 33, 7202–7214, doi:10.1021/acs.langmuir.7b01733.
419. Espinosa, J.R.; Vega, C.; Sanz, E. Ice–Water Interfacial Free Energy for the TIP4P, TIP4P/2005, TIP4P/Ice, and mW Models As Obtained from the Mold Integration Technique. *J. Phys. Chem. C* **2016**, 120, 8068–8075, doi:10.1021/acs.jpcc.5b11221.
420. Kumari, S.; Muthachikavil, A.V.; Tiwari, J.K.; Punnathanam, S.N. Computational Study of Differences between Antifreeze Activity of Type-III Antifreeze Protein from Ocean

Pout and Its Mutant. *Langmuir : the ACS journal of surfaces and colloids* **2020**, 36, 2439–2448, doi:10.1021/acs.langmuir.0c00065.

421. George, R.M. Freezing proceseses used in the food industry. *Trends in Food Science & Technology* **1993**, 4, 134–138, doi:10.1016/0924-2244(93)90032-6.
422. Bosch, E.; Vos, M. de; Humaidan, P. The Future of Cryopreservation in Assisted Reproductive Technologies. *Frontiers in endocrinology* **2020**, 11, 67, doi:10.3389/fendo.2020.00067.
423. Mazur, P. Cryobiology: the freezing of biological systems. *Science* **1970**, 168, 939–949, doi:10.1126/science.168.3934.939.
424. Fowler, A.; Toner, M. Cryo-injury and biopreservation. *Annals of the New York Academy of Sciences* **2005**, 1066, 119–135, doi:10.1196/annals.1363.010.
425. Knight, C.A.; Cheng, C.C.; DeVries, A.L. Adsorption of alpha-helical antifreeze peptides on specific ice crystal surface planes. *Biophysical Journal* **1991**, 59, 409–418, doi:10.1016/S0006-3495(91)82234-2.
426. Houston, M.E.; Chao, H.; Hodges, R.S.; Sykes, B.D.; Kay, C.M.; Sönnichsen, F.D.; Loewen, M.C.; Davies, P.L. Binding of an oligopeptide to a specific plane of ice. *Journal of Biological Chemistry* **1998**, 273, 11714–11718, doi:10.1074/jbc.273.19.11714.
427. Mangiagalli, M.; Bar-Dolev, M.; Tedesco, P.; Natalello, A.; Kaleda, A.; Brocca, S.; Pascale, D. de; Pucciarelli, S.; Miceli, C.; Braslavsky, I.; et al. Cryo-protective effect of an ice-binding protein derived from Antarctic bacteria. *FEBS J.* **2017**, 284, 163–177, doi:10.1111/febs.13965.
428. Kaleda, A.; Haleva, L.; Sarusi, G.; Pinsky, T.; Mangiagalli, M.; Bar Dolev, M.; Lotti, M.; Nardini, M.; Braslavsky, I. Saturn-Shaped Ice Burst Pattern and Fast Basal Binding of an Ice-Binding Protein from an Antarctic Bacterial Consortium. *Langmuir : the ACS journal of surfaces and colloids* **2019**, 35, 7337–7346, doi:10.1021/acs.langmuir.8b01914.
429. Zielkiewicz, J. Mechanism of antifreeze protein functioning and the "anchored clathrate water" concept. *J. Chem. Phys.* **2023**, 159, doi:10.1063/5.0158590.
430. Smolin, N.; Daggett, V. Formation of ice-like water structure on the surface of an antifreeze protein. *The Journal of Physical Chemistry B* **2008**, 112, 6193–6202, doi:10.1021/jp710546e.
431. Lee, H. Effects of hydrophobic and hydrogen-bond interactions on the binding affinity of antifreeze proteins to specific ice planes. *J. Mol. Graph. Model.* **2019**, 87, 48–55, doi:10.1016/j.jmgm.2018.11.006.

432. Midya, U.S.; Bandyopadhyay, S. Ice Recrystallization Unveils the Binding Mechanism Operating at a Diffused Interface. *The journal of physical chemistry. B* **2024**, 128, 1170–1178, doi:10.1021/acs.jpcb.3c05934.
433. Park, J.K.; Park, S.-J.; Jeong, B. Poly(l-alanine-co-l-threonine succinate) as a Biomimetic Cryoprotectant. *ACS Appl. Mater. Interfaces* **2023**, 15, 58092–58102, doi:10.1021/acsami.3c11260.
434. ANDERSON, N.S.; DOLAN, T.C.S.; REES, D.A. Evidence for a Common Structural Pattern in the Polysaccharide Sulphates of the Rhodophyceae. *Nature* **1965**, 205, 1060–1062, doi:10.1038/2051060a0.
435. Hermansson, A.-M. Rheological and microstructural evidence for transient states during gelation of kappa-carrageenan in the presence of potassium. *Carbohydrate polymers* **1989**, 10, 163–181, doi:10.1016/0144-8617(89)90009-X.
436. Nguyen, B.T.; Nicolai, T.; Benyahia, L.; Chassenieux, C. Synergistic effects of mixed salt on the gelation of κ-carrageenan. *Carbohydrate polymers* **2014**, 112, 10–15, doi:10.1016/j.carbpol.2014.05.048.
437. Westberry, B.P.; Mansel, B.W.; Lundin, L.; Williams, M.A.K. Molecular dynamics simulations and X-ray scattering show the κ-carrageenan disorder-to-order transition to be the formation of double-helices. *Carbohydrate polymers* **2023**, 302, 120417, doi:10.1016/j.carbpol.2022.120417.
438. Westberry, B.P.; Mansel, B.W.; Ryan, T.M.; Lundin, L.; Williams, M.A.K. X-ray scattering and molecular dynamics simulations reveal the secondary structure of κ-carrageenan in the solution state. *Carbohydrate polymers* **2022**, 296, 119958, doi:10.1016/j.carbpol.2022.119958.
439. Rafe, A.; Glikman, D.; Rey, N.G.; Haller, N.; Kulozik, U.; Braunschweig, B. Structure-property relations of β-lactoglobulin/κ-carrageenan mixtures in aqueous foam. *Colloids and Surfaces A: Physicochemical and Engineering Aspects* **2022**, 640, 128267, doi:10.1016/j.colsurfa.2022.128267.
440. Shahbazi, M.; Rajabzadeh, G.; Ettelaie, R.; Rafe, A. Kinetic study of κ-carrageenan degradation and its impact on mechanical and structural properties of chitosan/κ-carrageenan film. *Carbohydrate polymers* **2016**, 142, 167–176, doi:10.1016/j.carbpol.2016.01.037.
441. Ardestani, F.; Asl, A.H.; Rafe, A.; Miao, S. Preparation and characterization of zein-kappa carrageenan complex for encapsulation of saffron, and in vitro controlled release study. *Food Hydrocolloids* **2025**, 162, 110816, doi:10.1016/j.foodhyd.2024.110816.

442. Stephen, A.M.; Phillips, G.O. Food Polysaccharides and Their Applications; *CRC Press*, **2016**, ISBN 9780429116162.
443. Bleszynski, M.; Reil, M.; Kumosa, M. Hydroxyl Group Separation Distances in Anti-Freeze Compounds and Their Effects on Ice Nucleation. *International Journal of Molecular Sciences* **2020**, 21, doi:10.3390/ijms21228488.
444. Tam, R.Y.; Ferreira, S.S.; Czechura, P.; Chaytor, J.L.; Ben, R.N. Hydration index--a better parameter for explaining small molecule hydration in inhibition of ice recrystallization. *Journal of the American Chemical Society* **2008**, 130, 17494–17501, doi:10.1021/ja806284x.
445. Patel, M.; Park, J.K.; Jeong, B. Rediscovery of poly(ethylene glycol)s as a cryoprotectant for mesenchymal stem cells. *Biomater. Res.* **2023**, 27, 17, doi:10.1186/s40824-023-00356-z.
446. Patel, M.; Vernon, B.; Jeong, B. Low-Molecular-Weight PEGs for Cryopreservation of Stem Cell Spheroids. *Biomater. Res.* **2024**, 28, 37, doi:10.34133/bmr.0037.
447. Bar-Dolev, M.; Basu, K.; Braslavsky, I.; Davies, P.L. Structure–Function of IBPs and Their Interactions with Ice. In Antifreeze Proteins Volume 2: Biochemistry, Molecular Biology and Applications, 1st ed. 2020; Ramløv, H., Friis, D.S., *Eds.; Springer International Publishing; Imprint Springer: Cham*, **2020**; pp 69–107, ISBN 978-3-030-41948-6.
448. Hale, J.; Furch, A.; Gerhäuser, J.; Gaukel, V.; Wefers, D. Ice recrystallization inhibition activity of chemically defined carrageenans. *Food Hydrocolloids* **2024**, 110423, doi:10.1016/j.foodhyd.2024.110423.
449. Bore, S.L.; Piaggi, P.M.; Car, R.; Paesani, F. Phase diagram of the TIP4P/Ice water model by enhanced sampling simulations. *J. Chem. Phys.* **2022**, 157, 54504, doi:10.1063/5.0097463.
450. Piaggi, P.M.; Car, R. Phase equilibrium of liquid water and hexagonal ice from enhanced sampling molecular dynamics simulations. *J. Chem. Phys.* **2020**, 152, 204116, doi:10.1063/5.0011140.
451. Vega, C.; Martin-Conde, M.; Patrykiejew, A. Absence of superheating for ice I h with a free surface: a new method of determining the melting point of different water models. *Molecular Physics* **2006**, 104, 3583–3592, doi:10.1080/00268970600967948.
452. Vega, C.; Sanz, E.; Abascal, J.L.F. The melting temperature of the most common models of water. *J. Chem. Phys.* **2005**, 122, 114507, doi:10.1063/1.1862245.
453. Abraham, M.J.; Murtola, T.; Schulz, R.; Páll, S.; Smith, J.C.; Hess, B.; Lindahl, E. GROMACS: High performance molecular simulations through multi-level parallelism

from laptops to supercomputers. *SoftwareX* **2015**, 1-2, 19–25, doi:10.1016/j.softx.2015.06.001.

454. Abraham, M.; Hess, B.; van der Spoel, D.; Lindahl, E. GROMACS 2021.2 Manual. Available online: https://manual.gromacs.org/documentation/2021/index.html.
455. Stukowski, A. Visualization and analysis of atomistic simulation data with OVITO–the Open Visualization Tool. *Modelling Simul. Mater. Sci. Eng.* **2010**, 18, 15012, doi:10.1088/0965-0393/18/1/015012.
456. Matsumoto, M.; Yagasaki, T.; Tanaka, H. GenIce: Hydrogen-Disordered Ice Generator. *Journal of computational chemistry* **2018**, 39, 61–64, doi:10.1002/jcc.25077.
457. Case, D.A.; Aktulga, H.M.; Belfon, K.; Ben-Shalom, I.Y.; Brozell, S.R.; Cerutti, D.S.; Cheatham, T.[.; Cruzeiro, V.; Darden, T.A.; Duke, R.E.; et al. Amber 2021 **2021**.
458. Bernardi, A.; Faller, R.; Reith, D.; Kirschner, K.N. ACPYPE update for nonuniform 1–4 scale factors: Conversion of the GLYCAM06 force field from AMBER to GROMACS. *SoftwareX* **2019**, 10, 100241, doi:10.1016/j.softx.2019.100241.
459. Da Sousa Silva, A.W.; Vranken, W.F. ACPYPE - AnteChamber PYthon Parser interfacE. *BMC Research Notes* **2012**, 5, 367, doi:10.1186/1756-0500-5-367.
460. Montero de Hijes, P.; Espinosa, J.R.; Vega, C.; Sanz, E. Ice growth rate: Temperature dependence and effect of heat dissipation. *J. Chem. Phys.* **2019**, 151, 44509, doi:10.1063/1.5103273.
461. Nguyen, A.H.; Molinero, V. Identification of Clathrate Hydrates, Hexagonal Ice, Cubic Ice, and Liquid Water in Simulations: the CHILL+ Algorithm. *The journal of physical chemistry. B* **2015**, 119, 9369–9376, doi:10.1021/jp510289t.
462. Levitt, M.; Sharon, R. Accurate simulation of protein dynamics in solution. *Proceedings of the National Academy of Sciences of the United States of America* **1988**, 85, 7557–7561, doi:10.1073/pnas.85.20.7557.
463. Luzar, A.; Chandler, D. Hydrogen-bond kinetics in liquid water. *Nature* **1996**, 379, 55–57, doi:10.1038/379055a0.
464. Luzar, A. Resolving the hydrogen bond dynamics conundrum. *J. Chem. Phys.* **2000**, 113, 10663–10675, doi:10.1063/1.1320826.
465. Rozmanov, D.; Kusalik, P.G. Anisotropy in the crystal growth of hexagonal ice, I(h). *J. Chem. Phys.* **2012**, 137, 94702, doi:10.1063/1.4748377.
466. Arai, T.; Yamauchi, A.; Yang, Y.; Singh, S.M.; Sasaki, Y.C.; Tsuda, S. Adsorption of ice-binding proteins onto whole ice crystal surfaces does not necessarily confer a high thermal hysteresis activity. *Sci Rep* **2022**, 12, 15443, doi:10.1038/s41598-022-19803-3.

467. Chakraborty, S.; Jana, B. Optimum Number of Anchored Clathrate Water and Its Instantaneous Fluctuations Dictate Ice Plane Recognition Specificities of Insect Antifreeze Protein. *The journal of physical chemistry. B* **2018**, 122, 3056–3067, doi:10.1021/acs.jpcb.8b00548.

468. Heilig, A.; Göggerle, A.; Hinrichs, J. Multiphase visualisation of fat containing β-lactoglobulin–κ-carrageenan gels by confocal scanning laser microscopy, using a novel dye, V03-01136, for fat staining. *LWT - Food Science and Technology* **2009**, 42, 646–653, doi:10.1016/j.lwt.2008.08.006.

List of Figures

List of Tables